

Space Debris Or Natural?
*Impacts On NASA's Long Duration
Exposure Facility.*

A Thesis submitted for the
Degree of Doctor of Philosophy

by

Sunil Prabhakar Deshpande

July 1993

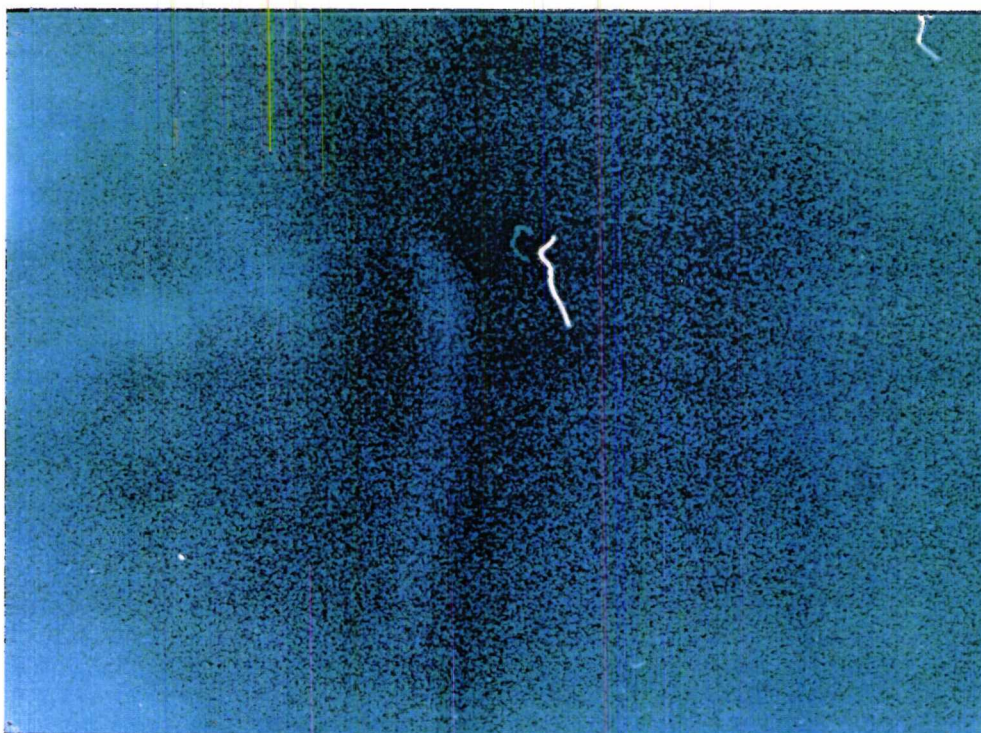
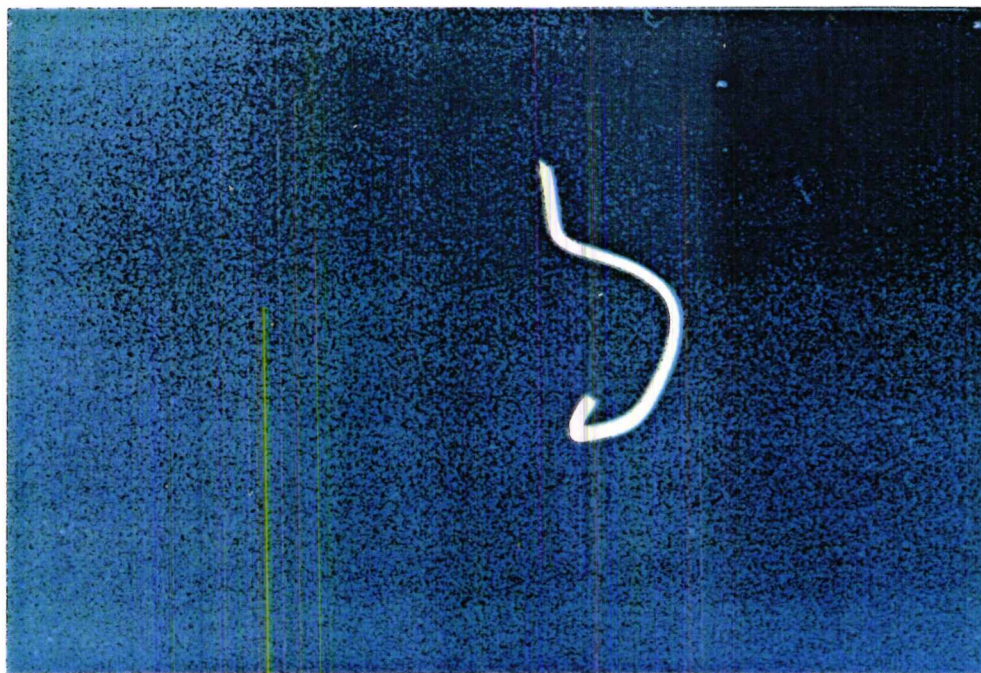
Unit for Space Sciences
University of Kent at Canterbury,
Canterbury,
Kent.
U.K.

To

Muriel and Prabhakar Deshpande

*"Rhoddoch bopeth I mi,
gobeithiaf nawr ddechrau cyflenwi eich breuddwydion."*

तुम्ही विलेल्या सर्व प्रोत्साहनावर
आता मी तुमचे स्वप्न साकार
करण्याचा प्रयत्न करीन.



Waiting for a Disaster?

The above photographs are actual pieces of space debris, known as superzips. These connectors are released when the upper stages of rocket boosters separate. The photographs show a close up of such a superzip and a queue of three all lined up. These objects are approximately 4-5m in length and 20cm wide and as such cannot be detected from ground based systems, as the continuously furl and unfurl.

The photographs were taken by astronaut F. Story Musgrave on STS-44, November 1991 at a distance well within the avoidance manoeuvre zone around the STS.

Photographs are courtesy of Mr. Carl Maag of T & M Engineering, California, USA.

Abstract

The Long Duration Exposure Facility has provided the most complete in-situ study of the near Earth environment to date. This thesis details the spacecraft conception and development culminating in a 69 month excursion into low Earth orbit. The techniques required to analyse the retrieved data are discussed, and indeed, these techniques are applicable to any spacecraft surface or terrestrial experimental hypervelocity impact project. The results have shown that all faces of the LDEF have been impacted by both natural and anthropogenic space debris to some extent. The current models employed to determine the relative proportions of these populations on the LDEF are shown to be inadequate, although the assumptions used are quite sweeping. The modelling presented shows a definite need to use a more anisotropic distribution when discussing the natural environment that incorporates both meteor streams and comet encounters. The problems and concerns surrounding the present anthropogenic space debris population is discussed in detail concluding with the need for better Earth and space borne detection systems and understanding of orbital dynamics of small particles, presently undetectable. An average

particle density for interplanetary particles of 1gcm^{-3} is derived from a comparison of data from different experimental surfaces on the Space face of LDEF. The impact direction distributions of both natural and anthropogenic space debris is illustrated, including an enhanced space debris distribution, which accounts for some of the limits in the presently tracked data sets. These data sets are discussed in terms of generation, ownership and orbital distribution.

Acknowledgements

I wish to acknowledge the support and guidance of my supervisor John Zarnecki and my professor and LDEF MAP Principal Investigator Tony McDonnell, whose combined guidance has led me on an interesting and varied exposure to the space science arena. Starting with the some what daunting task of assisting the on the ESA DISCOS contract, to the mundane counting of impact sites on spaceflight surfaces through the tortuous paths of project management and proposal writing and numerous public relation activities, culminating in the experience of a life-time on board the CNES Caravelle microgravity flight, and not to forget the odd delve into cometary analysis and flight dynamics of the tennis ball.

I am indebted to Dr (!) Ken Sullivan for making my job somewhat easier, though I am tempted to argue this point, in the development of the Sullivan model used in this work, to Simon Green and Neil Mackay for their valuable assistance given to me with producing data from their space debris model. All the guys of the Canterbury LDEF Team, Piers Newman, Matthew Paley, Steve Mullen, Michael Neish, David Gardner,

who have had the ignominious pleasure of working in the clean room gaining the invaluable data some of which is presented here. Many thanks must go to Matthew Paley for being just a whizz on the computer and making my shortfalls in the computing area less painful. All his magic assistance with the keyboard is well appreciated and sorely missed (lucky old BAS!). I must thank Dr. Paul Birchley for coming to my rescue at short notice and proof reading this epic, and actually enjoying it!!!! Many thanks must go to whole crew of STS-32 and NASA staff involved in the LDEF mission and especially astronaut Bonnie Dunbar whose deft touch made all this possible.

Whilst mentioning colleagues I owe a lot of my understanding of the space debris problems to Darren McKnight of Kaman Sciences Corp, USA, who was always willing to chat on the phone and freely offer advice. DISCOS accessing from the UK would have been a great source of grievance if it were not for both Rüdiger Jehn, and Heiner Klinkrad of ESA/ESOC. The great discussions on Italian lifestyle, the universe and jobs with Tim Stevenson kept me thinking I was glad to be a scientist and not an engineer. Many thanks are awarded to Carl Maag for pulling wonders with NASA getting my badges to fly on STS-57, EuReCa retrieval mission, and giving me some outstanding photos.

I must thank Roberta, Dave and Joshua Sampson for all their great meals and wish them every greatest possible success back down-under. The last few months of this momentous book has been made more enjoyable thanks to the concerted effort of the Indian cricket team ; India 3 - England 0 in the test score, this winter, made working in the lab that much more bearable at this mind numbing time.

I wish to convey my greatest appreciation and love to my parents Muriel and Prabhakar Deshpande without whom non of this would have been possible and indeed not worth much. All their love and support (both financially and emotionally) through all my schooling has been the inspiration to me to succeed even when at times the end

was far, far away. I must also thank Jaya, my sister, for being the sensible one amongst us, Vikas for being the one who enjoys life to the full and would enjoy it even more if he could get the car!! and Arun, the soon to be world renowned guitarist - Hurry Up!! Sunday lunches were always an event, at White Rose, when all together and I wish them all the very best for their many years to come.

Amongst this personal acknowledgement I owe a great deal of my sanity and patience to the great love and friendship that I have for Margherita and have received in turn. She has always been there when I needed to return to the real world offering her unrelenting support and love, and has tried with some success, I may add, to turn me into the well dressed, smart, cultured, debonair guy that she would like me to be!! I will get there soon, honest!

Finally I wish to acknowledge the Science and Engineering Research Council (SERC) UK, for supporting all the work presented here in a Grant N^o. 90300405 and latterly by the Unit for Space Sciences.

Contents

Abstract	<i>i</i>
Acknowledgements	<i>iii</i>
Contents	<i>vi</i>
Glossary of Acronyms	<i>xi</i>
Chapter 1 Introduction	1
Chapter 2 The Long Duration Exposure Facility (LDEF)	
2.1 LDEF : The Concept.....	6
2.2 LDEF Design and Attitude Stabilisation	8
2.3 Experimental Opportunity	11
2.4 The MicroAbrasion Package (MAP) (A0023)	
2.4.1 Experimental Overview	14
2.4.2 Experimental Design.....	15

2.5	Other Micrometeoroid Experiments	19
2.6	Launch And Retrieval Details	
2.6.1	Launch Manifest	23
2.6.2	Retrieval Status	25
	References.....	31

Chapter 3 Analysis Techniques

3.1	Introduction.....	33
3.2	Large Optical Scanning System (LOSS)	
3.2.1	System Objectives.....	34
3.2.2	LOSS Hardware	35
3.2.3	Specimen Scanning.....	37
3.2.4	LOSS Capabilities.....	40
3.2.5	Image Display And Printing	41
3.3	Scanning Electron Microscope (SEM)	
3.3.1	Microscopy.....	43
3.3.2	Energy Dispersive X-Ray Analysis (EDS)	44
3.4	Hypervelocity Impact Decoding	
3.4.1	Introduction.....	48
3.4.2	Marginal Penetration Equations	52
3.4.3	Semi-Infinite Target Cratering.....	54
3.4.4	Supra-Marginal Penetrations.....	56
3.4.5	Conversions Between Impact Scenarios	59
	References.....	63

Chapter 4 Results from the LDEF

4.1	MAP Data	
4.1.1	Penetration Distributions.....	66

4.1.2	Space Face Hole Size Distributions	67
4.2	Flux Distributions Measured on the LDEF	70
4.3	Corrected Flux Distributions for an 8° Offset LDEF	75
	References.....	79

Chapter 5 Space Debris

5.1	Introduction.....	81
5.2	Database and Information System Characterising Objects in Space (DISCOS)	
5.2.1	Introduction	82
5.2.2	Data Sources	83
5.2.3	Database Organisation	86
5.2.4	On Line Data Analysis	87
5.3	Unclassified Tracked Space Debris	
5.3.1	Detection And Tracking Systems	91
5.3.2	The Known Orbital Debris.....	95
5.4	Orbital Characterisation	
5.4.1	Types Of Orbits.....	104
5.4.2	Orbital Distribution Of Tracked Debris	109
5.5	Debris Prevention And Control	
5.5.1	Prevention And Removal Scenario	114
5.5.2	Atmospheric Drag	114
5.5.3	Prevention And Removal Techniques.....	116
5.6	Conclusions	
5.6.1	Environmental Characterisation.....	119
5.6.2	Space Vehicle / Mission Design	120
	References.....	122

Chapter 6 LEO Particulate Modelling

6.1	Introduction.....	125
6.2	Interplanetary Dust Models	
6.2.1	The Grün Flux Model At 1A.U.....	127
6.2.2	The Divine Model	132
6.3	Space Debris Models	
6.3.1	The Kessler Model	138
6.3.2	The Green/Mackay Model	144
6.4	Analysis Of Debris Densities	
6.4.1	Choice Of Debris Density	151
6.4.2	Spacecraft And Modelled Debris Densities	153
6.4.3	Comparison Of Apparent Debris Densities	156
6.4.4	Uncertainties In Deriving Debris Densities	159
6.5	Sullivan Model Extended	
6.5.1	Introduction	161
6.5.2	General Results For An 8° Offset LDEF	166
6.6	The USS Space Debris And Interplanetary Model For LDEF	169
	References.....	172

Chapter 7 LDEF Predictions and Inferences

7.1	Introduction.....	177
7.2	Interplanetary Particulate Predictions	
7.2.1	Determination of the Geocentric Particle Velocity (V_{pe}).....	179
7.2.2	Interplanetary Flux Compared to Grün and Divine	187
7.3	Orbital Predictions	
7.3.1	Determination of Orbital Components	191
7.3.2	Probable Causes for Flux Differences	197
7.4	Particle Density Distribution from Penetration Data	

7.4.1	F_{\max} Conversions for Space Face MAP DH Data	200
7.4.2	Deriving a Density Function	204
7.5	USS Modelled Impact Fluxes	
7.5.1	Interplanetary and Space Debris Fluxes.....	208
7.5.2	Comparison of Angular Distributions of Modelled Interplanetary and Space Debris Impacts.....	211
	References.....	226
Chapter 8 Conclusions		229
Appendix I.....		AI.i
Appendix II		AIi.i

Glossary of Acronyms

ABM	Apogee Boost Motor
ASAT	Antisatellite
BMEWS	Ballistic Missile Early Warning System
CCD	Charge Coupled Device
CMD	Carey, McDonnell, Dixon (general equation)
CME	Chemistry of Micrometeoroids Experiment
COSPAR	Committee on Space Research
CST	Central Standard Time
DISCOS	Database and Information System Characterising Objects in Space
EDS	Energy Dispersive X-Ray System
ESA	European Space Agency
ESOC	European Space Operations Centre, Darmstadt, Germany
EST	Eastern Standard Time
FRECOPA	French Co-operative Payload
GEO	Geosynchronous Orbit
GEODSS	Ground-based Electro-Optical Deep Space Surveillance System
GSFC	NASA Goddard Space Flight Centre, Maryland, USA.
GTO	Geosynchronous Transfer orbit

HEO	Highly Elliptical inclination Orbit
IDE	Interplanetary Dust Experiment
IDP	Interplanetary Dust Particle
ISSF	International Space Station Freedom
KSC	NASA Kennedy Space Centre, Florida, USA
LDEF	Long Duration Exposure Facility
LEO	Low Earth Orbit
LOSS	Large Optical Scanning System
M&D SIG	Meteoroid and Debris Special Investigative Group
MAP	MicroAbrasion Package
MEM	Meteoroid and Exposure Module
MFE	Microabrasion Foil Experiment
MIT	Massachusetts Institute of Technology
MOS	Metallic Oxide Silicon
NASA	National Aeronautics and Space Administration
NAVSPASPUR	Naval Space Surveillance System
NORAD	North American Air Defense
NRL	Naval Research Laboratory, Washington D.C., USA
PARCS	Perimetre Acquisition Radar Characterisation System
RAE	Royal Aircraft Establishment, Farnborough, UK
RCS	Radar Cross Section
SAEF	Spacecraft Assembly and Encapsulation Facility
SDIE	Space Debris Impact Experiment
SEM	Scanning Electron Microscope
SIG	Special Investigative Group
SIMS	Secondary Ion Mass Spectroscopy
SMM	Solar Maximum Mission Satellite
SQLPLUS	Standard Query Language Plus
SRM	Solid Rocket Motor
SSC	Space Surveillance Centre
SSR	NASA Satellite Situation Report
STS	Space Transportation System
TLE (or ELSETS)	NASA Two Line Elements
UHCRE	Ultra Heavy Cosmic Ray Experiment
USAF	United States Air Force
USS	Unit for Space Sciences, University of Kent at Canterbury, UK
USSPACECOM	United States Space Command

Chapter 1

Introduction

On the 4th October 1957 an SL-1 vehicle launched from Tyuratam launch site in the USSR carrying Sputnik 1 (1957 α 2), the first artificial Earth satellite. The space era had begun.

Since that time a total of 3,514 launches (1st April 1993) have occurred with some 7,310 objects currently tracked from the Earth of which 2,120 are payloads and 5,190 are debris objects. There have been some 15,283 decayed objects either payload or debris that have at one stage or another been in orbit and subsequently decayed. One such object that has been in Earth orbit is NASA's Long Duration Exposure Facility (LDEF).

In those early days one of the main objectives of space flight was to obtain information on the Earth and the space environment. Scientific payloads played the predominant driving force in the early space flight era until the ultimate goal of placing man in space. This duly happened on April 12th 1961, less than four years after the first spaceflight Vostok 1 (1961 μ 1) took Yuri Gagarin and the USSR to the forefront of the Space era.

With the emphasis on manned spaceflight the science programme took a place back stage, but has recently become a force again and in particular in conjunction with the manned spaceflight programme (*i.e.* International Space Station Freedom). The need to understand and characterise the near Earth environment now takes on an important rôle in the protection and survivability of satellites and manned space programmes. The increase activity in global satellite communication has led to the development of expensive and complicated satellites that currently orbit the Earth all subjected to the harsh environment. Temperatures can vary from 200°C to -40°C from sunlight to eclipse, posing thermal control problems, the continuous bombardment by interplanetary dust particles that sweep into the Solar System and Earth local system poses surface degradation problems, and now another hazard that of anthropogenic space debris adding to this problem. This anthropogenic space debris is left in orbit, as a result of man's endeavours to exploit the near Earth space region.

This thesis is based upon the LDEF satellite whose sole purpose was to gain scientific knowledge on the low Earth environment so that some day the data retrieved could be used to better understand and characterise the near Earth space environment. The characterisation of the interplanetary dust media, that is beyond the control of man, and more politically sensitive, the understanding of the potential damage that present space activities could be causing for the space faring peoples of the future, are discussed.

In Chapter 2 the Long Duration Exposure Facility is described in detail, including the final flight configuration and orbit geometry with it's gravity gradient stabilised orbit. Starting with the primary concepts laid down in the early 70's, the chapter details the changes involved and the experiments eventually carried on board the LDEF. It's extended stay in Low Earth Orbit (LEO) has proved invaluable in the collection of data for all experimenters concerned, although it has clouded some issues and raised others. Amongst the 57 different experiments carried there were 7 dedicated micrometeoroid and space debris impact experiments. The basis behind these measuring techniques are also described in Chapter 2 alongside the MicroAbrasion Package (MAP), the Unit for Space Sciences (USS) experiment to characterise the LEO particulate environment.

Particles that would impact the LDEF are travelling at speeds of 2kms^{-1} up to 70kms^{-1} for some interplanetary dust particles. With such high impact velocity both the impactor and target are drastically affected. In most cases an impact leaves little, if any, remnants of the impactor and the damage to surfaces is clearly distinguished from terrestrial flaws in the manufacture of the detector. Thin films have for a long time been used as impact detectors and as such an impact at these high velocities would leave a hole, or alternatively if the target is thick, such as a block, a crater would remain. Craters or holes, the impactor leaves very few clues to its origin, particle size, shape or impact velocity. Subsequently to determine such parameters impacts have been characterised over the years, using terrestrial calibration data and a set of hypervelocity impact scenarios developed for both thin films and solid blocks (termed semi-infinite targets). These include penetration equations and conversions between different impact types, holes/craters and the rationale behind the choice of impact equation and development is given in Chapter 3. Included in Chapter 3 is a detailed discussion of the current techniques employed by researchers at the Unit for Space Sciences in handling spaceflight hardware, detecting and subsequently analysing such data.

The results of the flux distributions based upon a series of different experiments, for the major pointing directions on LDEF are given in Chapter 4. At this stage the characterisation into interplanetary or anthropogenic space debris is not clear, as no clear chemical evidence on impactor residue has been detected, on impact sites at Canterbury. The only way to determine the relative contents is to model both populations.

Chapter 5 introduces the problems of anthropogenic space debris and details the European Space Agency's (ESA) commitment to characterising this problem with the Database and Information System Characterising Objects in Space (DISCOS). A detailed breakdown is given on the DISCOS rationale, data sources and data analysis capabilities of this database on-line at the European Space Operations Centre (ESOC), Darmstadt, Germany. Using the DISCOS database analysis of the currently tracked anthropogenic space debris is possible and this is also given in Chapter 5. This is presented in terms of numbers of objects in orbit, classified as payloads, or debris and the

affects causing the production of debris. A very useful rôle of DISCOS is in determining the primary orbital data set used to describe the orbit distribution that space debris models use. The characterisation of orbits, types and reasons for the present orbital debris distribution are also given and indeed it is this data set that will be discussed in Chapter 6 as the basis of the debris models used in this thesis.

The Grün and Divine models used in describing the interplanetary dust environment are introduced in Chapter 6 alongside the Kessler orbital debris model and the debris model developed “*in house*” by Green and later Mackay based upon the orbital data set given in Chapter 6. The effects of this debris model are examined for a satellite in a similar orbit to that of LDEF and the results show the classical “*butterfly*” distribution associated with other modelled predictions of space debris impacts on spacecraft. A detailed study into the likely density of space debris objects is reported using data from DISCOS and compared to the current density profiles given by Kessler and Anz-Meador, both of NASA JSC. The Sullivan model developed for LDEF analysis is briefly introduced with the main emphasis on the techniques developed to relate flux information from one face to the other of this gravity gradient stabilised spacecraft. The subsequent combining of the 3D model developed by Sullivan, with a mass and velocity distribution, has led to the USS interplanetary and space debris model which also incorporates the Green space debris model.

In Chapter 7 the modelled results and flux measurements are compared showing the possible breakdown of the two particle populations, but also the limitations of the models used. This is mainly in terms of the assumptions on the 3D isotropic nature of the interplanetary media and the likely asymmetry in the anthropogenic space debris due to Molniya orbits as reported in some debris models. A mean particle velocity that would satisfy a single velocity, 3D isotropic distribution, is derived from a velocity distribution using the Sullivan transformations. In comparing data sources and penetration equations, a density profile for particles impacting the Space face of LDEF is derived. This is consistent with the idea of two discrete populations impacting the LDEF, and the present understanding of particle densities. Using the USS model to

predict impact directions for both anthropogenic space debris and interplanetary particles and comparing this to actual impact directions and crater ellipticity a possible alternative method of deriving basic particle origin is discussed. This, by no means, can replace the actual chemical evidence but offers some insight into the likely distribution of both space debris and natural impacts .

With an understanding of the processes involved in hypervelocity impacts, the models derived for interplanetary and anthropogenic space debris it is possible to predict the effects of these two populations on the LDEF. Chapter 8 outlines the areas that require further analysis and understanding and clarifies the details already understood from the analysis of LDEF.

Chapter 2

The Long Duration Exposure Facility (LDEF)

2.1 LDEF : The Concept

The need for information about micrometeoroids, in the near Earth space environment, is as old as spaceflight itself. Micrometeoroids had been the object of study as early as 1958 in the Vanguard experiments, America's first scientific satellite programme consisting of three satellites launched between March 1958 and September 1959 (1958- β 2, 1959- α 1 and 1959- η) {2.1}. This early quest into learning more about the near Earth space particulate environment continued through the 1960's such that in 1970 the then so called Meteoroid and Exposure Module, hereafter MEM, was proposed by America's National Aeronautics and Space Administration (NASA), Langley Research Centre in Hampton, Virginia, as the first space shuttle payload {2.2}.

MEM was primarily a micrometeoroid experiment satellite employing the three main types of micrometeoroid experiments developed to date. The first was “The pressurised cell detector”, in which a sensor would read and report the loss of pressure that resulted from a penetration impact. These cells consisted of various “*skin*” thicknesses, pre-calibrated in ground tests, and incorporating data transmission equipment to relay information about the impacts and penetrations to the Earth. The second method was based upon a capacitor detector in which a penetration generated an electrical signal. The third design to be incorporated on MEM was the “*bumper shield*” class, as in the Whipple bumper shield. This shielding technique relied on a thin extended sheet of material causing the impactor to break up and diffuse out as a debris cloud over a larger area thus reducing the likelihood of spacecraft penetration.

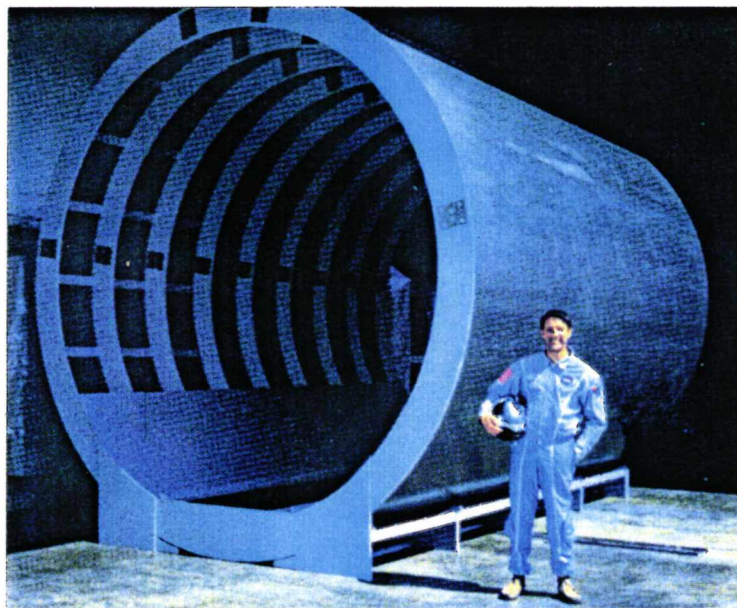


Figure 2.1 Mock up of the Meteoroid and Exposure Module (MEM) with astronaut Donn F. Eisele in the foreground.

With the advent of NASA's space transportation system (STS), more commonly known as the space shuttle, offering deployment and retrieval of a satellite from low Earth orbit (LEO) the need for data telemetry from such satellites was becoming obsolete. It was envisaged that MEM would fit into this deployment/retrieval scenario

and remain in LEO for several months, and the experiments returned to the laboratory for analysis on the Earth. The need for extra mass and cost budgets for telemetry equipment and the extra risk of a failure in this area were thus eliminated. To satisfy the STS deployment/retrieval criteria the conceptual design for MEM was a cylinder, as illustrated in figure 2.1, sized to fit in the STS payload bay.

In 1974 Langley Research Centre, for the Office of Aeronautics and Space Technology, (now known as the Office of Aeronautics, Exploration and Technology), became the official NASA managers of the MEM project and subsequently renamed it the Long Duration Exposure Facility (LDEF). With this change came added research goals. Alongside the main micrometeoroid research, other scientific areas were added :

- temporal study of the physical properties of materials exposed to the space environment
- performance tests of spacecraft systems
- evaluation of components used in powering spacecraft
- space physics and related fields.

What started out as a micrometeoroid dedicated spacecraft had evolved into a study of all aspects of the near Earth space environment encompassing a wide field of science and engineering : a truly complete in-situ study of the near Earth space environment.

2.2 LDEF Design and Attitude Stabilisation

The LDEF spacecraft design changed from the basic cylinder of MEM (figure 2.1) to the final dodecagon cross section of the LDEF. This cross sectional design made of comparatively heavy aluminium, to ensure structural integrity, gave the LDEF twelve flat peripheral sides and one "top" and "bottom." Aluminium beams called "longerons" connect a centre dodecagon frame to the two end frames, these are bolted together and thus the LDEF would assume any length required to fit into the payload manifest for a

given STS flight. The end frames are welded to their nearest “longeron”, once again for structural integrity. The “longerons” are then crossed by aluminium “intercostals” around the twelve sides of the LDEF thus producing an eighty-six tray framework, consisting of twelve longitudinal rows of six trays each and fourteen additional trays on the “top” and “bottom” ends as illustrated in figure 2.2.



Figure 2.2 LDEF frame showing longerons and intercostals, just before shipment to Kennedy Space Centre (KSC).

The LDEF was designed to be a passive, re-useable spacecraft without the need for complex power systems for data acquisition and orbital positioning. This enabled experiments to be designed which could benefit from the stable spacecraft attitude, with no accelerating forces due to jets from any attitude control system deployed. The LDEF was designed as a “gravity gradient stabilised” spacecraft, which meant that the ram direction (*i.e.* the direction of the velocity vector, in the orbital plane) remains constant. Thus the “top” and “bottom” ends became known as the Space and Earth faces as they remained facing out to space (+normal to the ram direction) and facing the Earth direction (-normal to the ram direction) respectively. This profile was maintained throughout the LDEF's orbital lifetime excluding, of course, the deployment and retrieval operations. The gravity gradient stabilisation is attained due to the LDEF spacecraft

being of cylindrical design with the long axis in a direction parallel to the Earth's gravitational field. The centre of mass of the spacecraft is located in the lower (Earth pointing direction) half of the spacecraft. Thus the long axis of the LDEF aligns with the gravitational field of the Earth keeping the Earth face facing the Earth.

As previously stated on deployment and retrieval the LDEF's orientation is changed dramatically and to align the spacecraft in a known pointing direction a viscous magnetic damper was situated at the centre of the Space facing end frame. One of the main mission orientations, alongside the gravity gradient stabilisation of the attitude, was the stabilising of the ram direction such that a particular longitudinal face would always remain in the ram direction. The faces around the LDEF's ram direction would become synonymous with the cardinal points on a compass such that the East named face remained in the ram direction throughout the LDEF's orbital lifetime and the West named face remained in the wake direction. The North and South faces were then fixed at $\pm 90^\circ$ to the ram direction. A further description of this orientation is given in section 2.3. The viscous magnetic damper was about half the size of a basketball and uses the Earth's magnetic field and a viscous fluid to gradually cancel de-stabilising vibrations and torques caused by deployment. The design consists of two concentric spheres, one rigidly attached to the LDEF and the other floating concentrically inside. These are separated from each other by a layer of silicone oil. Rigidly attached inside the inner sphere is a magnet, which tended to keep the inner sphere constantly aligned to the Earth's magnetic field. Motions out of the outer sphere are quelled by the resistive flow of the silicone oil and thus unwanted vibrations in the LDEF were damped. This unique attitude and face stabilisation aided the design and decoding of experimental data acquired as the exact orientation and exposure geometry of each experiment would be known throughout its orbital lifetime.

Two attachment points on opposite sides of the LDEF centre ring frame connects the STS side to provide the main support. A third fixture attaches to the payload bay deck of STS and a fourth at the centre of the Earth face connects to the STS via a special

beam known as the "*walking beam*". These attachments were configured to evenly spread the eleven ton load in flight.

Construction of the LDEF commenced in 1976 and was completed in August 1978. The LDEF underwent flight qualification dynamic and static tests at Langley Research Centre before being stored there in 1979 awaiting the experiments and STS for deployment.

2.3 Experimental Opportunity

With the LDEF infrastructure now complete the spacecraft, 30ft long and 14ft in diameter and weighing 8,400 pounds (empty), had the capacity to hold 86 experimental trays. In 1976 the LDEF was formally announced to the world wide technological and scientific community offering them the unique opportunity to gain frequent access to the LEO space environment for their experiments. Initially a letter of intent submitted with a brief experimental proposal and validation of institutional support was all that was required.

NASA was inundated with applications from all over the world to fill the 72 peripheral and 14 end experimental trays. Most of these trays were slightly larger than 3ft by 4ft, with the exception of the end trays that were 2.5 ft², These trays had depths ranging from 3" to 12". Experiments could occupy one or more trays situated around the LDEF to take advantage of the spacecraft's unique stabilisation properties.

In September 1981 the first international meeting of the LDEF experimenters was held at Langley Research Centre after the summer announcement that the LDEF preparation was underway for a December 1983 launch on STS, with a 9-12 month excursion into LEO. In total 57 different experiments were chosen to fly on board the first LDEF mission measuring all manner of space phenomena from micrometeoroid

impacts, thermal coatings of materials, radiation and even tomato seeds. These were ordered into four main areas

- materials, coatings and thermal systems
- power and propulsion
- science
- electronics and optics.

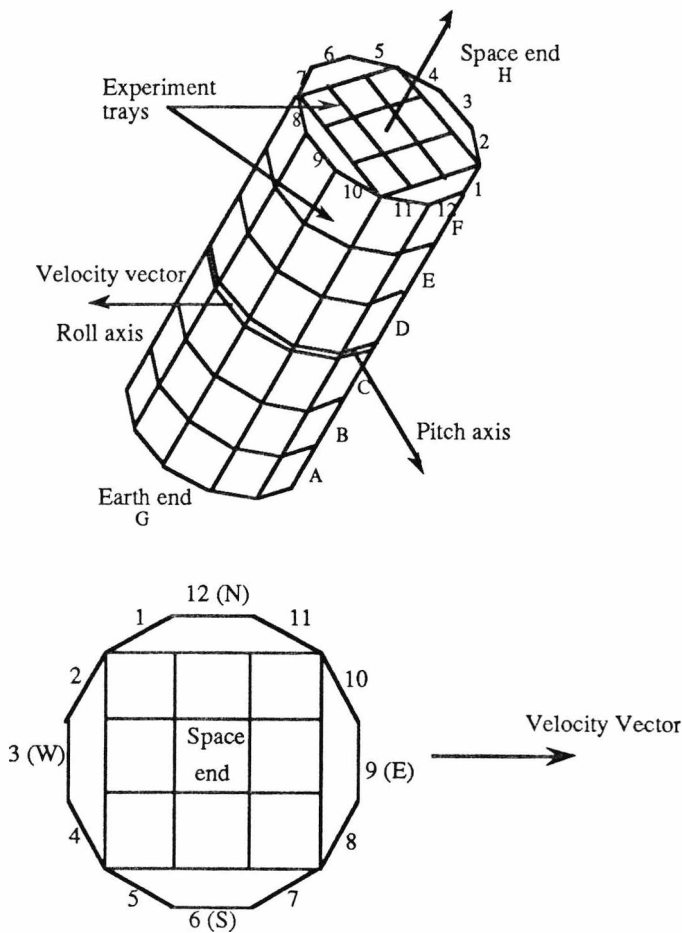


Figure 2.3 In Orbit orientation of LDEF and row identification.

As discussed in section 2.2 the LDEF was to be stabilised both longitudinally, Earth to Space faces, and in the ram direction such that the East face always remained as the leading face. These face names are really for convenience sake as the numbering of the peripheral faces was in fact as shown in figure 2.3. The nominal East face was row 9,

West face row 3 and then $\pm 90^\circ$ to these the North face row 12 and South face row 6. This however was not quite the case as became clear on retrieval (see section 2.6.2).

The experiments were distributed and logged over the LDEF as shown in figure 2.4 with each of the 57 experiments given a unique I.D. (e.g. A0023), although many experiments filled more than one or parts of one tray around the LDEF. The final weight of the LDEF, with experiments had risen to 21,400 pounds.

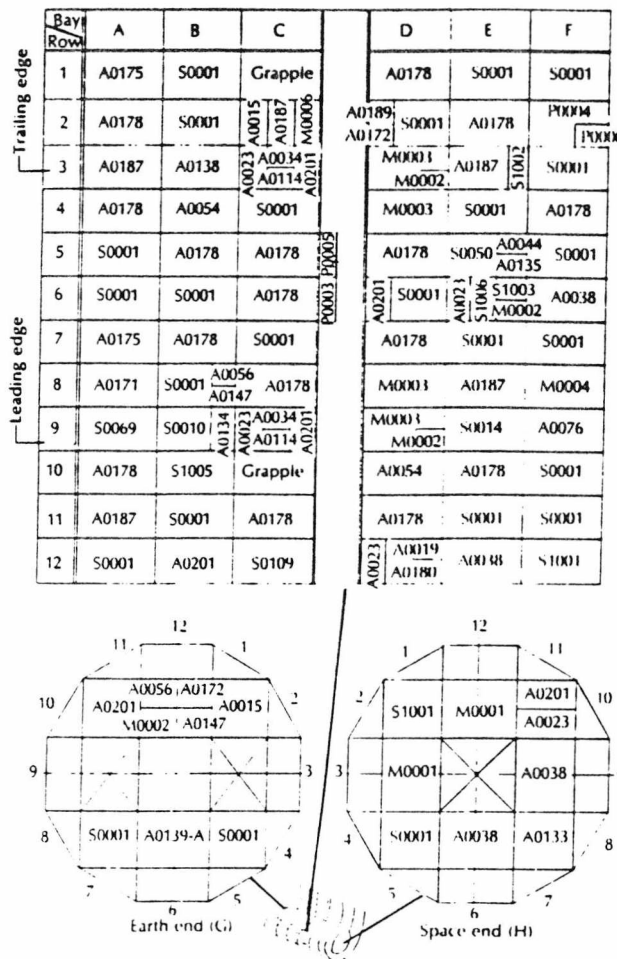


Figure 2.4 Distribution and identification of experiments on board the LDEF.

The truly international flavour of the LDEF becomes apparent with break down of experiments and their collaborators:

- 33 from private companies
- 21 from universities

- 7 NASA centres
- 9 Department of Defense (USA)
- 8 foreign countries (not USA).

2.4 The MicroAbrasion Package (MAP) (A0023)

2.4.1 Experimental Overview

One of the dedicated micrometeoroid experiments selected for the first LDEF was the microabrasion package (MAP), (A0023). Designed and built by at the University of Kent, Canterbury, UK under Prof. J.A.M.McDonnell. It was the second such experiment to be taken into LEO on STS following the very successful microabrasion foil experiment (MFE) on the STS-3 (Columbia) mission (1982-22A), in which the USS became the first non American establishment to fly an experiment on board the STS {2.3}.

At the time of inception, controversy over conflicting results from microphone programmes of the USA and USSR and penetration data from Explorer 16 (1962-βχ), Explorer 23 (1964-74A), Pegasus I (1965-09A), Pegasus II (1965-39A), Pegasus III (1965-60A) and Ariel II (1964-15A) left the micrometeoroid community unsure of the micrometeoroid population in general. The microphone data indicated a small particle population much greater than that indicated by penetration measurements {2.4}. There was a real need to clarify this situation and the LDEF proved the best opportunity.

Using improved sensitive thin foil penetration detectors {2.4} MAP was designed as a very cost effective way of analysing the LEO micrometeoroid environment, taking advantage of the retrievability of the LDEF. Thus all the analysis of MAP data would be carried out in the USS own laboratories. The microfoil technique offers high sensitivity

of detection and yet are rugged and simple. The sensitivity of foil detectors is achieved by the quality of the foil and its thickness. For example at 5 micrometres ($5\mu\text{m}$), and for a foil defect density of 1 per 10 cm^2 , optical scanning yields an effective sensitivity of 10^{-11}g impacting particle mass ($< 1\mu\text{m}$ diameter). If such foil defects are logged prior to flight then the reliability of detection is further enhanced. Coupling the optical scanning with hypervelocity impact feature analysis (including chemical analysis) by a scanning electron microscope (SEM), the post flight examinations reveal not only the flux of certain sized particulates but also mass or velocity inferred from the crater morphology. (The analysis techniques used are discussed in Chapter 3.)

Thus the main objectives of MAP were:

- (i) Definition of particulate flux distribution as a function of crater size or perforation thickness
- (ii) Determination of the 3-dimensional flux distribution
- (iii) Characterisation of the velocity and angular distributions of the particulates
- (iv) Discrimination between particle sources *e.g.* :
 - (a) Interplanetary micrometeoroids
 - (b) Man-made space debris
- (v) Particulate chemistry.

2.4.2 Experimental Design

The MAP system comprises of a double layer of foils and a stop plate, as shown in figure 2.5, in a similar fashion to the “*capture cell*” array. With two foils and a stop plate there are three possible impact scenarios as shown in figure 2.6. Any ejecta from either the first or second foil will be detected on the subsequent foil or stop plate within a cone with a typical radius of $\pm 30^\circ$.

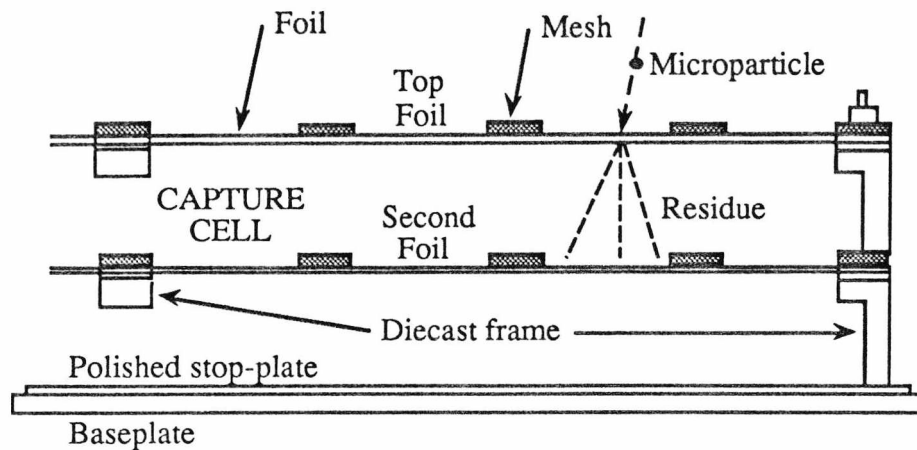


Figure 2.5 Cross section of the MicroAbrasion Package (MAP).

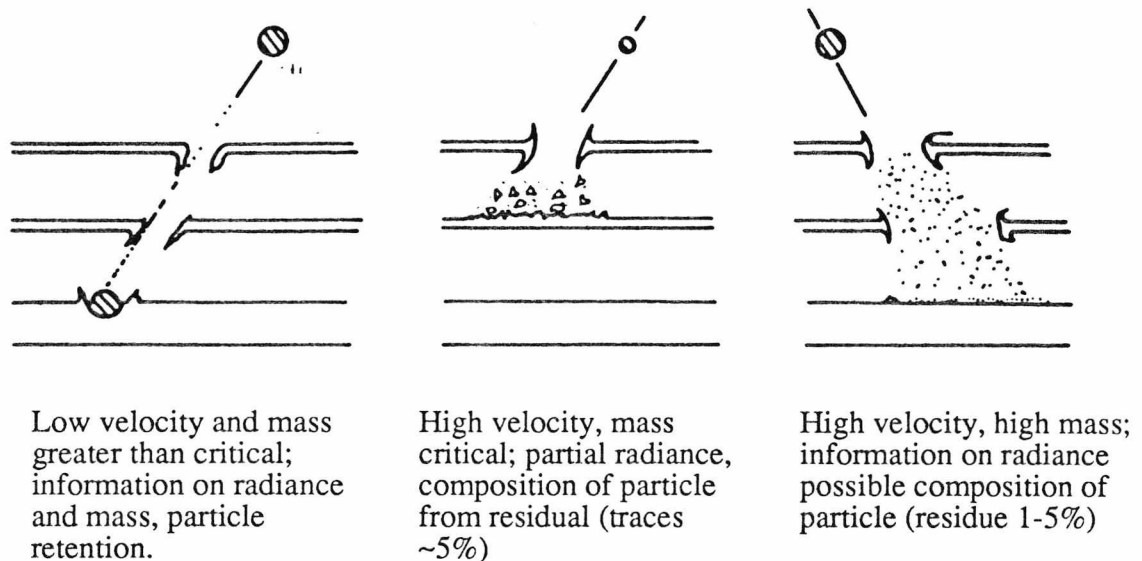


Figure 2.6 The three possible impact scenarios for MAP.

The foils are made of aluminium or brass with nominal thicknesses of 1.5 μm , 2.5 μm , 3 μm , 5 μm , 12 μm , 14 μm , 18 μm , 25 μm , and 30 μm bonded to a gold plated brass shimstock support mesh, which in turn are bonded to A-shaped frames, bolted to the stop plate and tray. The aluminium foils were generally T6 rolled temper aluminium of 99.9% purity except the 1.5 μm foils which were beaten foils. The brass foils flown were all of 5 μm nominal thickness.

Each frame is split into four segments with a unique identification code such that every segment on any MAP surface, top or bottom, is immediately identifiable. For example all the Space pointing frames start with the letter H to distinguish which face the frame came from, (*i.e.* East frame starts with E and so on). The next digit indicates what number frame, 1-8 on the periphery and 1-4 on the Space face. The next letter indicates whether the MAP surface is the top (t) (*i.e.* the first foil) or bottom (b) (*i.e.* the second foil) and finally the segment letter a, b, c, or d. Thus an impact site can be located on any MAP segment (*e.g.* H1ta, would be segment a on the first foil on the first MAP unit on the Space face, see figure 2.7).

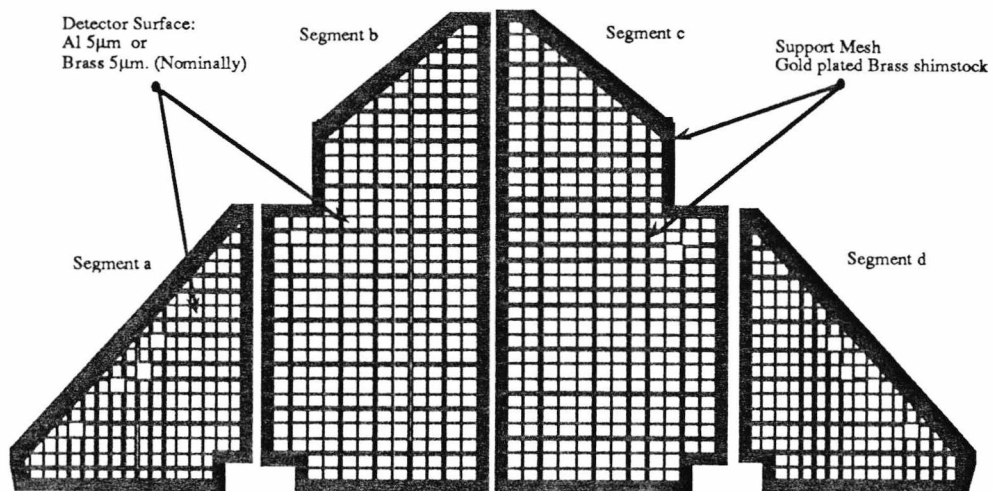


Figure 2.7 MAP surface diagram showing segments.

The MAP experiment was given the LDEF *I.D.* A0023 and was situated as shown in figure 2.4. In total MAP occupied one third of a tray on rows 9, 3, 6 and 12 (*i.e.* East, West, North and South faces and one half tray on the Space face which is illustrated in figure 2.8).

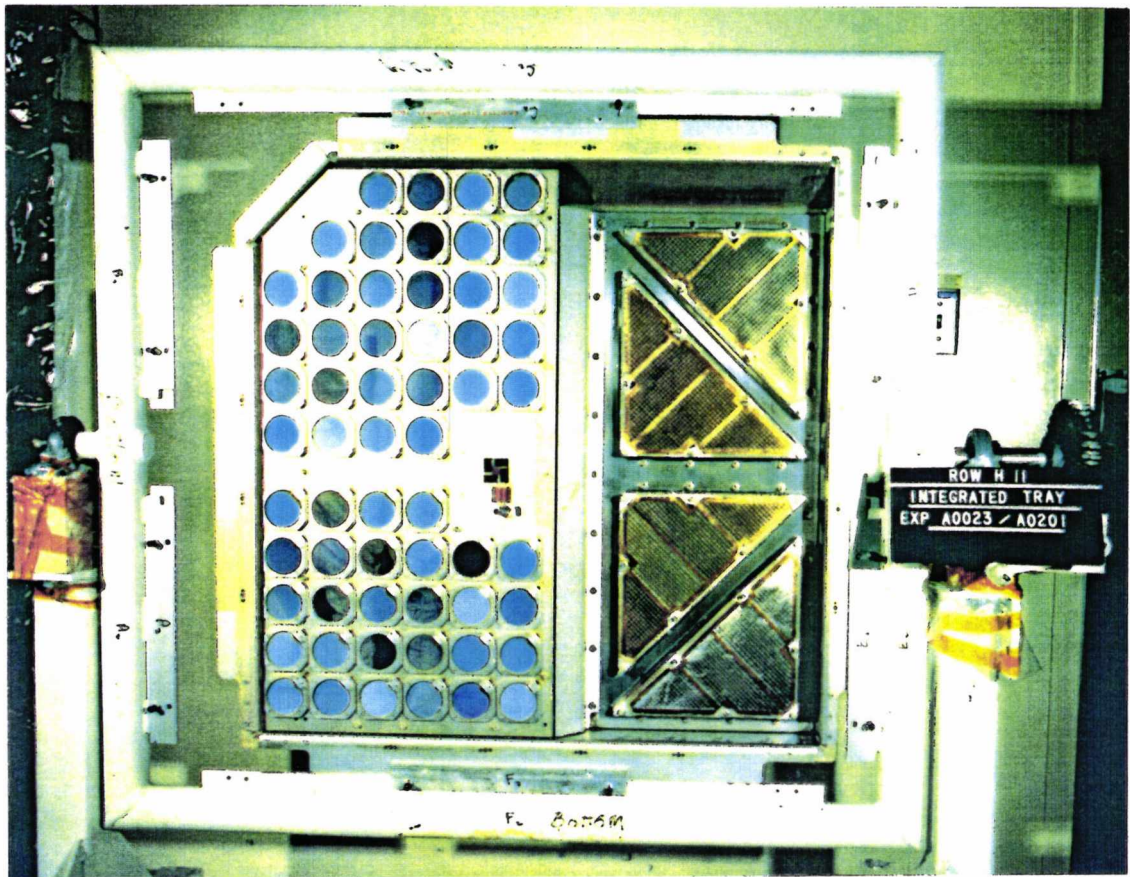


Figure 2.8 Space face tray prior to integration showing MAP.

Eight MAP units comprising of the two foils and stop plate were deployed on each of the peripheral faces and four on the Space face giving in total 72 foil surfaces (or 288 segments) for possible analysis. Table 2.1 illustrates the exposure area and foil thickness for each MAP frame on the LDEF. The reasons for deploying MAP on the so called cardinal points of the LDEF and the Space face as well as the advantages in doing so when decoding the results from MAP will be discussed in Chapter 7.

Material	Nominal Thickness	Exposed Area (cm ²)				
		North	South	East	West	Space
Aluminium	1.5 µm	62.4	124.8	62.4	124.8	368.0
	2.5 µm	124.8	62.4	124.8	62.4	
	3 µm		62.4		62.4	
	5 µm	243.2	243.2	243.2	243.2	
	12 µm	62.4	31.2	62.4	31.2	
	14 µm	60.8	60.8	60.8	60.8	
	18 µm	121.6	121.6	121.6	121.6	
	25 µm	213.6	213.6	213.6	213.6	
	30 µm	274.4	243.2	274.4	243.2	
Brass	5 µm	308.8	308.8	308.8	308.8	368.0

Table 2.1 MAP foil properties and distribution.

2.5 Other Micrometeoroid Experiments

Alongside MAP there were a host of other meteoroid and debris dedicated experiments to be selected for the LDEF. Some unusual areas of the LDEF proved to be of great interest to the meteoroid and debris investigators (section 2.6.2).

A summary of these experiments is given below :

A0138-1 Study of Meteoroid Impact Craters on Various Materials. (FRECOPA)

J.C.Mandeville {2.5}.

CERT/ONERA-DERTS, Toulouse, France.

This entirely passive detection system consisted of thick targets (compared to the impacting particle size) of pure metals and glass covering a total area of some 750cm². These surfaces were tungsten (150µm), aluminium (250µm) twice, copper (125µm), stainless steel (250µm) twice, and pyrex glass (1.9µm). The surfaces would be scanned by both optical and scanning electron microscopes to search for impact sites, and possible chemical analysis of any residue found.

A0138-2 Attempt at dust Debris Collection with Stacked Detectors.

J.C.Mandeville {2.6}.

CERT/ONERA-DERTS, Toulouse, France.

This experiment consisted of targets made of one or two thin metal foils placed in front of a thicker plate. This is similar to the MAP design but incorporating only one surface compared to MAP having two, then the stop plate. The surfaces were aluminium foil with varying thicknesses, 0.75 μm , 2 μm , 5 μm and 125 μm , and gold of 125 μm thickness. The analysis procedure is as described above for A0138-1.

A0187-1 The Chemistry of Micrometeoroids. (CME)

Friedrich Hörz, et al {2.7}.

NASA Lyndon B. Johnson Space Centre, Houston, Texas, USA.

This experiment's prime objective was to collect micrometeoroid residue around the impact site which would be analysed on return to Earth, using a scanning electron microscope with an associated energy dispersive X-ray analyser. The experiment involved both active and passive areas. The active unit comprised of two sets of clam shells that opened and closed exposing the main collector surface of 99.99% pure gold sheets 500 μm thick, to the space environment 8 days after the LDEF was deployed. The passive unit comprised of 99.9% pure aluminium panels of 300 μm thickness, bolted onto a structural framework, fastened to the LDEF tray.

A0187-2 Chemical and Isotopic Measurements of Micrometeoroids by Secondary Ion Mass Spectrometry.

John H. Foote, et al {2.8}.

McDonnell Centre for the Space Sciences, St. Louis, Missouri, USA.

This experiment was designed to measure the chemical and isotopic composition of micrometeoroids as opposed to their fluence. The experiment utilised a passive germanium target which was covered with a thin metallised plastic foil. The foil was coated, on the space facing area, with a gold-palladium film for thermal control and to protect the foil from the effects of atomic oxygen. The inner area was coated with tantalum to optimise the analysis of positive secondary ions by using the secondary ion mass spectroscopy (SIMS). An incoming meteoroid penetrated the outer foil then impacted the target plate below thus releasing ejecta onto the underside of the foil. This ejecta, containing both target and impactor material, was then analysed by SIMS.

A0201 Interplanetary Dust Experiment. (IDE)

S. Fred Singer, et al {2.9}.

University of Virginia, Charlottesville, Virginia, USA.

As the title depicts this experiment was designed to study the interplanetary micrometeoroid environment. This active experiment utilised metal-oxide-silicon (MOS) capacitor-type impact sensors with two different sensitivities (60% with oxide thickness of 0.4 μ m (high sensitivity) and 40% with thickness of 1.0 μ m (lower sensitivity)). After approximately every 2 hours the status of all the sensors was recorded on the experiments data system, including time of occurrence of the impact and the number of impacts. The analysis would involve tracking back the recorded data to give temporal information on the impact data recorded.

This however proved only useful for the first nine months of the LDEF's orbital lifetime.

S0001 Space Debris Impact Experiment. (SDIE)

Donald H. Humes {2.10}.

NASA Langley Research Centre, Hampton , Virginia, USA.

This dedicated experiment used large areas of thick aluminium plates to detect impacts from the micrometeoroid environment. With special interest given to the fluence of orbital man-made space debris. The analysis techniques used are described earlier (A0138-1).

Apart from these experiments there was another group of experimenters, known as P0007, Meteoroid Damage to Spacecraft, {2.11} which was a consortium of the investigators from the above experiments who would analysis other surfaces from the LDEF, that contained impact sites. On retrieval it was noted that the spacecraft had been subject to a large number of impacts and many more surfaces became available for analysis. Such surfaces included the experimental trays, clamps, the LDEF structural longerons and intercostals and the thermal close out covers from experiment A0178 {2.12} (Ultra-Heavy Cosmic Ray Experiment, UHCRE, Denis O'Sullivan, et al, Dublin Institute of Advanced Studies, Dublin, Ireland.) The following table shows the LDEF's faces and associated experiments. The UHCRE covers are also shown as they are currently being analysed at the Unit for Space Sciences (UKC) alongside the MAP experiment.

As can be seen from Table 2.2 the coverage on the LDEF by the dedicated micrometeoroid and debris experiments is extensive, and coupled with the UHCRE covers gives unlimited coverage of all possible impacts on the LDEF.

LDEF Face	Experiments
1	S0001, A0178
2	S0001 (x2), A0187, A0178 (x2)
3	S0001, A0187 (x2), A0138, A0023, A0201
4	S0001 (x2), A0178 (x2)
5	S0001 (x2), A0178 (x3)
6	S0001 (x3), A0201, A0023, A0178
7	S0001 (x3), A0178 (x2)
8	S0001, A0187, A0178
9	A0023, A0201,
10	S0001, A0178 (x2)
11	S0001 (x3), A0187, A0178 (x2)
12	S0001, A0023, A0201,
Space	S0001, A0023
Earth	S0001 (x2), A0201

Table 2.2 Coverage of micrometeoroid experiments around the LDEF.

2.6 Launch And Retrieval Details

2.6.1 Launch Manifest

In April 1981 the first STS shuttle flight took place (1981-34A). STS-1 (Columbia) was launched from Cape Canaveral on 12th April and landed at Edwards Air Force Base in California on April 14th. The space shuttle era had begun.

Later that year the LDEF was removed from storage in readiness for a target launch of December 1983. Pre-flight structural tests were conducted once again at Langley in 1982. In June 1983 the LDEF was shipped to SAEF II (Spacecraft Assembly and Encapsulation Facility) at the Kennedy Space Centre (KSC) in Florida and in November of that same year the LDEF project team moved from Langley to KSC to conduct pre-launch preparations, process and fasten the experiments to the LDEF. Launch was set for April 1984, on board the Challenger space shuttle STS-41C mission.

The LDEF was mated into the payload bay of Challenger and STS-41C (1984-34A) the eleventh shuttle flight lifted off from Pad A, launch complex 39 at 8.58am

(EST) on April 6th 1984 carrying the LDEF into low Earth orbit. Challenger's other main purpose was to catch and repair the ailing Solar Maximum Mission satellite (SMM or Solar Max: 1980-14A), which was launched in 1980 to study the Sun and had begun to fail after 10 months of operation.

At 12.26pm (EST) on April 7th 1984 (the 19th orbit of Challenger) at a point above the Pacific Ocean near Wake Island, the LDEF was deployed by astronaut Terry Hart using the shuttle's 50ft remote manipulator system (RMS). The LDEF became a satellite (1984 -34B) with a nearly circular orbit, eccentricity=0, inclination=28.51° and orbital altitude of 476km {2.1} (figure 2.9).

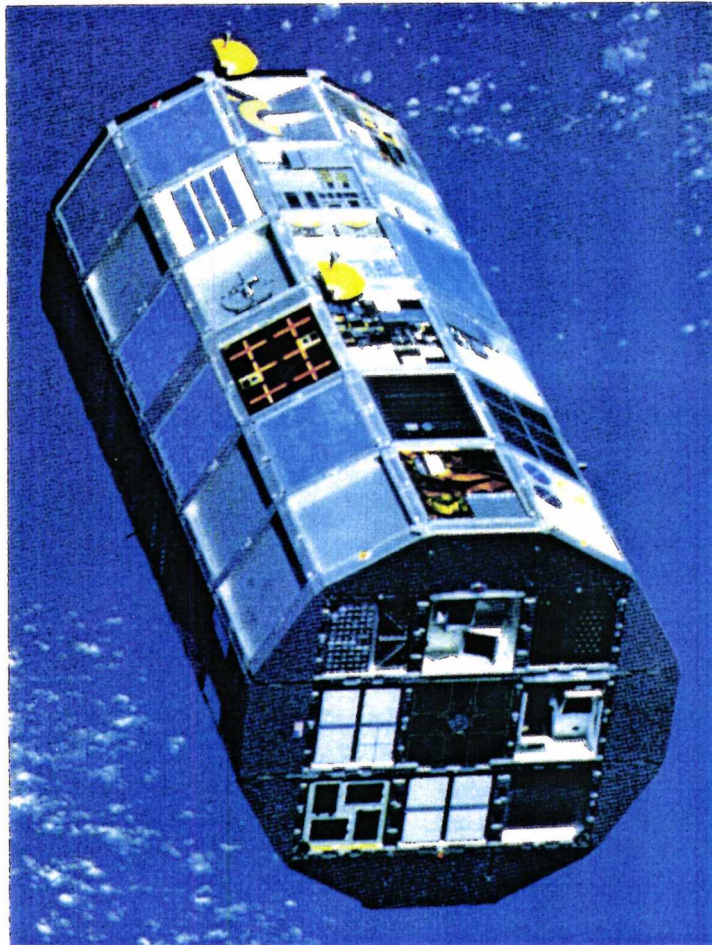


Figure 2.9 LDEF in orbit after deployment.

After successfully repairing Solar Max, the first such rescue and in-flight repair of a satellite to be performed, Challenger returned to Earth on April 13th landing at Edwards Air Force Base, California after a very successful 7 day mission.

As Challenger touched down plans were under way to retrieve the LDEF in early February 1985 which sadly never occurred due to the Challenger disaster. No one at that time could foresee what was actually going to happen to the LDEF and more importantly for the United States and NASA's space shuttle programme.

2.6.2 Retrieval Status

The initial retrieval via Challenger in February 1985 was re-scheduled to Autumn 1986 to accommodate other shuttle scheduling. Then on 28th January 1986, STS 51-L Challenger was launched and encountered the most terrifying accident to hit NASA and the whole of the on looking World. The explosion that ensued not only took the lives of those brave astronauts, it devastated the shuttle programme and with it the World's public confidence in NASA and manned spaceflight. Eventually after many enquiries and political wrangles the shuttle programme resumed with STS 26, Discovery, on 29th September 1988.

Around this time the international community of scientific investigators and NASA officials were becoming acutely aware of a great danger to the LDEF. The 11 year solar activity cycle was reaching a maxima and with it an increased oblation of the Earth's atmosphere leading to increased atmospheric drag on the LDEF. The previously unthought of could become a reality. The LDEF's orbit could be reduced so substantially due to this increased drag that it would re-enter the Earth's atmosphere (without the need of the shuttle) and break up. Almost 6 years of waiting for the return would have been lost along with the increased abundance and wealth of information gained from this extended stay in low Earth orbit.

NASA tracked the LDEF's decaying orbit and using solar activity prediction programs, predicted LDEF's re-entry date. LDEF's decaying orbit is graphically represented in figure 2.10.

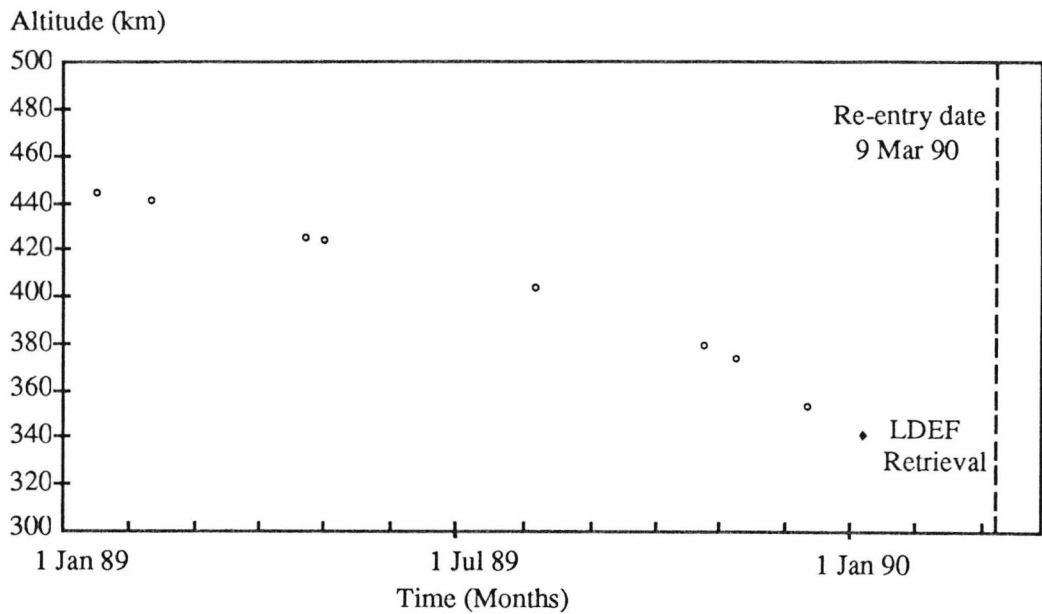


Figure 2.10 LDEF's decaying orbit and eventual retrieval date.

The LDEF retrieval was one of many in the revised NASA shuttle manifest and was weighed against other missions for over a year. The planned retrieval date slipped from June 1989 to July and then November and finally set for 18th December 1989 with the space shuttle Columbia. On 18th December 1989 the launch was yet again postponed until the second week of January 1990. Finally on January 9th 1990 STS-32, Columbia, launched to retrieve the LDEF from the Kennedy Space Centre.

To preserve the integrity of the LDEF data from jet plume contamination from the shuttle the elaborate R-bar manoeuvre {2.2} was employed to recover the LDEF. On the morning of January 12th 1990, Columbia approached the LDEF, passed below it, then circled in front of it to a position 400ft or so above the satellite. Columbia's payload bay was open and facing the Earth with the RMS extended toward the LDEF in readiness to grapple it. This would occur when the two spacecraft would be just 35ft apart.

At 9.16am (CST) on January 12th 1990 Mission Specialist Bonnie Dunbar grappled the LDEF, illustrated in figure 2.11. This was first opportunity to look closely at the damage sustained by the LDEF.

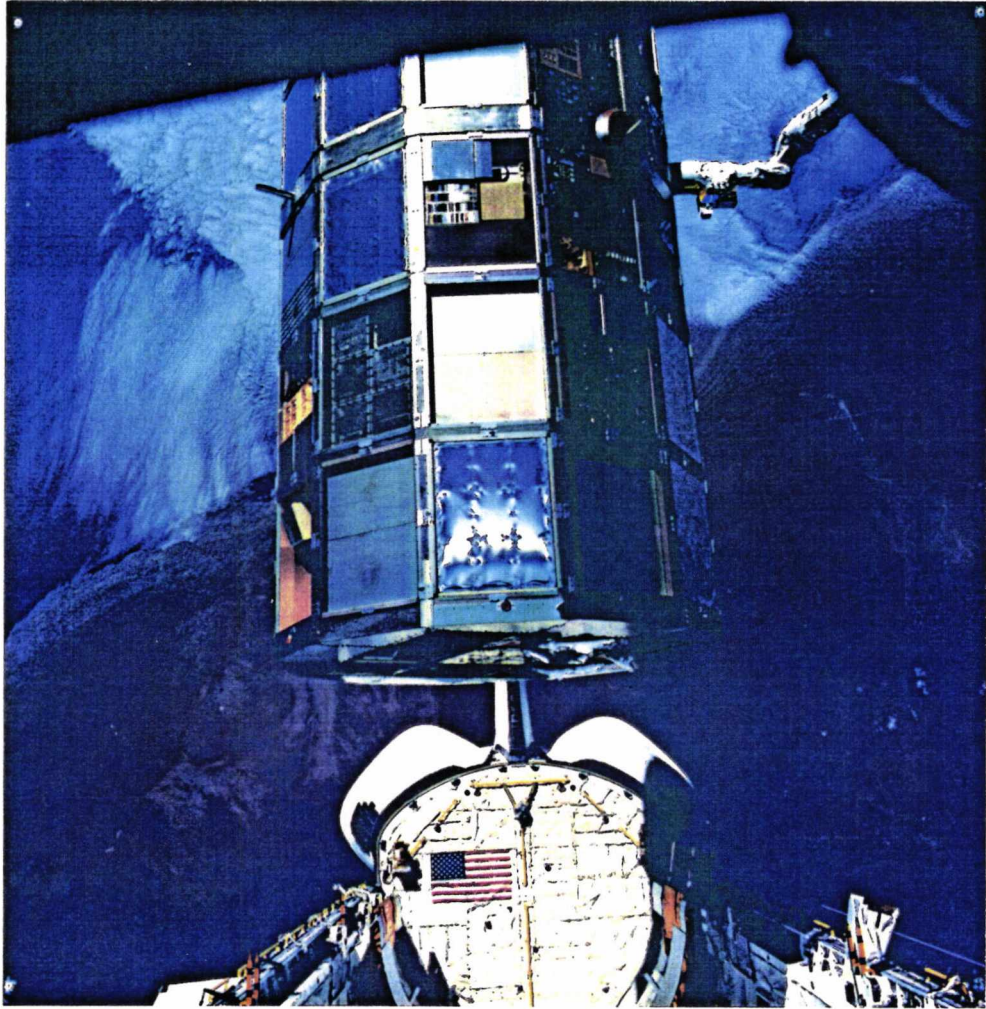


Figure 2.11 Astronaut Bonnie Dunbar successfully grapples the LDEF above the coast of Namibia.

Once grappled, Bonnie Dunbar then undertook 4.5 hours of gentle persuasion of the RMS/LDEF to rotate the LDEF and carry out a visual inspection, including a photographic survey of all the surfaces. Eventually the LDEF was lowered into the relative safety of Columbia's payload bay, with minimal damage, ready for its journey home. At this early stage there were visible signs of the damage caused by the extended

stay in low Earth orbit. These varied from the blackening of thermal paints and surfaces around impact sites, especially around the UHCRE thermal close-out covers to the dramatic peeling foils on the Space face of experiment M0001, Heavy Ions in Space from the Naval Research Laboratory (NRL), Washington D.C., as can be seen in figure 2.12.

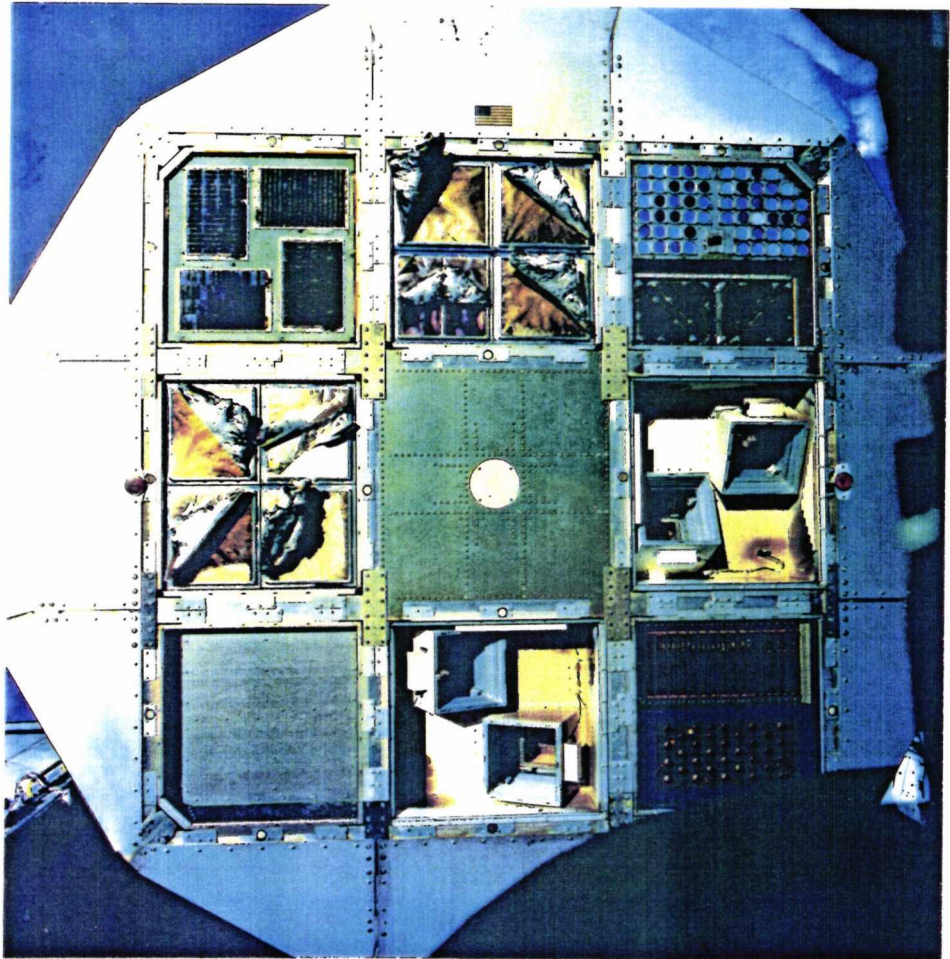


Figure 2.12 The Space face of LDEF shows the degradation of nearly 6 years in low Earth Orbit, in particular the multilayer insulation films on the NRL experiment have furled back.

On January 20th 1990 Columbia touched down on the concrete runway at the Edwards Air Force Base, with a gross weight of 115 tons, 5 tons heavier than any other shuttle mission. Thus the LDEF made history as the greatest time/area product

experiment on the space environment with an orbital duration of some 5.78 years, and the first retrieval of a spacecraft from low earth orbit ever to be performed.

For the scientists at KSC and around the World this was the just beginning. Ahead lay many years of analysis to extract the wealth of space information stored on the LDEF. Previous to the retrieval in 1989 NASA foresaw that the wealth of information acquired from the LDEF would be better used if a formal exchange of data , comparative studies and subsequent database on the LDEF were created. To oversee this, Special Investigative Groups (SIGs) were formed to cover the four main areas of the LDEF research :

- Materials SIG
- Radiation SIG
- Meteoroid and Debris SIG (M&D SIG)
- Systems SIG.

On January 26th 1990 Columbia arrived back at KSC with the LDEF still in it's payload bay from the "*piggy-back*" flight on board the NASA Boeing 747 from the Edwards Air Force Base. A few days later in the KSC Orbiter Processing Facility (OPF), the LDEF was lifted out of the payload bay, placed into a special container and moved to the Operations and Checkout Building. On February 1st 1990 the LDEF was turned over to the LDEF Langley team later to be known as the *KSC A-team*, who had gathered prior to the LDEF's return to KSC for the important post-retrieval analysis of the LDEF. This would later include inspecting and photo-documenting all the LDEF's experiments, close scrutiny of the spacecraft, ensuring contamination free removal of these experiments and safe clean return to their respective investigator's institute. A preliminary inspection was carried out between February 2nd and 22nd in SAEF II followed by a more detailed study and careful de-integration of all the experiments. At this stage it had become apparent that the LDEF was in fact deployed with an offset such that the true velocity vector was shifted by some 8° to the North face {2.13}, based on measurement of atomic oxygen

discolouration, the details and implications of this are discussed in Chapters 6 and 7. On March 29th 1990 the last tray had been removed and sent to it's investigator.

The close inspection and pre-distribution study culminated in, for the Meteoroid and Debris SIG, a very valuable insight into the effects of particulate damage on the LDEF, and in particular on surfaces previously not considered in the realm meteoroid and debris detection, leading to the M&D SIG preliminary report on impact features documented on the LDEF {2.14} (Known fondly as "*The Blue bible*"!).

References

- {2.1} The Royal Aircraft Establishment, Farnborough, (1986). "The RAE Table Of Earth Satellites 1957-1986", Stokten Press,
- {2.2} NASA Langley Research Center, (1991). "69 Months in Space: A History of the First LDEF (Long Duration Exposure Facility)".
- {2.3} J.A.M. McDonnell, W.C. Carey and D.G. Dixon, (1984). "Cosmic Dust Collection by the Capture Cell Technique on the Space Shuttle", Nature, Vol. 309, No. 5965 p237.
- {2.4} NASA SP-473, edited by L.G. Clark, W.H. Kinard, D.J. Carter Jr. and J.L. Jones Jr., (1984). "The Long Duration Exposure Facility (LDEF). Mission 1 Experiments". pp117-120.
- {2.5} NASA SP-473, edited by L.G. Clark, W.H. Kinard, D.J. Carter Jr. and J.L. Jones Jr., (1984). "The Long Duration Exposure Facility (LDEF). Mission 1 Experiments". pp121-123.
- {2.6} NASA SP-473, edited by L.G. Clark, W.H. Kinard, D.J. Carter Jr. and J.L. Jones Jr., (1984). "The Long Duration Exposure Facility (LDEF). Mission 1 Experiments". pp124-126.
- {2.7} NASA SP-473, edited by L.G. Clark, W.H. Kinard, D.J. Carter Jr. and J.L. Jones Jr., (1984). "The Long Duration Exposure Facility (LDEF). Mission 1 Experiments". pp127-130.
- {2.8} NASA SP-473, edited by L.G. Clark, W.H. Kinard, D.J. Carter Jr. and J.L. Jones Jr., (1984). "The Long Duration Exposure Facility (LDEF). Mission 1 Experiments". pp131-133.
- {2.9} NASA SP-473, edited by L.G. Clark, W.H. Kinard, D.J. Carter Jr. and J.L. Jones Jr., (1984). "The Long Duration Exposure Facility (LDEF). Mission 1 Experiments". pp134-135.

- {2.10} NASA SP-473, edited by L.G. Clark, W.H. Kinard, D.J. Carter Jr. and J.L. Jones Jr., (1984). "The Long Duration Exposure Facility (LDEF). Mission 1 Experiments". pp136-137.
- {2.11} NASA SP-473, edited by L.G. Clark, W.H. Kinard, D.J. Carter Jr. and J.L. Jones Jr., (1984). "The Long Duration Exposure Facility (LDEF). Mission 1 Experiments". p138.
- {2.12} NASA SP-473, edited by L.G. Clark, W.H. Kinard, D.J. Carter Jr. and J.L. Jones Jr., (1984). "The Long Duration Exposure Facility (LDEF). Mission 1 Experiments". pp101-104.
- {2.13} NASA, (1991). "LDEF Spaceflight Environmental Effects Newsletter" Vol.II No.1. pp3-4.
- {2.14} NASA, (1990). Compiled by T. See, M. Allbrooks, D. Atkinson, C. Simon, M. Zolensky. "Meteoroid and Debris Impact features Documented on the Long Duration Exposure Facility".

Chapter 3

Analysis Techniques

3.1 Introduction

One of the most important aspects in the analysis of space flight hardware is to keep the specimen pristine. Whatever the investigator is "*looking for*", in terms of space borne contamination, will almost certainly be changed once exposed to the air borne contaminants on the Earth.

In the analysis of impact data from space flight hardware one of the most important results to be acquired is the chemical nature of the impacting particle. This result will be grossly affected by air borne contaminants and render any information useless. This applies to any LDEF surface being analysed for chemical residue.

To accommodate the analysis on LDEF surfaces the USS has developed an analytic suite comprising of: a class 100 clean room, to store and process space flight surfaces for analysis; a Large Optical Scanning System (LOSS), housed in the clean room for primary analysis (section. 3.2) and a Philips 525M Scanning Electron

Microscope (SEM) with associated Energy Dispersive X-Ray analysis system (EDS) for chemical analysis of impactor residue (section. 3.3). With these three integral systems, contamination free analysis of LDEF surfaces is possible.

The techniques used in hypervelocity impact analyses for interpreting results obtained from the analytic suite are discussed in section. 3.4.

3.2 Large Optical Scanning System (LOSS)

3.2.1 System Objectives

The Large Optical Scanning System (LOSS) was designed "*in house*" at USS to accommodate the primary analysis of automatic detection and logging of impact sites detected on LDEF surfaces. At first these surfaces were to be MAP frames but as LDEF neared retrieval status it became clear that other surfaces, notably UHCRE covers were to be analysed using the same systems at the USS. LOSS had to accommodate the differing sizes of specimens from small segments of UHCRE covers (few cm²), to MAP frames (~315 cm²) and UHCRE covers (~0.3 m²).

The basic analysis output from LOSS was to be positional data of impact sites. This needed to be stored as an absolute co-ordinate system, such that sites could be revisited using other equipment. The system needed to cope with both supra-marginal (perforations) and marginal (craters on the surface with no clear exit point) impact sites. Alongside the position data, measurement of the size of the impact crater was required based upon either a photometric calibration for supra-marginal or optical measurement for marginal impacts. The final data output would be two, three colour (RGB) stereo images of the impact site giving the absolute position, size and magnification of the impact site, with a unique identification number, such that further analysis on crater morphology could be undertaken at a later date and a database on impact sites developed.

The design was based around an optical scanning table (stage) with an accompanying microscope and two CCD RGB cameras interfaced to a computer to run automatic scanning routines.

3.2.2 LOSS Hardware

The LOSS stage was custom built and designed by Deben Research and has a useable area of 100cm by 40cm, with a nominal position accuracy of $30\mu\text{m}$ when compensation is made for the backlash in the motors {3.1}. The optical microscope is a short focal length stereo microscope with five fixed magnifications connected to two RGB CCD colour cameras, with a resolution of 320 pixels by 320 pixels. This system gives aspect ratios (defined as pixel width/pixel height) of 1.41 with field widths of 12.6mm, 8.14mm, 4.93mm, 2.98mm and 1.94mm (*i.e.* areas of 112.64mm^2 , 46.97mm^2 , 12.26mm^2 , 6.29mm^2 and 2.68mm^2). One problem associated with short focal length microscopes is that the focal depth is short, typically $50\mu\text{m}$ in this case, causing defocussing of the specimen if surface flatness $>50\mu\text{m}$ over the scanning area. To overcome this, a manual focussing mechanism is attached such that the operator at the computer can re-focus the image.

In addition to the two RGB CCD cameras there is a third separate camera with a low magnification (field of view 181mm by 117mm), a long focal length and depth, mounted on a flexible mounting system. The high sensitivity of this camera, coupled with the long focal length and depth means that scanning of large specimens is possible without defocussing, and therefore decreases the time required to scan a specimen for impact site recognition (as opposed to the microscope with CCD cameras). Although the accuracy in feature location is degraded, once located the sites can be revisited at a higher magnification using the microscope for clarification and validation.

The specimens can be illuminated from above and below or both. Bottom illumination is either via a "goose-neck" fibre optic light, giving a high intensity spot of

light in line with the microscope, or a light box, both used for the detection of supra-marginal impacts. Top illumination is either via a pair of goose-necks or a ring illuminator, attached to the microscope. The latter gives the option to search for the raised crater lips associated with hypervelocity impact cratering, as illustrated in figure 3.1. Thus, this illumination technique is used to locate marginal impact sites and the verification of hypervelocity impact cratering at impact sites.

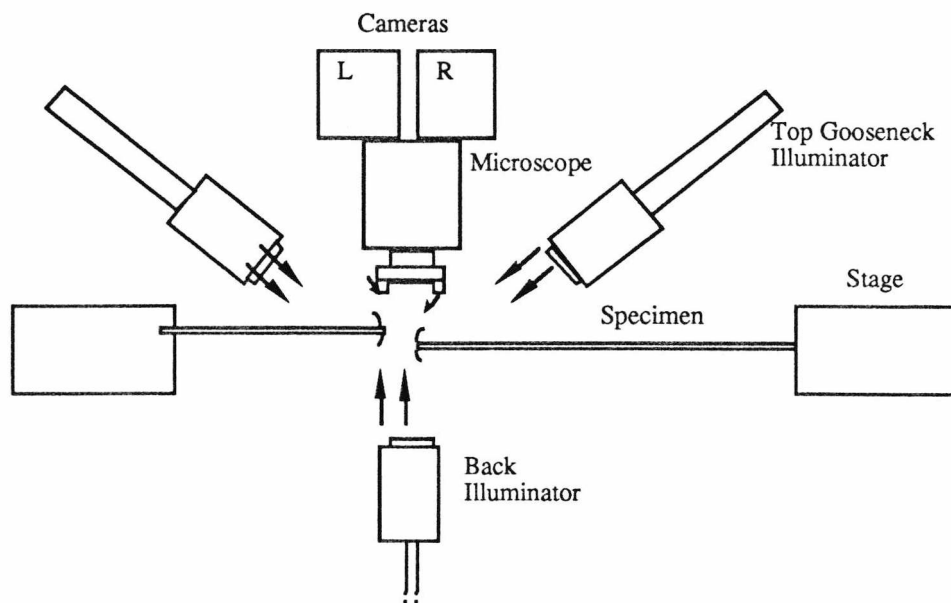


Figure 3.1 Schematic of illumination technique for LOSS

The stage, microscope, cameras and illumination and focussing devices are all housed in the clean room, and are fully operational from outside the clean room, thus reducing the handling of specimens and possible contamination of the surfaces. The system is controlled via a 80486 based P.C. running SCO Unix with associated video multiplexing and digitiser cards for the video image processing and viewing, as illustrated in figure 3.2. This allows any combination of images to be taken from the left or right camera with red, green or blue channels.

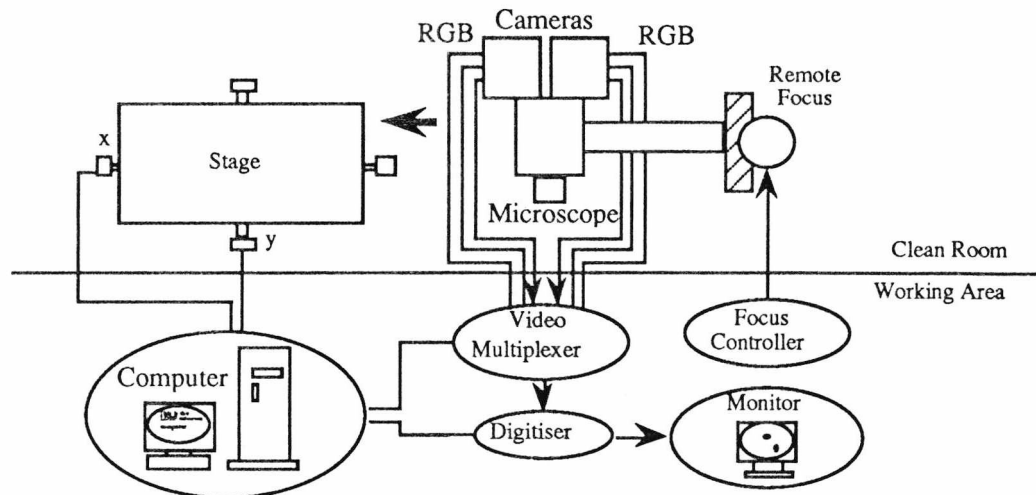


Figure 3.2 Schematic LOSS hardware.

3.2.3 Specimen Scanning

Before undergoing a scan an associated co-ordinate system needs to be devised for the specimen. Such that LOSS can locate and revisit impact sites and other scanning systems (eg. SEM) can locate the same sites. The co-ordinate system is designed to be flexible and is based on 3 calibration points on each specimen with associated “real” and “stage” co-ordinates.

The co-ordinate system has the following advantages :

- allows for thermal expansion of the stage
- specimens that do not lie flat and settle with time (UHCRE covers) can be re-calibrated
- specimens can be removed from the stage and replaced in a different orientation
- pieces of a larger specimen can be scanned using a consistent co-ordinate system provided the co-ordinates of the corners are known

- units for “*real*” co-ordinate system are determined purely by the units given by the user when defining the co-ordinates of the calibration marks. This allows co-ordinate systems defined by other groups (*e.g.* NASA) to be used.

Once the calibration marks and co-ordinate system has been logged the computer can use the scanning program “*AUTOSCAN*”, developed and designed by Matthew Paley at the USS {3.1} to drive the stage, scanning and logging the positions of features.

“*AUTOSCAN*” features include:

- optimal scan patterns over any polygonal object
- up to 20 rectangular or circular areas can be excluded from the scan (thus defining complicated areas to be scanned avoiding known defects)
- adjustable overlaps to ensure that large features are not excluded by the edge of the field of view
- overlaps automatically increased when this would not result in slower scan times
- field of view calculated from the true field of view and the angle of the microscope with respect to the co-ordinate system axis
- pauses after each move to allow vibrations in the system to die down
- options to increase the speed of scanning when looking for large features only
- features only accepted if they meet specified criteria
- unique identification numbers generated for each feature.

The scanning software allows the user to define the criteria on selection of features. This feature recognition allows the exclusion of defects such as tears based upon a circularity measurement of the feature. Thus the user scanning for supra-marginal impact sites can define a brightness level to search for (indicating the difference between supra-marginal impacts and marginal), a circularity limit (based upon the photometric

shape) and an area limit (size of feature). Once a feature matching this criteria has been located its position based upon the highest value of brightness or darkness (defined by the user) is logged alongside its "real" and "stage" co-ordinates, circularity measurement, area and unique identification number.

A typical scanning procedure would be:

- (i) create 3 calibration marks on the specimen
- (ii) attach the specimen to the LOSS stage
- (iii) arrange illumination (bottom/top, light box/goose-necks)
- (iv) adjust stage for weight of specimen and illuminator
- (v) choose co-ordinates for the calibration marks
- (vi) find the "stage" co-ordinates for the calibration marks
- (vii) load the two co-ordinate systems into "AUTOSCAN"
- (viii) find the "real" co-ordinates of the edges of the specimen
- (ix) find the co-ordinates ("stage" or "real") of all areas to be avoided
- (x) load data from (viii) and (ix) into "AUTOSCAN"
- (xi) choose selection criteria for feature acceptance
- (xii) start scan
- (xiii) possibly repeat scan using a different camera/colour
- (xiv) merge the results of the scans
- (xv) change to high magnification to improve accuracy
- (xvi) move the stage to each feature in turn
- (xvii) find exact co-ordinates of the feature
- (xviii) record the position, size and circularity of the feature
- (xix) take images of the feature as required

Figure 3.3 illustrates LOSS scanning a UHCRE cover.

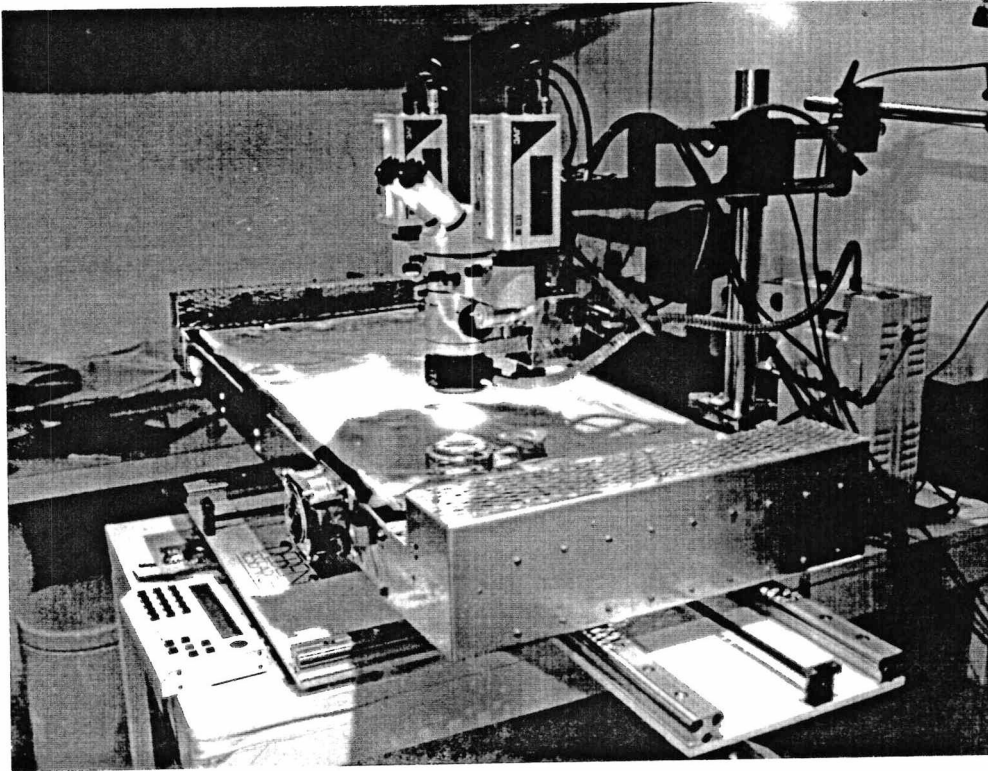


Figure 3.3 Scanning of a UHCRE cover using LOSS

3.2.4 LOSS Capabilities

The speed at which LOSS scans specimens is dependant upon the magnification used, the overlap and to a smaller degree the number of features per unit area {3.1}.

Times for a typical step in “AUTOSCAN” is given below:

- calculate next position instant
- move stage 6 sec (depends on load, accuracy and distance)
- take image 1 sec
- analyse image 1 sec
- log data instant

Giving a typical step time of some 8 seconds. Table 3.1 shows typical scan times for a specimen 100mm by 100mm, scanning at 20% overlap (Paley, 1993) {3.1}.

Magnification	Low	Medium	High
Field width (mm)	181	12.6	1.94
Field height (mm)	117	8.96	1.36
Field area (mm ²)	13553	72.3	1.69
Frames	1	177	6111
Time	8 secs	23.6 mins	13.5 hours

Table 3.1 Scanning times for "AUTOSCAN".

The accuracy with which LOSS measures the position of features on a scanning depends upon:

- position accuracy of the stage (nominally 30 μ m but this is degraded by heavy loads and backlash errors caused by motors changing direction)
- the magnification of the cameras (high magnification means a small field of view which reduces the following errors)
- inaccuracies in the calibration (setting up image width, image height and angle between the image and stage axis)
- distortions in the optics/cameras and digitiser.

The LOSS reproducibility in positioning has been remarkable. Even the smallest feature to be revisited has been located within the field of view. Although not necessarily in the centre, user commands, to the stage, can realign the feature such that it is at the centre.

3.2.5 Image Display And Printing

As all the images are stored with unique identification numbers on tape it is possible to carry out further image analyses and study of crater morphology at a later date. The

monochrome images from LOSS can be displayed directly, or from tape, onto a Sun 3/60 colour workstation (section. 3.3.1) as either 245 grey levels or pseudo colours on the screen. The Sun workstation has the software to measure the size and shape of the impact site more accurately than using a photometric calibration curve and so detailed analyses of ellipticity and other aspects of crater morphology can be undertaken with the images supplied by LOSS, even when the specimen is no longer available, provided as is the case with all LOSS images, there is the accompanying field of magnification and field of view sizes.

Hardcopies of images are available from a Tektronix 4693 RGB hot wax thermal screen printer (4 bits (16 shades) in each RGB component) and a polaroid palette (8 bits (256 shades) in each RGB component). Figures 3.4 and 3.5 show example output of crater features from LOSS.

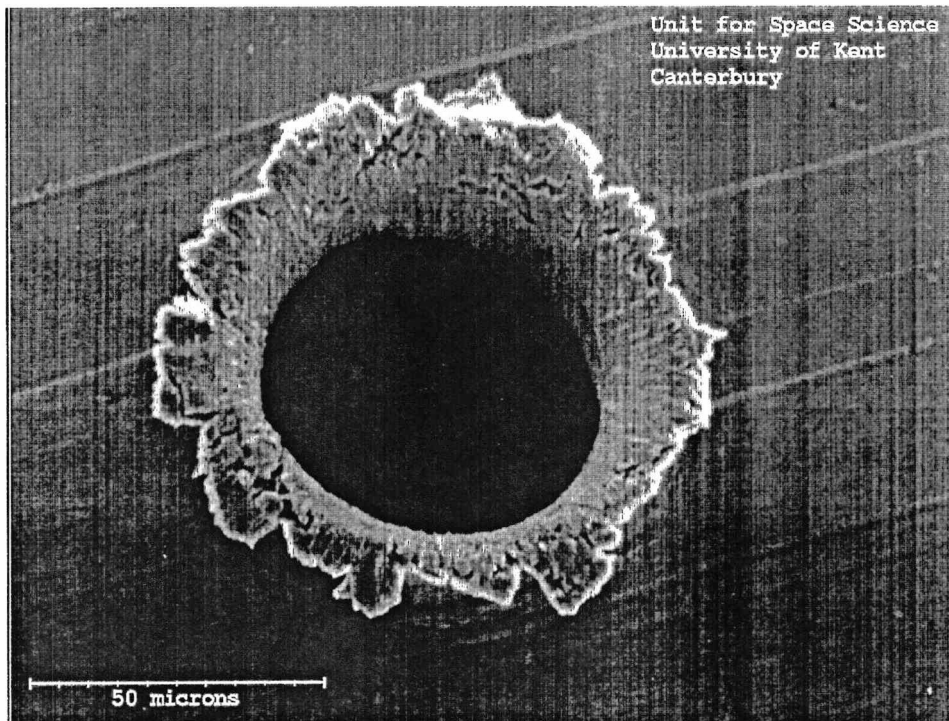


Figure 3.4 Impact through a 14 μ m aluminium MAP foil, taken using LOSS

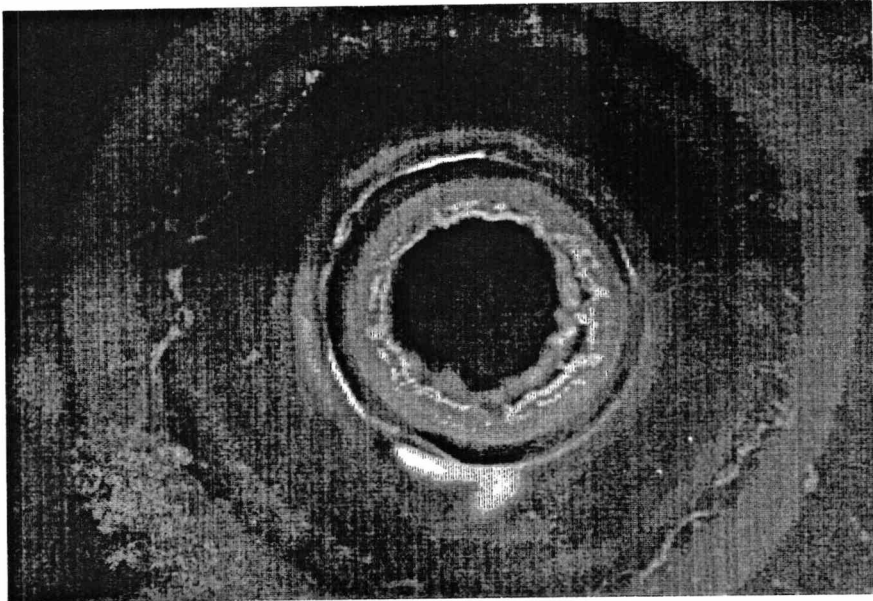


Figure 3.5 Impact in a UHCRE cover taken using LOSS

3.3 Scanning Electron Microscope (SEM)

3.3.1 Microscopy

Alongside LOSS the USS has a SEM suite to further analysis impact sites. This suite comprises of a Philips 525M SEM, an associated Energy Dispersive X-Ray System (EDS), a Sun 3/60 workstation and a Hummer VII sputtering system used for coating specimens, if required. The SEM has a chamber size that can accommodate a specimen of 10cm by 10cm. To prevent damage to the specimen from the electron beam the specimen can be coated, to various thicknesses, with a gold/palladium alloy using the Hummer VII sputtering system. This prevents damage to the specimen but leads to chemical contamination of the surface.

The SEM is used to search, locate and document marginal impact sites in the MAP experiment and other LDEF surfaces, especially the clamps (Newman, 1993) {3.2}. The SEM can also be used to verify the size and position of the smaller impact site

located using LOSS. The Sun workstation is used to log the position of the impact site and acquire digital pictures of the impact site with the associated information on magnification used. Alongside the digital pictures, 35mm photography is possible.

Once a site has been located a stereo image is taken by tilting the SEM specimen stage to $\pm 7.5^\circ$ and taking either digital or photographic images. Using the Sun workstation software it is possible to carry out further analysis of the crater morphology and accurate measurement of the characteristic hypervelocity crater lips and dimensions of crater diameter. Stereo reconstruction is possible to acquire the depth of craters in the clamps and the ellipticity of craters can be measured and possible impact directions inferred in some cases. A possible mechanism for decoding such information is discussed in Chapter 7. Figure 3.6 shows an impact site image taken from the SEM.

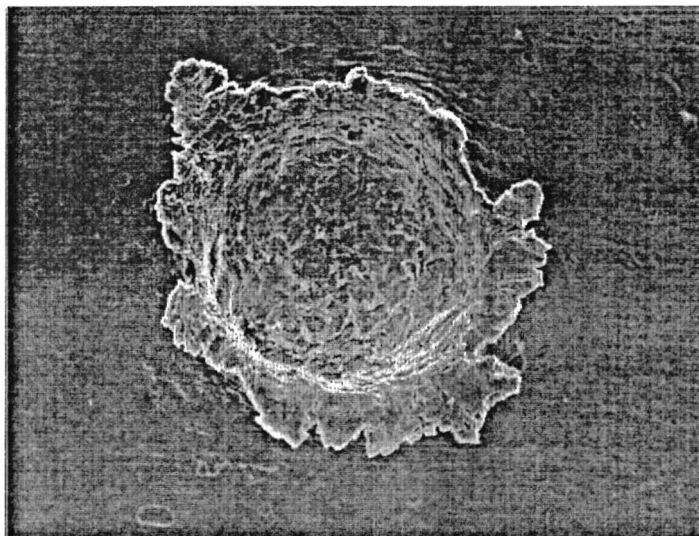


Figure 3.6 Impact crater on an LDEF clamp taken using the SEM.

3.3.2 Energy Dispersive X-Ray System (EDS)

Associated with the SEM and the Sun workstation is an EDS. This system detects the X-rays released by the specimen when bombarded by electrons in the SEM chamber. X-rays are emitted when the excited electrons in the atoms of the specimen fall back to

lower energy shells. The electrons being excited from lower energy shells by electron bombardment from the electron microscope LaB₆ crystal. Thus for specific atoms, and energy shells, discrete X-rays are emitted with distinct energies. EDS measures the X-ray energies emitted and thus the atoms causing the emission are known. The system is therefore used to characterise the chemical composition of the specimen. There is a limitation however, that isotopic abundances of a specific chemical species/element, cannot be measured. Therefore if energies associated with certain transitions in the oxygen atom, for example, are detected, there is now way of determining if this is due to ¹⁶O or ¹⁷O. For the analysis of impact residue, this is not a problem.

The chemical analysis of impact sites can take two forms:

- (i) X-ray mapping
- (ii) X-ray spectra.

The first type, X-ray mapping, reveals the chemical composition of the impact sites in terms of position on the image. Thus the system can be programmed to indicate the position of say gold and display via a colour co-ordinated map over the image. This then shows immediately where certain elements are to be found on the specimen and also the position of chemical inclusions which may have been produced in the manufacture of the specimen. Figure 3.7 illustrates an X-ray map of an impact in an aluminium clamp.

The second type, X-ray spectra, records the relative abundances of the elements present by measuring the relative abundance of the distinct X-rays emitted. Figure 3.8 shows an X-ray spectrum.

Using both techniques, impact site chemical analysis can reveal the origin of the impacting particulate. If a particle impacts a surface causing a hypervelocity impact crater or even penetration, both the detector and particle are subjected to an "explosive" rise in temperature and hence vapourisation of the particle and local detector area. Inside the crater lips there may be residue left from the impacting particle alongside the once molten detector. EDS analysis of such areas can reveal the origin of the impacting

particle knowing that the chemical composition of interplanetary particles and man-made space debris are quite distinct.

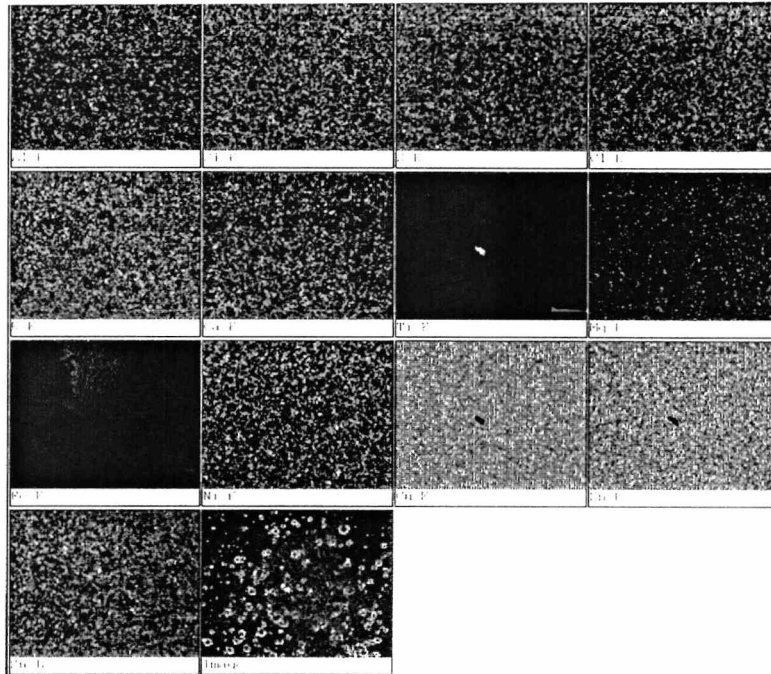


Figure 3.7 Example of an X-ray map of an impact site on an LDEF clamp.

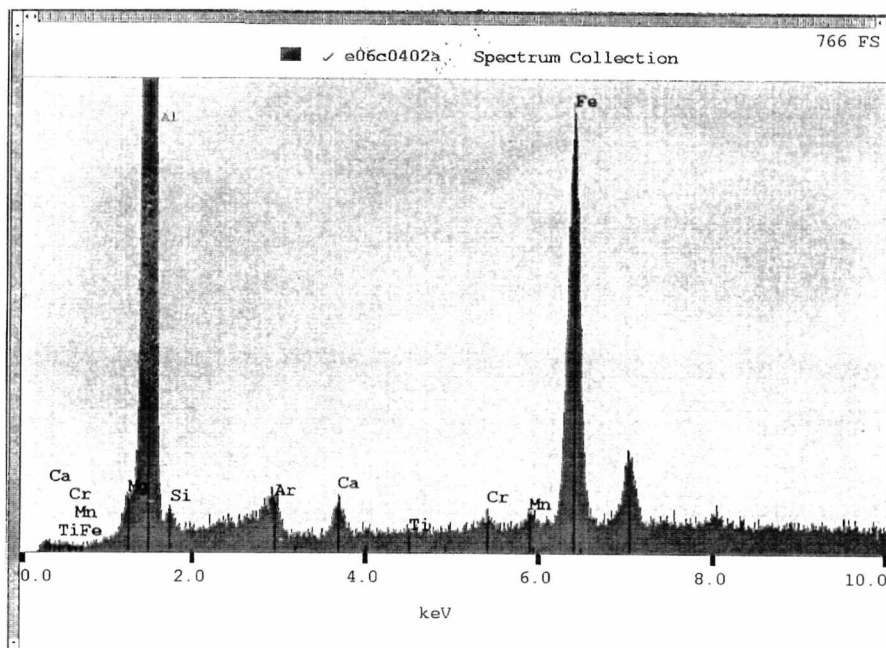


Figure 3.8 Example of an X-ray spectra of an impact crater on an LDEF clamp.

The criteria for chemically identifying impactors is set out in the M&D SIG interim report {3.3} and is as follows:

To positively identify natural impactors (*i.e.* interplanetary particles) the elements present are defined as mainly Fe with minor S and/or Ni. Various proportions of Mg, Fe and Ca \pm minor S, Ni and/or Al being also present. Positive identification is also given if non-terrestrial isotopic compositions (*i.e.* presence of solar wind implanted He or Ne) are detected and the comparison of certain elemental ratios such as Al/Mg, Ca/Mg and Ti/Mg as defined by Amari et al. (1991) {3.4}.

To positively identify man-made impactors (*i.e.* space debris) the criterium is in short, not any of the above. Mainly Al or Al₂O₃ \pm minor Fe, Ni, Cr, Cl, Na or C. Alternatively Fe with traces Cd, Ti, V, Cr, Ni, Mn, Co, Cu or Zn with the latter elements present in abundances greater than to be expected for common minerals is used to identify man-made impactors. Various proportions of Ca, Al, Si, Ti, K, Zn, Co, Sn, Pb, Cu, S, Cl, Au or Ag will also indicate a man-made impactor. A common man made material is stainless steel consisting of Fe, Cr and Ni.

The most likely places to find residues are in the craters on the clamps and inner lips of the craters. The MAP experiment surfaces can be analysed for residue chemistry although there is more chance of locating residue on the second surface foil (section. 2.4.2) than the first. The MAP second surface and stop plate are designed to detect ejecta spallation zones from the impacting particle and hence remnants of the particle.

To date no residue chemical analysis at USS has proved conclusive. This is mainly due to two reasons:

- (i) Impact residue has not been located around the impact sites or second surfaces of MAP.
- (ii) The detector surfaces have been found to contain a wide range of impurities. (Especially in the clamps, which were not designed as a pristine detector surface, the impurities coincide with the chemicals which would validate the particles origin.)

The M&D SIG reported in their interim report, May 1992, {3.3} that the level and composition of contamination be carefully analysed before residue analyses undertaken. Many materials contain impurities, though minute on the macro scale, are important at the micro scale which is necessary for the analysis of impactor residue. They also reported that the LDEF surfaces are sprinkled with particles of alkali-halide salts (from oceanic and human spray), paint flakes containing high concentrations of Ti and/or Zn and/or Mg, from LDEF paints that were shed due to atomic oxygen/UV action, flakes of Al from blankets and antenna arrays, and other less characterized materials. Alongside these elements ubiquitous contamination from Si was noted, mainly due to outgassing, and other contaminants were found to include O, C, H, Na, K, and Ca.

It is therefore clear that the high levels of contamination and lack of impactor residue both contribute to the scarcity of positive identification of the impactor origin.

3.4 Hypervelocity Impact Decoding

3.4.1 Introduction

There are two main distinct populations of particulates that will impact spacecraft in the near Earth space environment. They are namely anthropogenic space debris (man-made orbital debris), and the interplanetary dust or cosmic dust that is gravitationally attracted to the Sun and the Earth. The differences in these two populations in terms of particle characteristics, density, and velocity is well understood.

The interplanetary dust particles (IDP) are on average travelling at 40kms⁻¹ (Leinert & Grün, 1990) {3.5}, although, velocities can reach some 72kms⁻¹ if the ambient solar system velocity is added. The vector addition of the spacecraft and particle velocity dictate the impact velocity.

The man-made space debris, however, is orbiting the Earth and therefore has a much lower velocity and smaller velocity range (*e.g.* $v \sim 7.8\text{kms}^{-1}$ at 100km altitude and

$\sim 3.1\text{kms}^{-1}$ at 35,787km). If an impact occurred between a spacecraft and an orbiting particle in a circular orbit the resultant impact velocity would be the vector summation of the two. A spacecraft such as LDEF at 458km altitude, has an orbital velocity of 7.6kms^{-1} and therefore impact with a circular debris object would be at a maximum of 15.2kms^{-1} . Debris orbits however are not all circular, see Chapter 5, and so impact velocities can occur higher than twice the orbital velocity.

Impacts can occur at a wide range of velocities from $1\text{-}2\text{kms}^{-1}$ for space debris impacts up to 70kms^{-1} for IDP. This range of velocities is far greater than present terrestrial laboratory simulation, and so hypervelocity impact phenomena at these extreme values have to be extrapolated from the lower velocity regime produced in the laboratory. Impacts studied from space flight hardware reveal very little about the impacting particle and its characteristics. The only remnants may be some chemical residue, but definitely an impact crater and morphology. Crater morphology is the first indication of a hypervelocity impact. The hypervelocity impact scenario is said to exist when the pressure between the impactor-target interface, at the moment of impact, is such that the shock front produced in the target causes a transition of state from solid to plasma of the target and projectile, under certain conditions (Hill, 1990) {3.6}. Fluid dynamics then govern the resultant crater morphology with the hypervelocity impacts occurring at $1\text{-}2\text{kms}^{-1}$ as a minimum velocity.

For a given particle size and velocity, hypervelocity impacts can occur in three generalised cases, as shown in figure 3.9. They are (i) impact into a semi-infinite or thick target, that is, the target depth is much greater than the impacting particle diameter, (ii) impact onto a very thin film or foil, relative to the impacting particle termed *supra-marginal* and (iii) an intermediate case between these two in which the particle just penetrates the foil, marginal penetration limit.

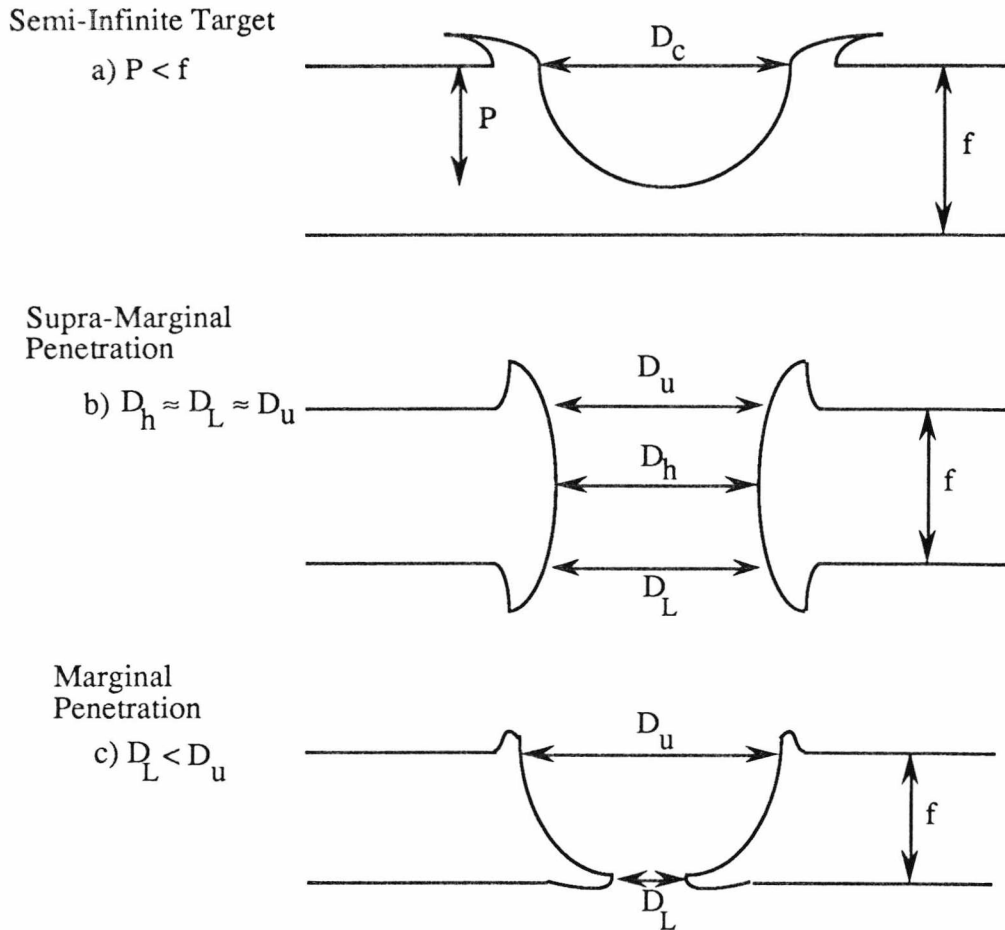


Figure 3.9 The three hypervelocity impact scenarios. f is the foil thickness, P the crater depth, D_c the crater diameter in a thick target, D_h is the hole diameter with D_u and D_L the entrance and exit hole diameters respectively.

In all three cases impacts produce circular craters with raised lips for impact angles up to 70° to the target normal. (Sullivan, 1992) {3.7}. Elliptical craters can be indicative of certain impactor directions and Chapter 7 will show how modelling can predict the ellipticity of impact craters as a function of LDEF face and impacting particulate, (*i.e.* space debris or interplanetary particles). The inside of craters in semi-infinite targets are generally smooth and hemispherical due to the dynamic fluid flow reached at impact, although the ratio of crater depth to diameter ranges from 0.4 to 1 (Laurance and Brownlee, 1986) {3.8}. It can be seen in crater analysis on LDEF clamps that the depth to diameter ratio varies with size of crater and LDEF face indicating either a velocity dependence, or particle population dependence, such as space debris particles

being more dense than IDP. In the case of supra-marginal impacts, the formation of spallation petals on the rear of the foil is dependant upon the particle and target densities. Circumferential lips on exit and entrance side of a foil indicates hypervelocity impact with particle density being equal to or less than the target density and high impact velocity (Carey et al., 1984) {3.9}.

The semi-infinite target scenario occurs when the target thickness is much greater than the particle diameter such that the particle cannot penetrate. The induced shock front dissipates before reaching the rear target surface. Figure 3.9a shows the condition that foil thickness (f) \gg particle diameter (d). The resultant crater has a diameter D_c and depth P .

For supra-marginal impacts, target thickness is of the order of or less than than particle diameter. In figure 3.9b the particle has penetrated the foil leaving an entrance and exit hole with identical raised lips, characteristic of a hypervelocity impact. In this case the particle was large enough, relative to the foil thickness, to leave exit and entrance diameters comparable, $D_L \approx D_U$. When $f \ll d$ the resultant hole diameter will approximate to the particle diameter, with some of the particle remaining intact and passing through with a reduced velocity.

Increasing the foil thickness for the same impacting particle in 3.9b eventually leads to the marginal impact scenario whereby the entrance diameter remains roughly constant but the rear surface is just held intact. This marginal limit for a given particle size and impact velocity represents the maximum foil thickness (f_{max}) that the particle would just penetrate. Theoretically marginal penetration is the limit of D_L tending to zero, this being the ballistic limit. Sullivan (1992) {3.7} argues the case for a minimum rear-foil hole size dependant upon relative projectile and target densities.

All three scenarios of hypervelocity impacts in figure 3.9 have been documented on the LDEF. Decoding the impact parameters from the observed crater morphology and position requires the use of impact equations developed from Earth based calibration and experimental testing, to spaceflight hardware analysis. One of the primary goals of the

LDEF study is to re-evaluate the validity of some of the impact equations developed. This is, however, outside the scope of this study (see Paley, 1993 {3.1}) and as such the equations presented here are used in the knowledge that LDEF will undoubtedly refine and develop new equations better fitted to the experimental data.

Most laboratory studies involve accelerators or light gas guns to fire particles from the micron sizes at 40kms⁻¹ up to millimetres at 6-7kms⁻¹. Both laboratory studies and space flight hardware analyses have contributed to the development of the hypervelocity equations given. A detailed study of hypervelocity equations and their development is given by Sullivan (1992) {3.7}.

3.4.2 Marginal Penetration Equations

For many years equations have been developed to understand the processes governing the formation of hypervelocity impact cratering. Most equations have been developed from laboratory experiments on aluminium foil targets (McDonnell, 1970,1979) {3.10} {3.11} using accelerators such as the 2MV Van de Graaff at the Unit for Space Sciences. The equations are then scaled for increase in dimension and velocity when moving to bigger particles. As a consequence as new penetration data became available the equations have been modified to incorporate such parameters as density, tensile strength and ductility in some cases. As early as 1965, Fish & Summers (1965) {3.12} derived a penetration equation incorporating such parameters as particle and target densities with a scaling factor for particle size (d).

The true mechanism behind the impact process is still not fully understood and the dependence of such macro parameters as density and tensile strength (Hill 1990) {3.6} appear to be consistent for the particular experimental data set in question. The penetration equations (3.1 to 3.9) describe f/d (foil thickness/particle diameter) as a function of various macro parameters and impact velocity {3.12, 3.13 3.11, 3.14 3.15 3.7} :

$$\frac{f}{d} = 0.57 d^{0.056} \epsilon^{-0.056} \left(\frac{\rho_P}{\rho_T} \right)^{0.5} V^{0.875} \quad \text{Fish \& Summers (1965) (3.1)}$$

$$\frac{f}{d} = d^{0.056} \rho_P^{0.52} V^{0.875} \quad \text{Naumann (1966) (3.2)}$$

$$\frac{f}{d} = 0.79 V^{0.763} \quad \text{McDonnell (1979) (3.3)}$$

$$\frac{f}{d} = 0.635 d^{0.056} \rho_P^{0.5} V^{0.67} \quad \text{Cour-Palais (1979) (3.4)}$$

$$\frac{f}{d} = 0.772 d^{0.2} \epsilon^{-0.06} \rho_P^{0.73} \rho_T^{-0.5} (V \cos \alpha)^{0.88} \quad \text{Pailer \& Grün (1980) (3.5)}$$

$$\frac{f}{d} = 1.023 d^{0.056} \left(\frac{\rho_P}{\rho_T} \right)^{0.476} \left(\frac{\sigma_{Al}}{\sigma_T} \right)^{0.134} V^{0.664} \quad \text{McDonnell \& Sullivan 1991b (3.6)}$$

Where V is the impact velocity (kms⁻¹), d is the particle size (cm), ρ_P and ρ_T are the particle and target densities (g/cc) respectively, σ_P , σ_T , the particle and target tensile strengths (MPa), ϵ is the foil ductility or percentage elongation, and is dimensionless, and α is the impact angle between the target normal and the projectile trajectory. Recently a re-evaluation of the understanding of the penetration formulae and scaling for different data sets from various experiments, has been undertaken by McDonnell and Sullivan, resulting in 3 equations (McDonnell & Sullivan, 1992) {3.16} to cover all types of impact scenario found (equations 3.7 to 3.9).

$$\frac{f}{d} = 0.970 d^{0.056} \left(\frac{\rho_P}{\rho_T} \right)^{0.476} \left(\frac{\sigma_{Al}}{\sigma_T} \right)^{0.134} V^{0.701} \quad \text{McDonnell 1992A (3.7)}$$

$$\frac{f}{d} = 1.272 d^{0.056} V^{0.806} \quad \text{McDonnell 1992B (3.8)}$$

$$\frac{f}{d} = 1.272 d^{0.056} \left(\frac{\rho_P}{\rho_{Fe}} \right)^{0.476} \left(\frac{\rho_{Al}}{\rho_T} \right)^{0.476} \left(\frac{\sigma_{Al}}{\sigma_T} \right)^{0.134} V^{0.806}$$

McDonnell 1992C (3.9)

Here σ_{Al} is the tensile strength of aluminium, ρ_{Al} and ρ_{Fe} the densities of aluminium and iron respectively. Equations (3.7) to (3.9) are generalised equations derived from impact data of iron particles impacting aluminium targets (McDonnell & Sullivan, 1992) {3.16} and valid from 4 to 16kms⁻¹. With the exception of equation (3.8), which is only valid for iron particles impacting an aluminium target, equations (3.7) and (3.9) have used iron onto aluminium data but scaled to account for other density targets. Equation (3.6) is used as the basis of the work as over the size range in question equations (3.6), (3.7) and (3.9) are consistent with each other.

Generalised marginal penetration equations are therefore available, developed from micrometre sized particles and scaled to the millimetre dimension by the incorporation of a scaling factor. The development of such marginal penetration equations were studied in detail by Sullivan (1992) and McDonnell (1992) {3.7, 3.16}. The choice of penetration equation depends on the closeness of an experimental configuration to the calibration data that was used in determining the relationship (McDonnell & Sullivan, 1992) {3.16}.

3.4.3 Semi-Infinite Target Cratering

Alongside thin foils flown in space on board the LDEF and other spacecraft, aluminium plates have been flown directly and indirectly as impact witness plates. The LDEF

infrastructure, clamps, longerons and intercostals were made of aluminium and along with dedicated impact experiments, have been cratered by impacts.

Impacts upon the Solar Maximum Mission spacecraft have been analysed by Laurance and Brownlee (1986) {3.8} and the size data derived has been converted to mass via a form of the Pailer and Grün equation, as shown below :

$$\frac{P}{d} = 0.772 d^{0.2} \epsilon^{-0.06} \rho_p^{0.73} \rho_T^{-0.5} (V \cos \alpha)^{0.88} \quad \text{Pailer \& Grün (1980) (3.10)}$$

In essence equation (3.10) is similar to equation (3.5), except that in this context the equation describes the semi-infinite crater depth, P . This assumes that the depth of the crater formed is independent of the target thickness, and so the semi-infinite crater depth corresponds to the thin foil marginal penetration thickness.

Summers (1959) {3.17} also describes semi-infinite target experiments into metallic surfaces developing the equation :

$$\frac{P}{d} = 2.25 \left(\frac{\rho_p}{\rho_T} \right)^{0.667} \left(\frac{V}{C} \right)^{0.667} \quad \text{Summers (1959) (3.11)}$$

where C is the speed of sound in the target material.

The two equations (3.10) and (3.11) relate semi-infinite crater depth to the impactor diameter and hence to mass, by assuming a spherical impactor of particle diameter, d , and assuming a particle density, ρ_p . The advantage of the Pailer and Grün equation (3.10) is that it has incorporated a dimensional scaling factor and can be used for a range of sizes.

Crater depth, however, is not a quantity easily measured from either laboratory experiments or space flight hardware. The parameter determined by such studies is the crater diameter, and hence a conversion between crater diameter and crater depth is required. Work by Laurance and Brownlee {3.8} on SMM louvres yielded a

depth to diameter ratio (P/D_c) of 0.62. The depth/diameter ratio is assumed to be a function of impacting particle size, density and velocity. The velocity dependence is borne out by examining the depth/diameter ratios around the LDEF, these vary from 0.64 ± 0.03 to 0.53 ± 0.03 (McDonnell et al, 1992) {3.18}, as the average impact velocity on the LDEF faces varies depending on the distance around from the the ram direction. Indeed in his Ph.D. thesis Sullivan {3.7} gives a discussion on depth/diameter ratios for a single velocity, of 5.2 km s^{-1} , based upon Rudolph (1967) {3.19} data from iron impacts onto gold, silver, copper and aluminium thick targets, where:

$$\frac{P}{d} = 2.188 \left(\frac{\rho_p}{\rho_T} \right)^{0.291} \quad (3.12)$$

He concludes that equation (3.12) is valid for this single velocity and a comparison of the three equations (3.10), (3.11) and (3.12) emphasises that the Pailer & Grün {3.15}, Summers {3.17} and the Rudolph {3.19} density scaled data agree to within half a decade of magnitude for crater diameter in their crater depth to mass conversions. Once again the mass is derived from assuming a spherical particle of diameter, d , and assuming a particle density, ρ_p .

A detailed study on crater depth/diameter ratios for LDEF clamps has been undertaken by Newman {3.2} and will be presented in his thesis.

3.4.4 *Supra-Marginal Penetrations*

One of the most useful parameters to be obtained from impact data studies is the marginal perforation limit (f_{\max}), and hence from this the minimum mass threshold for a given target thickness. This is needed when engineers are designing spacecraft shields, and walls. They need to know the minimum shielding required for the maximum impact protection.

A great number of experiments both those flown in space, and ground based experiments, have involved thin foils as the targets. Hence impact perforations are detected and a relationship is required to determine the impactor size from a given hole size. As the LDEF MAP foils were mainly aluminium, the studies by Carey et al (1984) {3.9} are the basis for the equations described below.

Carey et al. {3.9} established two semi-empirical equations, based on data from firing iron particles onto aluminium and gold foil targets. The two crater size equations are given below :

$$\frac{D_L}{d} = 1 + 1.5 (f/d) V^{0.3} \left[\frac{1}{1 + (f/d)^2 V^{-n}} \right] \quad \text{Fe} \rightarrow \text{Al} \quad (3.13)$$

$$\frac{D_L}{d} = 1 + 5 (f/d) V^{0.3} \left[\frac{1}{1 + 7 (f/d)^2 V^{-n}} \right] \quad \text{Fe} \rightarrow \text{Au} \quad (3.14)$$

Later these equations were generalised (Hill, 1990) {3.6} to give equation (3.15), below

$$\frac{D_L}{d} = 1 + 2.9 \left(\frac{\rho_T}{\rho_P} \right)^{0.6} \left(\frac{f}{d} \right) V^{0.3} \left[\frac{1}{1 + 2.9 \left(\frac{\rho_T}{\rho_P} \right) \left(\frac{f}{d} \right)^2 V^{-n}} \right] \quad \text{General} \quad (3.15)$$

where n is given by,

$$n = 1.02 - 4 \exp(-0.9 V^{0.9}) - 0.003 (20 - V) \quad (3.16)$$

with D_L being the exit hole diameter. The general equation will be referred to as the CMD equation (from Carey, McDonnell & Dixon).

In the derivation of these equations, at very small foil thicknesses, the crater size to projectile diameter ratio was fixed to tend to unity. This implies that when the projectile is much larger than the foil thickness the projectile perforates with a hole size equal to that of the projectile. As the foil thickness increases so does the hole size for a constant projectile diameter. The hole size then begins to reduce as the marginal perforation limit is reached. Equation (3.13) gives, for iron onto aluminium, a particle to target density ratio of 2.9 (7.87/2.71) whilst equation (3.14), iron onto gold, leads to a particle/target ratio of 0.40 (7.8/19.3). A simple density scaling approach may lead to the assumption that equation (3.14) represents a projectile of density 1.0gcm^{-3} impacting aluminium, due to the fact that the ratios are very similar (Carey et al, 1984) {3.9}. This then leads to the notion that equation (3.13) represents a high density particle impacting aluminium, (possibly indicative of anthropogenic space debris), whereas equation (3.14) represents a low density particle impacting aluminium (possibly indicative of micro-meteoroids).

In 1963 Maiden et al. {3.20} derived a crater size equation given below:

$$\frac{D}{d} = 0.45 (f/d)^{2/3} V + 0.9$$

Maiden et al. (1963) (3.17)

where D is crater diameter.

This equation had no projectile-target material scaling factors and the ratio of crater size to projectile size tended to a value of 0.9 as foil thickness is reduced to zero, compared to the theoretical concept of unity.

It is clear from figure 3.10, that when comparing equation (3.13) (Carey et al. {3.9}) and equation (3.17) (Maiden et al. {3.20}), for iron onto aluminium for velocities of 4kms^{-1} , 10kms^{-1} and 16kms^{-1} , that the trend at lower f/d values is similar. However the Maiden equation does not adequately describe the situation approaching the marginal perforation limit, also seen in figure 3.10.

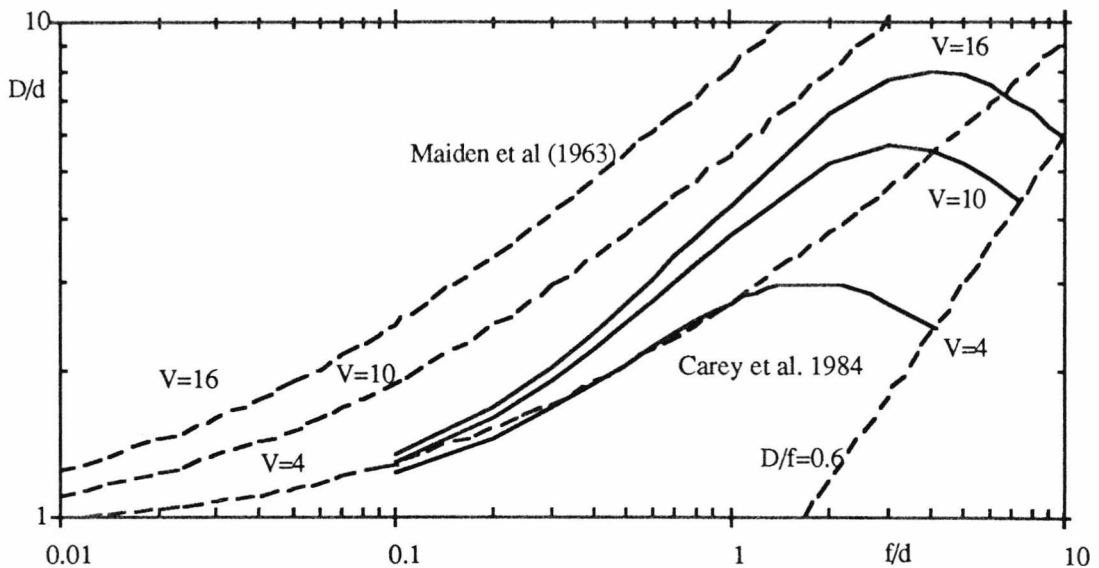


Figure 3.10. Carey et al (1984b) iron onto aluminium experimental crater hole size equations compared to that of Maiden et al (1963) (theoretical) for the corresponding velocities. V is in kms^{-1} .

The marginal perforation or ballistic, limit, is reached when either $D_L/f=1$ or $D_L/f=0.6$. The choice of ballistic limit is dependant upon the impact velocity. For impacts of iron onto aluminium below 16kms^{-1} the ballistic limit is defined as $D_L/f=0.6$ and at greater velocities at $D_L/f=1$, based upon experimental work by McDonnell (1979) {3.11}. This was used in establishing equation (3.3) (McDonnell, 1979) {3.11}, and is discussed by Sullivan (1992) {3.7}. A ballistic limit of $D_L/f=0.6$ is chosen as representative when discussing LDEF data.

3.4.5 Conversions Between Impact Scenarios

As previously mentioned impact data is available from various calibration experiments performed in the laboratory, and the various impact scenarios on spaceflight hardware, these are:

- (i) marginal penetrations
- (ii) semi-infinite target cratering

(iii) supra-marginal perforations.

The larger impacts are more probable on the semi-infinite targets as this constitutes by far the greater surface area on any spacecraft. Some experiments however, such as LDEF's MAP, use thin foils as detectors, whilst others, such as LDEF's IDE use semi-infinite targets. The main difficulty in using thin foils as detectors is in mounting the foils successfully for the stresses and strains encountered during spaceflight.

Most of the data from spacecraft and especially LDEF is counted as either crater counts, or hole counts in a given foil, (of thickness, f , μm) and thus individual cumulative flux plots are developed, one for crater counts the other for hole counts. These two cumulative flux data must be transformed to a uniform scale alongside the marginal penetration data, also collected as cumulative flux data. This will enable the particle flux to be defined over the largest possible size range (data dependent) from micrometres through to millimetre dimensions.

The uniform scale taken is the marginal perforation foil thickness (f_{max}), as this is the most practical measure to give to engineers designing spacecraft shields and walls, to prevent impact damage. The conversion from semi-infinite target crater diameter to marginal perforation thickness is considered first.

If a particle produces a crater diameter D_c and no perforation, it is required to convert this to its equivalent foil thickness, so that the same particle, under the exact impacting conditions will just penetrate a foil of the same material, of thickness, f . The equivalent foil thickness f , of a thick target crater of diameter D_c can be derived from the general relationship (Sullivan, 1992) {3.7}:

$$\left(\frac{f}{D_c}\right) = \left(\frac{d}{P}\right) \times \left(\frac{P}{D_c}\right) \times \left(\frac{f}{d}\right) \quad (3.18)$$

where (f/d) represents the marginal perforation limit, (d/P) and (P/D_c) are derived from thick target impact data (particle size d , crater depth P , and crater size D_c). The marginal

perforation limit can be calculated from any of the equations from (3.1) to (3.9), whilst the thick target data can be derived from (3.10 or (3.11) or the measured data.

The Pailer & Grün {3.15} equation (3.5) applies equally to thick targets, to define crater depth, as well as the thin foil marginal perforation thickness, as stated earlier. Taking the marginal penetration thickness, f , to be equal to the thick target crater depth, P , gives $(f/P)=1$ and using equation (3.18) this gives $(f/D_c) = (P/D_c)$. In section 3.4.3, Laurance and Brownlee {3.8} gave a mean value of 0.62 for the ratio (P/D_c) in the SMM louvres analyses using the Pailer & Grün {3.15} equation. Therefore this combination gives a constant value for the ratio of thin foil marginal perforation thickness to the thick target crater diameter.

$$\frac{f}{D_c} = 0.62 \quad (3.19)$$

Using the McDonnell & Sullivan {3.7} equation (3.6) and Rudolph {3.19} equation (3.12) applied to equation (3.18) gives

$$\frac{f}{D_c} = 0.869 d^{0.056} \left(\frac{\rho_P}{\rho_T} \right)^{0.636} \left(\frac{\sigma_{Al}}{\sigma_T} \right)^{0.134} \quad (3.18)$$

This implies that as the particle density increases so does the equivalent foil thickness. This is seen on the results published by Humes et al (1992) {3.21} on the IDE on board LDEF and studies carried out by Newman (1993) {3.2}. The exact relationship may not be that given by Sullivan (1992) {3.7} equation (3.18) but the general trend is clear.

The second conversion, between marginal perforation foil thickness and supra-marginal hole diameter is, in effect, the reversal of the conversion presented above. The projectile, in this instant, has penetrated the foil causing a rear-foil hole diameter of D_L , for a foil of thickness, f , the same projectile, under the same impact conditions. The

marginal perforation limit is now required. The general equation (3.15) can be used to determine a particle size, d , assuming a particle density and velocity, then re-iterated, with the ballistic limit of $f=0.6D_L$ to give f , the marginal perforation limit (f_{\max}).

An assumption for the particle density can be made from the crater morphology as set out by Carey et al. (1984) {3.9}. If the crater size is much larger than the foil thickness, then no impactor density information can be obtained from the crater morphology. However, if the crater size is of the order of the foil thickness, then some information can be gleaned. The presence of rear foil spallation petals, has been shown to indicate that the particle density is less than the target density. This morphological criteria could prove very valuable for the post flight analysis of impact perforations in the marginal regime, leading therefore to inferences on the impactor density. In this region one could use equation (3.13) (as suggested in section. 3.4.4), whereas, if rear spallation petals are lacking, this indicates that the particle density is higher than the target material and that equation (3.14) can be used (Carey et al., 1984) {3.9}. Alternatively the general equation (3.15) can be used as opposed to equations (3.13) or (3.14).

One of the main goals of LDEF analyses will be to re-evaluate and validate the equations and conversions discussed here. The results of a re-evaluation of the semi-infinite target conversions and penetrations depths are given by Newman (1993) {3.2}, and Paley (1993) {3.1} . They discuss the choice of the generalised Carey et al {3.9} equation (3.15) with respect to supra-marginal perforations on the MAP experiment on LDEF. The CMD equation (3.15) is used in Chapter 7 when comparing data from the MAP experiment with other flight data on the Space face and in deriving an average particle density for the impactors.

References

- {3.1} Paley, M.T. (*Ph.D. thesis to be submitted 1993*). "The Development of an Automated Optical Scanning System and Studies of the Earth Orbital Dust Environment". University of Kent at Canterbury, U.K..
- {3.2} Newman, P.J. (*Ph.D. thesis to be submitted 1993*). University of Kent at Canterbury, U.K..
- {3.3} "Meteoroid and Debris Interim Report", May 1992. Compiled by members of the LDEF Meteoroid and Debris Special Investigation Group.
- {3.4} Amari, S., Foote, J., Simon, C., Swan, P., Walker, R. and Zinnerm, E. (1991). "SIMS Chemical Analysis of Extended Impact Feature from the Tailing Edge Portion of Experiment A0187-2", NASA CP 3134, pp503-516.
- {3.5} Leinert, C & Grün, E. (1990). "Interplanetary Dust", *Physics and Chemistry in Space - Space and Solar Physics, Physics of the Inner Solar System, Vol 20*, (eds. Schwenn, R. & Marsch, E.) pp207-275, (Springer-Verlag, Berlin Heidelberg).
- {3.6} Hill, D.C. (1990). "The Micrometeoroid Hazard In Space: Techniques For Damage Simulation by Pulsed Lasers and Environmental Modelling", *Ph.D. Thesis*, University of Kent at Canterbury, U.K..
- {3.7} Sullivan, K. (1992). "Characterisation and Dynamic Modelling of the Near-Earth Space Particulate Environment.", *Ph.D. Thesis*, University of Kent at Canterbury, U.K..
- {3.8} Laurance, M.R. & Brownlee, D.E. (1986). "The Flux of Meteoroids and Orbital Space Debris Striking Satellites in Low Earth Orbit", *Nature* 323, pp136-138.
- {3.9} Carey, W.C., McDonnell, J.A.M. & Dixon, D.G. (1984). "An Empirical Penetration Equation for Thin Metallic Films Used in Capture Cell Techniques", *Properties and Interactions of Interplanetary Dust* (eds., Guise, R.H. & Lamy, P.), pp291-295.

- {3.10} McDonnell, J.A.M. (1970). "Factors Affecting the Choice of Foils for Penetration Experiments in Space", *Space Res.*
- {3.11} McDonnell, J.A.M. (1979). "Marginal Hypervelocity Penetration Studies of Single and Double Foil Structures; Experimental Measurements and the Possibilities of a 2MV Microparticle Accelerator For Comet Meteoroid Probe Design Explored", *Proc. Workshop on Comet Halley Probe Design, ESA SP-153*, pp93-97.
- {3.12} Fish, R.H. & Summers, J.L. (1965). "The Effect of Material Properties on Threshold Perforation", *Proc. Hypervelocity Impact Symposium 7th, Vol VI.*
- {3.13} Naumann, R.J. (1966). "The Near-Reach Meteoroid Environment", *NASA TN D-3717.*
- {3.14} Cour-Palais, B.G. (1979). "Space Vehicle Meteoroid Shielding Design", *Proc. Comet Halley Micrometeoroid Hazard Workshop, ESA SP-153*, pp85-92.
- {3.15} Pailer, N., & Grün, E. (1980). "The Penetration Limit Of Thin Films", *Planet. Space Sci.* **28**, pp321-331.
- {3.16} McDonnell, J.A.M. & Sullivan, K. (1992). "Hypervelocity Impacts on Space Detectors: Decoding the Projectile Parameters.", *Hypervelocity Impacts in Space*, (ed. J.A.M. McDonnell), Unit for Space Sciences, University of Kent at Canterbury, pp 39-47
- {3.17} Summers, J.L. (1959). "Investigation of High Speed Impact: regions of Impact and Impact at Oblique Angles", *NASA TN D-94.*
- {3.18} McDonnell, J.A.M., Deshpande, S.P., Niblett, D.H., Neish, M.J. and Newman, P.J. (1992). "The Near Earth Space Impact Environment - An LDEF Overview", accepted for publication in *Proc. IAF/COSPAR World Space Congress Washington 1992.*
- {3.19} Rudolph, V. (1967). "Untersuchungen an Kratern von Microprojektilen im Geschwindigkeitsbereich von 0.5 bis 10km/s", *Dissertation*, Ruprech-Karl Universität, Heidelberg.

- {3.20} Maiden, C.J., Gehring, J.W. & McMillan, A.R. (1963). "Investigation of Fundamental Mechanisms of Damage to Thin Targets by Hypervelocity Projectiles", NASA TR 63-225.
- {3.21} Humes, D.H. (1991). "Large Craters on the Meteoroid and Space Debris Impact Experiment", in: *LDEF-69 Months in Space, First Post-Retrieval Symposium*, NASA CP 3134, pp. 399-418.

Chapter 4

Results from the LDEF

4.1 MAP Data

4.1.1 Penetration Distributions

All top aluminium foils of 5 μ m thickness and greater were de-integrated and cumulative flux plots derived (McDonnell et al., 1990) {4.1}, as a first cut analysis prior to LOSS scanning. The number of penetrations of a given foil thickness were counted using a simple light box technique, in the clean room, and plotted as a cumulative number distribution against flux. Figure 4.1 illustrates the fluxes obtained and the numbers of impacts detected, for the 5 faces of the LDEF on which the MAP experiment resided. These are faces 9, 3, 12, 6, (East, West, North, South) and the Space face. The East flux is the highest and the West flux the lowest, as to be expected from the ram and wake directions respectively. The South and North faces however, even at this stage pose an interesting question. The South flux, for the majority of the plot up to 20 μ m foil thickness, exceeds that of the North flux.

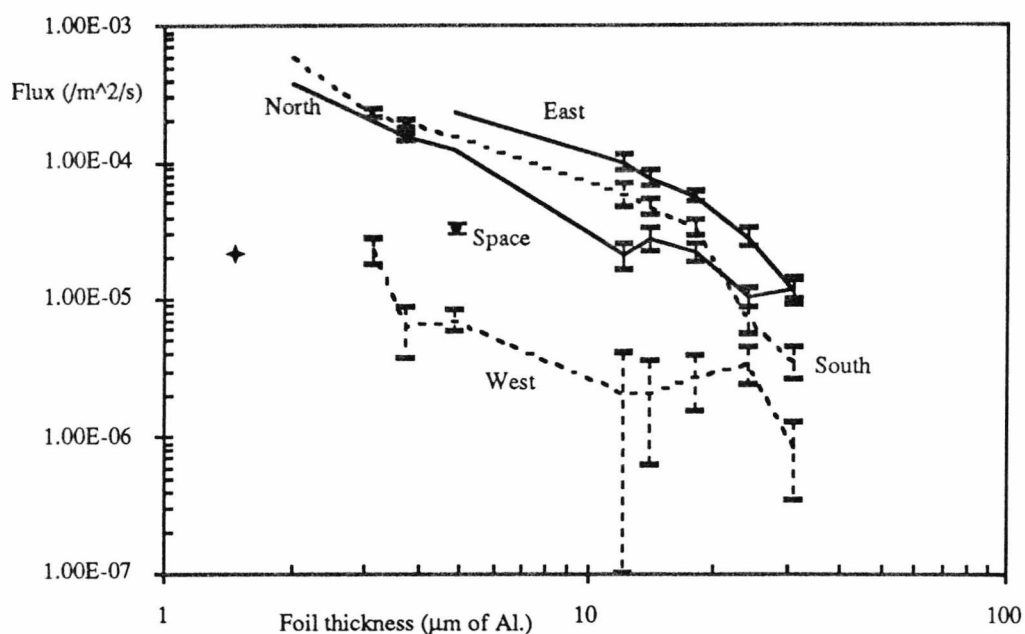


Figure 4.1 Initial results of light box scan of MAP foils on the East, North, South, West and Space face. The distribution is gained from counting number of impacts on a foil of given thickness. The errors are $1/\sqrt{n}$ flux, where n =number of impacts.

This is somewhat different to the expected result that would give the South and North faces identical fluxes if the LDEF was deployed without an offset and impacted by an isotropic particle distribution. The 8° offset, as reported in Chapter 2, would manifest itself with the North flux being greater than the South. This is in fact the opposite of what is seen below $20\mu\text{m}$ foil thickness. The possible reasons for this anisotropy are discussed in Chapter 7 and have brought about much interest especially in the analysis of anthropogenic space debris, and an anisotropic interplanetary dust population.

4.1.2 Space Face Hole Size Distributions

The MAP experiment situated on the Space face of the LDEF utilised $5\mu\text{m}$ aluminium and $5\mu\text{m}$ brass foils as the top surfaces. All four top surfaces have been scanned using the LOSS system and hole sizes, and positions logged. Aluminium surfaces H1ta-d and H4ta-d received 93 and 92 perforations in total, with a maximum size of $222\mu\text{m}$. The brass foils, H2ta-d and H3ta-d, received 70 and 99 perforations respectively, with a maximum size of $160\mu\text{m}$. The difference in the number of impacts detected on the

aluminium and brass foils is due to the differing detector material properties, as all these foils were located on the same baseplate on the Space face (Deshpande & Paley, 1992) {4.2}. The brass foils having a greater tensile strength and density ($\sigma=150\text{MPa}$, $\rho=8.9\text{gcm}^{-3}$), than the aluminium foils ($\sigma=80\text{MPa}$, $\rho=2.71\text{gcm}^{-3}$) presents a higher penetration threshold for a given particle mass, density and velocity and therefore detects less impacts than the aluminium foils for the same area time product. Tensile strength and density are two of the parameters associated with the most recent penetration formulae (see Chapter 3), although they play a part in the impact process the overall understanding of the detector and impactor material properties is still not clearly understood and defined.

The hole sizes were measured using the photometric sizes, as detected by LOSS {4.3, 4.4}, using the calibration curve determined from 4 known calibration holes, illustrated in figure 4.2, which were measured under the same lighting conditions as used in the scans.

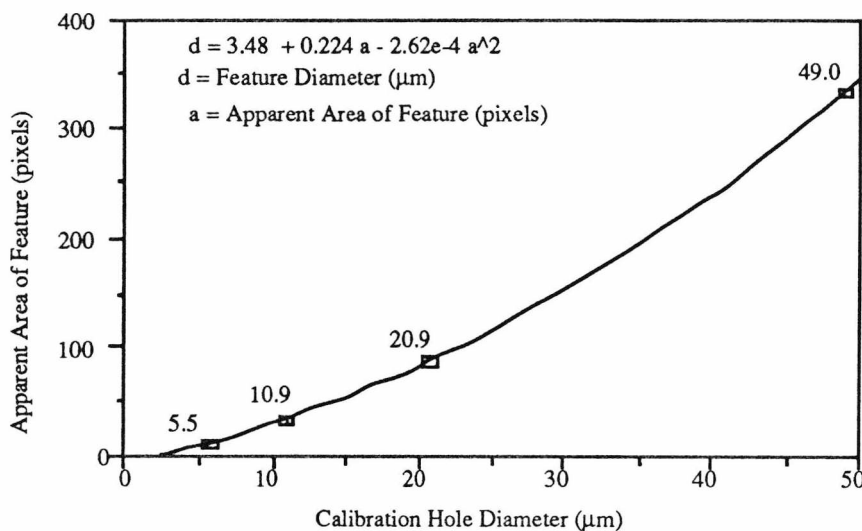


Figure 4.2 Calibration curve used to determine hole sizes from LOSS scanning procedure. The curve is derived from calibrated hole sizes viewed under the same lighting conditions as the *AUTOSCAN*.

The larger hole sizes that exceeded the calibration range were measured using a graticule. The hole sizes from the eight aluminium foil segments H1ta-d and H4ta-d were combined to give a cumulative flux distribution for aluminium and similarly for the eight

brass segments. Figure 4.3 illustrates the cumulative number distribution for the combined 5 μm aluminium surface and the combined 5 μm brass surface.

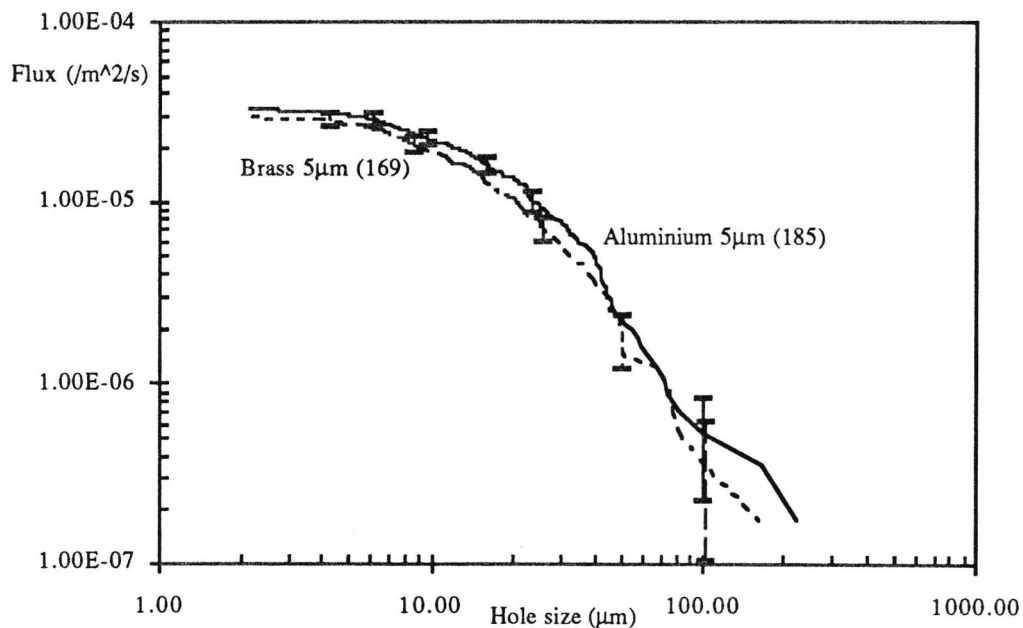


Figure 4.3 Results of D_H scan of the MAP 5 μm aluminium and brass foils on the Space face. The numbers of impacts detected are indicated with associated statistical errors.

It is clear that the flux distributions are different at the lower hole sizes but converge at 60 μm and larger hole sizes. When particles impact thin foils a hole is punctured through the foil and when the particle size is comparable to the foil thickness then the material properties of the the detector and particle shape the outcome of the hole size. However, when the particle size exceeds the foil thickness by a factor of 4 or greater, the hole size approximates to the particle diameter plus $\sim 10\%$ (McDonnell, personal communication). This is regardless of the foil's material properties. Hence at the larger hole sizes the cumulative flux distributions for aluminium and brass should converge as seen in figure 4.3 (within the statistical error bars given as $\pm \sqrt{n} \cdot \Phi$, where n is the number of impacts detected and Φ the flux).

4.2 Flux Distributions Measured on the LDEF

Apart from MAP there were other dedicated micrometeoroid experiments on the LDEF as outlined in Chapter 2. Figures 4.4 through to 4.8 illustrate the total fluxes received on the East, West, Space, North and South faces {4.5} as determined by MAP, SDIE {4.6}, FRECOPA {4.7}, intercostal data {4.8}, clamp data (Newman, 1993) {4.9}, with the associated errors and smoothed best fit line. A comparison of the East, West and Space smoothed data set is illustrated in figure 4.9 and similarly for the North and South faces in figure 4.10.

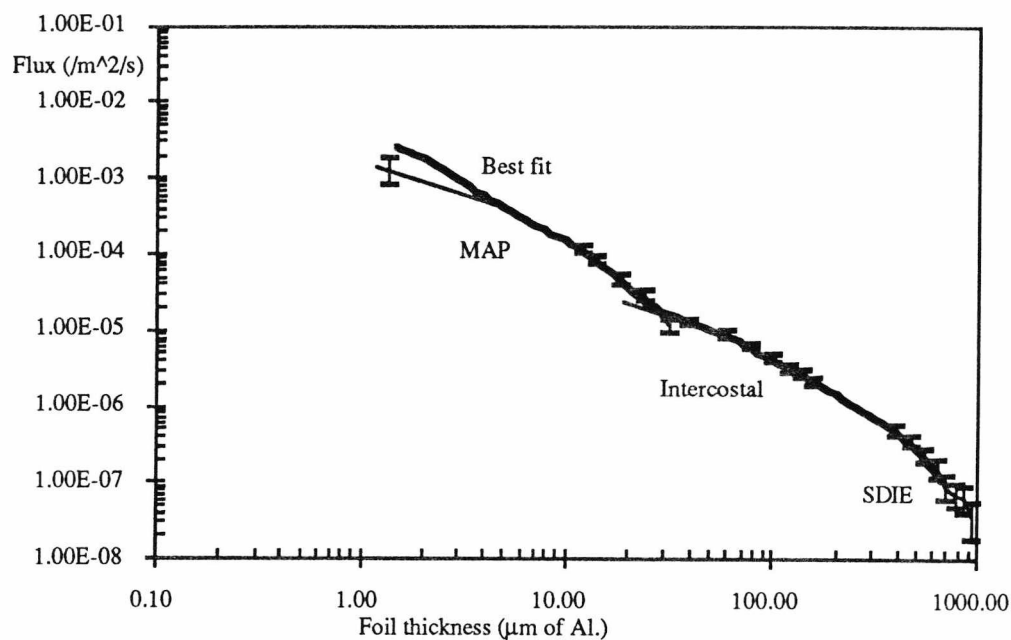


Figure 4.4 East smoothed best fit line through MAP, Intercostal and SDIE data in terms of f_{\max} .

The SDIE data was originally given in terms of D_c and has been converted to f_{\max} using equation (4.1) where:

$$f_{\max} = 0.75 D_c \quad (4.1)$$

based upon $T_c/D_c = 0.5 \pm 0.4$ for $D_c > 500 \mu\text{m}$ (Humes, 1991) {4.6}.

The clamp data (Newman, 1993) {4.9} has been transformed to f_{\max} using $f_{\max} = 0.9 D_c$.

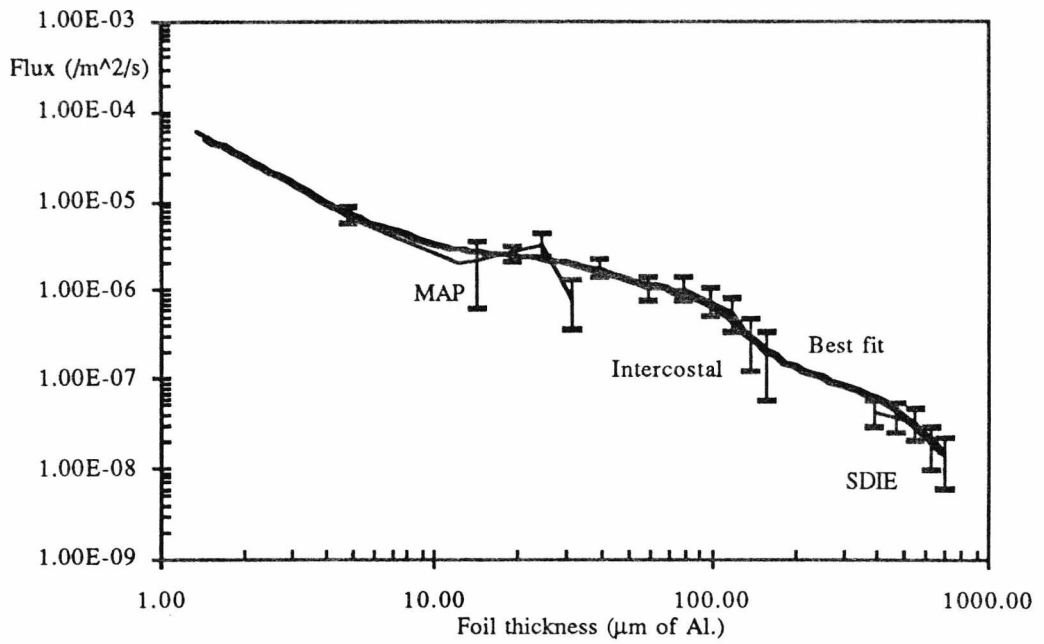


Figure 4.5 West smoothed best fit line through MAP, Intercoastal and SDIE data in terms of f_{max} .

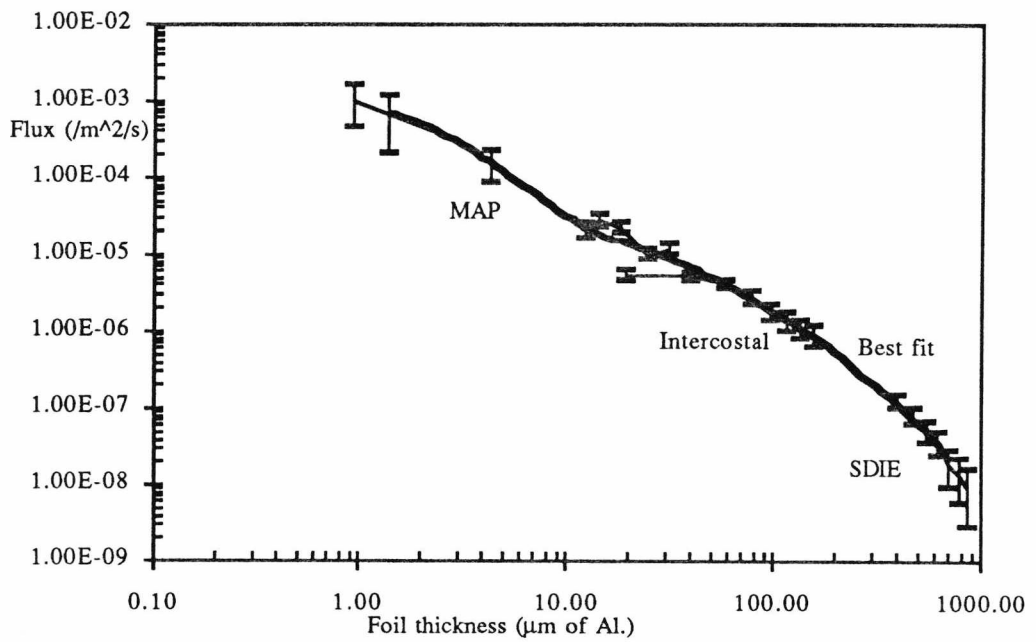


Figure 4.6 North smoothed best fit line through MAP, Intercoastal and SDIE data in terms of f_{max} .

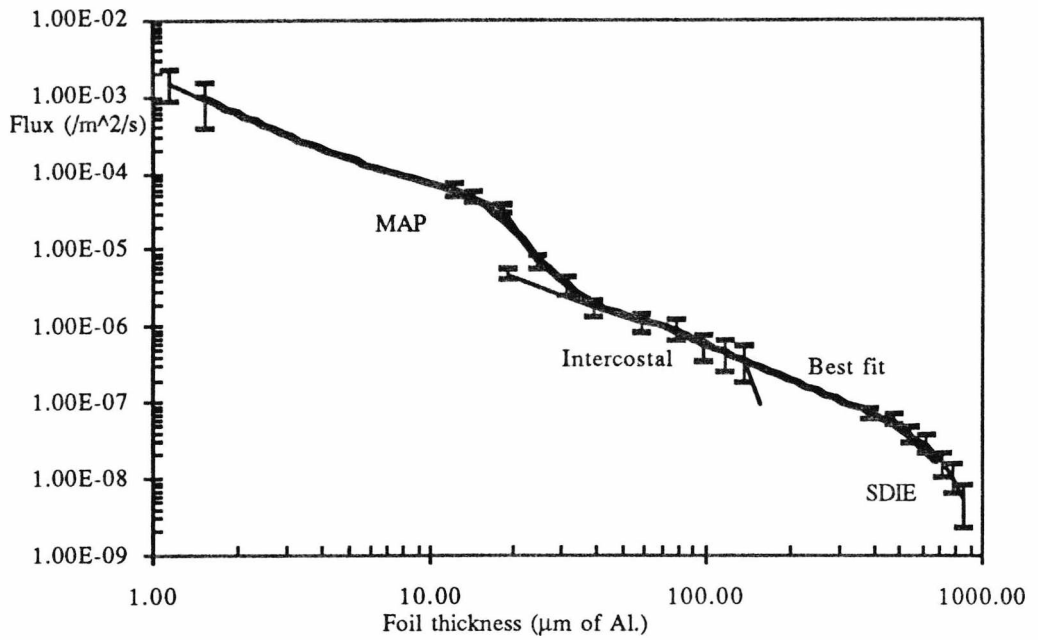


Figure 4.7 South smoothed best fit line through MAP, Intercostal and SDIE data in terms of f_{max} .

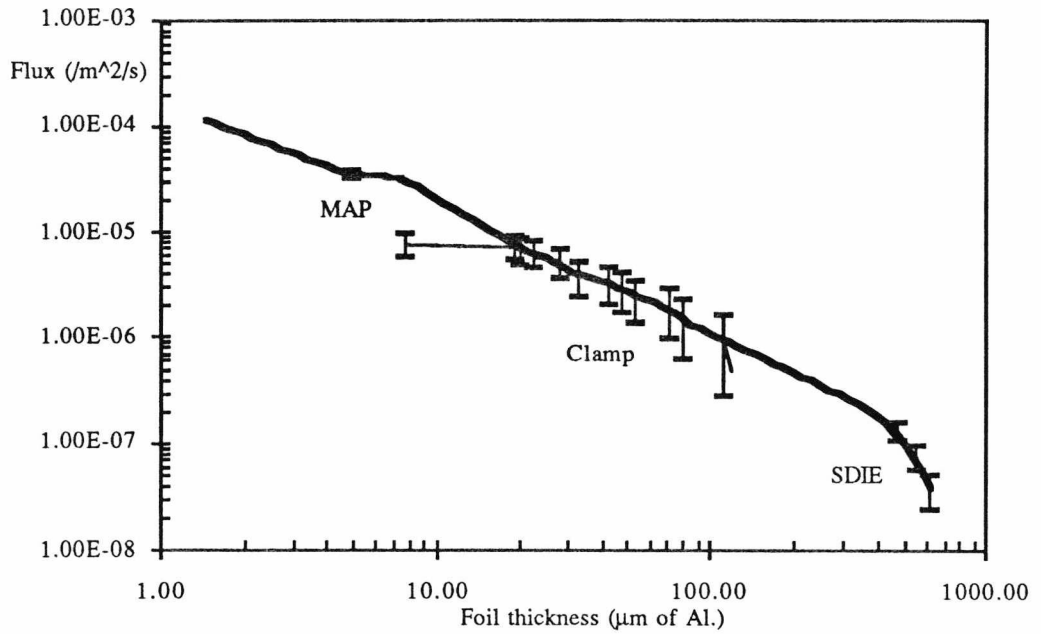


Figure 4.8 Space smoothed best fit line through MAP, Intercostal and SDIE data in terms of f_{max} .

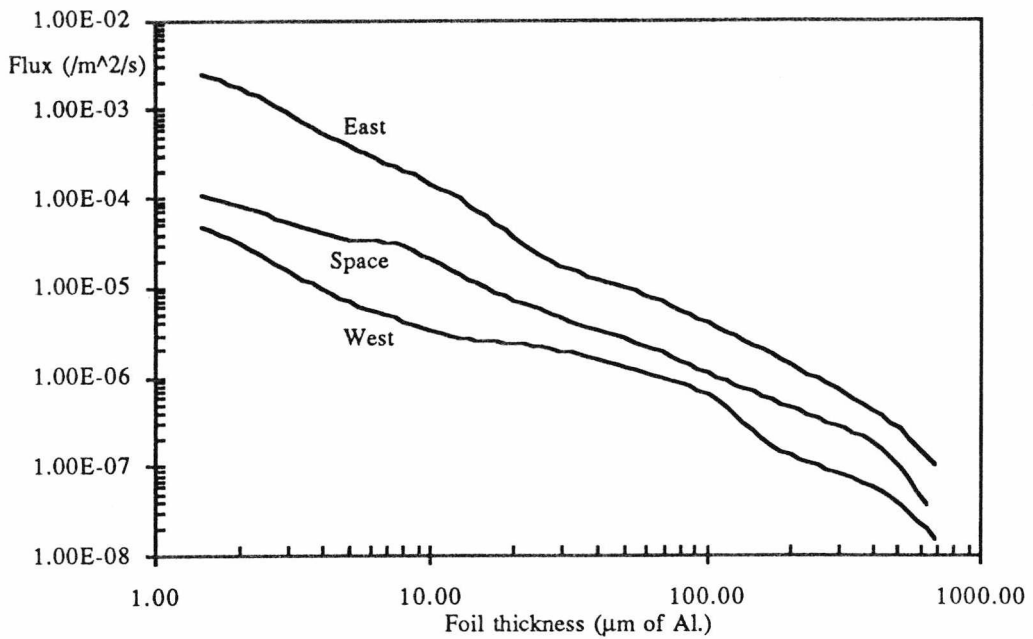


Figure 4.9 Comparison of East, West and Space face smoothed best fit lines in terms of f_{max} .

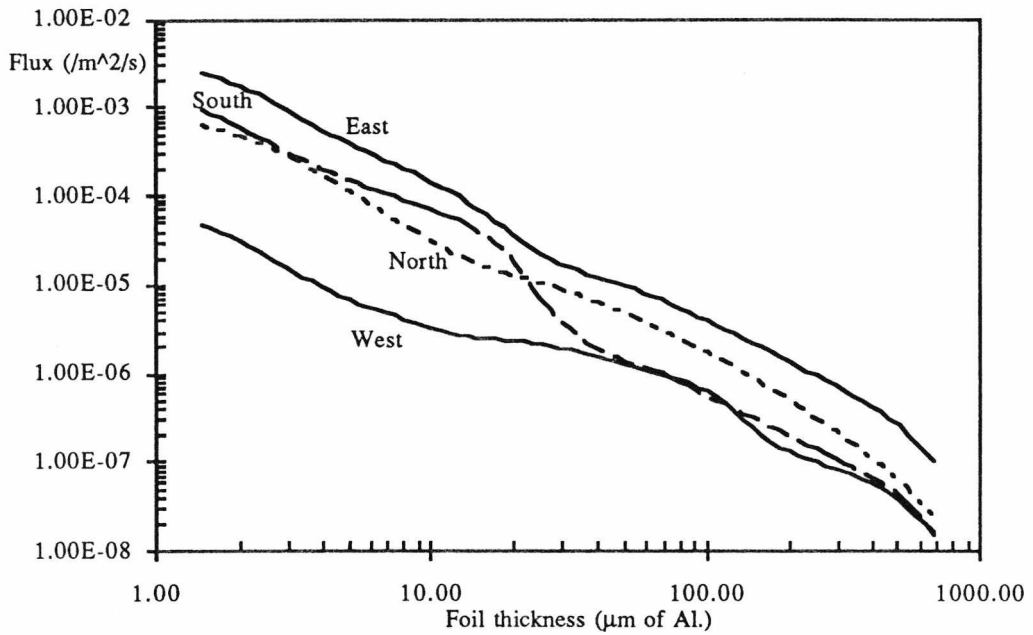


Figure 4.10 Comparison of East, West, North and South face smoothed best fit lines in terms of f_{max} . Showing the cross over between the South and North flux with the South flux larger than the North at small f_{max} , somewhat different to the expected result, when the 8° offset is taken into account.

The UHCRE cover data is illustrated in figure 4.11 (McDonnell et al., 1992) {4.5}, as the covers are a composite material, illustrated in figure 4.12, comprising of

teflon, silver and thermal paint it is unclear at present what conversion factors need to be applied.

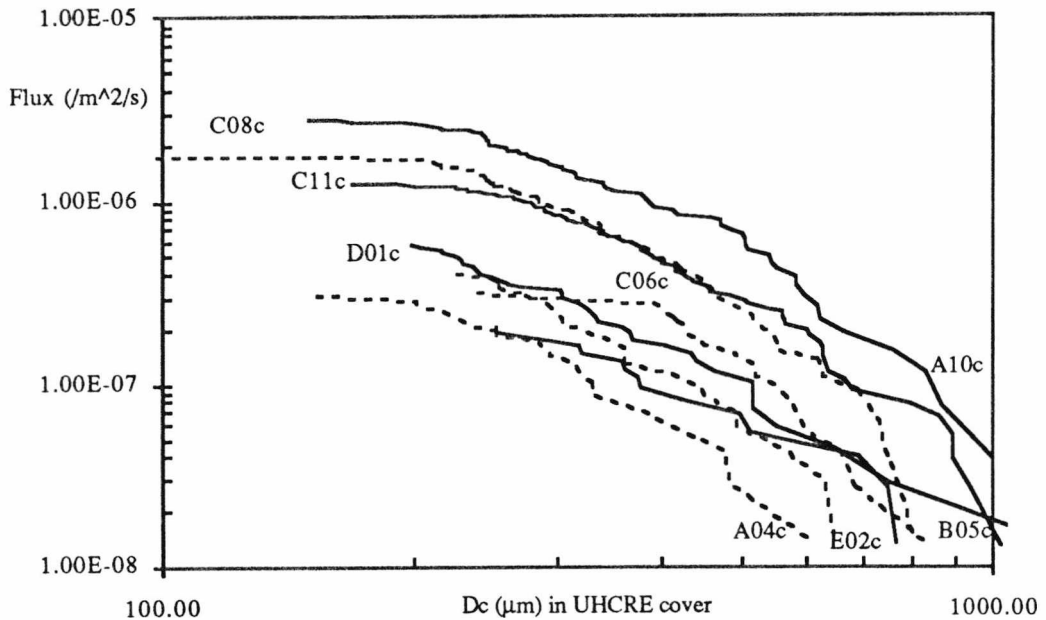


Figure 4.11 UHCRE cover data in terms of D_c (μm), crater diameter in the teflon cover. Shown are the flux curves for the 8 covers scanned using LOSS. The letters and numbers designate the face and row number on LDEF with the last letter representing which 1/3 segment of the cover is used.

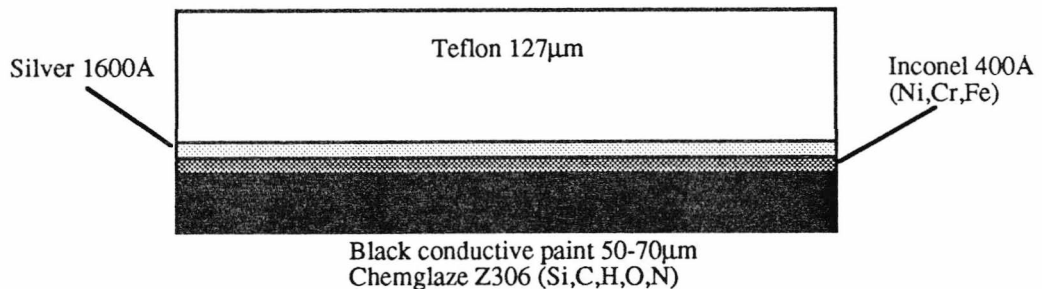


Figure 4.12 Cross section of UHCRE cover showing the composite nature of the cover.

Studies on this conversion factor, based upon similar conversions for aluminium foils and clamps are currently under way, combined also with a study of the effects of atomic erosion on the blankets, and in particular to the reduction in blanket thickness {4.10}.

It is clear that the anisotropy in the North and South faces as detected by MAP, is indeed a real effect. The South face flux is higher than the North flux for flux up to $20\mu\text{m}$ foil thickness, corresponding to a mass of $\sim 10^{-13}\text{g}$ based upon McDonnell &

Sullivan equation (1992) {4.11} (equation (3.6) in Chapter 3). The smoothed flux data set for the East, West, North, South and Space faces are given in Appendix I.

4.4 Corrected Flux Distributions for an 8° Offset LDEF

The fluxes illustrated in figures 4.9 and 4.10 are given as East, West, Space, North and South faces but these are not the true directions that are implied by East being the ram direction and West the wake direction. The offset of 8° to face 12 implies that the true ram direction is some 8° "north" of face 9. To account for this the fluxes have been corrected to give true ram, wake and peripheral fluxes. The corrections involve passing a fit through the data at a given foil thickness (Neish, {4.12} and McDonnell et al. {4.5}, 1992) and then using this fit to correct the flux seen on a given face to the true East, West, North, South directions (McDonnell et al. 1992) {4.5}. Figures 4.13 through to 4.15 illustrates the fit through the peripheral LDEF faces for three cases. Firstly the MAP data at 5µm foil thickness, Intercostal data at 50µm and 75µm foil thickness and SDIE data at 500µm foil thickness. The angular fits are determined from:

$$F=A +B \cos(x + \phi) + C \cos(2(x + \phi)) \quad (4.2)$$

where x is angle in degrees relative to the East face of LDEF, with the positive direction towards the North and ϕ is the offset angle of the maximum as determined by the best fit line. Tabulated results for the whole f_{\max} range are presented in Appendix I. It is interesting to note that when looking at this table the offset angle ϕ , changes with f_{\max} . Possibly an indication on differing populations of particles impacting the LDEF.

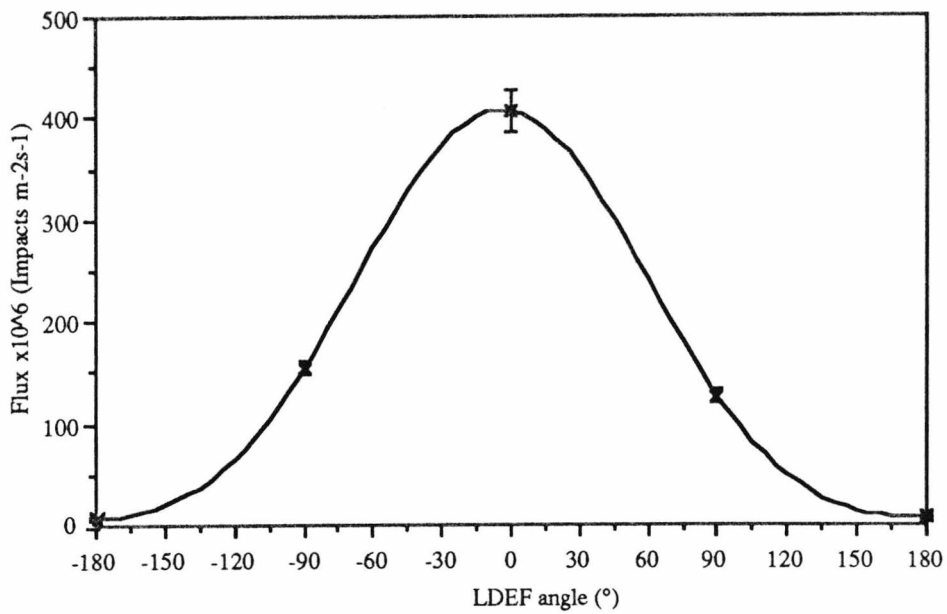


Figure 4.13 The best line fit through $5\mu\text{m}$ f_{max} data for the LDEF periphery using MAP data.

Using these fits it is possible to predict the fluxes impacting the ram, wake and peripheral directions. The face fluxes are then corrected to give the East, West, North and South faces with no offset present. The Space face is unaffected by the 8° offset as it is perpendicular to the ram/wake axis.

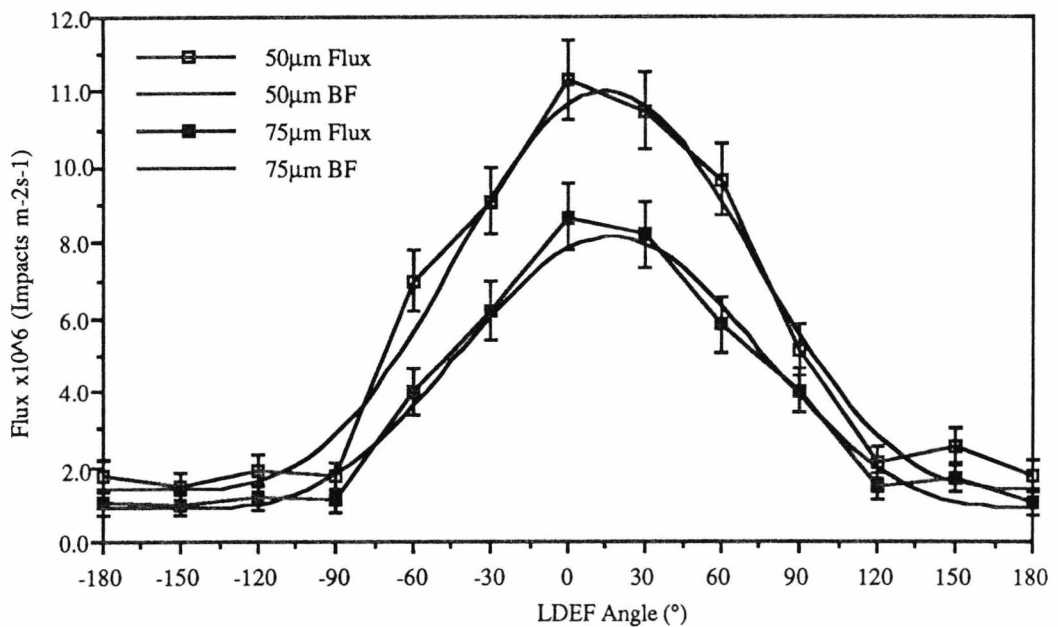


Figure 4.14 Best fit through $50\mu\text{m}$ and $75\mu\text{m}$ f_{max} for the LDEF periphery using intercostal data.

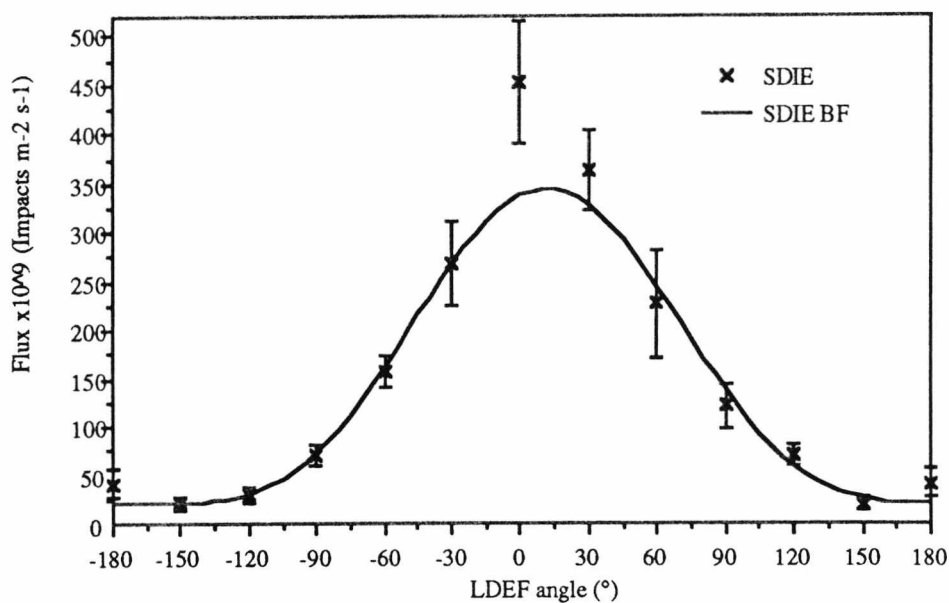


Figure 4.15 Best fit through 500 μ m f_{max} for the LDEF periphery using SDIE data.

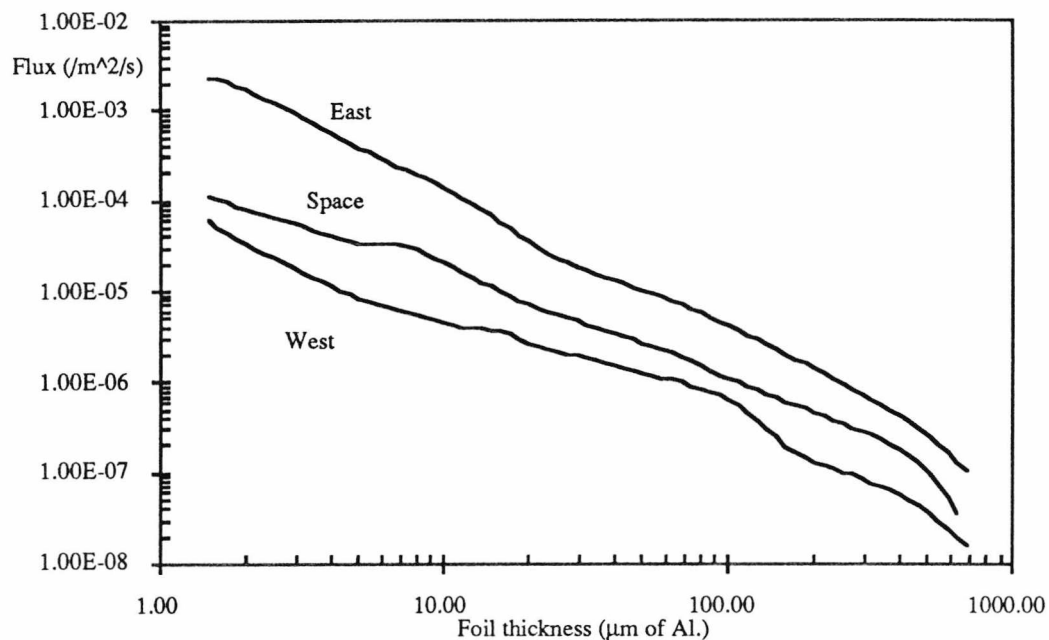


Figure 4.16 Offset corrected fluxes for the East and West face compared to the Space face that requires no correction.

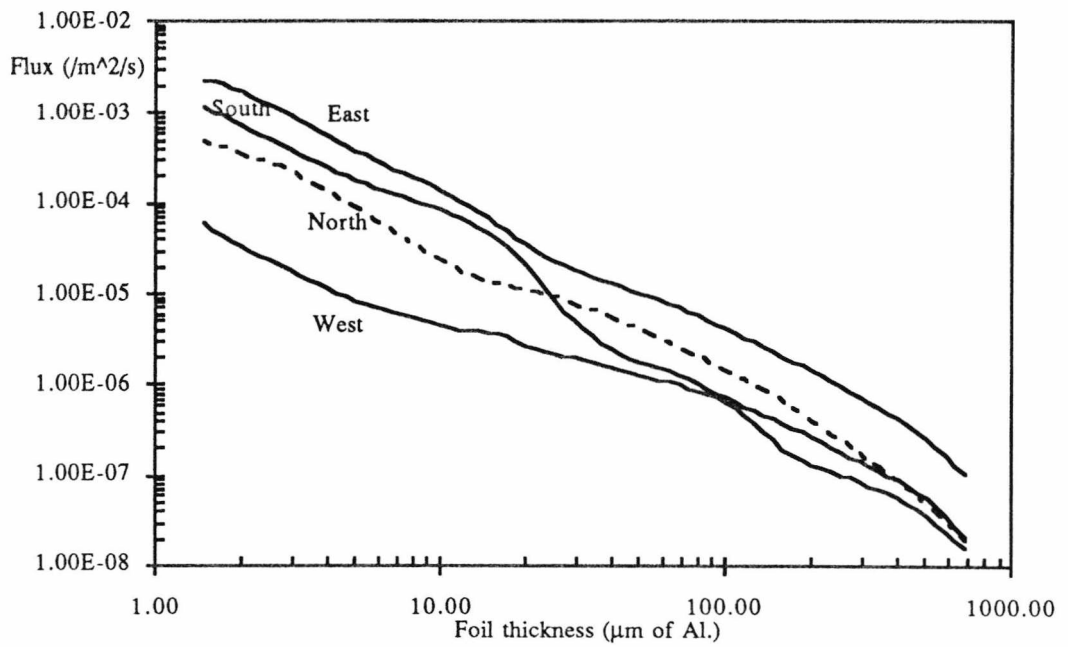


Figure 4.17 Offset corrected fluxes for the East, North South and West faces of LDEF.

The corrected fluxes are illustrated in Figures 4.16 to 4.17 in terms of foil thickness of aluminium. It is these fluxes that can be used to determine the impact damage on a spacecraft in LEO, for the ram, wake and peripheral directions if gravity gradient stabilised, or an average flux of these, if the spacecraft is not stabilised.

References

- {4.1} McDonnell, J.A.M., Deshpande, S.P., Green, S.F., Newman, P.J., Paley, M.T., Ratcliff, P.R., Stevenson, T.J. and Sullivan, K. (1991). "First Results of Particulate Impacts and Foil Perforations on LDEF", *Adv. Space Res.* 11, (12), p 109.
- {4.2} Deshpande, S.P. & Paley, M.T. (1992). "Supra-Marginal Impacts Detected on the Microabrasion Package (MAP) Experiment Situated on LDEF's Space Face." *Hypervelocity Impacts in Space*, (ed. J.A.M. McDonnell), Unit for Space Sciences, University of Kent at Canterbury, pp 166-172.
- {4.3} Paley, M.T. (1992). "An Automated System for Obtaining Impact Penetration, Location, Size and Circularity on a Foil with Special Reference to the LDEF." *Hypervelocity Impacts in Space*, (ed. J.A.M. McDonnell), Unit for Space Sciences, University of Kent at Canterbury, pp 48-53.
- {4.4} Paley, M.T. (*Ph.D. thesis to be submitted 1993*). "The Development of an Automated Optical Scanning System and Studies of the Earth Orbital Dust Environment". University of Kent at Canterbury, U.K..
- {4.5} McDonnell, J.A.M., Deshpande, S.P., Niblett, D.H., Neish, M.J. and Newman, P.J. (1992). "The Near Earth Space Impact Environment - An LDEF Overview", accepted for publication in Proc. IAF/COSPAR World Space Congress Washington 1992.
- {4.6} Humes, D.H. (1991). "Large Craters on the Meteoroid and Space Debris Impact Experiment", in: *LDEF-69 Months in Space, First Post-Retrieval Symposium*, NASA CP 3134, pp. 399-418.
- {4.7} Mandeville, J.C. & Borg, J. (1991). "Study of Cosmic Dust Particles On Board LDEF The FRECOPA Experiments A0138-1 and A0138-2.", in: *LDEF-69 Months in Space, First Post-Retrieval Symposium*, NASA CP 3134, pp. 419-434.
- {4.8} Meteoroid and Debris Special Investigation Group, LDEF Database, NASA JSC, Houston.

- {4.9} Newman, P.J. (*Ph.D. thesis to be submitted 1993*). University of Kent at Canterbury, U.K..
- {4.10} Mullen, S. & McDonnell, J.A.M. (1993). "LDEF LEO Particulate Environment Characterisation", Final Report to ESA of ESa Contract No. 110745
- {4.11} Sullivan, K. (1992). "Characterisation and Dynamic Modelling of the Near-Earth Space Particulate Environment.", *Ph.D. Thesis*, University of Kent at Canterbury, U.K..
- {4.12} Neish, M.J., McDonnell, J.A.M. and Niblett, D.H. (1992). "Angular Distribution of the Flux of Microparticles Incident on the Surface of the Long Duration Exposure Facility: Possibilities for Deconvolution." *Hypervelocity Impacts in Space*, (ed. J.A.M. McDonnell), Unit for Space Sciences, University of Kent at Canterbury, pp 217-222.

Chapter 5

Space Debris

5.1 Introduction

Once man first launched a spacecraft into space, he had began an all too familiar path of systematically exploiting his environment, for his own gain, without thinking too much of the consequences. Sadly space debris is another one of those man-made ecological hazards. Not entirely to blame for all the numbers of space debris objects currently in orbit around the Earth, man could however have prevented many of them.

The study of space debris can be broadly catalogued into two areas:

- (i) spacecraft launched and associated debris
- (ii) environmental effects on spacecraft.

The first issue, that of spacecraft and associated debris is the major contributor to the space debris problem and will be discussed in section 5.3. The second issue, effects of the environment on spacecraft, mainly involves the degradation of surfaces. Space is one of the most hostile environments known to man. Man cannot survive without a life

support system and extensive protection in space. The main hazards encountered in Earth orbit include the vacuum of space and extremes of temperatures, high radiation energies (cosmic rays of galactic origin $\sim 100\text{MeV}$ and the Sun $\sim 1\text{MeV}$), atomic oxygen fluence and the bombardment by micrometeoroid particles (ranging from 10^{-16}g to gramme sizes and up to a maximum $V_{\infty} = 72\text{kms}^{-1}$)

Any spacecraft in Earth orbit, manned or otherwise, will be subjected to the cumulative effects of all these hazards coupled with the continuous thermal cycling as the spacecraft passes from day to night. The main cause of space debris from these hazards is the break down of materials through thermal cycling and the ejecta and damage caused by micrometeoroid impacts. Impacts can produce smaller ejecta debris and expose surfaces to further damage from thermal cycling and atomic oxygen erosion if in low Earth orbit ($\sim 350\text{km}$ to 500km). This “new” space debris can then impact other spacecraft and the situation escalates. Spacecraft can therefore be impacted by both space debris particles and the natural interplanetary particles constantly being attracted to the Earth by gravitational attraction. The size range of this small space debris is of the order $10\mu\text{m}$ to 1cm .

To date there has been one recorded case of a catastrophic impact with a piece of space debris{5.1}, which destroyed Cosmos 1275 (1981-053A) on 24th July 1981.

5.2 Database and Information System Characterising Objects in Space (DISCOS)

5.2.1 Introduction

In 1988 the European Space Agency (ESA) Space Debris Working Group concluded in the ESA SP-1109 that “For future manned missions (*e.g.* the Columbus programmes and Hermes) it is essential to establish a European database of all space debris.....” {5.2}.

In response to these findings a concerted effort was started by ESA to obtain various “tools” to support the findings and to continue to monitor the space debris environment through the Space Debris Advisory Group. One such “tool” to be developed was the Database and Information System Characterising Objects in Space (DISCOS). The Unit for Space Sciences and the Computer Laboratory at the University of Kent, were awarded the contract to design and implement DISCOS at the European Space Operations Centre (ESOC) Darmstadt, Germany under an ESA contract (8173/89/D/MD).

DISCOS functions were outlined by ESA to include:

- collision dynamics and probability
- time evolution models
- re-entry predictions
- in orbit collision and re-entry assessments.

5.2.2 Data Sources

Due to the lack of operational availability of European tracking data on non-cooperative targets, most of the “real time” orbit information originates from the USSPACECOM(United States Space Command) surveillance network. (Formally all objects in space were tracked by NORAD (North American Air Defense), under national security regulations). The data is gathered from a series of radar and optical detection systems in a global network and the output is in form of Two Line Elements (TLE) or ELSETS giving information object identifier, orbital parameters, ballistic coefficient, mean motion derivatives and drag terms. A detailed study of the USSPACECOM tracked object data is given in section 5.3.

The USSPACECOM ELSETS are updated every week and constitute the primary dataset for the temporal tracked objects.

Alongside the ELSETS there are three other object data sources:

- (i) the RAE Table of Earth Satellites

- (ii) NASA Satellite Situation Report
- (iii) Teledyne Brown Engineering History of On-Orbit Fragmentations

and two solar and geomagnetic activity data files:

- (iv) NASA Long Term Solar and Geomagnetic Activity Prediction.
- (v) ESOC SOLMAG data.

The RAE Table of Earth Satellites is published by Macmillan Press for the Defense Research Agency Farnborough formally the Royal Aircraft Establishment (RAE) {5.3}. The table includes :

- (i) Table of Earth Satellites

Listing all the launches and spacecraft launched since 1957, orbital parameters and epochs at launch and at certain epochs thereafter, decay epoch or expected lifetime. Shape, size and mass details are also given.

This is the only source to do so.

- (ii) Space Object Box Scores (by country and by site)

These give details of the number of launches per country and per site through the reporting period (1957-1986).

(At present only the third edition of the table is on-line at ESOC covering 1957-1986. However, an updated version is available and is in the process of being installed.)

The NASA Satellite Situation Report (SSR) is distributed every three months by NASA Goddard Space Flight Centre (GSFC) {5.4}. The report includes:

- (i) Objects in Orbit

Orbital data taken from USSPACECOM ELSETS but reduced to perigee, apogee and inclination for objects currently in orbit at the time of reporting.

- (ii) Objects Decayed

Decay data and identifier for objects decayed in the reporting period.

- (iii) Objects Launched, Catalogued and Decayed
Includes objects launched and/or catalogued and decayed within the reporting period.
- (iv) Space Objects Box Score
Objects in orbit and decayed listed by country and organisation.

A History of On-Orbit Satellite Fragmentations is produced by Teledyne Brown Engineering for Lockheed under a NASA contract {5.5}. Typically updated once a year. Report includes:

- (i) Satellite Break-up Status
Similar to SSR with limited parent satellite data and debris data for the date of the break-up.
- (ii) Satellite Fragmentations (Detailed Data)
Addition information to (i) includes date, time, location and altitude of the event and the number of fragments generated and still in orbit.
- (iii) Anomalous Events
Limited data on anomalous events including parent satellite and remarks on the event.

Alongside the object data sources DISCOS uses two solar and geomagnetic data files to accompany the analysis of decay probabilities {5.6}. The reason for the need for solar activity data will be discussed in section 5.3.

The ESOC SOLMAG Data Files include:

- (i) SOLMAG Measurement File
This contains solar and geomagnetic activity measurements in monthly steps from 1957.
- (ii) SOLMAG Activity Forecast File

Provides predictions for mean solar and geomagnetic activities, based on previous solar cycle histories, with spacings of one month for one or more solar cycles.

The NASA Long Term Solar and Geomagnetic Activity Prediction files are issued every three months by NASA's Marshall Space Flight Centre (MSFC) and contain solar and geomagnetic activity predictions in steps of one month for more than one solar cycle ahead. Examples of the object source data are given in Appendix II.

5.2.3 Database Organisation

The DISCOS data tables are stored in *ORACLE* and interrogated via *SQLPLUS* (Standard Query Language PLUS) on a VAX 3800 running VMS, at ESOC {5.6}.

To ensure integrity of the data sources only the database manager has write permission to the tables. Any user can access data from any number of tables and produce their own personal table of data separate from the DISCOS primary data tables.

Object data tables in DISCOS are not direct comparisons to the source data tables. An optimum system was devised to produce hybrid tables containing information from the four object sources to combine data more efficiently and reduce redundancy. Thus data from a given data source will appear in a number of DISCOS tables. To keep track of specific object data the *COSPAR* International Designator is used as the flag. This flag is unique to every launched object including the rocket, satellite, and fragments if any were released. Thus to interrogate one or more DISCOS tables, using *SQLPLUS*, one would query the database using the International Designator for that object if a specific object data is required or indeed any field header in that table. (e.g. Select * from RAE_ORBIT where inclination=28; This would select all the information in table RAE_ORBIT where the inclination field reads 28.)

Once the user has selected the information he requires and produced a private data table then analysis on this data set can be undertaken {5.7}. Figure 5.1 illustrates the DISCOS user facilities.

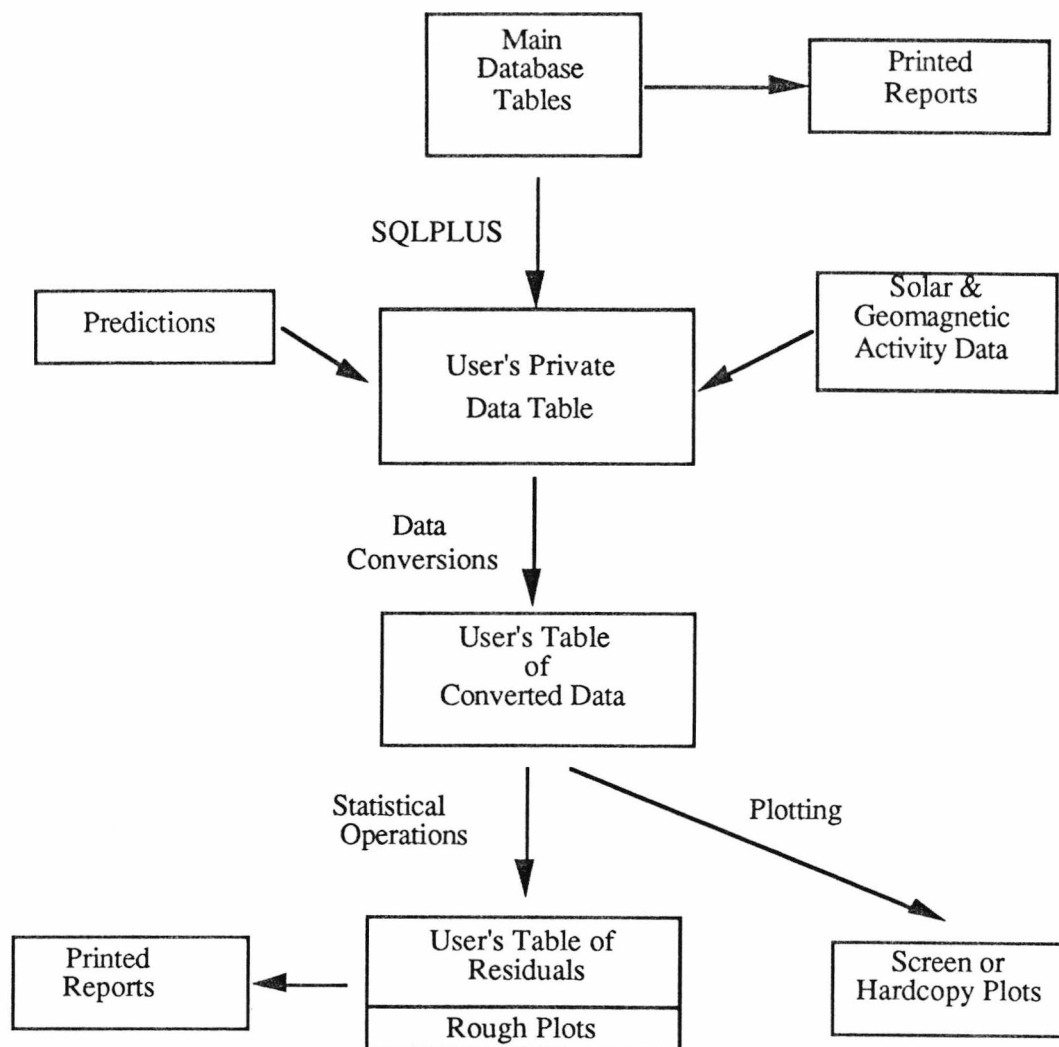


Figure 5.1 Overview of DISCOS user facilities.

5.2.4 On Line Data Analysis

To allow a comprehensive analysis, in orbit or otherwise, prediction, DISCOS allows one to perform table-to-table transformations driven by on-screen menus, from and to any of the following epoch and orbit states {5.6}:

- (i) Epoch Transformation
Modified Julian Day 1950.0 in days

Modified Julian Day 2000.0 in days

calendar date as (YY)YY/MM/DD hh/mm/ss.ss

ELSETS data format as (YY)YY DDD.DDDDDDDDD

ORACLE date formats as YY/MTH/DD hh/mm/ss.ss

- (ii) Reference Co-ordinate Frame Transformation
 - mean system of 1950.0
 - mean system of 2000.0
 - mean system of date (compensated for precession)
 - true system of date (compensated for precession and nutation)
 - ELSETS system (mean equator and true equinox of date)

- (iii) Orbit State Prediction Theory
 - osculating orbit state
 - doubly averaged Kozai elements (SGP theory)
 - doubly averaged modified Brouwer elements (SGP4/SDP4 theory)
 - doubly averaged modified Brouwer elements (SGP8/SDP48 theory)
 - singly averaged Kozai elements (Liu & Alford theory)
 - doubly averaged Kozai elements (SGP theory)
 - doubly averaged modified Brouwer elements (Aeronautic theory)

- (iv) Orbit State Format (in inertial reference frame)
 - cartesian state vector (km and kms^{-1})
 - Kepler state vector (km and deg or rad)
 - ELSETS state vector (km and deg or rad)
 - equinoctial state vector for $e=0$ (km and deg or rad)
 - equinoctial state vector for $e=0$ and $i=0$

- (v) Fast Angular Variable

mean anomaly
eccentric anomaly
true anomaly

All of these epoch and orbit state transformations are linked to the DISCOS data tables via a pre-compiler interface "*Pro*FORTRAN*". This same pre-compiler is used to link a number of statistical analysis and graphical display software. Thus the user via on-screen menus, can select data (columns) from his private tables, or DISCOS main database tables, and apply any of the following analysis tools:

- (i) Graphical Visualisation
 - histograms (2-D and 3-D)
 - scatter plots (2-D and 3-D)
 - surface plots (3-D)
 - polar plots of $r(\phi)$ functions
 - $y(x)$ function plots

- (ii) Regression Analysis
 - linear (single valued or multiple regression)
 - logarithmic (single valued)
 - exponential (single valued)

- (iii) Curve Fitting
 - simple polynomial (via Chebyshev)
 - Chebyshev polynomial
 - cubic spline
 - harmonics (Fourier series)

- (iv) Surface Fitting
 - polynomial (Bi-cubic spline)

The results of the regression, curve fitting and surface fitting analysis are stored in tables and can be directly inspected in graphical form. The graphical outputs can be routed to a screen, or to a range of output devices and is run under *GKS*.

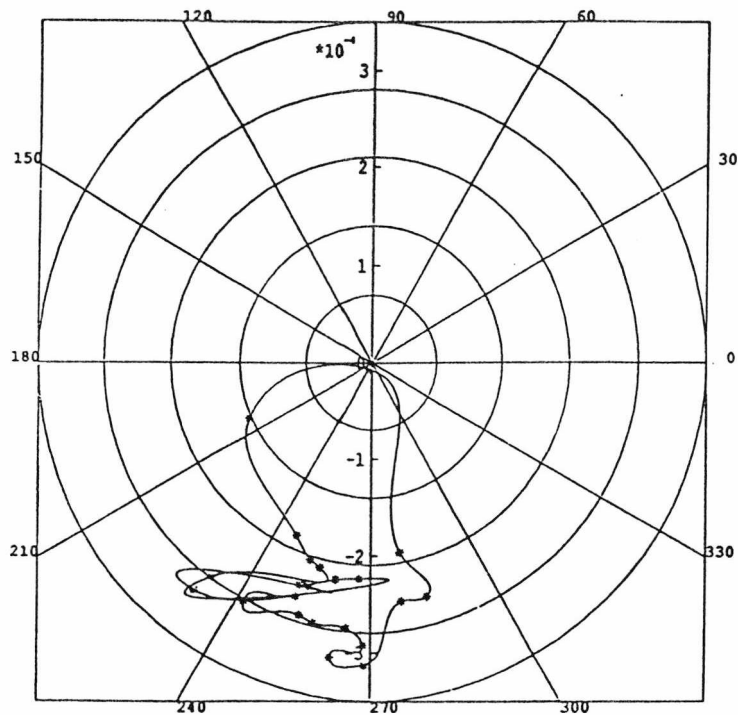


Figure 5.2 Example of DISCOS output. Seasat-1 (1978-064-A) time history of orbital elements (Nov 89- Apr 90). The radii represent values of the eccentricity, the angles represent values of argument of perigee.

Figure 5.2 shows an example of DISCOS output. Section 5.3 and 5.4 illustrate two types of analysis that the author has undertaken with DISCOS data to interrogate the known space debris environment. Using this data, studies into a new size dependant density distribution for space debris was undertaken and the results are reported in Chapter 6.

5.3 Unclassified Tracked Space Debris

5.3.1 Detection And Tracking Systems

As previously stated in section 5.2.2, USSPACECOM track objects in the near Earth space region under national security regulations. As a consequence only tracked data of so called unclassified objects is released to the scientific community for analysis. Hence any tracked data available, through DISCOS for example, has been cleared by the United States Defense Department for scientific use and contains data on unclassified objects only. Classified objects cover all military satellites, and counter espionage satellites and any subsequent part there of, *i.e.* fragments from such satellites whether directly or indirectly produced. The data set of tracked objects is therefore only a subset of what is actually tracked, and due to the sensitivity of the classified data it is impossible to calculate, from our viewpoint, what fraction of the total tracked objects we are privileged to use.

Global coverage is obtained via a series 19 Ballistic Missile Early Warning System (BMEWS) radar detection systems (10 radar, 9 phased radar, 1 radar interferometer) and 6 electro-optical sensors around the Earth. BMEWS is primarily devoted to missile attack warning, however several United States Air Force (USAF) radars are routinely used for space object tracking (Johnson, 1992) {5.8}. Figures 5.3 and 5.4 show the detection cone distribution, at 500km altitude, for radar and electro-optical tracking stations around the Earth {5.9}.

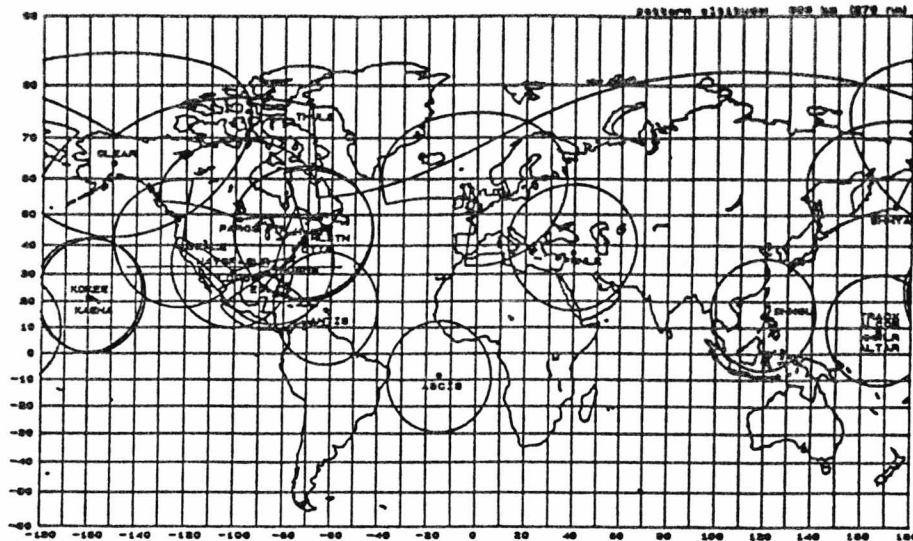


Figure 5.3 Radar detection coverage afforded by USSPACECOM at 500km altitude.

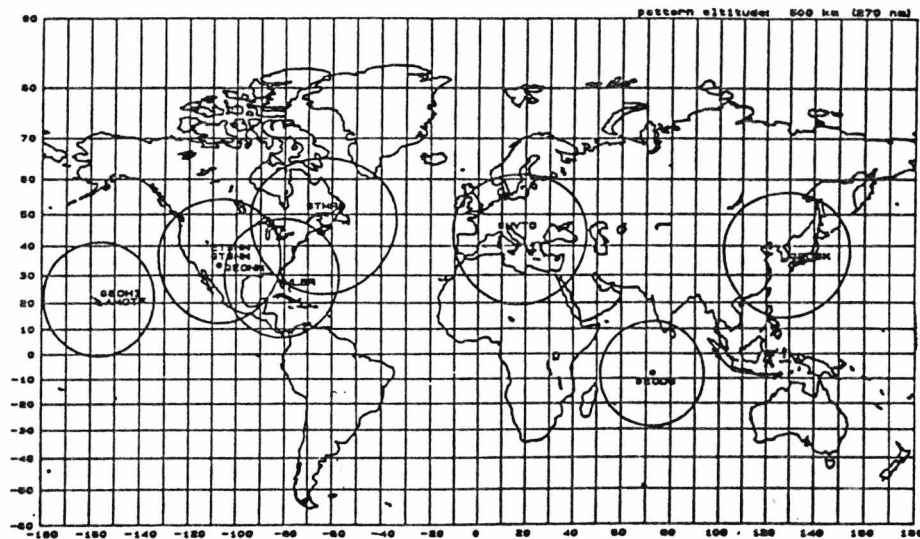


Figure 5.3 Electro-optical detection coverage afforded by USSPACECOM at 500km altitude.

The coverage obtained at 500km is very good and assuming the beam pattern is conical, the Equator region should be covered by at least two radar and one electro-optical station down to an altitude of 210km. There is however, a difficulty in detecting objects that are orbiting in elliptical orbits with low inclinations. This is because elliptical orbits spend a smaller fraction of their time at low altitudes where USSPACECOM detection is possible, and there are also fewer ground based sensors to detect low inclination orbits (Kessler 1992) {5.10}. For a typical eccentric orbit with perigee altitude of 350km and

apogee altitude of 35,787km, only 2.2% of orbital period is below 1,000km and 1.5% below 500km (McKnight 1990) {5.11}.

For an object to be entered in the USSPACECOM ELSETS it has to be reliably tracked by two or more ground stations and recovered by a ground station on it's next orbit. This then, coupled with the operational effectiveness of the detection system, puts constraints on detection of objects dependant on their size and orbital altitude.

Figure 5.5 shows USSPACECOM's operational system capability to detect space debris. Extremal operational limits are 8cm diameter at 100km (at LEO) and 100cm at 100,000km (mainly geosynchronous Earth orbit (GEO) satellites), although the actual limit of resolution of these systems will not be released as they are mainly under the national security umbrella. The sharp interchange in the optical and radar detection limits around 4,000km, is mainly due to the high relative speeds of objects in this altitude (*i.e.* 6.2kms⁻¹ at 4,000km up to 7.8kms⁻¹ at 100km) and thus the difficulties in detection using electro-optical systems.

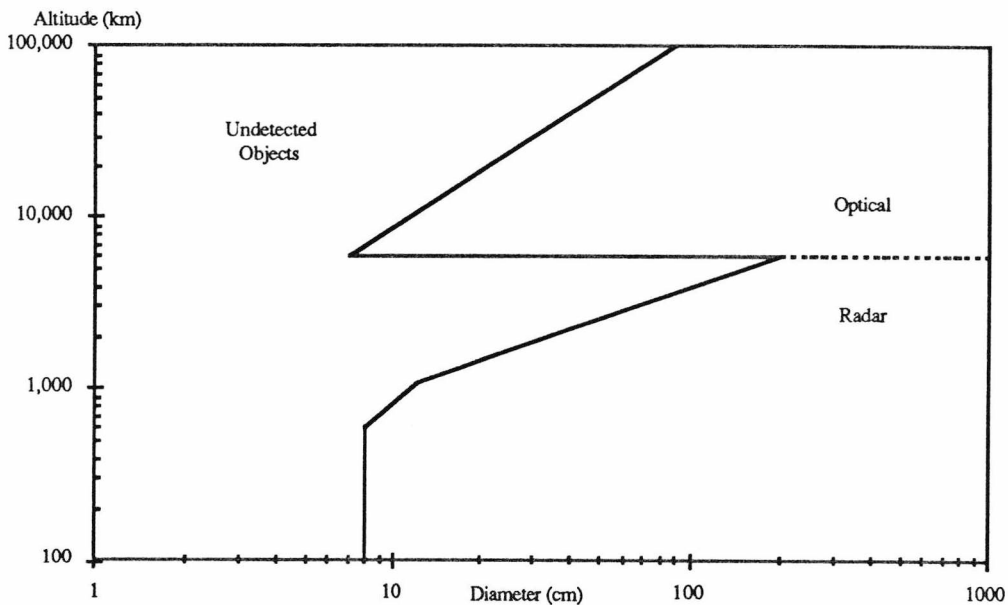


Figure 5.5 Detection limits and operational capabilities of USSPACECOM tracking facilities.

Ground based radars have an effective search range limited to a few thousand kilometres, although some radars can track a satellite out to geosynchronous altitude, some 35,787km or so. Radar network performances were dramatically improved with

the introduction of phased array radars, that are able to track many objects simultaneously (200-300), with transmitter peak power in the 10-20MW range. This is very useful in tracking space debris since mechanical-steering radars can track only one object at a time in normal conditions. Such radar systems as the AN/FPS-85 phased-array radar operated at Eglin, Florida, and the Perimetre Acquisition Radar and Characterisation System (PARCS), also a phased array radar, operated at Cavalier, North Dakota together collect one third of all the observations received daily at the Space Surveillance Centre (SSC) at the Cheyenne Mountain Complex, near Colorado Springs, where all tracked data is gathered and analysed {5.9}.

The Ground based Electro-Optical Deep Space Surveillance system (GEODSS) together with Baker-Nunn cameras constitute the electro-optical detection system. The GEODSS main telescopes have a field of view of some 2.1° and carry a 36cm radiometre to measure light variations of the targeted space object. The Baker-Nunn cameras primarily designed for detection of spacecraft in deep space have been decommissioned as of April 1992 (Johnson 1992) {5.8} and are being superseded by the quicker and more accurate computer driven, GEODSS system. In addition to GEODSS, now being used to track space debris in near Earth orbits, USAF also maintains and operates a number of cameras for close-up photography of satellites for intelligence purposes. (e.g. two such cameras : code named *Teal Amber*, and *Teal Blue*, at Malabar, Florida, and Mount Haleakala, Hawaii, respectively).

Another very sensitive sensor able to track space debris is the Naval Space Surveillance System (NAVSPASPUR) consisting of one main and two auxiliary, very powerful transmitters {5.9}. These erect an electronic fence across the United States (latitude 33° N), such that any space object passing through the fence interferes with the radio beam, and is picked up by one or more of the six receiving stations, on continental USA, continuously monitoring the fence.

5.3.2 The Known Orbital Debris

The operational detection limits placed upon the tracked objects, leaves a large gap in data below the 8cm size limit presently trackable and to some extent in the debris density in elliptical low inclination orbits. The most damaging particle size range for satellites and spacecraft, manned or otherwise, lies in the 1mm to 10 cm range, for catastrophic collisions, and in the micron to millimetre dimensions for surface degradation. Figure 5.6 shows the sources and size range of space debris that is to be expected. It is clear when examining figure 5.6, and comparing the size ranges to the operational detection limit presently afforded, that most categories of space debris are undetectable from the ground

For figure 5.6, high intensity explosions are characterised as explosions occurring where the charge is in direct contact with the spacecraft structure (*e.g.* propellant ignition). Conversely low intensity explosions implies the charge not in contact with the spacecraft structure (*e.g.* pressurised canister exploding).

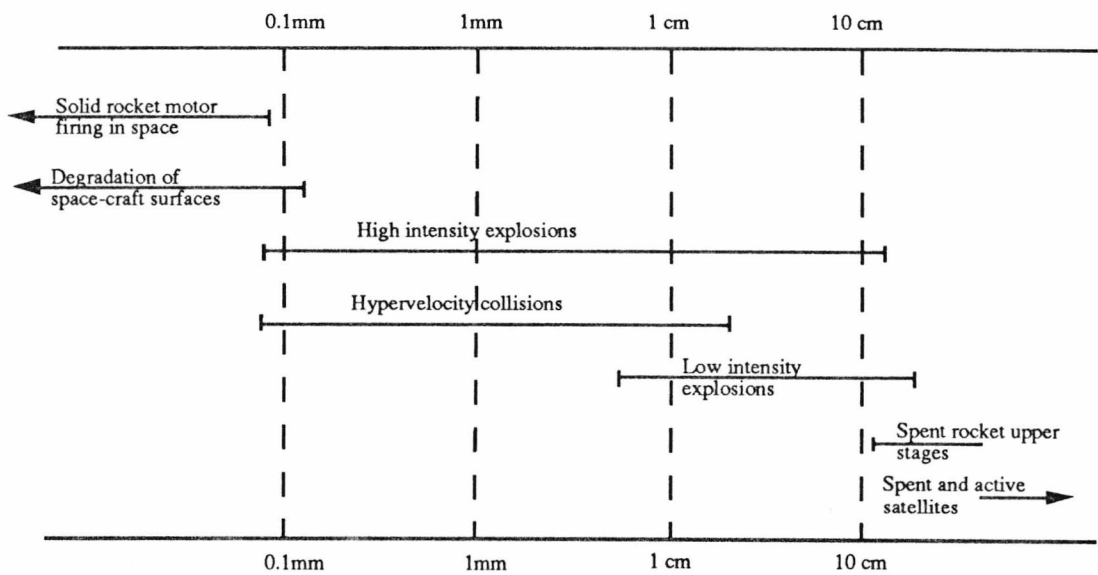


Figure 5.6 Classification of space debris with associated sizes

Using DISCOS data the author has produced a time evolution of tracked objects for debris, payloads and launches per year over the period 1957 to 1st January 1993. In total there have been 3495 launches since 1957 leading to 7055 objects being tracked (as

of 1st January 1993) by USSPACECOM, with an estimated total mass of about 3×10^6 kg.

The results are illustrated in figure 5.7.

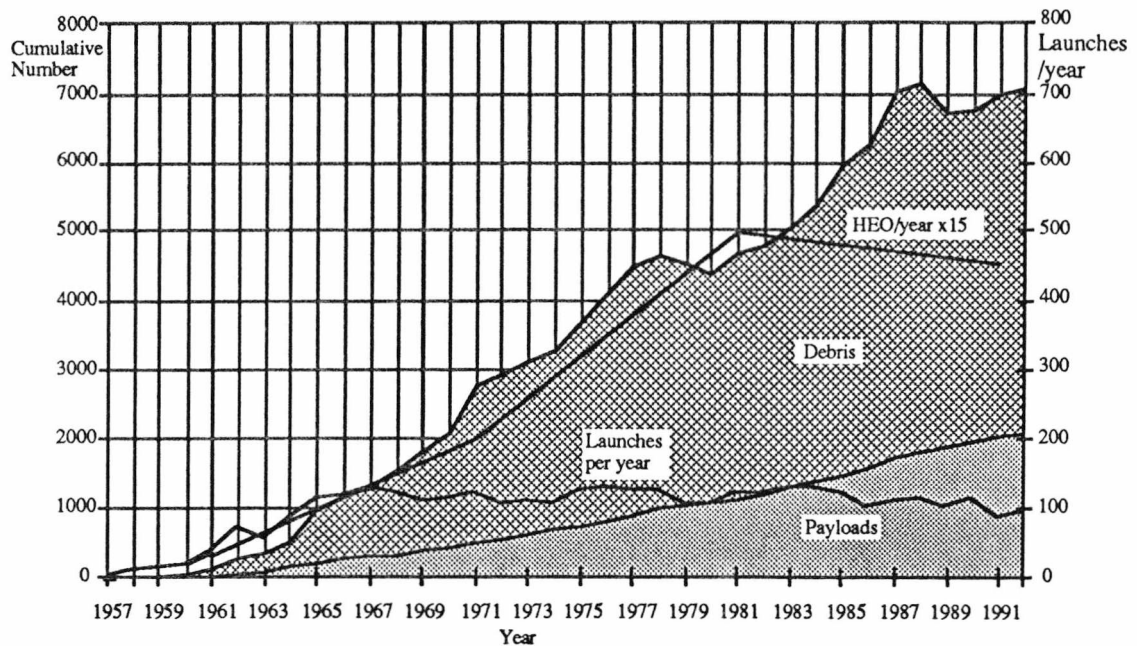


Figure 5.7 Time evolution of debris and payloads in orbit since spaceflight began until 1st January 1993. The left hand axis represents the cumulative number of debris and payloads in orbit and the right hand axis the number of launches per year and also the number of HEO launches x15 per year.

It can be seen that the debris population is continually increasing alongside the number of payloads in orbit. This is to be expected as the number of payloads (*i.e.* satellites) will increase as socio-economic forces dictate better communication and scientific services. As the number of payloads increase so does the number of associated operational debris (explosive release bolts, connectors). The interesting fact to note is that although the payloads, in orbit, increases yearly, the number of launches per year has remained constant, around the 105 mark since 1966. As launcher technology advances and the socio-economic accountability of space faring nations becomes more prominent, the idea of “piggy-back” and multiple satellite deployments per launch, increases. This is turning out to be most advantageous to the poorer countries of the World, who benefit from cheaper launch costs and so can use satellite technology to enhance their World standing.

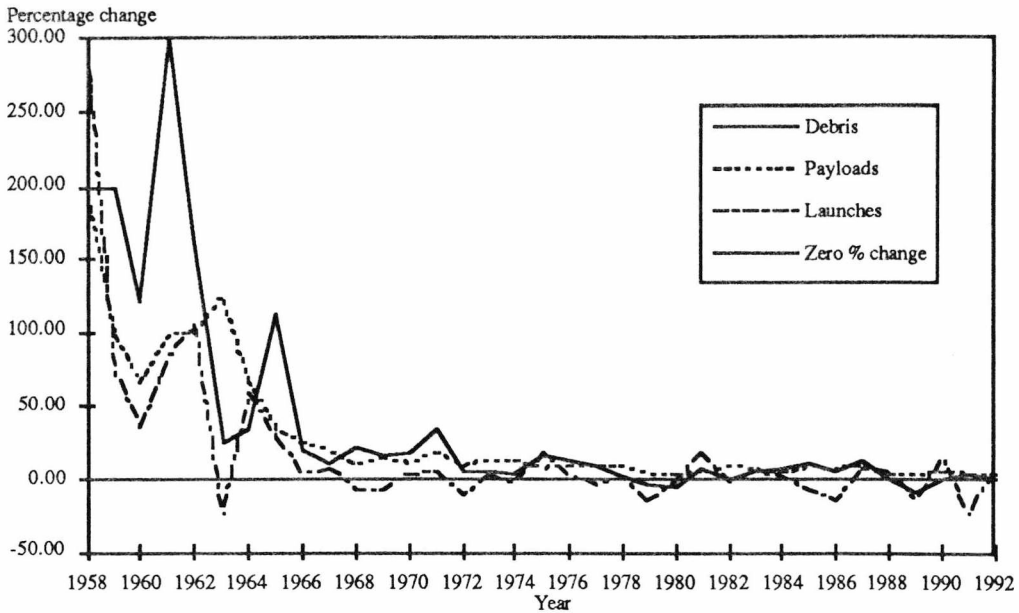


Figure 5.8a Percentage growth rates in payloads, launches and debris since spaceflight began until 1st January 1993.

It is clear from figure 5.7 that there are definite sources and sinks to the tracked objects. Figures 5.8a and 5.8b show the percentage growth rates for debris, payloads and launches per year, from 1958 to 1992 and from 1970 to 1992 respectively. It is clear that the maximum change occurred in the early days of space exploration, which is entirely as to be expected but there has been a distinct “levelling off” in the numbers of tracked objects.

Since 1980 the percentage growth rate in debris has been of the order of 2.8% annually, somewhat lower than the corresponding growth rate in payloads in orbit at 5.6%, and markedly different to the -0.15% growth rate in launches per year. Figure 5.8b also shows that from 1985 to 1992 the percentage growth rates for debris, payloads and launches are 2.9%, 5.5% and -2.9% respectively. These percentage changes are discussed alongside predicted changes given by Kessler, for his Debris model in Chapter 6.

It is clear, from figure 5.7, that there were definite reductions in the numbers of debris objects in orbit during 1979 and 1990. The debris population actually fell by 3.8% and 5.4% in 1979 and 1980 and again in 1989 and 1990 by 9% and 1% respectively.

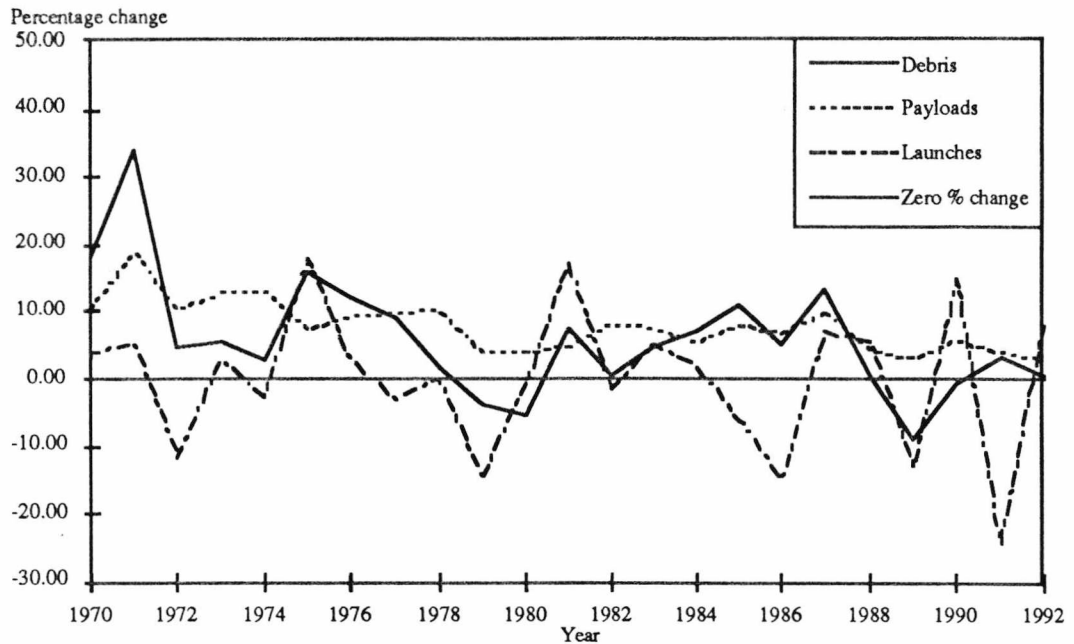


Figure 5.8b Percentage growth rates in payloads, launches and debris from 1970 until 1st January 1993.

This corresponds to maxima in the 11 year Solar activity cycle of which the most recent occurred in July 1989. This was the highest level recorded Solar activity peaking at 245×10^4 Jy in the 10.7cm flux measure {5.1}. A further discussion on the effects of solar activity and the mechanism for a “cleaning-up” process by increasing the atmospheric drag on an object, is given in section 5.5.2

Alongside the effects of atmospheric drag due to Solar activity, the two other sinks are retrieval and de-orbiting. Retrieval, to date can only be accomplished via NASA's STS and consequently only one spacecraft has been retrieved and that is LDEF. This is a very expensive and limited sink, totally dependant upon the STS payload bay dimensions. De-orbiting is used to destroy the spacecraft via atmospheric drag as it re-enters the Earth's atmosphere. Re-orbiting however is much more common and is playing a bigger role in the prevention of debris. Briefly, re-orbiting is the process by which GEO satellites that have come to the end of their working life are boosted to so called “graveyard orbits”, high above the main satellite orbits presently used. Further discussion on debris prevention and removal techniques is given in section 5.5.3.

Sources	Sinks
Launches	Atmospheric drag
Payloads	Retrieval
Breakups (i) ASAT	De-orbiting/ Re-orbiting
(ii) Explosion	
(iii) Collision	
(iv) Surface erosion	

Table 5.1 Tracked objects sources and sinks.

Apart from the obvious increase in space activity leading to more objects in space there are break-ups contributing to the tracked population. These are shown in Table 5.1. The ASAT break-ups are mainly due to Soviet (presently CIS) anti-satellite testing, the deliberate destruction of satellites, for offensive and defensive capability studies.

Using DISCOS it is possible to extract information on the events causing, and ownership of, space debris, and this has been performed and the results are presented below. As of the 1st Jan. 1993 there have been 112 recorded break-ups at an average of 4 break-ups per year, with 4 recorded in 1992, of which 3 were classed as propulsion related and 1 unknown. This is somewhat different to the 6 break ups registered in 1991, with 4 classed unknown, with 1 deliberate and 1 propulsion related. Figure 5.9 illustrates the 112 break-ups by cause.

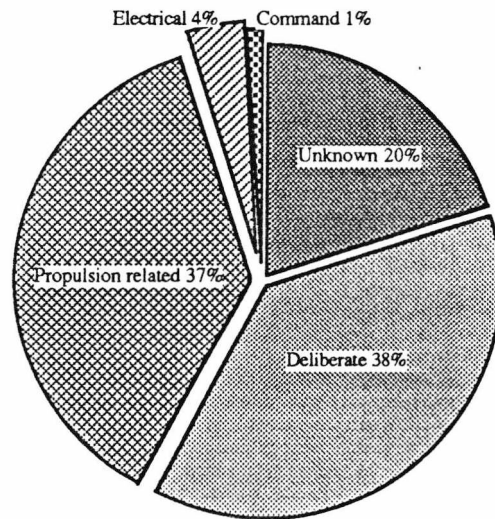


Figure 5.9 Classification of the 112 break-ups from 1961 until 1st January 1993.

It has come to light recently [5.12] that there is a design flaw with the CIS (USSR) Proton launch vehicle that has resulted in at least 6 break ups during 1983-1992, creating up to 60 new trackable objects in LEO after each event. This is of great concern and a joint US/CIS team lead by Kaman Sciences Cooperation (USA) (Darren McKnight and Nick Johnson), is actively pursuing a solution to this problem. Of these 112 break-ups the most severe 10, with regard to the current debris population, are shown in Table 5.2.

International Designator	Object Description	Fragment Count		Fragmentation Event		Day of Event
		Max	June 1991	Inclination (°)	Altitude (km)	
1970-025C	Nimbus -4 R/B	362	295	99.88	1075	17 Oct. 1970
1981-053A	Cosmos-1275 S/C	303	288	82.96	980	24 July 1981
1961-OM13	Transit-4A R/B	296	212	66.82	990	29 June 1961
1973-086B	NOAA-3 R/B	197	182	102.05	1515	28 Dec. 1973
1978-026C	Landsat-3 R/B	208	163	98.85	910	27 Jan. 1981
1976-077B	NOAA-5 R/B	157	156	102.02	1510	24 Dec. 1977
1975-052B	Nimbus-6 R/B	386	153	99.6	1100	1 May 1991
1974-089D	NOAA-4 R/B	145	135	101.69	1465	20 Aug. 1975
1969-82AB	OPS-7613 R/B	260	121	69.96	920	4 Oct. 1969
1986-01C	SPOT-1 R/B	488	110	98.70	805	13 Nov. 1986

Table 5.2 Ten most severe break ups and in recent times and number still in orbit on June 1991.

It is noted that the most severe break-up to date was that of 1986-01C, SPOT-1 rocket body launched by ESA on the Ariane launcher. The fragment count at event totalled 488, but it can be seen that this has been diminished quite drastically to 110 within 4 years. The break-up of 1981-053A, Cosmos 1275 spacecraft showed all the indications of a collision with space debris. These 10 break-ups account for 26% of the current tracked population, and so it can be seen that the major contributor to the tracked object population is indeed fragmentation debris. Only 6% of tracked objects are operational payloads, with 71% attributed to either mission related debris (29%) or fragmentation debris (42%) as illustrated in figure 5.10.

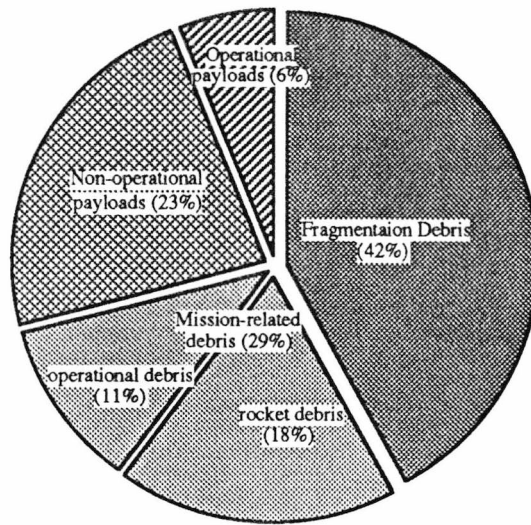


Figure 5.10 Classification of debris presently tracked by USSPACECOM.

Of the 7055 objects tracked 4954 are debris, that is distinct from the 2101 payloads. Figure 5.11 through to figure 5.13 show the debris, payloads, then total of tracked objects per country, as of 1st Jan. 1993.

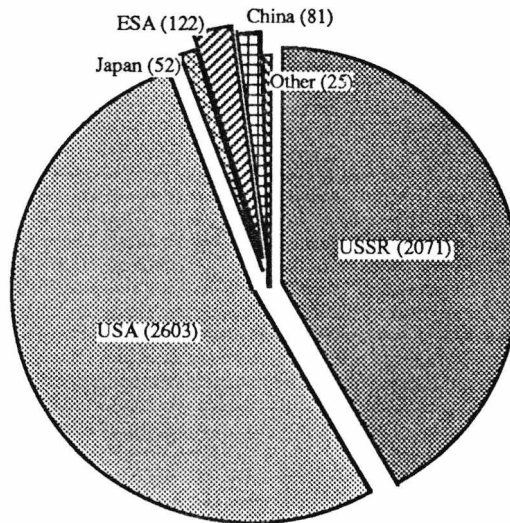


Figure 5.11 Ownership of the 4954 tracked debris objects in orbit as of 1st January 1993.



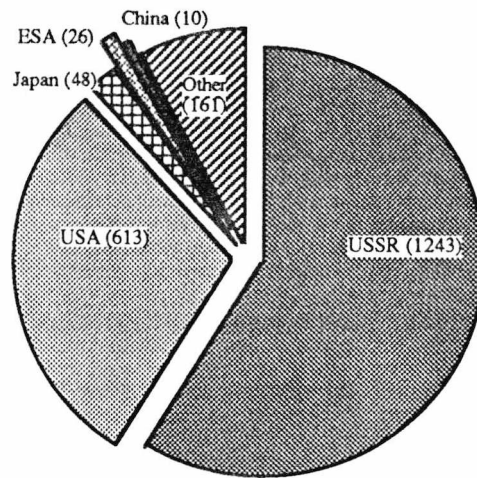


Figure 5.11 Ownership of the 2101 tracked payloads in orbit as of 1st January 1993.

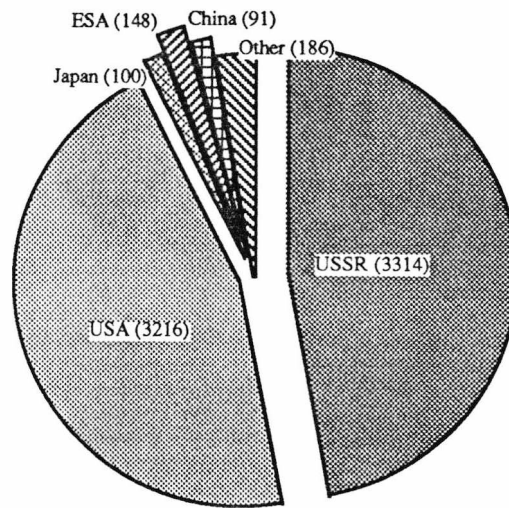


Figure 5.11 Total ownership of the 7055 tracked objects in orbit as of 1st January 1993.

It is obvious that although the USSR accounts for the majority of payloads and debris in total, and in fact the bulk of launches per year are undertaken by the USSR, the USA has more debris objects than the USSR. The ratio of tracked debris objects to tracked payload objects, per country/organisation is given in Table 5.3.

Country	% of total tracked objects owned	Number of debris per payload
USSR	46.9	1.66
USA	45.7	4.25
Other	2.6	0.16
ESA	2.1	4.69
Japan	1.4	1.08
China	1.3	8.10

Table 5.3 Country/organisation by % of owned tracked objects.

Table 5.3 clearly illustrates that in order of debris contributors China figures top, followed by ESA, USA, USSR, Japan and Other. The USSR appears fourth in Table 5.3, which is surprising when considering the number of launches undertaken and the number of payloads currently in orbit.

In summary then, it is clear that the major factor contributing to the tracked objects is fragmentation debris whether directly induced or otherwise. There are an estimated 2×10^7 particles of size $>0.1\text{cm}$ presently in orbit of which only 7055 objects greater than 8cm are tracked. The greatest danger to spacecraft comes from the numerous particles of size $<8\text{cm}$ presently undetectable. As demonstrated by the Cosmos 1275 spacecraft break-up, this debris is a major threat to space missions. The tracked objects can be used to estimate, with a few assumptions, the number of particles over the size range, to give an estimation of a spacecraft's susceptibility to impacts. An analysis of such a situation is given in Chapter 7 with the method used described in Chapter 6. The main benefit in tracking objects has come in the mission analysis and in-flight monitoring for current space missions. Launch windows for LEO missions are calculated with the knowledge of position of all of these objects. Indeed in recent times these benefits have paid dividends, as on September 15th 1991 STS-48, Discovery, carried out an in-orbit manoeuvre to avoid the Cosmos 955 rocket body (1977-91B) which would have impinged on the shuttle's $2\text{km} \times 2\text{km} \times 5\text{km}$ collision ellipsoid, which

defines the threshold for avoidance manoeuvre {5.1}. The Cosmos 955 rocket body had a reported mass of 1440kg and cross sectional area of 10-15m². Impact with STS-48 would have been at an estimated 10.6kms⁻¹ destroying both. About six weeks later STS-44, Atlantis, made a similar manoeuvre to avoid another Soviet rocket body, Cosmos 851 (1976-85B) {5.1}. The preponderance of Soviet objects in space is not unexpected as most of their objects are in long lived orbits, as is demonstrated by these two in-orbit manoeuvres to avoid rocket bodies launched some 15-16 years ago.

5.4 Orbital Characterisation

5.4.1 Types Of Orbits

Geocentric orbits are divided into a few loosely defined groups (Johnson &McKnight, 1987) {5.9} based mainly on launch site and the satellite primary objective.

- (i) LEO : Low Earth Orbit, with periods up to 127 minutes, corresponding to an altitude of 2,000km, for a circular orbit. This is sometimes subdivided into LEO1 and LEO2 with periods of less than 105 minutes, (altitude less than 1000km) and 105 minutes to 127 minutes respectively.
- (ii) GEO : Geosynchronous Earth Orbits, with periods of $1,436 \pm 16$ minutes (altitudes $35,785 \pm 300$ km). A special case of a GEO is the Geostationary orbit used for telecommunication. This is an Equatorial GEO with inclination 0° giving the appearance of a stationary satellite above the ground point.
- (iii) HEO : Highly Inclined Elliptical Earth Orbit, which includes such specific orbits as the Tundra orbits with orbital period of $1,430 \pm 20$ minutes (~24hrs) and Molniya orbits with 710 ± 10 minutes (~12hrs) orbital periods

- (iv) GTO : Geosynchronous Transfer Orbits, with perigee in LEO and apogee near 35,785km

The LEO region is mainly used for Earth Observation satellites, including counter espionage satellites, scientific satellites and manned missions such as the Mir space station, STS missions, and the proposed ISSF. The GEO region giving an orbital period of 24hrs gives rise to the greatly exploited Geostationary ring for telecommunication satellites. However, satellites in Geostationary orbit, and hence stationary above a ground point on the Equator, can cover large areas of transmission but provide low elevation angles at latitudes above 30° (*i.e.* most of the northern hemisphere). HEO on the other hand is used to give coverage over the northern hemisphere, although not stationary, a number of satellites can be used to give continuous coverage, unhindered by latitude and more specifically the close proximity of large buildings reducing the signal received. The USSR has exploited such orbits with the Molniya orbit and there is an increasing voice in Europe to exploit another HEO orbit called M-HEO, multi-regional HEO {5.13}. This would enable 24hr satellite coverage of Europe, North America and the Far East using just 6 satellites. Utilising 3 apogee loops over Europe, North America and the Far East, low apogee altitude, increasing in-orbit mass and power savings. Molniya or Tundra orbits could be used but more satellites would be required and more cost for launch to higher apogee. Tables. 5.4 and 5.5 demonstrate the M-HEO choice and orbital parameters.

	M-HEO	Molniya	Tundra
Orbital period (hrs)	8	12	24
Apogee altitude (km)	27,000	39,000	47,000
Perigee altitude (km)	1,000	1,000	24,000
No. satellites required	6	12	9

Table 5.4 HEO satellite orbit for 24hr coverage of Europe, North America and the Far East.

No. of Satellite	6
Perigee altitude	27,000 km
Apogee altitude	1,000 km
Orbital period	8 hrs
Inclination	63.435°
Argument of perigee	270°
Ascending node	60° apart
Mean anomaly	180°
Useful orbit time	4 hrs
Handover condition	2 satellites visible at altitude of 20,500km

Table 5.5 Orbital parameters for a M-HEO satellite constellation.

Finally the GTO region is used to launch satellites into GEO by deploying the satellite into LEO as opposed to launching straight into GEO due to mass and power constraints. These orbits are highly elliptical with eccentricity >0.65 and so cross the GEO region on apogee at which point an apogee burn motor (ABM) fires changing the satellite's orbit to that of a GEO.

Objects in geocentric orbit are perturbed by two main forces. These are :

- (i) The non-spherical symmetric geocentric gravity field
- (ii) Atmospheric drag (solar activity)

There are other perturbing forces such as solar radiation pressure and Lunar and Solar gravitational perturbations but these are minor {5.14}. The Earth's gravitational field is modelled as a spherically symmetric field with perturbations due to non-sphericity. These perturbations are due to the Earth's oblateness and specifically to the J_2 term of the gravitational field expansion ($J_2=0.001082$). This causes the plane of inclined orbits (inclination $>0^\circ$) to revolve in a retrograde direction (nodal regression) about the Earth's polar axis and the line of apsides (between perigee and apogee) to advance in the direction of orbital motion, except in the case of high inclinations ($i > 90^\circ$). The rate of nodal regression is given by

$$\Delta\Omega = -3 \pi J_2 \left(\frac{R_e}{a(1-e^2)} \right)^2 \cos i \quad (\text{radians rev}^{-1}) \quad (5.1)$$

where R_e is the mean radius of the Earth and e the eccentricity of orbit. The advance of the line of apsides is given by

$$\Delta\omega = -3 \pi J_2 \left(\frac{R_e}{a(1-e^2)} \right)^2 \left(2 - \frac{5}{2} \sin^2 i \right) \quad (\text{radians rev}^{-1}) \quad (5.2)$$

For orbits with $i > 90^\circ$ (retrograde motion) the cosine term in equation (5.1) becomes negative and the motion of nodal regression is in the same direction as the Earth's rotation and revolution about the Sun. Regression rates equal to the Earth's rotation are not possible but rates equal to the Earth's revolution about the Sun ($\sim 1^\circ$ per day) occur for $i \sim 98^\circ$, the exact value is dependant upon the satellite orbit geometry {5.15}. This near-pole orbit, orbit is known as Sun-Synchronous, offering constant solar illumination angle, and is used by Earth observation satellites, such as ERS-1 (European Research Satellite)

From equation (5.2) it is clear that no apsidal advance occurs if $2 - (5/2) \sin^2 i = 0$. This occurs at $i = 63.4^\circ$ and is in fact the inclination of the Molniya orbits. The USSR exploit this special "stable" HEO for their communication satellites to maintain apogee over high geographic latitudes. It can be seen that an object, which remains in orbit for a number of years, provided it is not in a polar orbit, will, due to these perturbations, have its lines of nodes rapidly averaged out. In addition the lines of apsides are also randomised, except for orbits with inclinations near 63.4° .

It is clear that satellites are placed into geocentric orbits based upon the satellites function but also on the launch site position. This is governed by economics coupled to mass and power budgets for a satellite launch. For example it is energetically more favourable to launch prograde with the Earth's rotation, than retrograde (against the Earth's rotation). Another consideration is moving a satellite once in orbit is very expensive requiring additional launch mass in the way of propellant and motors, and altering the inclination of an orbit is once again energetically costly. The result is that all launch sites, with the exception of Israel (for political reasons), launch prograde, and are

situated west of a clearing, (*i.e.* the sea or uninhabited area) in case of an accident on launch. The launcher is placed into the inclination of that launch site latitude, thus a launch from the Kennedy Space Centre at 28.5° latitude would enter an orbital inclination of 28.5°, by launching due east. Departures from latitude based inclinations are, of course possible, but require extra propellant.

Country	Launch Site	Latitude	Longitude
USSR (CIS)	Tyuratam (Baikonur)	45.6° N	63.4° E
	Kapustin Yar	48.4° N	40.1° E
	Plesetsk	62.8° N	40.1° E
USA	Kennedy Space Centre (ETR)	28.5° N	81.0° W
	Vandenberg (WTR)	34.7° N	120.6° W
	Wallops Island	31.0° N	75.4° W
France	Hammaguir	31.0° N	8.0° W
USA/Italy	Indian Ocean Platform (San Marcos)	2.9° S	40.3° E
Australia/UK	Woomera	31.1° S	136.8° E
Japan	Uchinoura (Kagoshima)	31.2° N	131.1° E
	Tanegashima	30.4° N	131.0° E
ESA	Kourou (French Guiana)	5.2° N	52.8° W
China	Shuang Cheng-tzu (Jiquan)	40.6° N	99.8° E
	Xichang	28.1° N	102.3° E
India	Sriharikota	13.9° N	80.4° E

Table 5.6 Global location of launch sites.

There are a number of launch sites around the World used by a number of different countries/agencies. Although not exclusive to launching from their own country, there is still not the freedom, to launch from another country's launch site in a co-operative manner. Table 5.6 gives the global position of some launch sites. It is envisaged that more launch sites will be developed once developing space nations flourish. One such "*Space Port*" under consideration is in Australia at Cape York, 12.4° S and 142.2° E which would provide easy access for USSR and Far East to geostationary orbits above the equator.

One would therefore expect a manifestation of launch site latitude onto the inclination distribution of satellites and other tracked objects.

5.4.2 *Orbital Distribution Of Tracked Debris*

Geocentric orbit parameters for the tracked debris population were obtained from DISCOS using SQLPLUS commands. The data file "WSC.DAT" held at 323UKC login at ECD1 (ESOC VAX/VMS machine) contains data on 6610 objects in orbit on the 1st January 1992. Figure 5.14 illustrates some of the data contained in WSC.DAT.

Idyr	Idlno	Idpno	Mean motion	Eccentricity	Inclination	Shape	Piece size	Weight
1961	OMI	178	15.8473694	0.0025369	66.9855			
1961	OMI	195	16.0753216	0.0010853	66.8085			
1961	A-D	4	8.65616757	0.0230024	95.875			
1961	A-D	5	8.68987208	0.0119179	95.8315			
1961	A-E	1	13.6269969	0.0102084	32.4362	Cylinder	0.79 long 1.09 dia	86
1961	A-E	2	13.6189398	0.0102587	32.4364	door-knob + 32m boom	1.0 lomg 1.09 dia	109
1961	A-E	4	13.6219979	0.0102446	32.4373			
1961	DEL	2	12.2243321	0.1191227	38.8624	Cylinder	1.5 long 0.46 dia	24
1961	DEL	6	13.1065806	0.0833043	38.9098			
1961	DEL	7	13.0525017	0.0870528	38.8631			
1961	OMI	11	14.1900631	0.0087922	66.7172			
1961	OMI	110	13.6850277	0.0112589	67.0109			
1961	OMI	112	14.2105161	0.0064418	66.7803			
1961	OMI	115	13.4443765	0.0176632	67.0538			

Figure 5.14 Example extract of WSC.DAT.

Alongside the eccentricity, inclination and mean motion a size and weight is given where known. The orbital parameters were obtained from the USSPACECOM ELSETS stored in the SAT_PIECE_EPOCH DISCOS table. The shape and weight fields for the objects were obtained from the RAE Table of Earth Satellites 1986 edition, stored in the table PIECE_SPEC in DISCOS. The SQL command retrieved the eccentricity, inclination and mean motion for objects in SAT_PIECE_EPOCH and then using the objects I.D. cross referenced with PIECE_SPEC to retrieve the respective shape and weight where known. Of the 6610 objects only 1904 had an associated shape and weight. To determine the

orbital distribution of these objects in terms of eccentricity, e , inclination, i , and semi-major axis, a , the mean motion of the object was selected and converted to semi-major axis using:

$$n = \mu^{1/2} a^{-3/2} \quad (5.3)$$

where n is the mean motion, a is the semi-major axis and $\mu = G(M+m)$. With G the gravitational constant ($6.672 \times 10^{-11} \text{ Nm}^2\text{kg}^{-2}$) and M , m the mass of the Earth ($5.976 \times 10^{24} \text{ kg}$) and satellite mass respectively. This then gives, converting the mean motion from revolutions per day

$$a = \sqrt[3]{\left(\frac{86400}{2\pi n}\right)^2 (398602)} \quad (5.4)$$

Taking the Earth's radius (R_e) as 6,371km it is then possible to calculate apogee (A), perigee (P), apogee and perigee altitudes (A_h and P_h) with a knowledge of the eccentricity (e).

$$A = a(1+e) \quad (5.5)$$

$$P = a(1-e) \quad (5.6)$$

$$A_h = A - R_e \quad (5.7)$$

$$P_h = P - R_e \quad (5.8)$$

Finally the orbital period can be calculated from

$$T = 2\pi (a^3/\mu)^{1/2} \quad (5.9)$$

The data file WSC.DAT was transferred to the UKC UNIX machine to determine the orbital distribution and to carry out an analysis of space debris densities (see Chapter 6). Figure 5.15 shows a 3 dimensional representation of the 6610 orbits, reduced from WSC.DAT. There are distinct areas that stand out such as the region of $i < 25^\circ$, $e < 0.2$, $a \sim 30,000\text{km} - 50,000\text{km}$ the geostationary ring, $i \sim 60^\circ$ around the critical inclination for no apsidal advance. Figures 5.16a and 5.16b show the distribution of objects in terms of eccentricity and inclination. Clear inclination bands are visible indicating the main launch sites, such as 28.5° for due East launches from the Kennedy Space Centre.

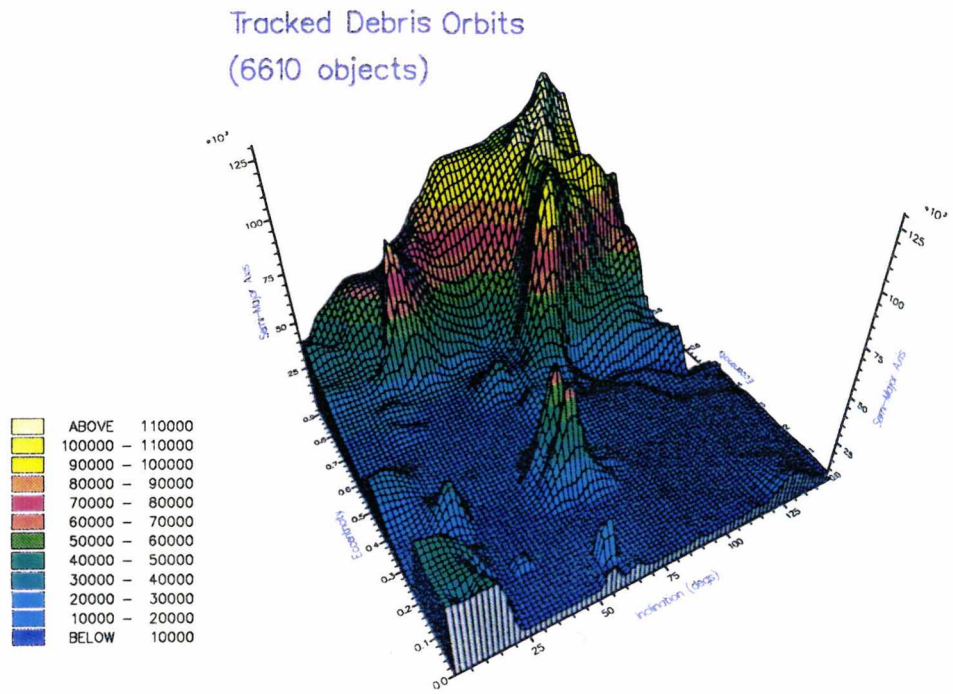


Figure 5.15 3-D representation of the 6610 orbits as defined in DISCOS, illustrating the definite inclination bands and high eccentricity orbits.

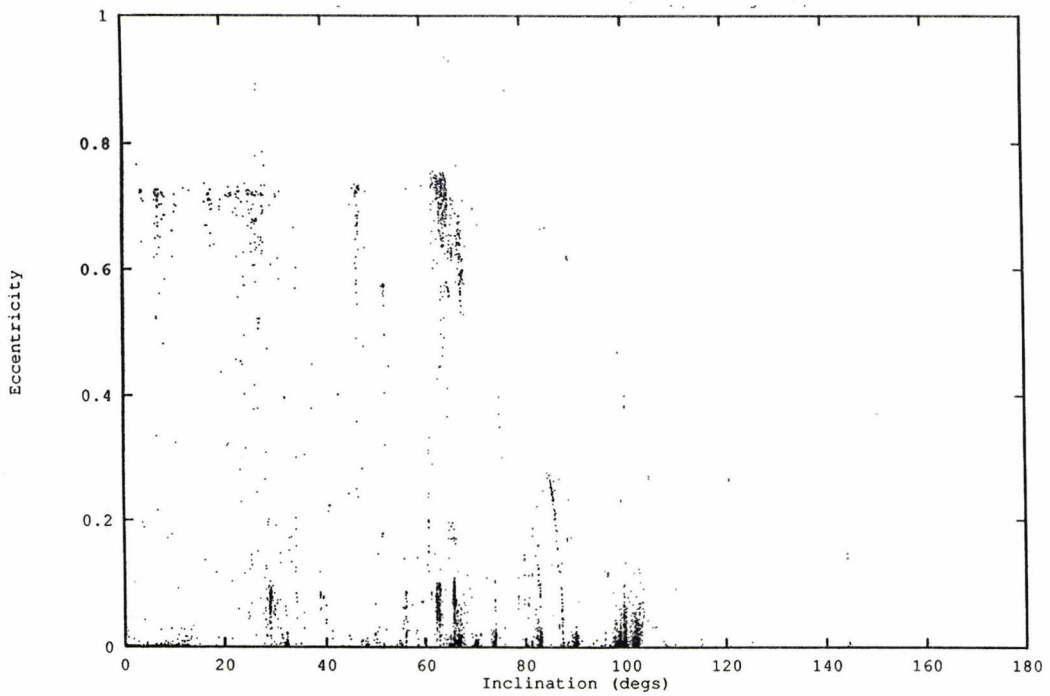


Figure 5.16a The distribution of tracked objects in terms of eccentricity and inclination.

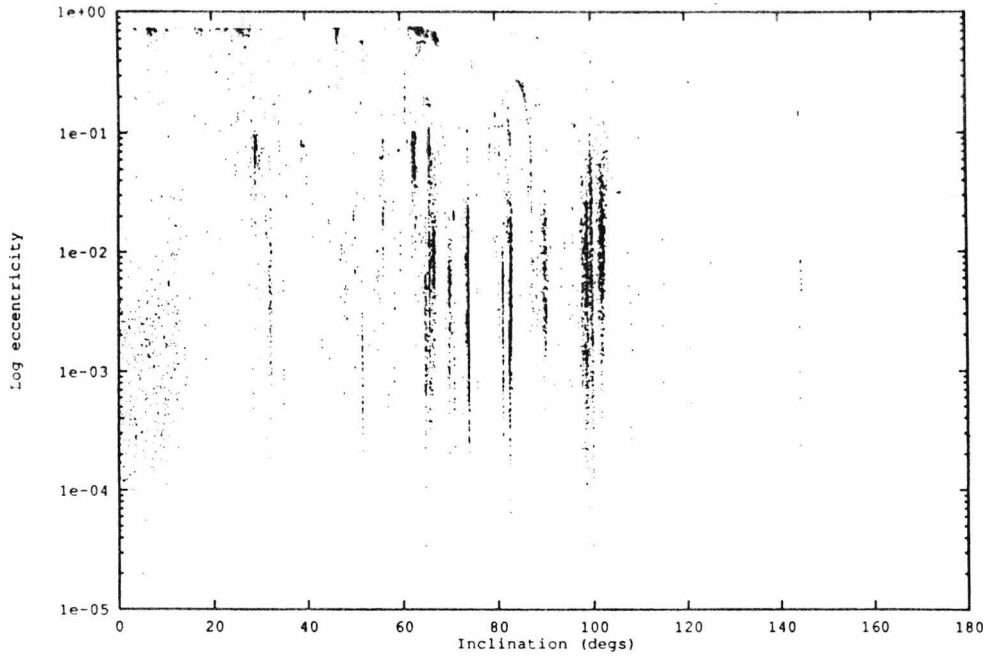


Figure 5.16b Distribution of tracked objects in terms of the log of eccentricity and inclination.

Figure 5.16b shows clearly that the majority of objects (85.8%), have eccentricities of 0.1 or less. Geostationary objects appear in the bottom left hand corner with low inclination and very low eccentricity. It is interesting to note that 93.1% of the objects have eccentricity, $e < 0.65$, with 57.8% $e < 0.01$. A plot of semi-major axis against inclination reveals the main LEO and GEO regions as shown in figure 5.17.

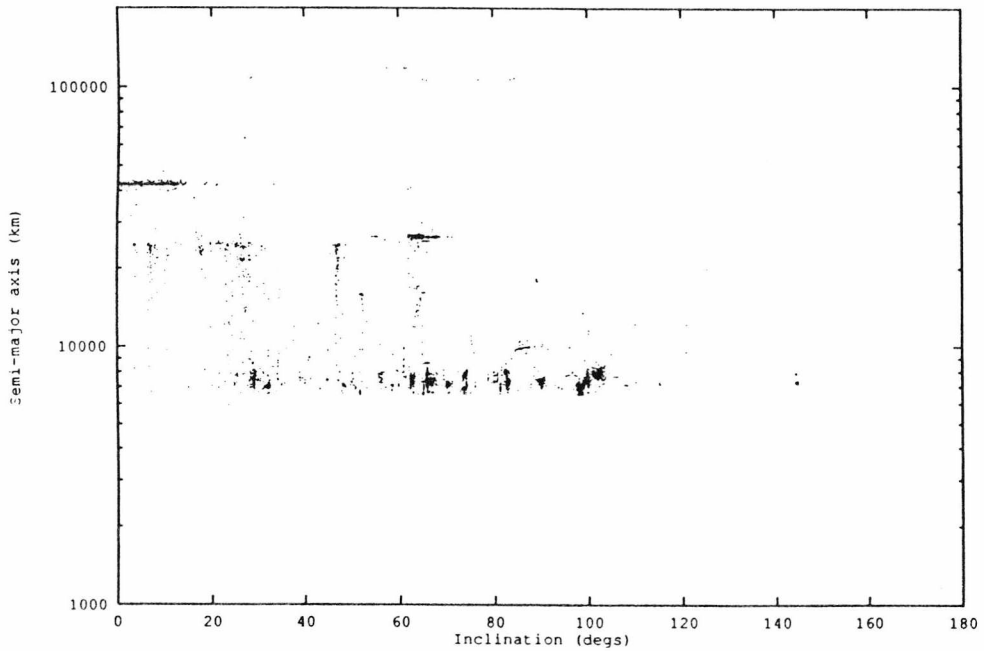


Figure 5.17 Tracked objects in terms of semi-major axis and inclination.

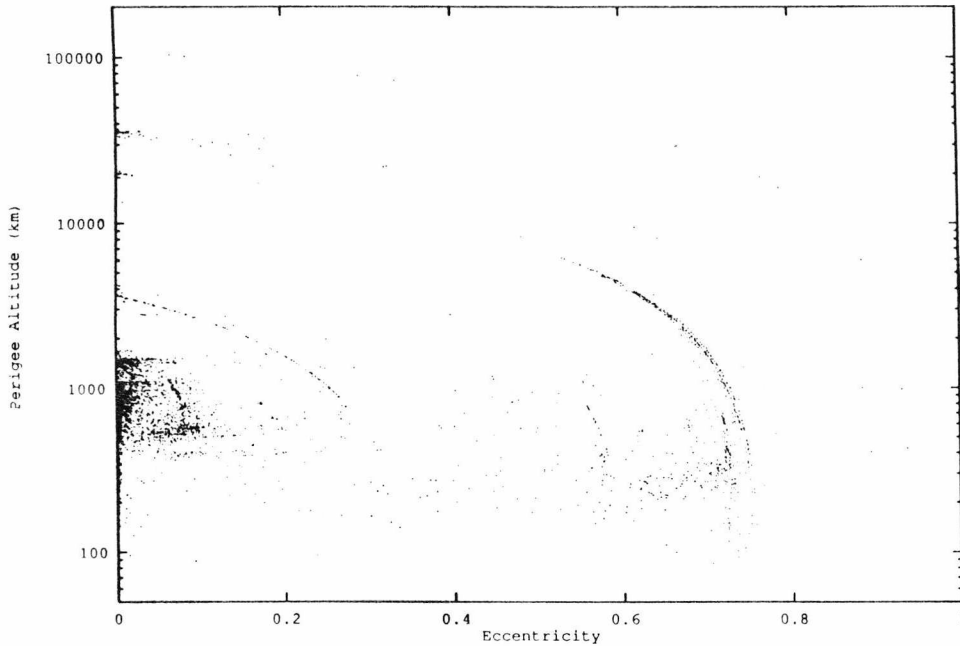


Figure 5.18 Tracked objects in terms of perigee height and eccentricity.

Figure 5.18 stands out as showing lines of constant period manifesting as arcs on the perigee altitude versus eccentricity plot. The two main arcs correspond to orbital periods of 3 hours and 12 hours respectively. The 3 hour orbit is believed to contain debris from the Pogos satellite 1966-56A, which between 12 July 1975 and 20 January 1976 broke up with some 79 catalogued objects. The cause of the break-ups are unknown {5.1}. The 12 hour orbit is the Soviet Molniya orbit.

It is clear then, that the tracked debris objects are not isotropic in space and distinct orbital distributions exist. The tracked debris objects are but a small fraction of the predicted debris in orbit. The model predictions are based on this larger population and the analysis of impacts on spacecraft can reveal the extent of the small, presently, untrackable space debris. Such models and predictions are discussed in Chapter 6.

5.5 Debris Prevention And Control

5.5.1 Prevention And Removal Scenario

There is clearly a problem with the rate of debris production in all regions of near Earth space. The amount of debris can be controlled in one of two ways : debris prevention or debris control. Table 5.7 highlights some of these techniques.

Prevention	Removal
Design and operations.	Retrieval.
Expulsion of residual propellants and pressurants.	Propulsive manoeuvres (de-orbit).
Battery safety (vent or fuse).	Drag augmentation. (Atmospheric drag)
Retention of covers and separation devices.	Solar sails.
Propulsive manoeuvres (re-orbit).	Tether, sweeping laser.

Table 5.7 Debris reduction methods.

5.5.2 Atmospheric Drag

The Earth's atmosphere contributes to the removal of debris via atmospheric drag de-orbiting the spacecraft. The density of the Earth's atmosphere decreases approximately exponentially with altitude. The lower atmosphere, up to ~100km is dominated by gravity and atmospheric circulations, whilst the upper atmosphere is dominated by gravity and solar activity. The density of the atmosphere around ~600km can vary by an order of magnitude or so with solar activity. An increase in solar activity produces heating and thus expansion of the atmosphere, increasing the density at a given

height. Solar activity cycles every 11 years and so then the atmospheric density height changes. There is a slight lag between maximum solar activity and maximum density, at a given height, due to the thermal expansion properties of the atmosphere. The drag experienced by a spacecraft is therefore dependant upon spacecraft altitude, atmospheric density, and spacecraft surface area {5.14 & 5.16}.

The drag force on an object in a circular orbit of radius r is

$$f = C_d A q \quad (5.10)$$

where q is the dynamic pressure given by

$$q = \frac{\rho(h) v^2}{2} = \frac{\rho(h) \mu}{2r} \quad (5.11)$$

C_d is the drag coefficient = $2+W$ (accommodation coefficient) = ~ 2

A is the cross sectional area

v is the velocity

$\rho(h)$ is the atmospheric density at altitude h

$\mu = 3.986 \times 10^{14} \text{ m}^3 \text{ s}^{-2}$.

The rate of loss of altitude

$$\frac{dr}{dt} = \frac{-C_d A \rho(h) \sqrt{\mu r}}{m} \quad (5.12)$$

where m is the object mass.

The decay rate is therefore a function of the surface area to mass ratio (A/m) termed the ballistic coefficient. (This coefficient is listed as one of the terms in the NASA ELSETS). Satellites in LEO circular orbits of altitude 200-400km re-enter within months, 500km years and subsequently higher orbital lifetimes up to 100,000 years plus. The effect of atmospheric drag is to reduce the apogee altitude by a greater amount than the perigee altitude (King Hele, 1987) {5.14}. Therefore objects with a high ballistic coefficient, *i.e.* small fragments, will have short lifetimes and rapidly circularised orbits. A recent study by Dr. P.R. Ratcliff at the USS has suggested that $1\mu\text{m}$ particles in circular orbits, with a mass density of 4 g/cc, typical of solid rocket motor firings (SRM),

would have lifetimes of the order of 1 hour and less for 450km altitude (Ratcliff 1992) {5.17}. This is seen in the section 5.4 with the preponderance of objects with $e < 0.1$ with low altitudes. The effect of solar activity increases decay, decreasing orbital lifetimes and this is also seen in section 5.3.2 as a decrease in the debris objects in orbit, as shown in figure 5.7. This corresponds to a maxima in solar activity, peaking around July 1989, taking into account thermal expansion properties of the atmosphere.

It is clear then that atmospheric drag can be used to de-orbit spacecraft and this is discussed later within drag augmentation. It is to be noted that this method of de-orbiting can only be applied to LEO objects.

5.5.3 Prevention And Removal Techniques

Several of the techniques listed in Table 5.6 are currently being employed by some space users at this time {5.18}. This is demonstrated by the introduction of debris catchers for explosive bolts, multiple payloads on a single launch, and a general “*cleaning up*” of the processes involved in spacecraft orbiting (*i.e.* a reduction of operational debris).

The de-orbiting method of debris removal, from space, has been used on some occasions, predominantly with Soviet Progress supply vehicles and space stations {5.19}. De-orbiting occurs over the oceanic areas, with the few exceptions such as Cosmos 557, Salyut 2, Salyut 7/ Cosmos 1686 {5.20}. Most re-entering spacecraft and objects are destroyed by entry heating, although solid pieces of Skylab, Cosmos 954, Salyut 7/ Cosmos 1686 reached the Earth. NASA's STS can be used for retrieval thus preventing the debris and break up associated with de-orbiting techniques. This however, has limited scope and is only applicable to sizes of spacecraft that can be accommodated in the payload bay area of the STS. To date only one such retrieval to Earth has taken place, and that is of LDEF.

The prevention of debris through break-ups via explosion is by far the greatest concern. The recovery of large objects although difficult and expensive is far easier than that of thousands of fragments. As stated earlier fragmentation events accounted for

42% of tracked debris and so limiting this source is a major concern. The venting of propellants and pressurants, once operation orbit is accomplished, has been expedited for LEO rocket bodies and will undoubtedly reduce the risk of explosive break-ups. There are however, more than 100 liquid upper stages in the vicinity of the geostationary orbit still as yet unvented, and this should be expedited as soon as possible as concern is growing for the catastrophic effect on telecommunications satellites in this region if an explosive break-up was to occur. The overcharging of batteries and other electrical discharging should also be limited as this has accounted for a number of small break-ups.

Re-orbiting of satellites into "*graveyard orbits*" is one way of safing GEO satellites. Once the satellites have reached their end of life they can be boosted to orbits well above the GEO region up to several hundred kilometres, thus preventing any continual unwanted interference with other objects in the GEO belt. For GEO satellites this is the only practical solution to reduce collision probabilities and this method has successfully performed on approximately 60 occasions. Study is still required to determine the fuel reserve required to boost the satellites without increasing risk of explosion, and a multiple-burn strategy will probably be adopted which takes into account uncertainties in the propellant estimate. At present the minimum raising altitude of 300-400km is recommended {5.18}.

This method is only applicable to objects in altitudes greater than 25,000km. It is far more economical to de-orbit objects below this altitude, due to the Earth's gravitational field. The mass penalties for removal of objects in LEO can be as much as 15% of inserted mass for a thrust lasting 250 seconds from a circular orbit of 1,600km {5.18}. It is therefore economically favourable not to boost from LEO as launch cost is dependant upon spacecraft launch mass.

The launch of spacecraft into GEO is achieved through the intermediate GTO, which has high eccentricity, a low altitude perigee (150-500km), and an apogee near the geostationary belt. Characteristic of these orbits are long periodic changes in the altitude of the perigee due to gravitational perturbations of the Earth, Sun and Moon. The orientation of the orbit with respect to the Sun and Moon determine whether the perigee

altitude will increase or decrease. Therefore launching at a favourable time when the perigee altitude of the GTO orbit is low, would minimise the orbital lifetime, by increasing air-drag perturbations. Unfortunately launch time constraints such as thermal aspects, attitude sensors, eclipse time of the spacecraft conflict with minimum GTO lifetime. However, an appropriate choice of initial perigee altitude (180-200km) could limit the GTO lifetime significantly.

Drag augmentation, propulsive manoeuvres, solar pressure movement, and tether removal are at present only concepts. Some envisage devices to increase cross sectional area via inflatable devices, thus increasing atmospheric drag and de-orbiting. Drag augmentation is only realistic in the low LEO region below 600-700km, although some lifetime reduction is feasible for orbital altitudes up to 1,200km. Propulsive manoeuvres require active propellant/attitude firing to force a de-orbit, thus increasing the likelihood of propellant related explosive break-up.

Other novel debris removal ideas include a controlled "*space tug*" deployed in space to rendezvous with, and de-orbit, large derelict objects, the use of solar sails to increase drag using solar radiation pressure and thus induce small changes in the orbital parameters. A tether may be used for removal via either momentum exchange on deployment or retrieval and electromagnetic drag. A recent test using such a tether was conducted on board STS-46, Atlantis, in early August 1992, but proved unsuccessful due to mechanical problems. The tether technique is however being actively pursued. A sweeper mechanism capable of withstanding debris impacts without inducing further debris has been discussed although present material technology and the effective size, maybe kilometres to actively sweep up an area, prevents the design of such a vehicle. Destruction by laser may be useful but it must be performed so that the debris object is totally evaporated, otherwise additional objects are created.

It is to be noted, however, that drag augmentation and solar pressure devices will increase the physical area, and thus the collision cross section of the object to be removed.

5.6 Conclusions

Space debris is a problem but one which can be actively controlled and prevented but only through a global effort by all space-faring nations. There are two main areas that need to be developed : environmental characterisation and space vehicle/mission design.

5.6.1 Environmental Characterisation

This chapter has hinted that the present data on the larger objects, though useful, is not the main area of concern. This area is the size range presently undetectable from the Earth, from microns to centimetres. To address this problem in characterising the environment a wide range of activities needs to be undertaken. These include analyses of spacecraft data, such as LDEF, SMM, experimentation and computer modelling. Chapter 6 will demonstrate developments in the modelling of the space debris environment, based upon both experimental data (LDEF, SMM etc) and data from DISCOS.

Listed are some ideas to further aid the debris environmental characterisation :

- (i) Advanced detection methods {5.21} : are needed to further characterise the debris population below the 10cm size limit. This would need advances in present ground based radar, optical systems and the development of space based systems.

- (ii) Radar cross section modelling : to attain greater accuracy in the estimation of debris sizes from radar and optical measurements. Theoretical, laboratory studies coupled with in-situ measurements would be needed.

- (iii) Debris monitoring and management system {5.22} : to characterise the population over the complete size range. This would require a database on the debris population

containing all pertinent information, from USSPACECOM data to impact studies data (e.g. LDEF). DISCOS is a step towards this goal.

(iv) Break-up modelling {5.23} : to study processes involved, amount and type of debris produced from fragmentation and to limit further break-ups. This requires theoretical studies, computer modelling and test programs. International co-operation on the exchange of data on spacecraft break-ups is required.

(v) Debris cloud evolution modelling {5.24} : which is linked closely to break-up modelling requires theoretical studies of fragmentation dispersion in-orbit.

(vi) Lifetime of small debris {5.25 & 5.17} : to determine the orbital lifetime of the untrackable debris fragments. Such models by Ratcliff 1992 are been used to shape the outcome of debris environmental modelling.

(vii) Traffic models {5.26} : are required to predict future launch rates and profiles.

5.6.2 Space Vehicle / Mission Design

Various methods have been discussed in section 5.5.3 on prevention and removal techniques and some of these are listed here, with the main areas of uncertainty and development highlighted.

(i) Safing of on-orbit vehicles : is expensive and technical trade-offs are inevitable in implementing such procedures. Theoretical studies coupled with engineering analyses and testing are required.

(ii) Design of litter free systems : has the same uncertainties and required development as above.

(iii) Earth re-entry disposal {5.27} : is again costly and re-entry manoeuvres will require new design or modification of present systems.

(iv) Disposal orbit for GEO spacecraft {5.28} : has cost and technical trade-offs to boost the orbit at end of life, coupled with the uncertainty of propellant estimate at this time. Engineering analyses, economic viability and computer modelling is required.

(v) Shielding : can be costly and affect performance. Spacecraft shielding system reliability needs to improve by means of theoretical, engineering and experimental analyses.

and finally

(vi) Active collision avoidance : systems are costly and further engineering and experimental testing is required.

It is clear then that there exists the ability to limit further space debris. Such groups as the European Space Debris Advisory Group, The International Academy of Astronautics Committee on Safety, Rescue and Quality, and various NASA Spaceflight centres are all actively pursuing research and development in a wide range of debris prevention, removal, and monitoring programs. Databases such as DISCOS and the Johnson Space Centre database give access to space debris data on tracked debris, solar activity, impact results from test programs and experimental results from spacecraft such as LDEF, SMM. Using this data as a basis for debris models, and the development of some of the models discussed, will enable the space faring nations to actively pursue a damage limiting exercise, in their utilisation of space.

References

- {5.1} McKnight, D. S. *Personal communications*.
- {5.2} The Report of the ESA Space Debris Working Group (1988). "Space Debris.", **ESA SP-1109**.
- {5.3} King-Hele, D.G., Walker, D.M.C., Pilkington, J.A., Winterbottom, A.N. (1987). "The RAE Table of Earth Satellites 1957-1986." Macmillan Publishers Ltd., England.
- {5.4} "Satellite Situation Report". (1989), Vol. 29, No.4, **GSFC, Code 513**.
- {5.5} Johnson, N.L., Nauer, D.J., (1987). "History of On-Orbit Fragmentations.", Third edition (prepared for Lockheed EMSCO), **CS88-LKD-001**, Houston.
- {5.6} Zarnecki, J.C. (1990). "Space Debris Database DISCOS, Final Report". ESA Contract No. 8173/89/D/MD.
- {5.7} Deshpande, S.P. and Green, S.F., (1992). "Can Objects in Geostationary Transfer Orbit (GTO) Affect the Debris Population at Low Earth Orbit (LEO)?" *Hypervelocity Impacts in Space*, (ed. J.A.M. McDonnell), Unit for Space Sciences, University of Kent at Canterbury, pp100-106.
- {5.8} Johnson, N.L. (1992). "U.S. Space Surveillance". for publication in Proc. IAF/COSPAR World Space Congress, Washington D.C. 1992.
- {5.9} Johnson, N.L. and McKnight, D.S. (1987). "Artificial Space Debris." Orbit Book Co., Malabar, Florida, 1987.
- {5.10} Kessler, D.J. (1992). "Origin of Orbital Debris Impacts on LDEF's Trailing Surfaces." in *LDEF, Second Post Retrieval Symposium*, San Diego, 1992.
- {5.11} McKnight, D.S. and Johnson, N.L. (1990). "Breakups and Their Effect on the Catalog Population". AIAA/NASA/DOD Orbital Debris Conference: Technical Issues & Future Directions, Baltimore, 1990. Paper No. **AIAA 90-1358**.

- {5.12} Chernyavskiy, G.M., Johnson, N.L., and McKnight, D.S. (1993). "Identification and Resolution of an Orbital Debris Problem with the Proton Launch Vehicle." presented at the First European Space Debris Conference, Darmstadt, Germany, 5-7 April, 1993.
- {5.13} Solari, G. and Viola, R. (1992). "M-HEO: The Optimal Satellite System for the Most Highly Populated regions of the Northern Hemisphere." ESA Bulletin No.70 pp81-88.
- {5.14} King-Hele, D.G. (1987). "Satellite Orbits In An Atmosphere: Theory and Applications." Blackie and Son Ltd, Glasgow, 1987.
- {5.15} Green, S.F. (1991). "Optical Detection of Space Debris, Workpackage 2100 Report, Debris Characterisation." for ESA/SIRA, UK.
- {5.16} Nazirov, R.R., Pivovarov, M.L., Ryazanova, E.E., Sukhanov, A.A. (1992). "Analysis of Space Debris Evolution Due to Atmospheric Drag and Solar Radiation Pressure." for publication in Proc. IAF/COSPAR World Space Congress, Washington D.C. 1992.
- {5.17} Ratcliff, P.R. and McDonnell, J.A.M. (1992). "The Leo Microparticle Population: Computer Studies of Space Debris Drag Depletion and of Interplanetary Capture Processes." for publication in Proc. IAF/COSPAR World Space Congress, Washington D.C. 1992.
- {5.18} McKnight, D.S. and Flury, W. (1992). "Position Paper on Orbital Debris", compiled by an ad hoc Expert Group of the International Academy of Astronautics, Committee on Safety, Rescue and Quality 1992. (Summary presented for publication in Proc. IAF/COSPAR World Space Congress, Washington D.C. 1992.
- {5.19} Proceedings of an ESA Workshop held at ESOC, Darmstadt, Germany (1985). "Re-entry of Space Debris.", **ESA SP-246**.
- {5.20} Proceedings of an International Workshop held at ESOC, Darmstadt, Germany (1991). "Re-entry of Salyut-7/Cosmos-1686.", **ESA SP-345**.
- {5.21} Potter, A., Kessler, D., Nieder, R., and Reynolds, R. (1991). "Summary of the AIAA/NASA/DOD Orbital Debris Conference: Technical Issues and Future Directions.", *Advances in Space Research*, Vol. 11, No. 12, pp (12) 5-(12) 18.

- {5.22} Klinkrad, H. (1991). "DISCOS: ESA's Database and Information System Characterising Objects in Space.", *Advances in Space Research*, Vol. 11, No. 12, pp (12) 43-(12) 52.
- {5.23} McKnight, D.S. (1991). "Determination of Breakup Initial Conditions.", 29th Aerospace Sciences Meeting, **AIAA91-0299**, Reno NV, January 7-10, 1991; *J. of Spacecraft*, Vol. 28, No. 4, pp 470-477.
- {5.24} Kessler, D.J. (1990). "Orbital Debris Environment for Spacecraft in Low Earth Orbit.", *AIAA/NASA/DOD Orbital Debris Conference*, Baltimore, 1990. Paper No. **AIAA 90-1358**.
- {5.25} Chobotov, V. and Spencer, D. (1991). "Debris Evolution and Lifetime Following an Orbital Breakup.", *J. of Spacecraft*, Vol. 28, No. 6, pp 670-676.
- {5.26} Kessler, D.J., Reynolds, R. & Anz-Meador, P. (1989). "Orbital Debris Environment for Spacecraft Designed to Operate in Low Earth Orbit.", **NASA TM-100471**.
- {5.27} Eichler, P. and Bade, A. (1990). "Strategy for the Economical Removal of Numerous Larger Debris Objects from earth Orbit.", presented at the 41st Congress of the IAF, Paper **IAA-90-567**.
- {5.28} Flury, W. (1991). "Collision Probability and Spacecraft Disposition in Geostationary Orbit.", *Advances in Space Research*, Vol. 11, No. 12, pp (12) 67-(12) 79.

Chapter 6

LEO Particulate Modelling

6.1 Introduction

To accurately predict the particulate impact damage on a given spacecraft, a reliable model must first be derived. The original models in the 1960's were mainly based upon interplanetary dust particulates, as anthropogenic space debris had not become an issue. This was the case for the development of the Cour-Palais Meteoroid Environment Model in 1969 {6.1}. Although at the time the model was developed with very little spaceflight data, mainly meteoroid observation, it is still valid for the interplanetary particulate environment because of the distinct lack of space debris at that time.

Since then any models based upon near Earth spaceflight data analyses have to be reduced to the interplanetary environment by removing the space debris component. The Grün et al.(1985) model {6.2} dispenses with this problem by calibrating the Lunar micrometeoroid flux to the flux seen at 1A.U.. This flux is then easily converted to the flux at the Earth, at any given altitude, using the Earth's gravitational focussing and such quantities as Earth shielding factors, if a specific spacecraft is used. Recently Divine

(1992) {6.3} has developed a model for the interplanetary dust environment based upon various meteoroid data sets, including radar observations, spacecraft data and the Grün interplanetary flux model {6.2}.

The interplanetary flux is therefore only one source of particulates in LEO. The second source to be modelled is that of the anthropogenic space debris. Kessler et al. (1989) {6.4} developed a model for space debris at altitudes $\leq 2000\text{km}$ and particle sizes down to $1\mu\text{m}$ (see section 6.3.1). Green et al. (1992) {6.5} developed a debris model based upon the Green (1990) {6.6} model specifically to model impacts on the LDEF, and it is this model that shall be the focus for interpreting the LDEF data.

Sullivan (1992) {6.7} developed both a 3D and 2D model to model the flux impacting the LDEF and discusses, in depth, the development of these models alongside the Cour-Palais, Grün and Kessler models. The 3D model is based upon a stationary spacecraft above the Earth, impacted by particles from all direction with the same velocity. This case is used to describe the interplanetary particle distribution where it is assumed the particles come in from all direction, except when shielded by the Earth. The 2D model is based upon an isotropic distribution of particles in the orbital plane of the spacecraft. This 2D model is used to describe space debris particulates, as at the time most debris was assumed to be in circular orbits. Both models were developed to predict the number of impacts on the faces of LDEF, as a percentage of the total number hitting, and as a consequence do not use real data in terms of an input (*i.e.* actual space debris and interplanetary particulate data are used as an input). The models, however, characterise the relationships between the various faces of the LDEF and can be used to obtain a single velocity, that could be attributed to the interplanetary flux distribution (Sullivan, 1992) {6.7} by transforming the flux impacting one face to the flux received by another face, assuming these to be only attributed to interplanetary particles. The transformation of these fluxes are velocity dependant and so, using the 3D model to supply the parameters needed to perform the transformation (see section 6.5), a velocity attributed to this model is obtained and is therefore that assigned to the interplanetary particles, assuming an isotropic distribution. The Sullivan model has been re-developed

to include the Grün flux and a velocity distribution to obtain the interplanetary particle flux impacting the LDEF. Both the space debris and interplanetary models are applied to the LDEF and compared to LDEF data in Chapter 7.

Brief outlines of the Grün, Divine, Kessler, Green/Mackay models and a comparison of the Sullivan model for a symmetrical LDEF to that of the offset LDEF, as was found to be the case on retrieval, are presented.

6.2 Interplanetary Dust Models

6.2.1 The Grün Flux Model At 1A.U.

The Grün et al. (1985) interplanetary flux model {6.2} has been incorporated into most of NASA's spacecraft environmental models {6.8}. The model describes the interplanetary flux at 1A.U., based upon data from lunar rock crater sizes, in-situ spacecraft measurements and the β -meteoroid environment for particle masses of 10^{-18} g to 1g, impacting a spinning flat plate detector.

To establish the model Grün characterised the particles as having a particle density, ρ_p , of 2.5gcm^{-3} with a velocity of 20kms^{-1} . These data were obtained from various studies on captured particles ($\rho_p=2\text{-}3\text{gcm}^{-3}$) (Brownlee, 1978) {6.9}, lunar microcraters, (Smith et al, 1974 {6.10} and Nagel et al. 1976 {6.11}) ($\rho_p\sim 1\text{gcm}^{-3}$) although Le Sergeant d' Hendecourt and Lamy (1980) found $\rho_p=3\text{gcm}^{-3}$ {6.12}. With 20-40% $\rho_p < 1\text{gcm}^{-3}$ and the majority between $2\text{-}3\text{gcm}^{-3}$, Grün derived the particle density as 2.5gcm^{-3} . The velocity measurement came from various meteor observations and satellite measurements (Zook, 1975) {6.13} and Grün took an average velocity of 20kms^{-1} which is also assumed to be that for particles impacting the lunar surface. The meteoroid flux was also assumed to be isotropic with respect to the Earth.

The lunar mass flux distribution is taken for masses above 10^{-9} g as below this it is assumed that secondary cratering is not negligible (Flavill et al. 1978 {6.14}; Allison &

McDonnell, 1981 {6.15}). The lunar mass flux distribution was derived from the best fit through the lunar microcrater cumulative size distribution of Morrison & Clanton (1979) {6.16}. Crater size measurements from lunar samples provided the data and using solar flare track measurements to age the craters a cumulative mass flux distribution was obtained. However, Zook (Zook et al., 1977 {6.17}, 1980 {6.18}) argue that the method calibration of solar track data, assuming constant production rate, and hence a determination of exposure age was not valid and so calibration using in-situ spacecraft flux measurements was used. The spacecraft data used were that of Naumann (1969) for the Pegasus I, II and III satellites {6.19}. Although the satellites were in Earth orbit, the flux measurements were reduced to 1A.U. by taking into account gravitational enhancement, and the orientation of the satellite detectors.

At masses $>10^{-9}$ g the lunar mass flux distribution was ignored in favour of HEOS-2 (Hoffmann et al., 1975a,b {6.20 and 6.21}; Grün & Zook, 1980 {6.22}), and Pioneer 8 and 9 data (Berg & Grün, 1973) {6.23}, taken far from the Earth to avoid gravitational enhancement and shielding corrections, and the β meteoroid flux.

The β -meteoroid flux is established for masses $\leq 10^{-10}$ g, based upon the fragmentation of meteoroids through collision, and is described below. Small particles, in the Solar system, are affected by radiation pressure. This effect is commonly described by the radiation pressure constant β , given below:

$$\beta = \frac{F_{\text{rad}}}{F_{\text{grav}}} \quad (6.1)$$

where F_{rad} is the Solar radiation pressure force and F_{grav} the gravitational force of attraction between the particle and the Sun. A small particle generated from a collision of two larger meteoroids, with $\beta \sim 0$ at a distance, r , from the Sun, will move on an unbound trajectory if :

$$(1-\beta)U + E \geq 0 \quad (6.2)$$

where,

$$U = -\frac{GM}{r} \quad (6.3)$$

and

$$E = \frac{1}{2} V^2 \quad (6.4)$$

U is the specific potential energy in the Solar gravitational field, E , the specific kinetic energy of the fragment particle, with heliocentric velocity V . G is the gravitational constant and M the mass of the Sun. Therefore a particle with $\beta > 0$ will be unbound to the Solar System and this occurs when:

$$\beta = \frac{r}{2a_p} \quad (6.5)$$

where a_p is the semi-major axis of the parent particle. It was further assumed that the specific kinetic energies of the parent and fragment were the same, so that:

$$E = GM \left(\frac{1}{r} - \frac{1}{2a_p} \right) \quad (6.6)$$

If the collision occurs at perihelion of the parent's orbit then

$$r = a_p (1 - e_p) \quad (6.7)$$

where e_p is the parent orbit eccentricity, then a minimum value for β is obtained, for unbound trajectories given by:

$$\beta \geq \frac{1}{2} (1 - e_p) \quad (6.8)$$

Many parent bodies have large eccentricities and as such fragmented particles in unbound orbits will be many. Values for β of 0.1 for particle masses $\leq 10^{-10}$ g and a maximum of 0.5 for masses 10^{-15} g to 10^{-12} g imply that most of these particles become β -meteoroids, (Grün et al., 1985) {6.2}. Most of these particles within 1A.U. of the Sun

have an assumed spatial density, $N(r)$, given by equation (6.9) (Linert et al, 1981) {6.24} and relative collision speeds, $V(r)$, given by equation (6.10).

$$N(r) \propto r^{-\nu} \qquad \nu = 1.3 \text{ for } 0.3 \text{ A.U.} \leq r \leq 1 \text{ A.U.} \qquad (6.9)$$

$$V(r) = V_0 \left(\frac{r}{r_0}\right)^{-0.5} \qquad V_0 = 20\text{kms}^{-1}, r_0 = 1 \text{ A.U.} \qquad (6.10)$$

It was also assumed that the size distribution does not change with r for $r > 0.03\text{A.U.}$ and $N(r) = 0$, for, $r \leq 0.03\text{A.U.}$, and that the flux distribution of β -meteoroids is similar concentrated to the ecliptic plane as does the distribution of interplanetary particles.

The β -meteoroid flux was then calculated iteratively and defined to intercept the interplanetary flux plot at a mass of 10^{-16}g . Grün therefore produced a mathematical description of the interplanetary flux at 1A.U. by incorporating the lunar flux measurements, in-situ spacecraft measurements and this β -meteoroid flux model. The Grün flux with appropriate source data is shown in figure 6.1, below.

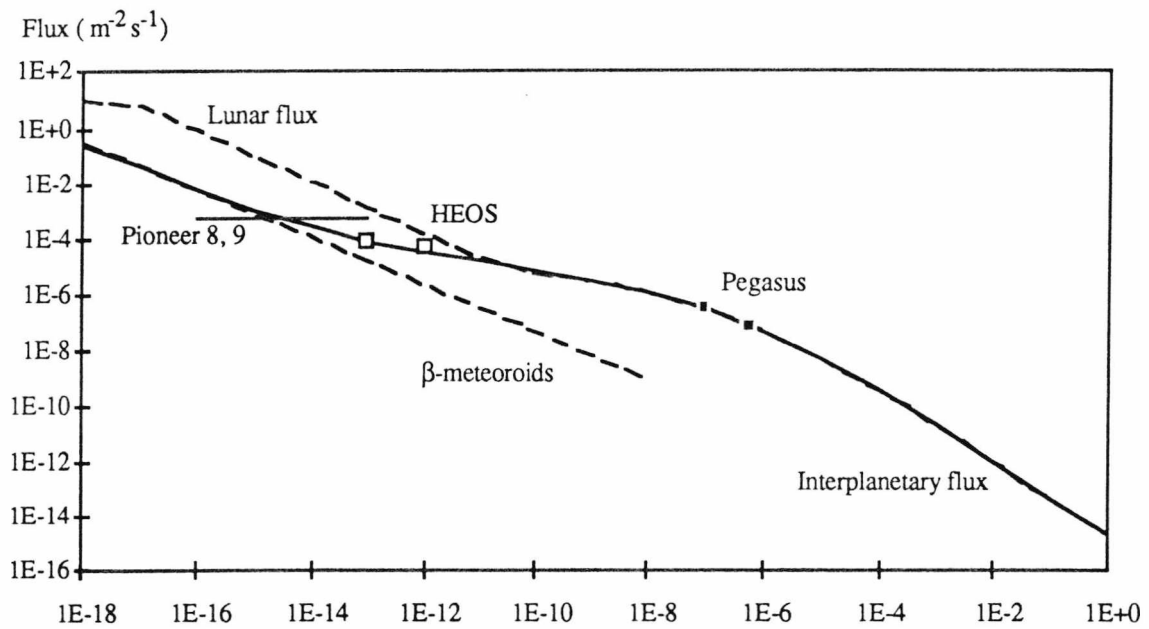


Figure 6.1 Grün Interplanetary flux model with source data.

This β -meteoroid flux would manifest itself on the LDEF as impacts corresponding to 10^{-15}g to 10^{-12}g impacting from the direction of the Sun, and so a

comparison LDEF orbital position data and Sun pointing data would be required to determine the β -meteoroid impacts. To obtain the flux in LEO from that at 1A.U. the Grün flux is multiplied by the gravitational enhancement factor, χ given by equation (6.11) and then by the Earth shielding factor, ξ (6.13) to determine the flux impacting a randomly tumbling spacecraft in LEO. Therefore the flux on a randomly tumbling spacecraft in LEO, $F_{s/c}$ is given by equation (6.15), where F_{IP} is the Grün flux at 1A.U..

$$\chi = 1 + \frac{V_{esc(r)}^2}{V_{\infty}^2} \quad (6.11)$$

where V_{∞} is the particle velocity at infinity, and escape velocity at r , is given by equation (6.12).

$$V_{esc(r)}^2 = \sqrt{\frac{2GM_E}{r}} \quad (6.12)$$

where $r = R_E + H$, (R_E being the Earth's radius and H the orbital altitude).

$$\xi = \frac{1 + \cos\theta}{2} \quad (6.13)$$

where θ is the Earth shielding angle for a random tumbling spacecraft given by equation (6.14).

$$\sin\theta = \frac{R_E}{R_E + H} \quad (6.14)$$

$$F_{s/c} = \chi \xi F_{IP} \quad (6.15)$$

To fully utilise the Grün flux model for engineering purposes agencies such as NASA's JSC have incorporated a velocity distribution, *e.g.* Erickson meteor distribution (1968) {6.25} and a density distribution.

6.2.2 *The Divine Model*

Divine(1992) developed a model for interplanetary meteoroids based upon various meteoroid data sets {6.3}. These sets include such established data as the Grün interplanetary flux distribution {6.2} (section 6.2.1), radar meteoroid measurements, zodiacal light and space flight data from an abundance of spacecraft. The spacecraft data used span nearly 15 years of meteoroid data, from Helios flux and event data, Pioneer 10 and 11 meteoroid experiments, and more recently data from the Galileo and Ulysses dust detection experiments, called DDS, Dust Detection System and GRU, from the Principal Investigator, Grün, respectively.

The model predicts five distinct populations of interplanetary meteoroids based upon computer modelling and Hamiltonian mechanics (action variables) to describe both, qualitatively and quantitatively, the meteoroid data sets. The results lead to the formation of separable particle mass distributions in orbital inclination, eccentricity and perihelion distance. The five populations have each been named using a characteristic associated with that particular population. They are in order of increasing mean mass; eccentric, inclined, halo, core and asteroidal.

A brief description of each of the data sets used by Divine to determine the five populations is given. The Grün interplanetary flux model {6.2} was used as the basis for the Divine model as this model utilises several data sources as can be seen from the discussion in section 6.2.1.

The extensive radar meteor data of Sekanina and Southworth (1975) {6.26} was used as this gave the most thorough examination of meteors entering the Earth's atmosphere. The median mass threshold for the data was 10^{-4} g, and the data were corrected for observational selection effects before incorporating the orbital parameters and velocity distribution into the analysis.

Zodiacal light measurements from Helios, (Leinert et al. 1981) {6.24}, Pioneer 10, (Levasseur-Regourd & Dumont, 1980) {6.27}, and the Earth, (Hanner et al., 1974) {6.28}

were used. The heliocentric distances vary from 0.3 to 4A.U. but all are in the ecliptic and hence the scattering function given by Leinert & Grün (1990) {6.29} was employed.

Two data sets from the Helios 1 were used. The first was the Helios flux data (Grün, 1981), for a spin averaged flux from the two dust impact ionisation sensors (ecliptic and south sensors) on Helios 1 {6.30}. The data represents the flux as a function of heliocentric distance between 0.31 and 0.98A.U., with a single mass threshold of 10^{-10} g. The second, the Helios event data for some 235 individual impacts, also reported by Grün, 1981. In this data set the mass threshold is evaluated for an impact velocity of 20kms^{-1} and particle density of 2.5gcm^{-3} . This is due to one of the sensors (ecliptic) being covered by a foil whose threshold mass for penetration exceeds that for the sensors themselves for impact velocity of 18kms^{-1} or less. This mass threshold for penetration increases as the density of the impacting particle decreases.

Pioneer 10 and 11 data are used as described by Humes (1980) for spin averaged penetration fluxes from the impact detectors on board {6.31}. The detectors penetration threshold depend upon impactor density as they are of the puncture cell type. The mass penetration threshold for Pioneer 11 was a factor of 7 above that of Pioneer 10, with the heliocentric distance being between 1 and 9A.U. and 1 and 18A.U. respectively.

Galileo data are used from the impact ionisation detector, as presented by Grün et al. 1991, for spin averaged fluxes on the inbound passage at 0.88A.U. and the outbound passage at 1.45A.U.. Similarly Ulysses spin averaged flux data (Grün et al., 1991) from 1 to 4A.U. outbound is used {6.32}.

A summary of the model distribution for the five populations is given in Tables 6.1 to 6.3, which clearly show the individual properties of each population and their respective contribution to the meteoroid data sets.

Population	Core	Inclined	Eccentric	Halo	Asteroidal
Radial	<2AU	<0.75 AU	< 2AU	> 4AU	> 2AU
Eccentricity	0.3	0.05	0.85	0.3	0.3
Inclination	10°	35°	10°	uniform	10°
Mass	10^{-5}g	10^{-8}g	$10^{-13.5}\text{g}$	10^{-7}g	10^{-3}g

Table 6.1 Distribution peaks for the Divine populations given for radial distance from the Sun, orbital eccentricity and inclination and particle mass.

Population	Core	Inclined	Eccentric	Halo	Asteroidal
Particle density (gcm^{-3})	2.5	2.5	0.25	2.5	2.5
Geometrical albedo	0.05	0.02	0.05	0.02	0.02
Mass factor (g)	5830	2.17×10^8	9.66×10^{13}	6.7×10^4	65.1
Area factor (m^2)	41.8	8.95×10^6	3.2×10^{15}	1300	0.0507

Table 6.2 Properties of the Divine populations.

Population	Core	Inclined	Eccentric	Halo	Asteroidal
Radar meteors	0.4				0.6
Zodiacal light	0.7	0.1		0.1	0.1
Grün model	0.7	0.1	0.1		0.1
Helios fluxes					
ecliptic	0.9	0.1			
south	0.5	0.5			
Helios events					
ecliptic	0.8	0.2			
south	0.3	0.5	0.2		
Pioneer 10	0.3			0.7	
Pioneer 11	0.4			0.6	
Galileo	0.7	0.1	0.1	0.1	
Ulysses	0.3			0.7	
Column Total	6.0	1.6	0.4	2.2	0.8
	(54.5%)	(14.5%)	(3.6%)	(20%)	(7.3%)

Table 6.3 Approximate contribution of Divine populations in terms of the meteoroid data sets used.

Figures 6.2 to 6.5 illustrate the Divine populations, showing the five populations in terms of mass, inclination, eccentricity and radial distributions.

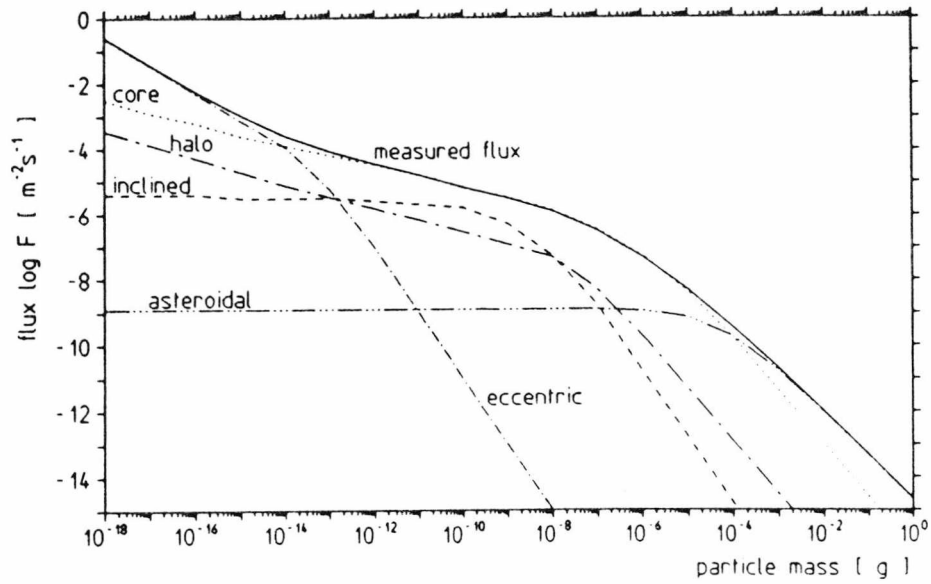


Figure 6.2 Divine cumulative mass distribution showing the five populations, compared to the measured flux.

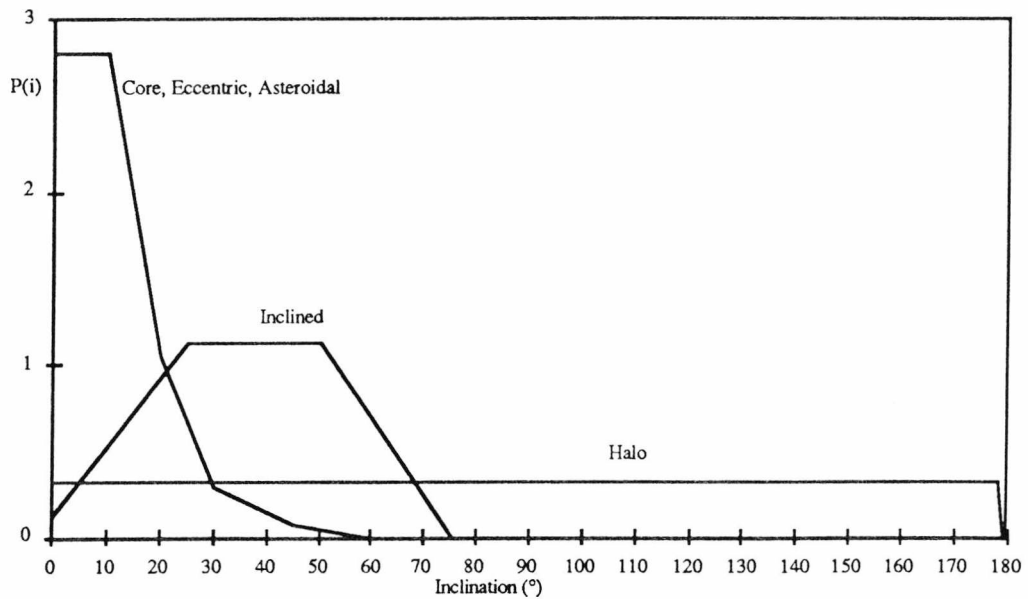


Figure 6.3 Divine inclination distribution for the five populations.

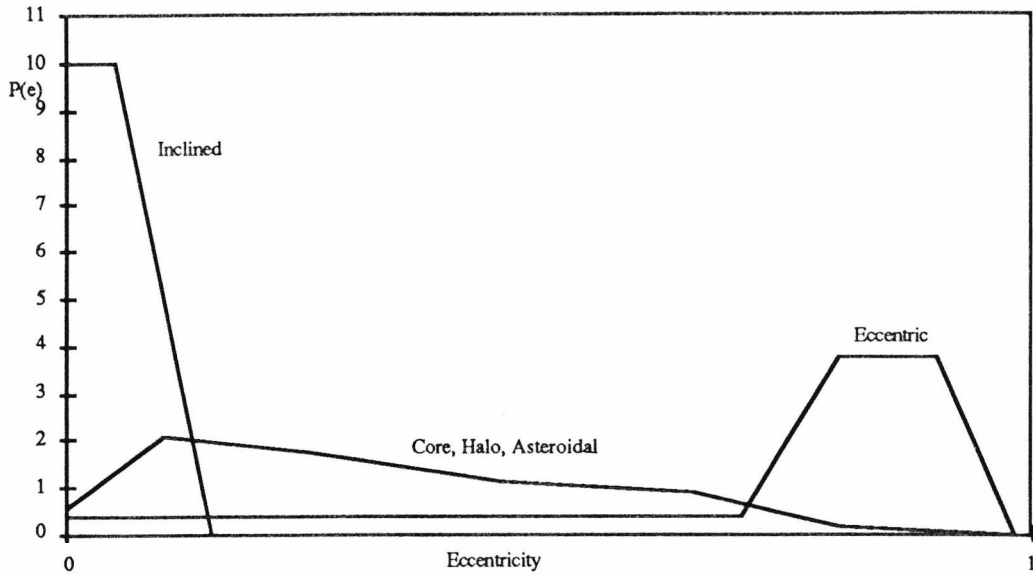


Figure 6.4 Divine eccentricity distribution for the five populations.

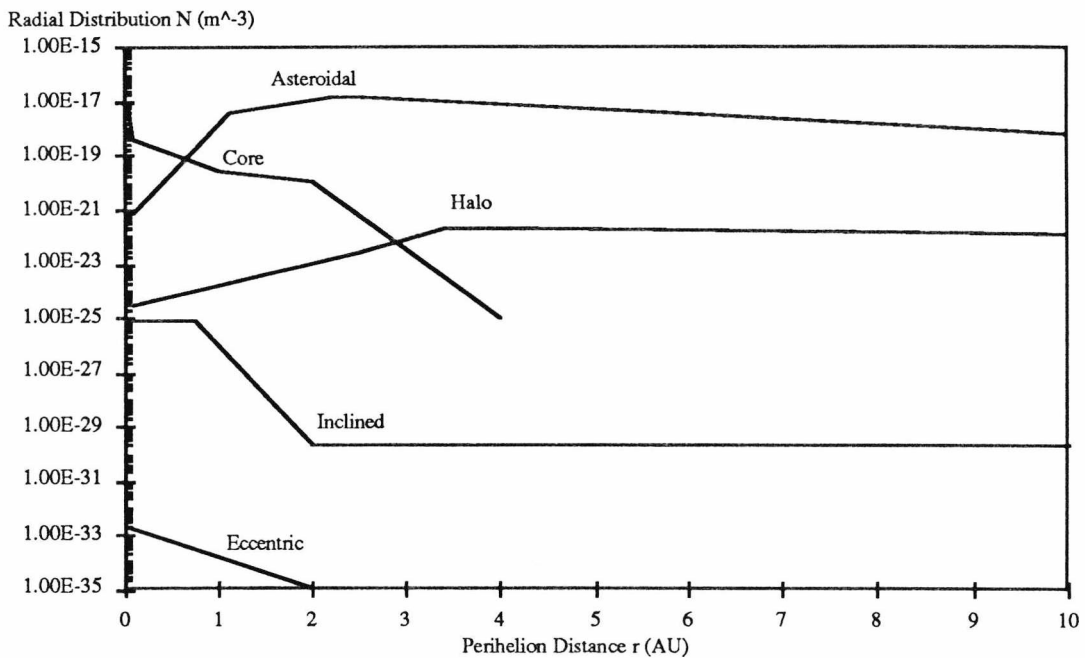


Figure 6.5 Divine radial distribution for the five populations.

The Divine model was run for a massless detector in the Earth's non-circular heliocentric orbit (*i.e.* run for a massless Earth) for four threshold masses of $10^{-4}g$, $10^{-5}g$, $10^{-9}g$, $10^{-12}g$ (Divine 1992 {6.33}). The total flux per population is given in figure 6.6 and the average impact velocity over the mass range in figure 6.7.

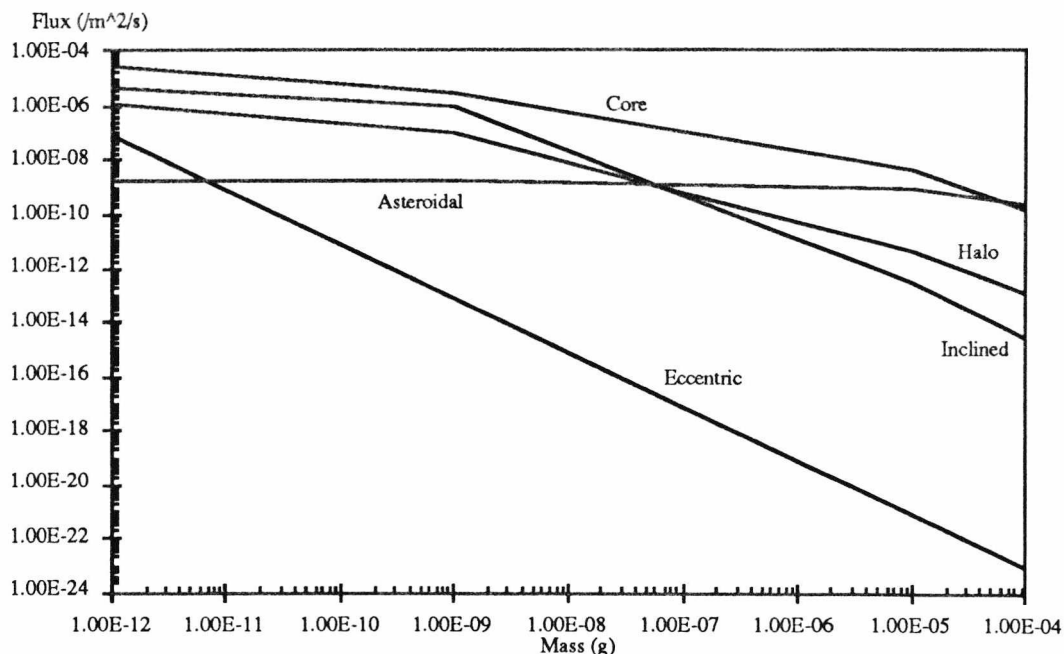


Figure 6.6 Divine mass distribution run for a massless Earth.

It is clear from figure 6.6 that across the size range the core population is the dominant population. The inclined population and halo population contribute a small amount although interestingly at around 10^{-7} g, they invert.

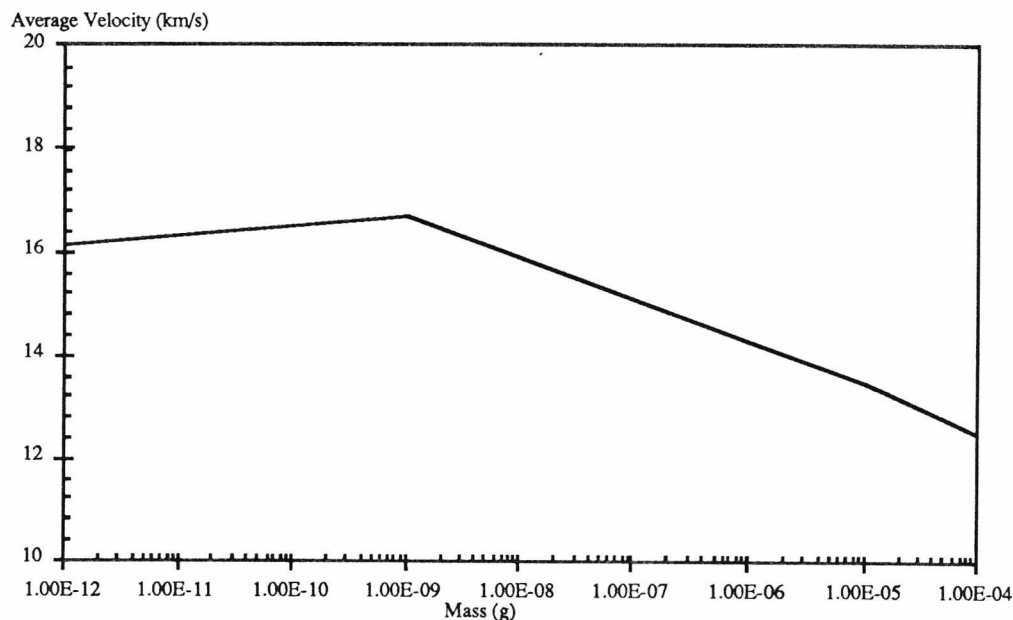


Figure 6.7 Average impact velocity as determined from Divine using the total of the five populations.

It is interesting to note that the respective mean velocities for these populations are halo (48.89kms⁻¹), eccentric (23.57kms⁻¹), inclined (21.65kms⁻¹), core (13.92kms⁻¹) and finally asteroidal (11.53kms⁻¹). The relevance of the velocity distribution over the mass range will become evident in Chapter 7, on the interpretation of LDEF data.

6.3 Space Debris Models

6.3.1 The Kessler Model

The space debris environment has been characterised and modelled by Kessler et al. (1989) based upon in-situ space flight data from SMM, ground based measurements from USSPACECOM and mathematical modelling of debris accumulation {6.4}. This model describes the orbital debris population in LEO for an orbital altitude of ≤ 2000 km and for particle sizes down to 1 μ m.

Data from the analysis of SMM louvres (Laurance & Brownlee, 1986) gave the first positive chemical indications of impacts from space debris {6.34}. This gave the orbital debris particulate environment for the 1 μ m to 100 μ m sizes (Sullivan, 1992, {6.7}), which is easily converted to a mass flux plot assuming a particle density of 2.5gcm⁻³, and a particle velocity of 8kms⁻¹ (Laurance & Brownlee, 1986) {6.34}.

Ground based measurements provided by the Massachusetts Institute of Technology (MIT), in 1984, gave the orbital flux for the size regime between 2cm and 10cm {6.4}. Infrared observations were also used for the determination of object albedo for mass density calculations. USSPACECOM data on tracked objects for sizes >10cm were used to complete the data set (see Chapter 5 on Space Debris).

The baseline year for the model was chosen as 1985 and then mathematical modelling of debris trafficking and fragmentation is used to predict the current orbital debris flux. The effects of solar activity (see section 5.5.2) and assumed growth rates for debris production, via launch trends, and fragmentation events were also included. The

cumulative flux, F , ($\text{m}^{-2} \text{yr}^{-1}$) of orbital debris, is derived in this way, is given by equation (6.15).

$$F(d,h,i,t,S) = k \cdot \Phi(h,S) \cdot \Psi(i) \cdot [F1(d) \cdot g1(t) + F2(d) \cdot g2(t)] \quad (6.16)$$

where

$$\Phi(h,S) = \frac{\Phi(h,S)}{\Phi1(h,S) + 1} \quad (6.17)$$

$$\Phi1(h,S) = 10^{(h/200 - S/140 - 1.5)} \quad (6.18)$$

and

$$F1(d) = 1.05 \times 10^{-5} d^{-2.5} \quad (6.19)$$

$$F2(d) = 7.0 \times 10^{10} (d + 700)^{-6} \quad (6.20)$$

$$g1(t) = (1 + 2p)^{(t-1985)} \quad (6.21)$$

$$g2(t) = (1 + p)^{(t-1985)} \quad (6.22)$$

The flux, $F[\text{m}^{-2} \text{yr}^{-1}]$, is given in terms of particle size, $d[\text{cm}]$, with the term, k , being a surface orientation factor such that for a randomly tumbling plate this equals 1. Year of determination is expressed as, t , with the spacecraft orbital altitude, $h[\text{km}]$ for $h \leq 2000\text{km}$. The solar activity flux as measured by the 13 month smoothed 10.7cm wavelength flux is expressed as S in 10^4Jy and retarded by 1 year from t . The term $\Psi(i)$ is the spacecraft inclination function given by figure 6.8 and the terms $F1(d) \cdot g1(t)$ and $F2(d) \cdot g2(t)$ account for the growth of the smaller and larger particles respectively, with p being the annual mass growth rate for trackable objects.

An impact velocity distribution was defined as a function of spacecraft inclination, and averaged over all altitudes, figure 6.9, and assuming that space debris orbits were all circular. Therefore the impact velocity distribution was a simple case of velocity vector addition. It has been demonstrated in section 5.4.2 that the assumption of circular debris orbits is not valid and section 7.5.2 will demonstrate that the preponderance of near-circular debris orbits ($e < 0.1$) can have dramatic consequences for the impact flux on the Space face of LDEF.

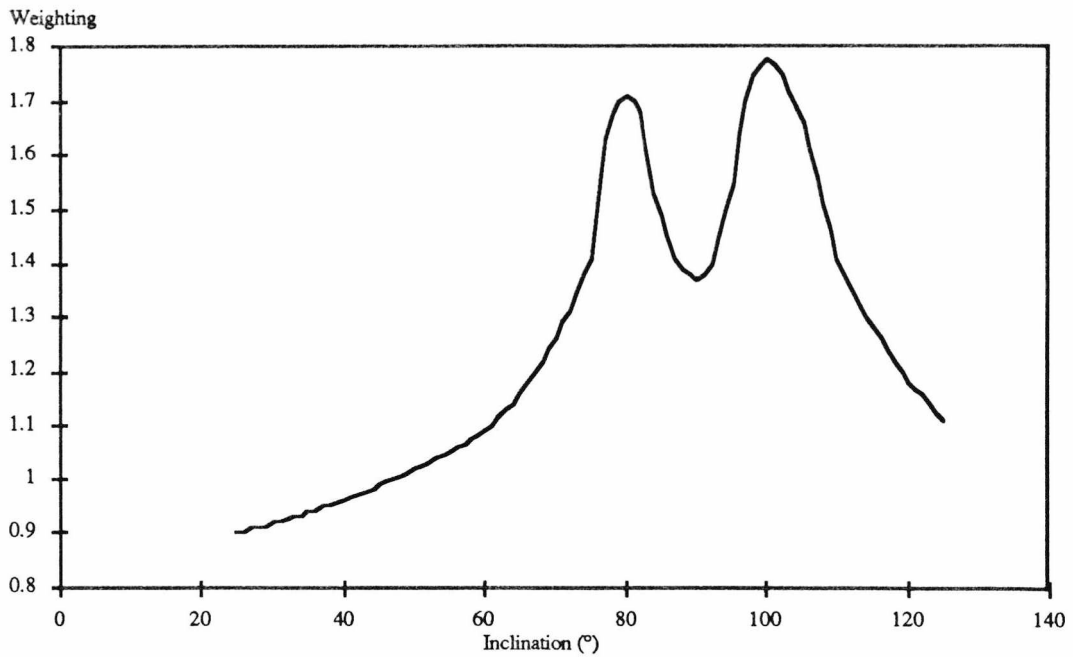


Figure 6.8 Kessler inclination weighting distribution.

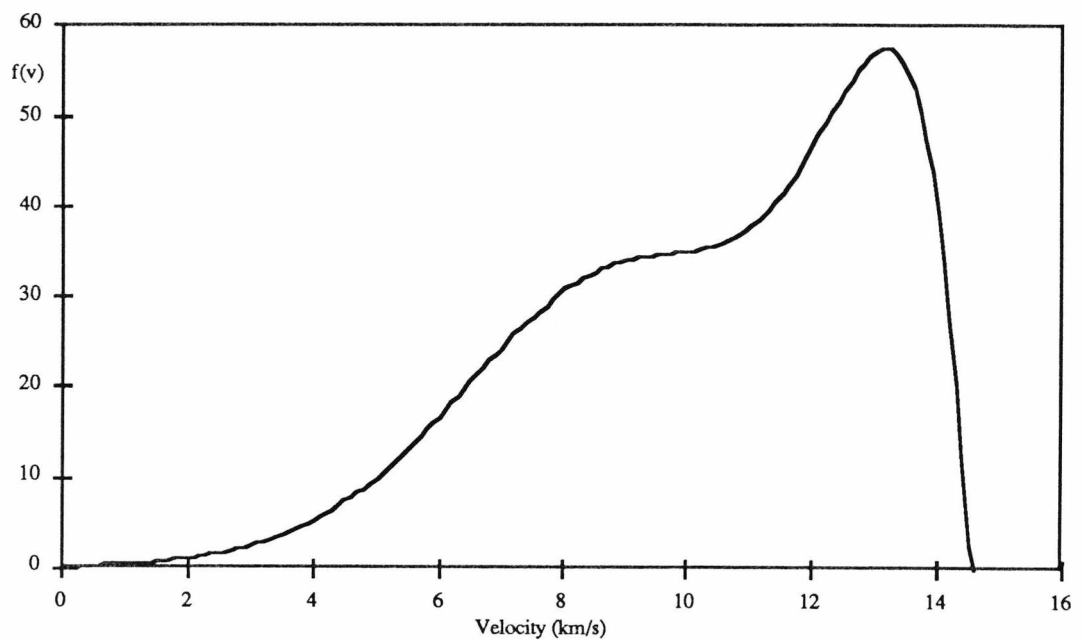


Figure 6.9 Kessler velocity distribution run for a random tumbling plate at 500km altitude, $t=1995$, $S=90Jy$, and $p=0.1$.

The results for a spacecraft flown through the Kessler orbital distribution are given in figure 6.10. It is clear from figure 6.10 that an exclusion zone of some $\pm 30^\circ$ exists.

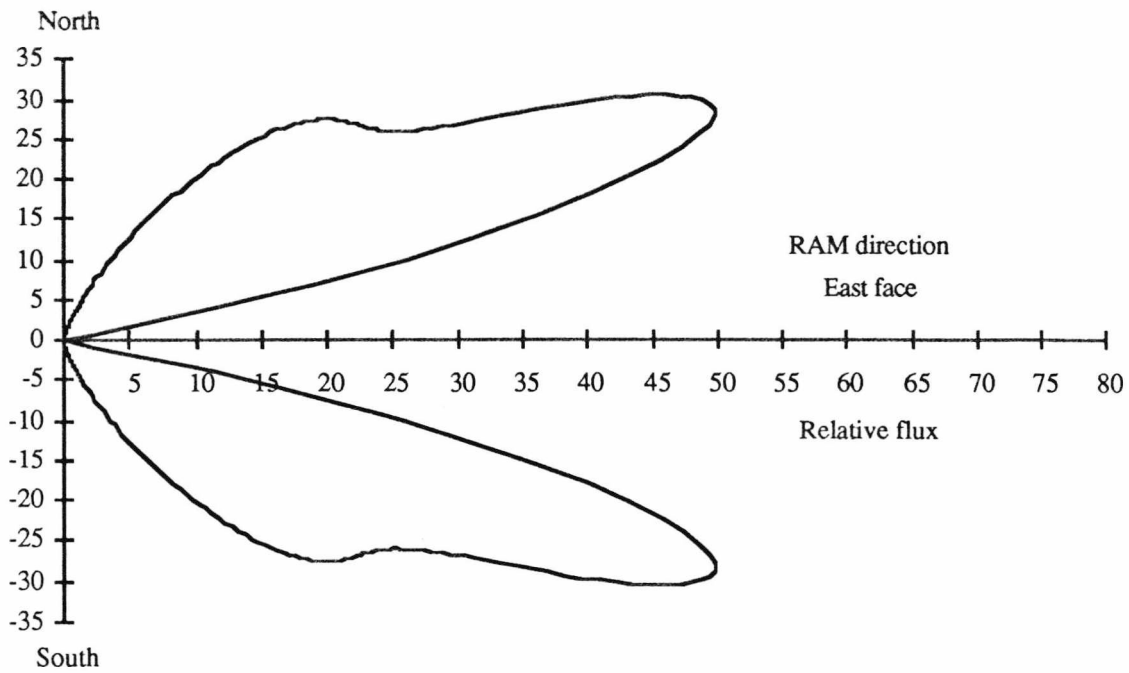


Figure 6.10 Kessler flux distribution for a spacecraft with an altitude of 500km, and inclination of 30°. The relative flux is illustrated as a function of the impact angle, measured from the origin.

This has become synonymous to orbital debris modelling and known as the classical “*butterfly*” distribution and is due entirely to the geometry of impacts from the distinct orbital debris inclinations.

In the Kessler treatment of space debris an average mass density distribution was defined as:

$$\rho = 2.8 \text{ gcm}^{-3} \quad (d \leq 1\text{cm}) \quad (6.23)$$

$$\rho = 2.8 d^{-0.74} \text{ gcm}^{-3} \quad (d > 1\text{cm}). \quad (6.24)$$

The density function was calculated from a best fit to observed break-up data, area to mass calculations from observed atmospheric drag, ground fragmentation tests and intact satellite characteristics for the larger sizes ($d > 1\text{cm}$). For the smaller sizes the mass density of aluminium was taken, as the majority of space debris in this size range consists of aluminium oxide (SRM /ABM burns) and paint flakes.

The Kessler model proved to be more accurate, in predicting impacts from space debris, than the classical 2D model according to Sullivan (1992) {6.7}. The orbital inclination distribution leads to the characteristic “*butterfly*” distribution of space debris; however, the assumption of only circular orbits is rapidly becoming dated. Indeed,

Kessler (1992) in a paper on LDEF analyses {6.35} has indicated that a large portion of debris is in fact in non-circular orbits and as a consequence some objects are being missed by existing tracking systems and this has been discussed in Chapter 5.

Anderson in 1990 {6.36} initiated an update to the Meteoroid and Orbital debris Environment definition for the Space Station Freedom, which was based on the Grün interplanetary flux and the Kessler model described above. The current model is backed up by data from the Arecibo and Goldstone radars for the size range between 0.2 and 2cm, previously extrapolated from impact analyses on spacecraft to USSPACECOM data. The expected debris growth rates are estimated from a decrease in US launches coupled with an increase in world wide launches. These are obviously influenced by both political and economic constraints. Current traffic models suggest a compound growth rate of some 5 to 10%, corresponding to $p=0.05$ and $p=0.1$. The actual rate has always been less than this due to postponed or failed launches. The baseline rate of $p=0.05$ is taken with a "90% confidence level" upper limit of $p=0.1$, a compound 10% per year increase. This would occur if an increase in launch activity is coupled with an increased use of higher long life orbits. It is to be noted, however, that the average percentage change since 1985 of in orbit debris, payloads and launches has been 2.9%, 5.5% and -2.9% respectively (see Chapter 5).

The value of q , expected growth rates for small debris is selected as $q=0.02$ based upon an accidental breakup rate of 1 per year and with no intentional breakups. Unintentional fragmentation events come from either explosion or collisions between objects. The former represents a simple linear source, which is the population growth, and the latter is exponential in nature as fragmentation events are a function of the square of the population. The model has been adapted such that the former process dominates until the year 2011, and thereafter the model assumes the second process becomes significant, increasing the small particles. If these assumptions hold then $q=0.04$ by the beginning of 2011. The fragmentation models used have also been tuned to historical fragmentation events thus increasing the accuracy of the overall model. In 1992 there

were 4 catalogued break-ups, 1 of unknown cause and 3 propulsion related (see Chapter 5).

The model assumes that the distribution with altitude for the small material matches the catalogued distribution. The actual amount by which the fluxes differ could be as high as a factor of 5 down to 0.2 for every 200km away from the 500km altitude that the size measurements were taken from. This uncertainty comes mainly from the uncertainty discussed in Chapter 5 concerning detection of any sized object in eccentric orbits and the lack of calibration spheres in orbit.

Anderson also revised the density profile from equations (6.23 and 6.24) to:

$$\rho = 4.7 \text{ gcm}^{-3} \quad (d \leq 0.62\text{cm}) \quad (6.25)$$

$$\rho = 2.8 d^{-0.74} \text{ gcm}^{-3} \quad (d > 0.62\text{cm}). \quad (6.26)$$

With the emphasis on direct measurements of actual objects in orbit, studies of orbit decay and fragmentation experiments, Kessler's initial model was a good representation for object sizes above 30cm, but represented the mean of a broad distribution; as the density of individual objects can vary widely. In section 6.4 the validity and uncertainties surrounding this density distribution are discussed and compared to other density models given by Anz-Meador et al. (1992) {6.37} and Deshpande et al. (1992) {6.38}.

The Anderson updated orbital debris model is run for the launch and retrieval status of LDEF and shown in figure 6.11. The orbital environment has clearly shifted, mainly due to drastic the increase in solar activity from $90 \times 10^4 \text{Jy}$ to $245 \times 10^4 \text{Jy}$, with the subsequent increase in the orbital decay of the LDEF. During high solar activity more electrons are collected in the Earth's magnetosphere, resulting in an increase in the density of field lines; this effect is monitored by the 10.7cm radio flux measure, *i.e.* is used as an indicator of solar activity. All the other parameters apart from year of determination and orbital altitude are constant. The general shape of this size debris distribution is used later as a input to the Green/Mackay Debris model but modulated by "real" size data from objects in DISCOS {6.5}.

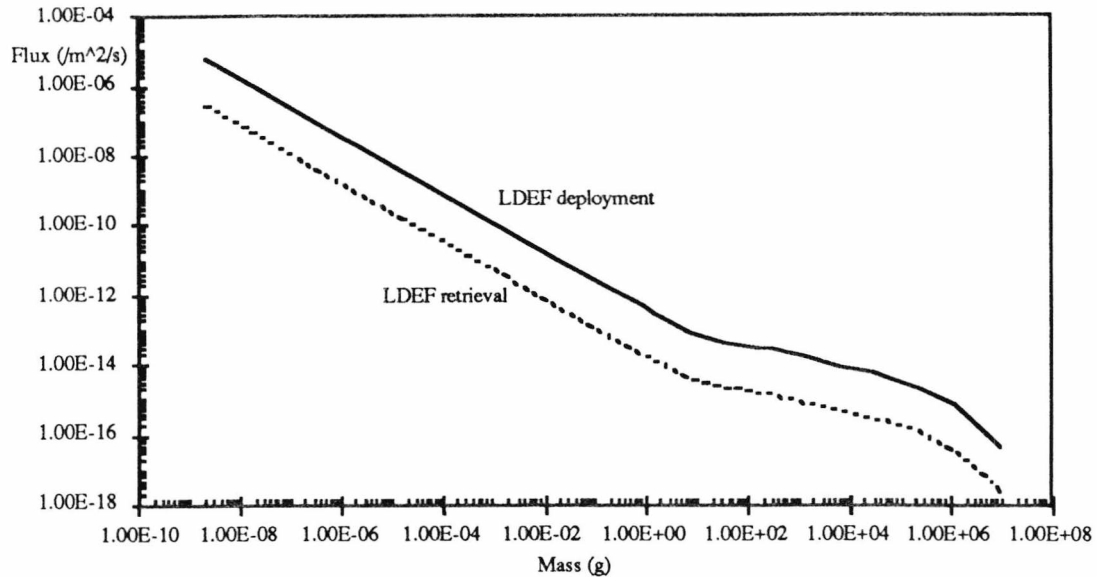


Figure 6.11 Anderson modified Kessler model run for the LDEF deployment status (Yr=1984, Alt=476km, S=90Jy, p=0.05, q=0.02) and for LDEF retrieval status (Yr=1990, Alt=330km, S=245Jy, p=0.05, q=0.02).

6.3.2 The Green/Mackay Model

Within the USS a separate debris model has been developed by Dr. S.F. Green, which describes the space debris environment in terms of spatial density, 3-dimensional velocity vectors and size distribution (Green & McDonnell, 1991) {6.6}.

Geocentric space is defined into altitude (h) and latitude bins (b) as described in figure 6.12 in which a spacecraft is flown given the orbital elements a and i. The spacecraft orbit is limited to a circular one at present.

The model orbit distribution is defined by the distribution of known tracked objects as determined by DISCOS (Chapter 5). The initial model used only orbits from the NASA Satellite Situation Report for 31 December 1988 and binned into 8 perigee altitude bins (q-bins), 12 inclination bins (i-bins) and 4 eccentricity bins (e-bins) with the following assumptions :

- known debris orbits are representative of the total population
- longitudes of the nodes are random
- lines of apsides are random

- orbital distribution is constant with debris sizes.

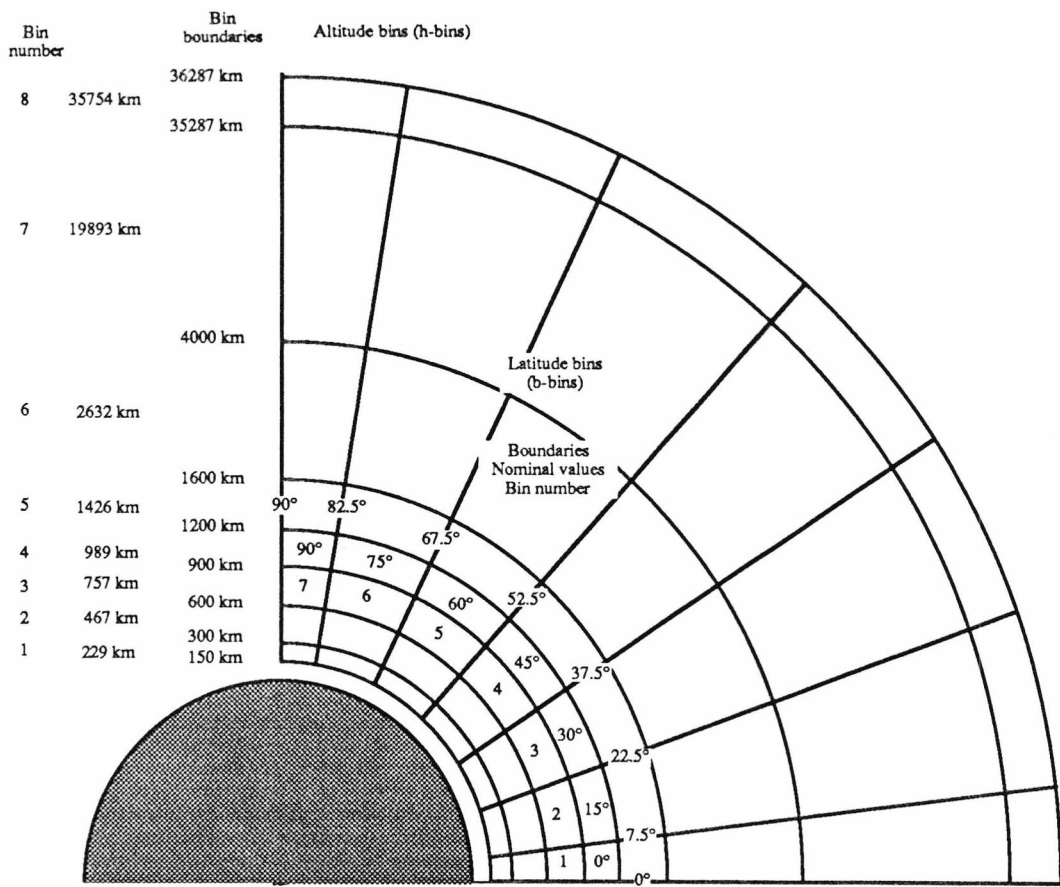


Figure 6.12 Green definition of geocentric space.

It has been shown that for fragmentation events (McKnight & Lorenzen, 1989 {6.39} and Jehn, 1991 {6.40}) that the debris from such events become evenly spread over the orbit and so the line of apsides become random. The distribution of debris follows various phases starting with the initial event with an ellipsoid forming on the orbit, through to a torus of debris about the initial orbital inclination and finally a band of debris with latitude $\pm i$ of initial orbit, over several years (Jehn, 1991) {6.40}. The assumption of random nodes is valid provided the modelled spacecraft is in orbit for a long period with an inclination $\neq 90^\circ$. This arises from the precession of both the spacecraft and the debris orbit randomising the distribution of debris, and producing the band of debris as described by McKnight & Lorenzen (1989) {6.39}. Finally there is assumed no preferential orbit based upon size of particle, although particles with a high ballistic coefficient will tend to circular orbits, and if their starting orbit is eccentric, then

obviously a rapid circularisation and loss of apogee height will incur. This could increase the small particles, with high ballistic coefficients, that have decayed to and remain in circular or near circular orbits.

The spatial distribution of debris is determined in the volume defined by the hb-bins (figure 6.12) rotated by 90°, with symmetrical bins in the southern hemisphere. The spatial density is therefore given by :

$$D_{hb}(d) = N(d) \frac{\sum_{qei\text{-bins}} f_{qei}(d) f_h f_b}{W_{hb}} \quad (6.27)$$

where $N(d)$ is the total population of debris of diameter $\geq d$, f_{qei} is the fraction with orbits in a given qei-bin, f_h and f_b are the fraction of time spent within the h-bin and b-bin limits respectively and W_{hb} is the volume of the hb-bin.

All that is then required to fulfil the input requirements is the desired debris size distribution obtained by normalising the Kessler debris distribution to the size distribution of the tracked objects {6.5} and distributed with the same weightings for objects in the qei bins. Then the syntax of the model follows :

- For each location of the spacecraft (hb-bins around the orbit) and for each debris q-bin (1-8), e-bin(1-4) and i-bin(1-12)
- determine if and at what velocity, the debris will pass through the hb-bin occupied by the spacecraft.

Then for each debris size

- determine the density of debris in the hb-bin and thus
- determine the impact speed and direction
- determine the contribution to the flux impacting the spacecraft.

The Green model was run for the nominal LDEF orbit of altitude 458km, $i=28.5^\circ$ and $e=0$ and the results are shown in figures 6.13 to 6.15 for all debris orbits.

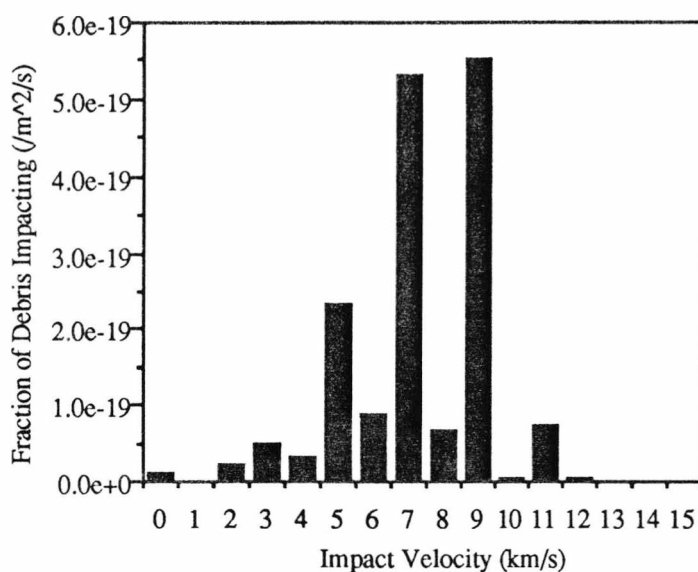


Figure 6.13 Impact velocity distribution, from Green model, on a spacecraft with an altitude 467km, $i=28^\circ$ and $e=0$, for all debris.

The velocity distribution is similar to that of Kessler for the 2D model and a classical butterfly distribution is apparent from figure 6.14 peaking at around $\pm 60^\circ$.

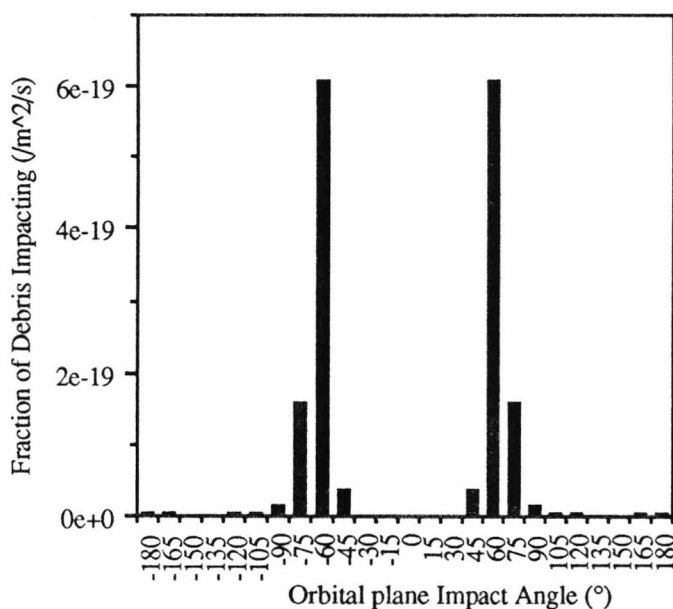


Figure 6.14 Impact angle in the orbital plane, using Green model, on a spacecraft with an altitude=467km, $i=28^\circ$, and $e=0$, for all debris.

It is also clear that a small fraction of debris impacts at $\pm 180^\circ$ from the ram direction (0°) and at $\pm 5^\circ$ elevation angle.

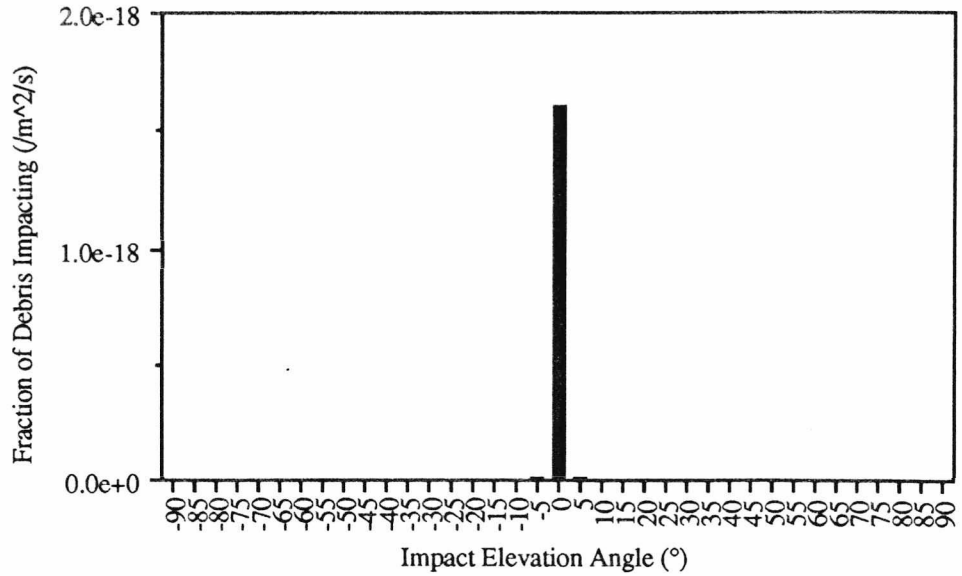


Figure 6.15 Impact elevation angle, using Green model, on a spacecraft with an altitude=467km, $i=28^\circ$, and $e=0$, for all debris.

A study by the Deshpande and Green, based upon this model, has been published showing the effect of debris in GTO type orbits ($e>0.65$) on a spacecraft in LEO. The results show that debris impacts from these orbits can occur from 60° to 180° around the spacecraft ram direction and up to 35° in elevation angle (Deshpande & Green, 1992) {6.41}. Figures 6.16 through to 6.18 illustrate these results.

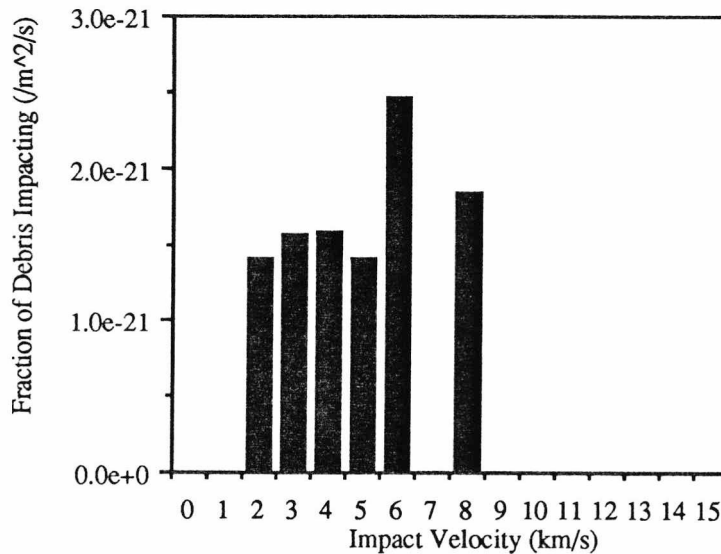


Figure 6.16 Impact velocity, using Green model, on a spacecraft with an altitude of 467km, $i=28^\circ$, $e=0$ from only GTO debris ($e>0.65$).

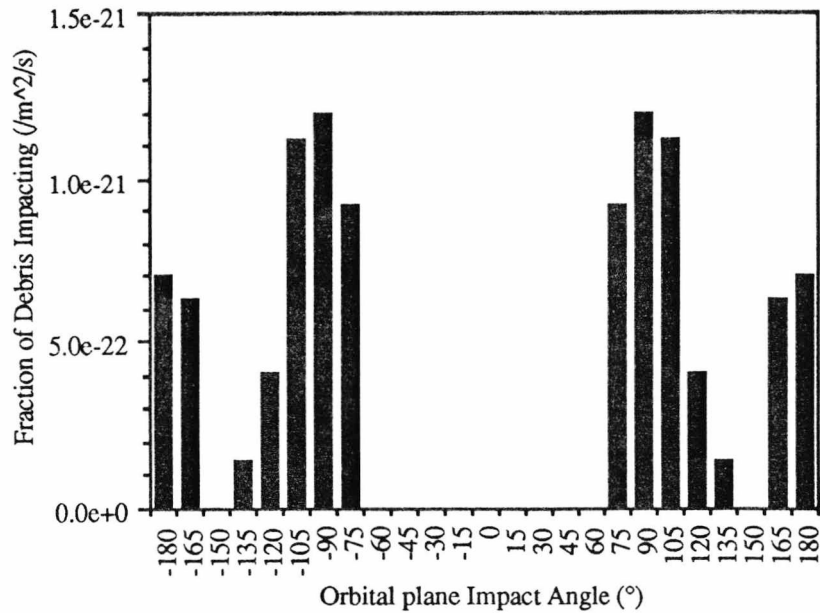


Figure 6.17 Impact angle in the orbital plane, using Green model, on a spacecraft with an altitude=467km, $i=28^\circ$ and $e=0$ from only GTO debris ($e>0.65$).

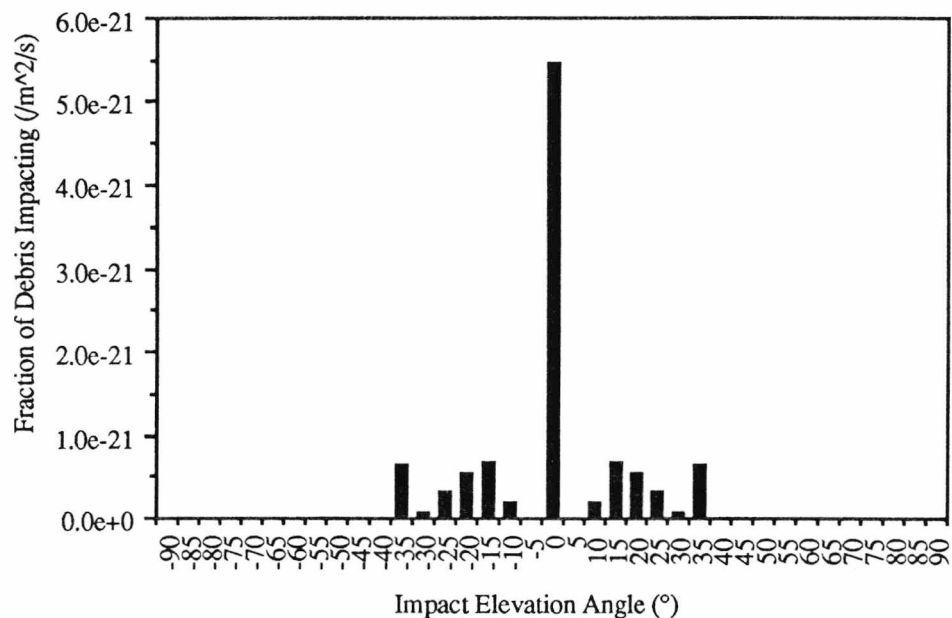


Figure 6.18 Impact elevation angle, using Green model, on a spacecraft with an altitude=467km, $i=28^\circ$, and $e=0$, from only GTO debris ($e>0.65$).

Although in terms of total debris the fraction impacting at 180° is of the order of 1% it may in terms of penetration, of a given foil thickness, be far more important due to the higher encounter velocity (figure 6.16), provided that the results are not completely dominated by the interplanetary dust impacts.

From this study it was clear that impacts from space debris were possible on both the Space and West faces of LDEF and so a better description of the debris distribution was required.

Mackay and Deshpande {6.5} utilised the Green model {6.6} by inputting the author's orbit distribution as described in Chapter 5, as individual qei-bins, thus dispensing with the need for large bin quantisation for the debris orbits. The spacecraft, nominally defined as a sphere was re-defined as the LDEF incorporating the 14 faces and as such velocity, direction and flux measurements for each face were derived. The model run the spacecraft through the hb-bins with an altitude range of $\pm 100\text{km}$, as the larger objects orbit obviously did not intersect that of LDEF, with the resultant collision. The size distribution is given by figure 6.19 and is calculated, as above, by normalising the Kessler debris distribution for 1990 with the size distribution as given in figure 6.20, from DISCOS data.

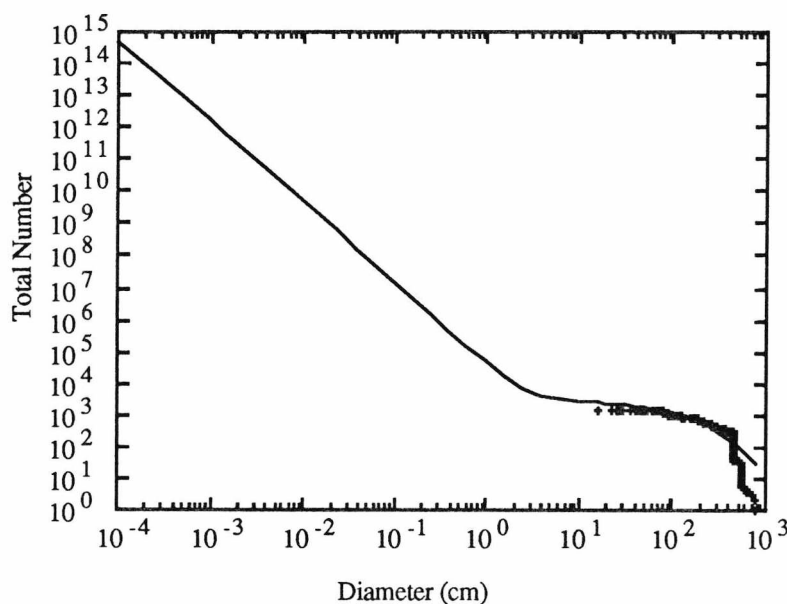


Figure 6.19 Size distribution, showing the DISCOS data which modulates the Kessler size function.

The DISCOS data contained size, shape and weight information (see section 6.4). This was reduced to a mean size and a cumulative plot obtained, which was fitted using a least squares fit to obtain the curve in figure 6.20.

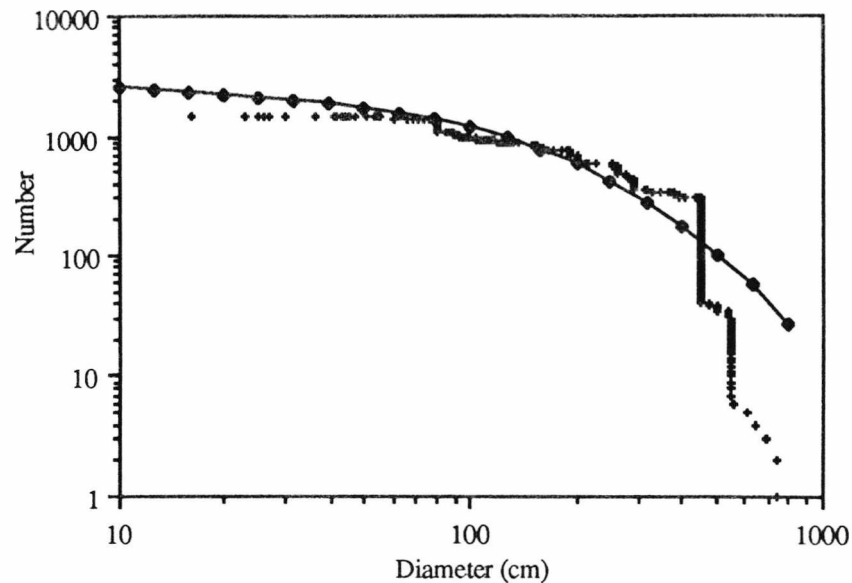


Figure 6.20 Best fit through data retrieved from DISCOS, used to modulate the Kessler size distribution.

The results of this debris model were incorporated into a 3-D numerical model for space debris and interplanetary dust that is used to calculate incident flux data on the LDEF (Green, Deshpande & Mackay, 1992) {6.5}. A summary of this combined model is presented in section 6.6 and the results are discussed in Chapter 7 to explain the LDEF flux measurements.

6.4 Analysis Of Debris Densities

6.4.1 Choice Of Debris Density

The material density used in spacecraft design depends upon the structure and use. The most common metals used in spacecraft structure are aluminium, steel and aluminium/aerolam board honeycomb. The densities therefore range from 8.9gcm^{-3} , for steel, through 2.7gcm^{-3} for aluminium down to 0.151gcm^{-3} for the least dense honeycomb structure. This is a large density range and covers all the materials currently

used in spacecraft design. It is therefore clear that selecting an average density can be spacecraft dependant.

In the debris models derived by Kessler (1989) {6.4} and Anderson (1990) {6.36} the density is related to the particle size (d) with a constant value for the smaller sizes (equations 6.23-6.26). Debris density measurements for the smaller sizes are extremely scant and so vary widely. To illustrate this problem, consider the following materials density profile (Table 6.4) based on a summary review of the STS materials usage (neglecting tiles) (Anderson, 1992) {6.36}:

Estimated volume fraction	Mass density (gcm^{-3})	Representative materials
0.65	2.8	Aluminium, glass
0.15	1.8	Epoxy-glass, rubber
0.05	4.5	Titanium
0.15	7.8 to 8.9	Copper, steel

Table 6.4 STS material break down.

This gives a mean density ranging from 3.48gcm^{-3} to 3.65gcm^{-3} .

This may, however, not be typical of spacecraft for several reasons. Firstly, many objects involved in fragmentation events are believed to have had a higher fraction of dense materials used in their construction (*e.g.* the Delta second stages contain about 70% steel, 20% aluminium and 10% titanium). Second, low density objects are more affected by atmospheric drag (see Chapter 5) and thus decay more rapidly. Fragment shape is also a main factor in determining density. The Delta rocket walls are of thickness 0.2 and 0.5cm and so fragments larger than this would be irregular in size with an effective density less than that of steel (Anderson, 1990) {6.36}.

Anderson (1990) revised the Kessler density distribution based on the Delta rocket recommending a "heavy" distribution given by 10% (by volume) at 1.8gcm^{-3} , 50% at 2.8gcm^{-3} , 10% at 4.5gcm^{-3} and 30% at 8.9gcm^{-3} . This then gives the mean

density of 4.7gcm^{-3} as stated in equation (6.25). Although it is to be noted that at the millimetre dimension and smaller the density tends to the material density for any debris.

6.4.2 *Spacecraft And Modelled Debris Densities*

A density distribution that differs from Kessler has been published by Deshpande et al. (1992) based solely on spacecraft data extracted from DISCOS {6.38}. The spacecraft data on size, weight and shape were extracted from DISCOS and reduced from the original 1904 objects to 1852 objects with shapes that could be easily transformed to two parameters, namely length (l) and diameter (d).

Operational requirements and launcher capabilities limit the size and mass of spacecraft and as such they fall into two main design categories: a central cylinder shape with wings mainly used to house solar arrays, and spheres or cylinders with l/d of the order of 0.5. Hence the reduction to l and d parameters, which excluded such objects with large wings, windmills, and spans whose dimensions and orientation were not known.

The mean cross sectional area (S) was calculated based upon the parameters, l and d , and using the assumptions derived by King-Hele (1987) {6.42}. The mean cross-sectional area for a tumbling cylinder will always lie between two extreme values:

- for rotation like an aeroplane propeller (perpendicular to the viewing/velocity direction) S is given by:

$$S = ld \quad (6.28)$$

- when tumbling end over end, S is given by:

$$S = (2/\pi) (ld + 0.25\pi d^2) \quad (6.29)$$

For all other possible directions of spin axis, the average area is given by:

$$S = ld (0.818 + 0.25 d/l) \quad \text{for } l/d > 0.5 \quad (6.30)$$

$$S = 0.5 (0.25\pi d^2 + ld) \quad \text{for } l/d < 0.5 \quad (6.31)$$

otherwise

$$S = 0.25\pi d^2 \quad (6.32)$$

An effective diameter (d_{eff}) based on a sphere of equivalent cross sectional area was then derived for each of the 1852 objects. Figure 6.21 illustrates the mean densities of spacecraft derived using the masses and volumes obtained from DISCOS plotted as a function of d_{eff} .

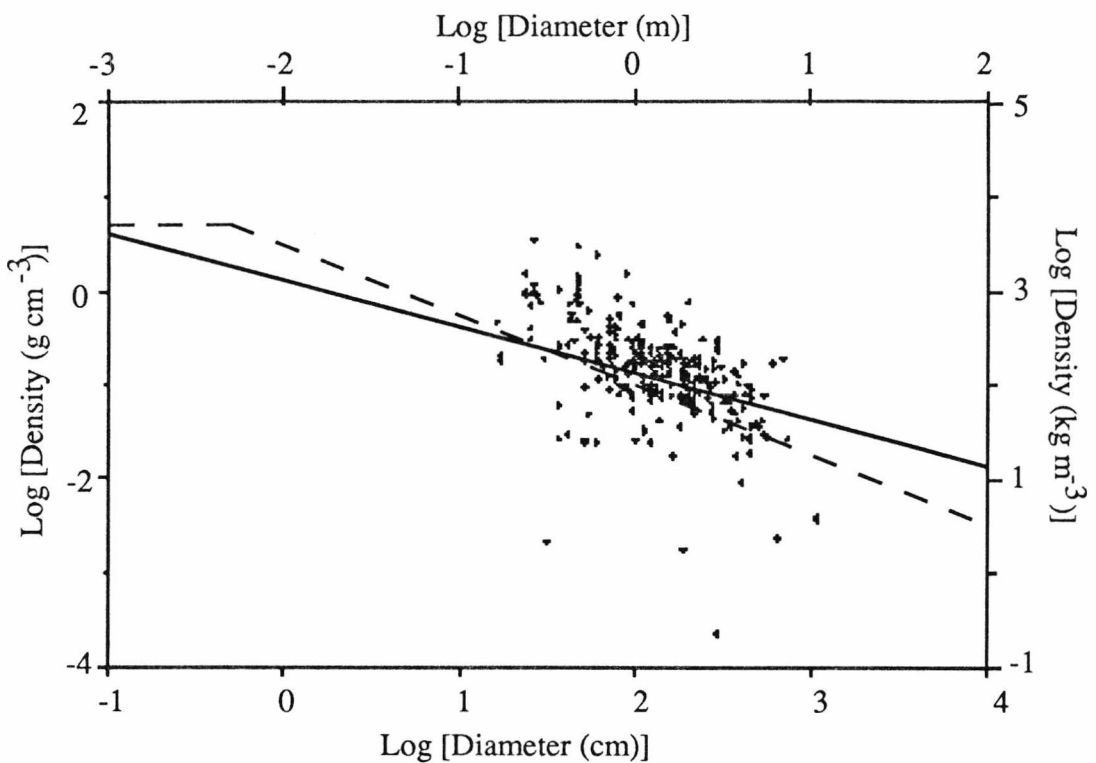


Figure 6.21 Calculated mean densities for spacecraft from DISCOS data. The dashed line is the density function from Anderson, and the solid line is the best fit through the data.

The best-fit power law, equation (6.33), differs somewhat from that of Kessler and Anderson (equations (6.23-6.26)) although there is an extremely large scatter in the data due to operational design requirements on spacecraft ($1\sigma =$ a factor of 2.6).

$$\rho = 1.29 d^{-0.49} \quad (6.33)$$

where ρ is expressed in gcm^{-3} and d in cm.

The expected mean densities of debris may be estimated from their likely range of shapes and sizes, examples of which are given in Table 6.5. This table illustrates the types of objects that are likely to be in orbit, based upon shapes of spacecraft and spacecraft components. Satellites constitute the greatest number of spacecraft in orbit as opposed to STS, Mir space station, and these have distinct shapes, spheres, cylinders of various sizes, due to launcher constraints. Other objects such as fragmentation debris is represented as plates of various thicknesses and dimensions. Table 6.5 gives some idea of the range of material density and shapes/sizes that are physically probable and comments to accompany the choices.

Shape	Material (gcm-3)	Size	Orientation	Comments
Hollow spheres. 6mm walls	$\rho \sim 4.7$ $\rho = 1.5 - 9.0$	$d = 0.01$ to 2m $d < 0.01$ m		Satellites and components Small, solid fragments
Cylinder $l/d = 5$ 6mm walls	$\rho \sim 4.7$ $\rho = 1.5 - 9.0$	$l = 25$ m, $d = 5$ m to $l = 0.06$ m, $d = 0.012$ m	 	Cylindrical satellites and large components.
Cylinder $l/d = 0.5$ 6mm walls	$\rho \sim 4.7$ $\rho = 1.5 - 9.0$	$l = 1$ m, $d = 2$ m to $l = 10$ mm, $d = 20$ mm	 	Booms, struts and rods. Small fragments/fibres
Plates: 6mm thick $t = 1$ mm $t = 0.1$ mm	$\rho = 0.15 - 9.0$ $\rho = 1.5 - 9.0$ $\rho \sim 4.0$	$d \sim 1$ to 0.01 m $d \sim 2$ mm to 1.1m $d \sim 0.2$ to 10mm	 	Satellite panels. Small panels Paint flakes.

Table 6.5 Representative space debris shapes and densities

Figure 6.22 illustrates the size dependent mean densities derived for hollow spheres and cylinders to represent the large fragments or whole spacecraft compared with

the densities of spacecraft materials and data for true spacecraft. A typical wall thickness for spacecraft of 6mm was used and a material density of 4.7gcm^{-3} . The shaded area for hollow cylinders indicates the uncertainty in the derived effective diameter due to the range of possible orientations for the hollow cylinder $l/d=5$ (the range of values for the cylinder $l/d=0.5$ lie within this limits). The smallest debris objects are likely to consist of single materials and therefore have a range of density from $\sim 1.5\text{gcm}^{-3}$ to 8.9gcm^{-3} whereas the density of the larger debris fragments are dominated by structure (*i.e.* amount of enclosed space, rather than the material density). A range of single densities are also plotted in figure 6.22 for comparison.

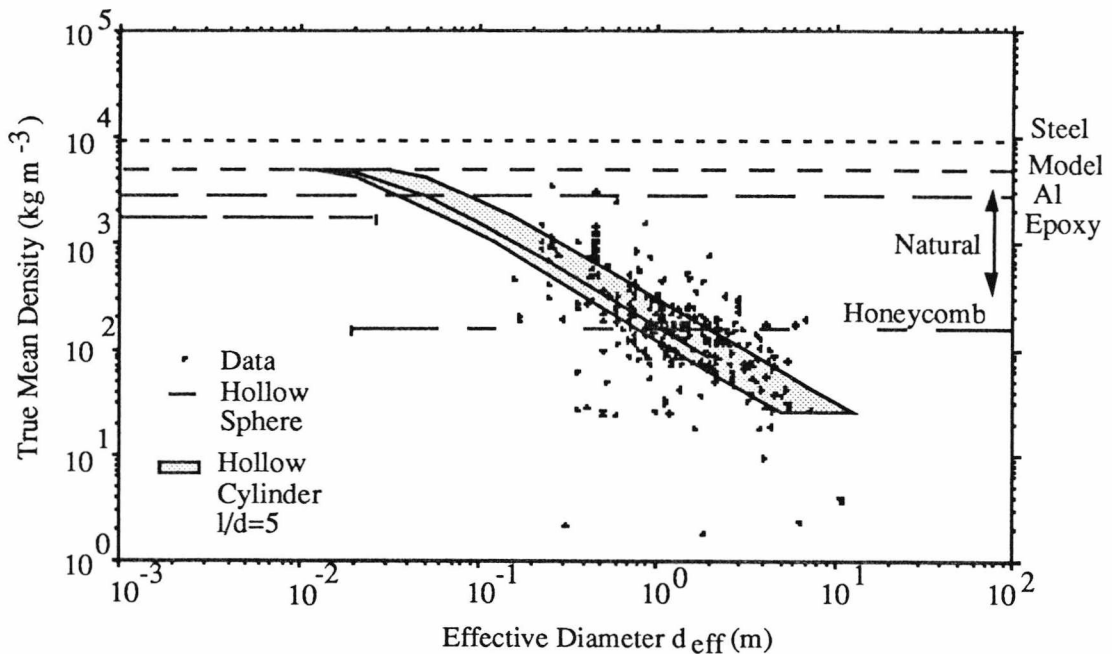


Figure 6.22 Mean densities of spacecraft with assumed wall thickness of 6mm, materials and DISCOS data.

6.4.3 Comparison Of Apparent Debris Densities

It has been shown that the density/size function for Kessler (1989) {6.4} /Anderson (1990) {6.36} varies from that of Deshpande et al. (1992) {6.38} and this variation is solely due to the sources of and type of data used.

Kessler and Anderson both used a wide selection of data sources from break-up data, atmospheric drag calculations to derive spacecraft ballistic coefficients, and

fragmentation tests. The Deshpande model is based on actual spacecraft data with no break-up data involved. Anz-Meador (1992) {6.37} has carried out an analysis of apparent densities for objects in orbit based upon orbital data from USSPACECOM.

Anz-Meador calculates the ballistic coefficient of an object from the change in perigee/apogee over a series of orbits. This is achieved by utilising the Müller atmospheric model for orbit decay modelling and a knowledge of the RCS (Radar Cross Section) data, also supplied by USSPACECOM. The result is a density/size distribution solely based upon RCS data and the orbit decay of the object (mass is derived from the calculated ballistic coefficient and the known RCS).

The so-called apparent density, based upon homogeneity of the constituent material and no knowledge of internal construction, has been plotted in two regimes. One for operational debris and the other for fragmentation debris, although it is not clear on how this division is made. The so-called mass density based upon simple object geometry, spheres and plates with a material thickness, was also plotted. However the author cited that this leads to a large number of spherical debris of the order of a metre in diameter, which is not understandable. The paper studied, however, contains an error in the calculation for the spherical case based on shells of wall thickness 5mm. The error centres around the omission of a wall thickness measurement when calculating the effective diameter of the sphere. This leads to a reduction in the density by a factor of 2, assuming that the stated equations were derived from the plotted data. It is therefore not possible to readily compare those results to the results in section 6.4.2 as there is no way of confirming the equations fit the data plotted without the original data.

The apparent density distribution appears to be in general agreement with the standard model (Kessler/Anderson) and a plot of 747 spacecraft and rocket boosters using the same analysis gives a best fit of:

$$\rho = 2.88 d^{-0.73} \quad (6.34)$$

where ρ is in gcm^{-3} and d in cm. (All the equations from Anz-Meador cited here have been converted to consistent units *i.e.* (ρ) in gcm^{-3} with (d) in cm as opposed to (ρ) in gcm^{-3} and (d) in m, as in the paper studied).

This compares well with equation (6.24) where $\rho = 2.8 d^{-0.74}$ with a somewhat flatter curve. The fragmentation and operational debris have best fits given by :

$$\rho = 0.311 d^{-0.69} \quad (6.35)$$

and $\rho = 0.635 d^{-0.57}$. (6.36)

These results differ greatly from equation (6.33) thus indicating that the density of debris objects varies quite drastically dependent upon size and origin based on this type of study.

Anz-Meador concludes that there is a difference between the density of operational and fragmentation debris but in general the mass density approaches that of aluminium or less {6.37}. The assumption of simple geometries indicates that the plate model is more physically probable, at least for objects greater than about 1m characteristic size, although with the error in the spherical case it is difficult to quantify this.

The differences in results are clearly seen in figure 6.23 which illustrates the DISCOS data set and the results for fragmentation and operational debris scenarios given by Anz-Meador.

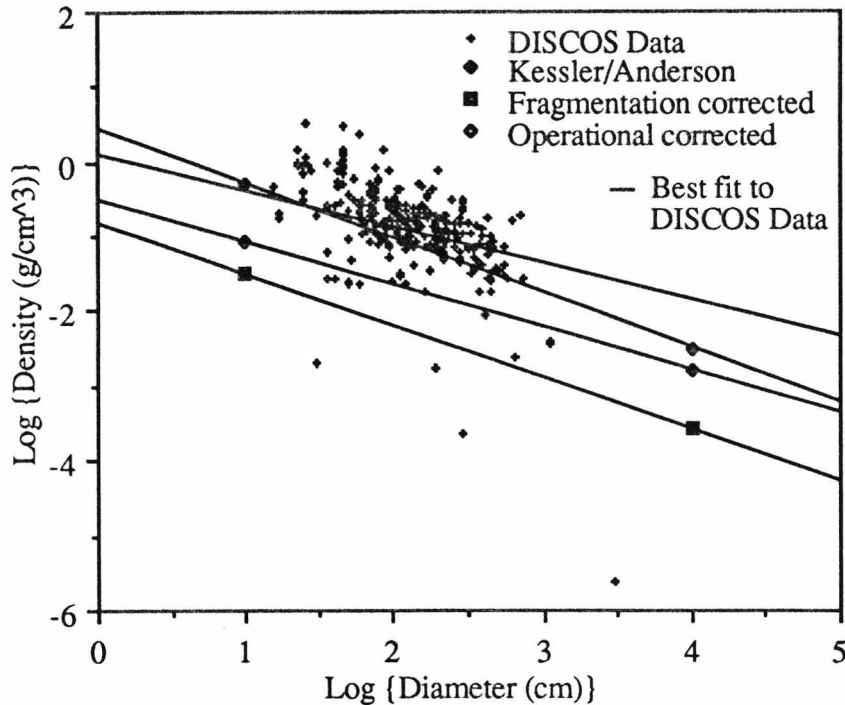


Figure 6.23 Comparison of density functions. Anz-Meador functions are corrected fragmentation and operational debris, compared with the Kessler/Anderson function and DISCOS data.

6.4.4 Uncertainties In Deriving Debris Densities

With differing approaches implying differing results for debris density there are obvious uncertainties, and caution needed, when employing such density/size distribution for data modelling. When observing debris from the ground in a “*snap shot*” fashion be it with radar or optical systems there is a large uncertainty in the object's true size and shape. For radar detection there are problems in calibrating RCS data to true cross sections when the shape, size and surface properties are unknown (Deshpande et al., 1992) {6.38}. Comparisons of theoretical relationships with observed RCS/true area ratios (Potter et al., 1989) {6.43} for spherical and polygonal spacecraft result in uncertainties of more than a factor of 5 for objects with $d/\lambda \sim 1$ (d is the debris diameter and λ the radar wavelength). Uncertainties also exist for the small debris ($RCS \sim (d/\lambda)^4$) due to Rayleigh scattering and when the debris is large the RCS value oscillates about the true value. Errors in the

catalogued RCS data can be very large due to measurement sensitivity or irregularly shaped objects, with standard deviations of 100% of the RCS value across the entire size spectrum (Johnson & McKnight, 1987) {6.44}, which results in 50% errors in diameter.

The derivation of size from optical detection can potentially introduce much larger errors, since the observed intensity is a function of cross sectional area, albedo and the scattering phase function. Many spacecraft have large specularly reflecting surfaces and as such the phase angle may be extremely irregular. Such an object may appear extremely bright at certain orientations when sunlight (or Earthshine) is reflected towards the observer, with a consequent over-estimate of the size for a given mean albedo. The resulting diameter may be in error of some 50% when the albedo and phase function are taken into account (Deshpande et al. 1992) {6.38}.

Observational uncertainties therefore play a major role, with errors in derived size due to albedo or RCS calibration typically of the order of a factor of two and in extreme cases greater than 5. With these uncertainties in size a conversion to mass introduces the additional uncertainty in the adopted density.

Uncertainties in the debris shape can cause the largest errors in derived size. With a “*snap shot*” observation shape and orientation are unknown. The mean cross-section may be derived from observations over a whole rotation but the shape will be indeterminate. In this case the mass can only be derived assuming a spherical shape and hence large errors can occur. If, however, time resolved observations are made {6.45}, an estimate of the shape of the body is possible and the true volume may be estimated, from which a more accurate mass may be derived. An indication of the effect of shape factors may be obtained from the idealised objects in Table 6.5

Study has shown that for the cylinder with $l/d=5$ the smallest and largest derived effective diameters for the extreme orientations would be $0.6d_{\text{eff}}$ and $1.1d_{\text{eff}}$ respectively. The corresponding values for a cylinder with $l/d=0.5$ are $1.1d_{\text{eff}}$ and $0.9d_{\text{eff}}$. For a flat plate with $d/t=100$ (very large values are unlikely due to the limits of surfaces present on spacecraft or lack of physical strength) the derived values could range from $0.15d_{\text{eff}}$ to $1.4d_{\text{eff}}$ {6.38}.

For an object of known size, the mean density derived in similar fashion described earlier, will have a factor ~ 3 uncertainty, for objects of sizes larger than a few cm, and a factor of ~ 2 for the smallest objects which are likely to consist of only one material.

For individual roughly spherical objects, sizes and masses derived from observations will have uncertainties of at least a factor of 2 and 4 respectively. For those of unknown shape these uncertainties could be larger than a factor of 10.

Therefore space debris density functions are predominantly a statistical value, highly dependent upon observational data. The material density of space debris is still of importance in characterising the debris population as a whole and indeed is needed when considering the penetration and cratering effects of particles on spacecraft surfaces. The extend of cratering and penetration of surfaces is highly dependant upon particle density as has been seen in Chapter 3. Any information on space debris density is of value when no chemical residue is present to ascertain the impactor origin, and only crater morphology is available.

6.5 Sullivan Model Extended

6.5.1 Introduction

The Sullivan 3D model has been extensively discussed in Sullivan (1992) {6.7} and as such only the basic principles will be re-iterated here followed by the extension and comparison to these results in section 6.5.2.

Sullivan in his model describes an isotropic, single velocity particle cloud that impacts at first a stationary LDEF. The geometry of the LDEF and the Earth shielding then limit the isotropic distribution such that no particles can emanate from the Earth. The Earth shielding factor, as established by Sullivan, is the ratio of the flux as received upon a detector, when the detector is shielded by the Earth, to that of the flux incident upon a flat plate which suffers from no shielding and is given by:

$$ESF_n = \frac{F_n(0)}{F_{2\pi}(0)} \tag{6.37}$$

when the detector is stationary relative to the isotropic particulate cloud. $F_n(0)$ is the flux impacting the given face (n) and $F_{2\pi}(0)$ is the unshielded 2π steradian, viewing angle, both when stationary.

This implies that :

$$ESF_{Space} = 1 \tag{6.38}$$

$$ESF_{Earth} = \cos^2 \Omega \tag{= 0.078} \tag{6.39}$$

$$ESF_{Peripheral} = \frac{(\pi - \Omega) + 0.5 \sin(2\Omega)}{\pi} \tag{= 0.676} \tag{6.40}$$

where Ω is the Earth shielding half angle subtended at the spacecraft and is given by :

$$\sin \Omega = \frac{(R_E + h_a)}{(R_E + H)} \tag{6.41}$$

The values in brackets are calculated using R_E as the Earth radius (6378km), H the orbital altitude and h_a the effective atmospheric height at which rapid particle de-orbiting occurs (185km) (Ratcliff & McDonnell, 1991) {6.46}.

The LDEF is then flown through this distribution and percentage flux rates at a constant mass, are recorded using the velocity addition of vectors to describe which face will be struck and the appropriate perpendicular impact velocity and K Factor. The K Factor is the ratio of the flux impacting a given face when stationary to that when moving as described by:

$$K_n = \frac{F_n(V_{se})}{F_n(0)} \tag{6.42}$$

where $F_n(V_{se})$ is the shielded flux impacting a face moving with velocity V_{se} and $F_n(0)$ the shielded flux when stationary. Combining equations (6.37) and (6.42) then leads to the result:

$$F_{2\pi}(0) = \frac{F_n(V_{se})}{K_n \text{ESF}_n} \quad (6.43)$$

Equation (6.43) is then the general result relating the shielded, moving flux for a given face $F_n(V_{se})$, to the unshielded, 2π steradian viewing angle, stationary flat plate flux, $F_{2\pi}(0)$, by a division of that face's ESF and K Factor.

The model therefore calculates the percentage arrival flux (at constant mass), the average perpendicular impact velocity, average impact velocity and K Factors for each face. The program was written in Fortran and was called 3DFLUX.FOR. The results are illustrated in Table 6.6 for a geocentric particle velocity of 10kms-1.

NATURAL
 Altitude: 458 km
 Geocentric Particle Velocity: 10.000 km/s
 Angular Offset in Degrees: 0.000

Row	K Factors	Perp Vel	Impact Vel	% Arrival Fluxes
9	2.965	12.114	14.877	17.759
8	2.639	11.434	14.670	15.826
7	1.850	9.555	13.854	11.113
6	1.000	6.955	12.093	6.010
5	0.404	4.323	9.286	2.429
4	0.132	2.375	5.886	0.789
3	0.068	1.653	3.917	0.405
2	0.132	2.375	5.882	0.788
1	0.404	4.322	9.282	2.421
12	1.000	6.950	12.093	5.992
11	1.851	9.550	13.856	11.091
10	2.640	11.431	14.672	15.810
13 (Space)	1.000	6.668	12.135	8.873
14 (Earth)	1.000	1.870	11.605	0.696

Table 6.6 Output of 3DFLUX.FOR with 0° offset.

The method of transformation from West face foil thickness data to Space face data was devised by Sullivan (1992) {6.7}, is illustrated in figure 6.24.

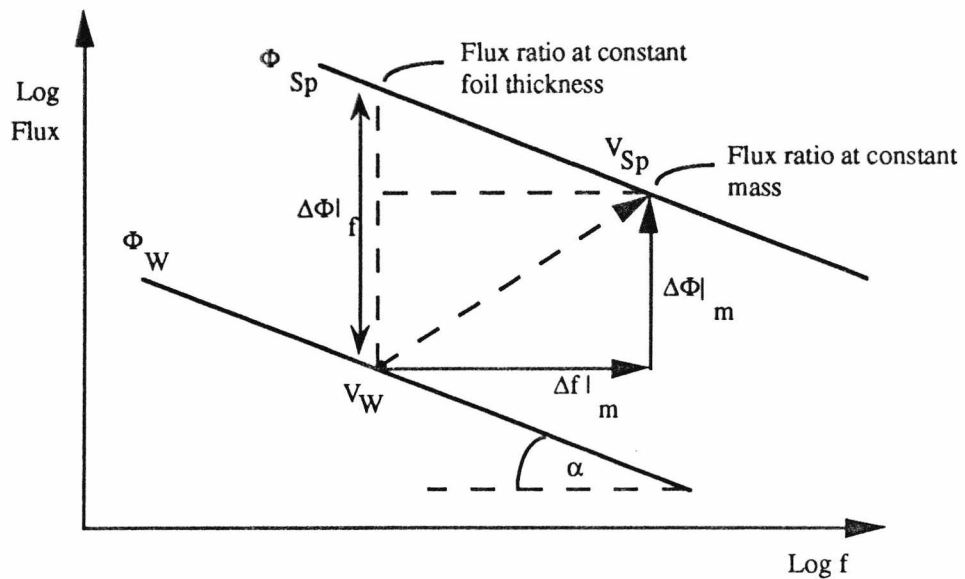


Figure 6.24 Transformation for LDEF West flux to Space flux.

This was based upon the general relationship :

$$\frac{f}{d} \propto d^S V^\beta \quad (6.44)$$

where S is the particle dimension scaling factor and β the velocity exponent. Given that the characteristic velocities for the West and Space face are V_w and V_{Sp} respectively the relative increase in foil thickness of the West face to that of the Space face, at constant mass, is then given by equating masses in equation (6.44) leading to equation (6.45) :

$$\Delta f|_m = \left(\frac{V_{Sp}}{V_w} \right)^\beta \quad (6.45)$$

This change in foil thickness is termed the mass sensitivity, implying an increase in foil thickness of the West face necessary to detect a particle of the same mass as that on the Space face.

The vertical mapping $\Delta\Phi|_m$, illustrated in figure 6.24, corresponds to the detection geometry effect due to the sweeping up effect of the spacecraft through the initially isotropic particle cloud and is given by:

$$\Delta\Phi|_m = \frac{K_{Sp} ESF_{Sp}}{K_W ESF_W} \quad (6.46)$$

Where K_{Sp} and K_W are the respective K Factors for the Space and West face and similarly ESF_{Sp} and ESF_W the Earth shielding factors. Figure 6.24 also illustrates that the flux ratio at constant foil thickness, or constant crater size, can be calculated by incorporating both these mapping (equation (6.45) and (6.46)), coupled with the slope of the distribution. If the slope of the mass flux plot is given as α , then the flux ratio at constant foil thickness can be expressed as :

$$\Delta\Phi|_f = \left(\frac{K_{Sp} ESF_{Sp}}{K_W ESF_W}\right) \left(\frac{V_{Sp}}{V_W}\right)^{\left(\frac{3\alpha\beta}{1+\alpha}\right)} \quad (6.47)$$

It is clear that both the K Factors and impact velocity are functions of the geocentric particle velocity, of the isotropic particle cloud, and hence the transformation between the West and Space face is also dependant on geocentric particle velocity. It is therefore possible to calculate the geocentric particle velocity that superimposes the West to Space transformation. This is given by equation (6.48) assuming a constant particle density, a constant mass (*i.e.* $m_{Sp}=m_W$) and that $\Phi_W = A (f_W)^\beta$, (*i.e.* the measured foil thickness flux distribution for the West face is linear on the log-log plot)

$$\frac{V_W}{V_{Sp}} = \left(\frac{1}{f_{Sp}}\right)^{\left(\frac{1}{\beta}\right)} \left(\frac{\Phi_{Sp} K_{Sp} ESF_{Sp}}{A K_W ESF_W}\right)^{\left(\frac{1}{\beta}\right)} \quad (6.48)$$

Chapter 7 will utilise these general equations in describing the perceived interplanetary particle environment, as measured on the LDEF based on the West face being solely interplanetary impacts and secondly adopting a fraction attributed to space debris impacts. The relevant geocentric particle velocity for this isotropic cloud is obtained for the two cases and discussed.

6.5.2 General Results For An 8° Offset LDEF

The results given by Sullivan 1992 are based upon the LDEF being in the correct gravity gradient stabilised orbit; however, in section 2.6.2 it was stated that the LDEF had been deployed with an average offset of some 8° and a tilt of some 1.1°, both towards row 9. The implications of this are that the West face can now be exposed to more space debris than first envisaged, although the amount of debris may be small in terms of penetration, the initial assumptions for decoding LDEF fluxes have been revised. The West face has a debris component due to two factors ; 1) the offset, and 2) the assumed greater numbers of eccentric debris orbits, as discussed in Chapter 5, and published by Kessler (1992) {6.35} based upon the analysis of residue chemistry published by Bernhard et al. (1992) {6.47}.

The Sullivan model has been extended and run to include the offset of 8°. The program has been called EX3DFLUX.FOR and the results for a geocentric particle velocity of 10kms⁻¹, displayed in Table 6.7. The results, for various geocentric particle velocities, are represented graphically in figures 6.25 to 6.27. The difference to the Sullivan results is that the north (Row 12) flux increases by some 21%, the south (Row 6) flux decreases 19% and the west (Row 3) flux increases by some 6%.

NATURAL				
Altitude: 458 km				
Geocentric Particle Velocity: 10.000 km/s				
Angular Offset in Degrees: 8.000				
Row	K Factors	Perp Vel	Impact Vel	% Arrival Fluxes
9	2.940	12.065	14.863	17.616
8	2.459	11.036	14.527	14.751
7	1.613	8.906	13.487	9.690
6	0.809	6.226	11.442	4.860
5	0.303	3.710	8.396	1.819
4	0.100	2.046	5.072	0.599
3	0.072	1.705	4.087	0.428
2	0.178	2.792	6.779	1.065
1	0.530	4.984	10.122	3.173
12	1.211	7.677	12.668	7.258
11	2.085	10.147	14.154	12.490
10	2.786	11.743	14.772	16.683
13 (Space)	1.000	6.668	12.135	8.873
14 (Earth)	1.000	1.870	11.605	0.696

Table 6.7 Output for EX3DFLUX.DAT with 8° offset.

The average impact and perpendicular velocities and K Factors also change in the same fashion though not with the same percentage change. This can be seen by comparing Table 6.6 with 0° offset, to Table 6.7 with an 8° offset.

The equations for the K Factors and average perpendicular impact velocity differ in value, but not form, to those presented by Sullivan 1992 {6.7}.

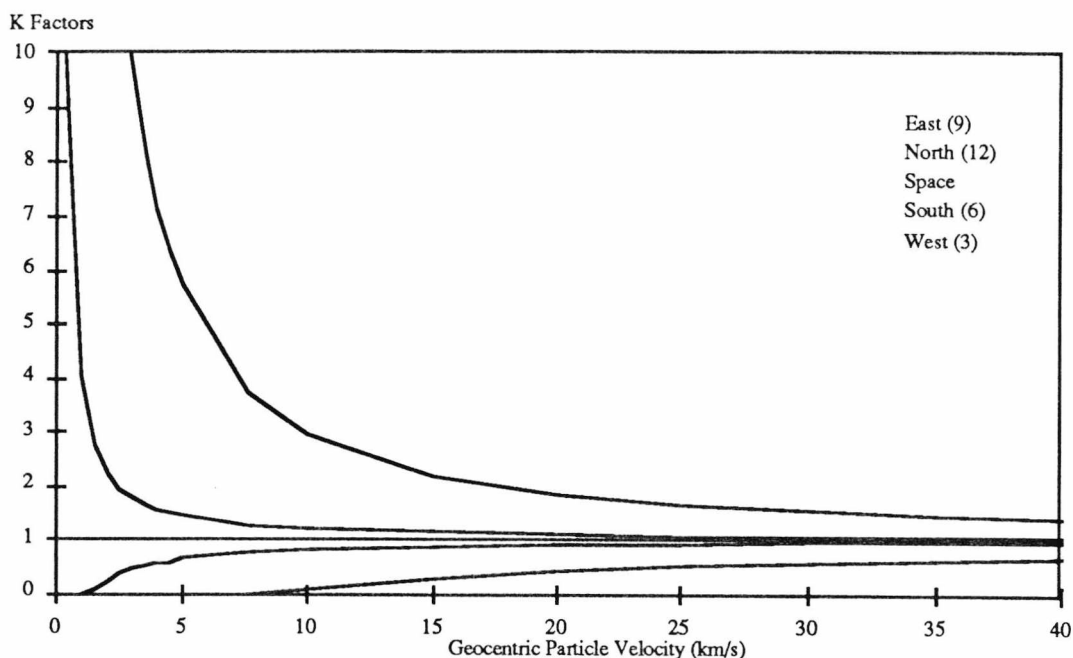


Figure 6.25 Graphical representation of the K Factors as a function of geocentric particle velocity, for LDEF faces that contained MAP surfaces.

The K Factors (figure 6.25) can be written in terms of V_{pe} , the geocentric particle velocity, except for K_{Sp} and K_{Ea} as shown in equations (6.49) to (6.54).

$$K_E = \frac{V_{pe} + 27.459}{V_{pe} - 0.00004} \tag{6.49}$$

$$K_N = \frac{V_{pe} + 3.099}{V_{pe} - 0.021} \tag{6.50}$$

$$K_S = \frac{V_{pe} - 1.292}{V_{pe} + 2.683} \tag{6.51}$$

$$K_W = \frac{V_{pe} - 9.017}{V_{pe} + 6.259} \quad (6.52)$$

$$K_{Sp} = 1 \quad (6.53)$$

$$K_{Ea} = 1 \quad (6.54)$$

The average perpendicular impact velocities are a linear function of V_{pe} above 10kms^{-1} as shown in figure 6.26 and given by equations (6.55) to (6.60).

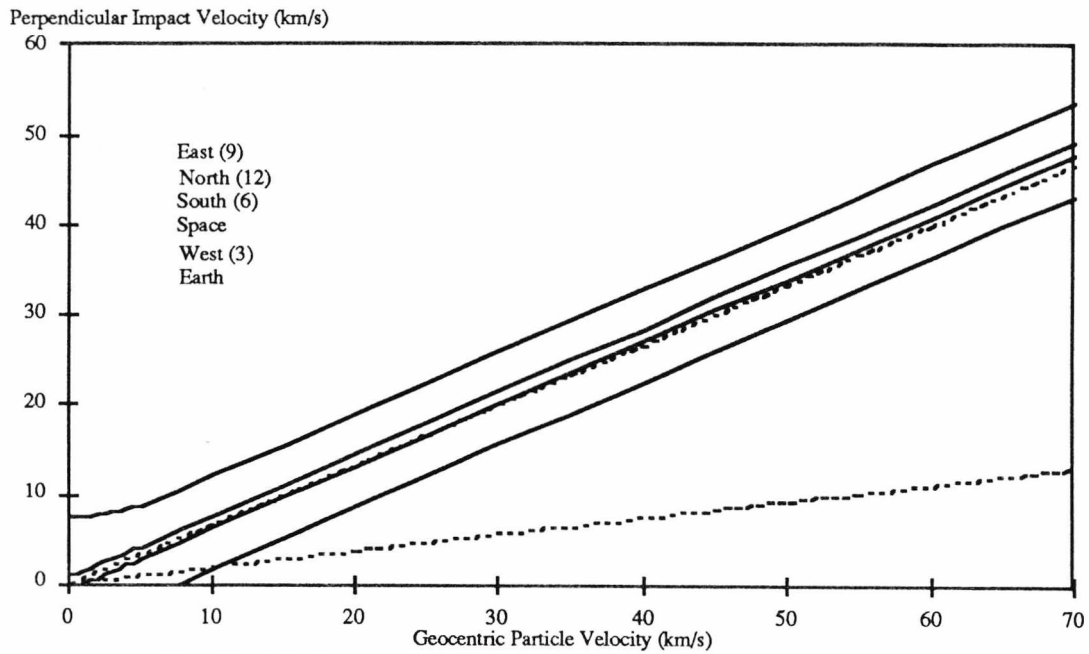


Figure 6.26 Graphical representation of the perpendicular impact velocity as a function of geocentric particle velocity.

$$V_E = 0.6949 V_{pe} + 5.116 \quad (6.55)$$

$$V_N = 0.6951 V_{pe} + 0.726 \quad (6.56)$$

$$V_S = 0.6955 V_{pe} - 0.728 \quad (6.57)$$

$$V_{Sp} = 0.667 V_{pe} \quad (6.58)$$

$$V_W = 0.6954 V_{pe} - 5.249 \quad (6.59)$$

$$V_{Ea} = 0.1869 V_{pe} \quad (6.60)$$

The percentage of encountered flux at constant mass, is illustrated in figure 6.27 as a function of V_{pe} . It is these revised results that are used in the discussions in Chapter 7.

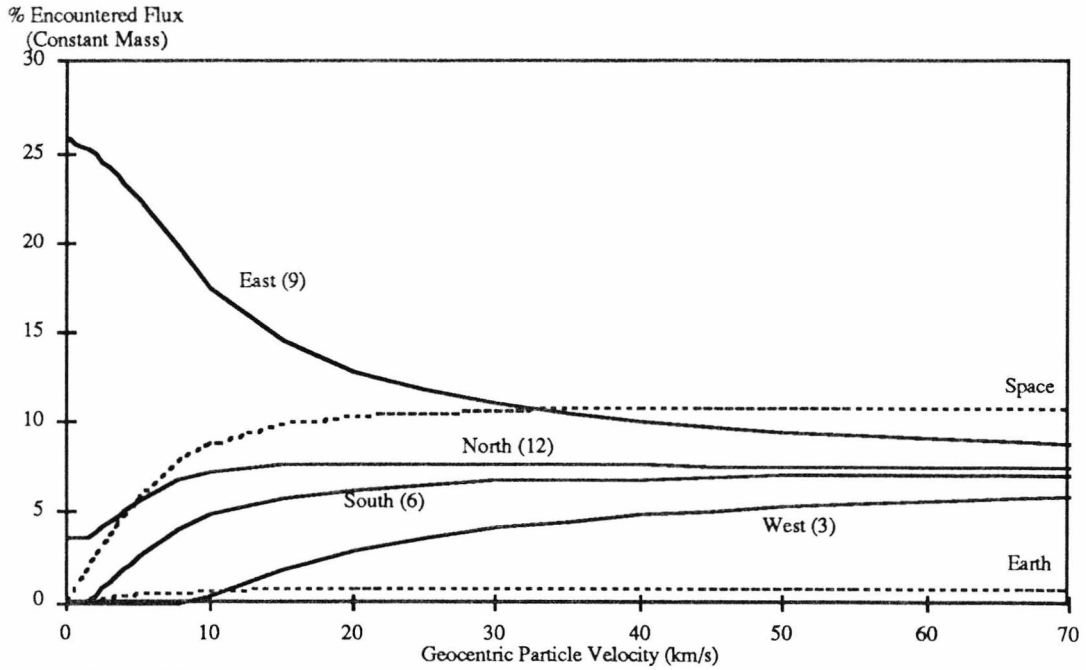


Figure 6.27 Percentage of encountered flux, at constant mass, on the LDEF as determined from the program EX3DFLUX.FOR.

6.6 The USS Space Debris and Interplanetary Model For the LDEF

The basic Sullivan isotropic cloud model {6.7} has been further updated by Mackay to incorporate a velocity and mass distribution {6.5}.

For each incoming trajectory that is allowed (*i.e.* taking into account the Earth shielding properties) a velocity distribution is applied to the particle distribution. The velocity distribution used is that of Erickson (1968) {6.25} for sporadic photographic meteors. This velocity distribution has been corrected for altitude, as the original data was determined between 75km and 125km. The distribution is illustrated in figure 6.28.

The mass distribution is that of Grün {6.2} as given in section 6.2.1, but transformed from 1A.U., to the LDEF altitude accounting for the gravitational enhancement and normalised such that the sum of the trajectories gives the Grün mass distribution.

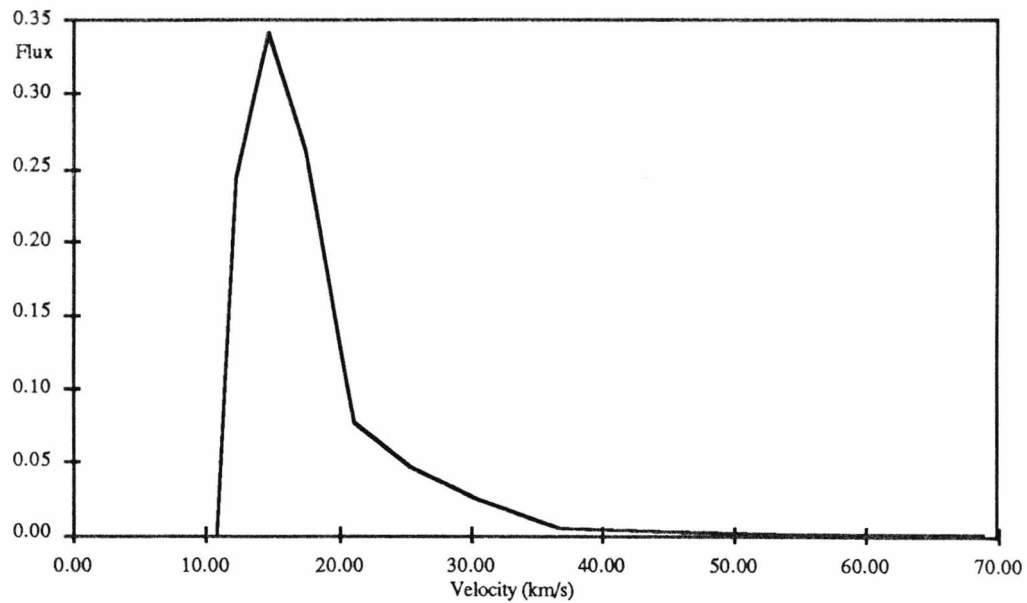


Figure 6.28 The Erickson velocity distribution at LDEF's altitude.

In essence the isotropic model has been convolved with the Grün (1985) mass distribution and the Erickson (1968) velocity distribution to give the interplanetary model for LDEF. Combined with the debris model discussed in section 6.3.2 this has given the USS Space Debris and Interplanetary Model for LDEF (Green, Deshpande & Mackay, 1992) {6.5}.

The model outputs are as follows :

a) For a spherical spacecraft :

- The angular distribution of impacts
- The velocity distribution of impacts

b) For a polygonal spacecraft (nominally LDEF) :

- The angular distribution of impacts on each face, relative to the surface normal
- The distribution of impact velocities and their normal components on each face
- Mean and maximum impact velocities (and mean normal components) on each face
- The flux perforating a given foil thickness of metal foil for each face

- The crater size distribution for each face.

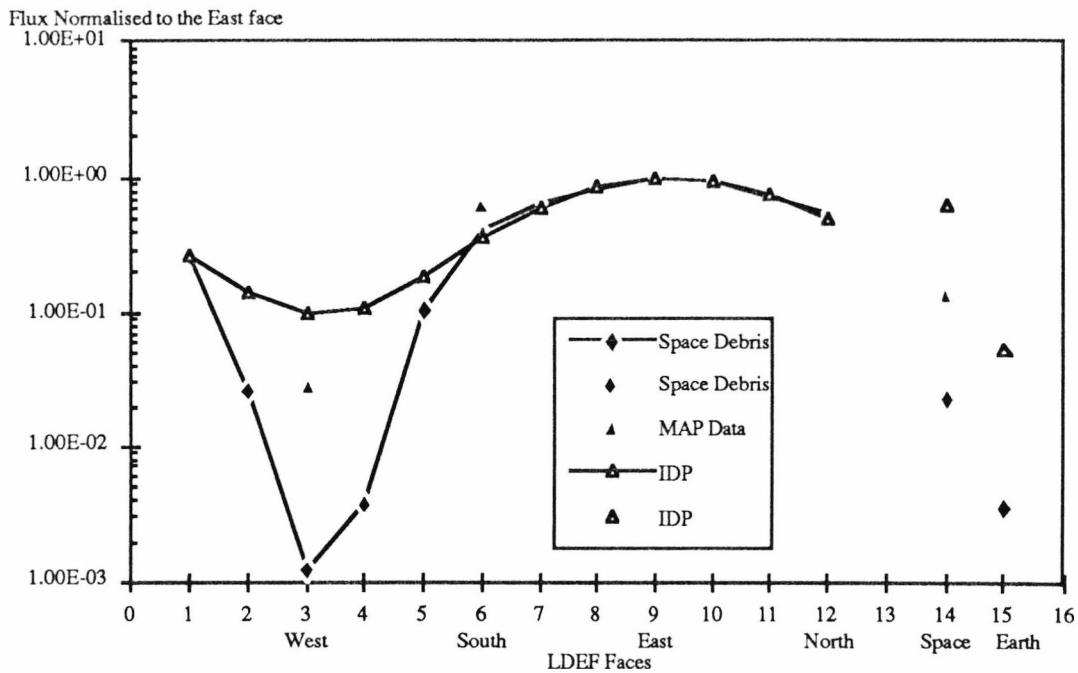


Figure 6.29 Comparison of Space Debris and IDP (Interplanetary particulates) modelled results with MAP data for penetration depth of $5\mu\text{m}$ of aluminium

Figure 6.29 illustrates the output of the model showing the interplanetary and space debris predictions for the LDEF, normalised to the East face, and compared to MAP data. It is to be noted that the absolute levels of debris to interplanetary impacts can only be ascertained from chemical residue analysis of LDEF surfaces and in particular with the ratios of East to West, West to Space and Space to Earth. The LDEF is the best source of information and the models are devised to explain and predict these results. The model predicts the total combined fluxes within a factor of three of the observed values, the discrepancies are therefore in the assumptions made in both the interplanetary and space debris modules and are discussed in Chapter 7. With the release of positive identification of impactor origin (Bernhard et al, 1992) {6.47} the LDEF model inputs have been adapted and the implications for LDEF predictions, discussed in the next chapter (Chapter 7).

References

- {6.1} Cour-Palais, B.G. (1969). "Meteoroid Environment Model - 1969 [Near Earth to Lunar Surface]", NASA SP-8013.
- {6.2} Grün, E., Zook, H.A., Fechtig, H. & Giese, R.H. (1985). "Collisional Balance of the Meteoritic Complex", *Icarus*, 62, pp244-272.
- {6.3} Divine, N. (1992). "Five Populations of Interplanetary Meteoroids", JPL Interoffice Memorandum IOM-5217-92-14/15.
- {6.4} Kessler, D.J., Reynolds, R. & Anz-Meador, P. (1989). "Orbital Debris Environment for Spacecraft Designed to Operate in Low Earth Orbit.", NASA TM-100471.
- {6.5} Green, S.F., Deshpande, S.P. & Mackay, N.G. (1992). "A 3-D Numerical Model for Space Debris and Interplanetary Dust Fluxes Incident on LDEF". for publication in Proc. IAF/COSPAR World Space Congress, Washington D.C. 1992.
- {6.6} Green, S.F. & McDonnell, J.A.M. (1992). "A Numerical Model for Characterisation of the Orbital Debris Environment". *Hypervelocity Impacts in Space*, (ed. J.A.M. McDonnell), Unit for Space Sciences, University of Kent at Canterbury, pp251-256.
- {6.7} Sullivan, K. (1992). "Characterisation and Dynamic Modelling of the Near-Earth Space Particulate Environment.", *Ph.D. Thesis*, University of Kent at Canterbury, U.K..
- {6.8} Anz-Meador, P.D. *Personal communication.s.*
- {6.9} Brownlee, D.E. (1978). "Microparticle Studies of Sampling Techniques", *Cosmic Dust* (ed. J.A.M. McDonnell), Wiley, Chichester, U.K., pp295-336.
- {6.10} Smith, O., Adams, N.G. & Kahn, H.A. (1974). "Flux and Composition of Micrometeoroids in the Diameter Range 1-10 μ m", *Nature*, 252, pp101-106.

- {6.11} Nagel, K., Neukum, G., Dohanyi, J.S., Fechtig, H. & Genter, W. (1976). "Density and Chemistry of Interplanetary Dust Particles Derived from Measurements of Lunar Microcraters", *Proc. Lunar Sci. Conf. 7th*, pp1021-1029.
- {6.12} Le Sergeant d'Hendecourt, L.B. & Lamy, P.L. (1980). "On the Size Distribution and Physical Properties of Interplanetary Dust Grains", *Icarus*, 43, pp350-372.
- {6.13} Zook, H.A. (1975). "The State of Meteoritic Material on the Moon", *Proc. Lunar Sci. Conf. 6th*, pp1563-1572.
- {6.14} Flavill, R.P., Allison, R.J. & McDonnell, J.A.M. (1978). "Primary, Secondary and Tertiary Microcrater Populations on Lunar Rocks: Effects of Hypervelocity Impact Microejecta on Primary Population", *Proc. Lunar Sci. Conf. 9th*, pp2539-2556.
- {6.15} Allison, R.J. & McDonnell, J.A.M. (1981). "Secondary Cratering Effects on Lunar Microterrain: Implications for the Micrometeoroid Flux", *Proc. Lunar Sci. Conf. 12th*, pp1703-1716.
- {6.16} Morrison, D.A. & Clanton, U.S. (1979). "Properties of Microcraters and Cosmic Dust of Less Than 1000Å Dimensions", *Proc. Lunar Sci. Conf. 10th*, pp1649-1663.
- {6.17} Zook, H.A., Hartung, J.B. & Storzer, D. (1977). "Solar Flare Activity: Evidence for Large Scale Changes in the Past", *Icarus*, 32, pp106-126.
- {6.18} Zook, H.A. (1980). "On Lunar Evidence for a Possible Large Increase in Solar Flare Activity $\sim 2 \times 10^4$ Years Ago", *Proc. Conf. Ancient Sun* (eds R.O. Pepin, J.A. Eddy & R. Merrill), pp245-266.
- {6.19} Naumann, R.J., Jex, D.W. & Johnson, C.L. (1969). "Calibration of Pegasus and Explorer XXIII Detector Panels", **NASA TR R-321**.
- {6.20} Hoffmann, H.J. Fechtig, H. Grün, E. & Kissel, J. (1975a). "First Results of the Micrometeoroid Experiment S215 on HEOS 2 Satellite", *Planet. Space Sci.*, 23, pp215-224.

- {6.21} Hoffmann, H.J. Fechtig, H. Grün, E. & Kissel, J. (1975b). "Temporal Fluctuations and Anisotropy of the Micrometeoroid Flux in the Earth-Moon System", *Planet. Space Sci.*, 23, pp985-991.
- {6.22} Grün, E. & Zook, H.A. (1980). "Dynamics of Micrometeoroids in the Inner Solar System", *Solid Particles in the Solar System* (eds. I. Halliday & B.A. McIntosh), Reidal, Dordrecht, pp293-298.
- {6.23} Berg, O.E. & Grün, E. (1973). "Evidence of Hypervelocity Cosmic Dust Particles", *Adv. Space Research*, 13, pp1047-1055.
- {6.24} Leinert, C., Richter, I., Pitz, E. & Planck, B. (1981). "The Zodiacal Light from 1.0 to 0.3 AU", *Astron. Astrophys.*, 103, pp177-188.
- {6.25} Erickson, J.E. (1968). "Velocity Distribution of Photographic Meteors", *J. Geophys. Res.*, 73, pp3721-3726.
- {6.26} Sekanina, Z. & Southworth, R.B. (1975). "Physical and Dynamical Studies of Meteors", **NASA CR-2615**.
- {6.27} Levasseur-Regourd, A.C. & Dumont, R. (1980). "Absolute Photometry of Zodiacal Light", *Astron. & Astrophys.*, Vol. 84, No. 3, pp277-279.
- {6.28} Hanner, M.S. et al. (1974). "Zodiacal Light and the Asteroid Belt: The View from Pioneer 10", *J. Geophys. Res.*, Vol. 79, No. 25, pp3671-3675.
- {6.29} Leinert, C & Grün, E. (1990). "Interplanetary Dust", *Physics and Chemistry in Space - Space and Solar Physics, Physics of the Inner Solar System, Vol 20*, (eds. Schwenn, R. & Marsch, E.) pp207-275, (Springer-Verlag, Berlin-Heidelberg).
- {6.30} Grün, E. (1981). "Physickalische und Chemische Eigenschaften des Interplanetaren Staubes - Messungen des Mikrometeoritenexperimentes auf Helios", **BMFT-FB-W 81-034**.
- {6.31} Humes, D.H. (1980). "Results of Pioneer 10 and 11 Meteoroid Experiennets: Interplanetary and Near-Saturn", *J. Geophys. Res.*, Vol. 85, No. A11, pp5841-5852.
- {6.32} Grün, E. et al. (1991). "Interplanetary Dust Measurements by the Galileo and Ulysses Dust Detectors during the Initial Mission Phases".
- {6.33} Divine, N. *Personal communications*.

- {6.34} Laurance, M.R. & Brownlee, D.E. (1986). "The Flux of Meteoroids and Orbital Space Debris Striking Satellites in Low Earth Orbit", *Nature* 323, pp136-138.
- {6.35} Kessler, D.J. (1992). "Origin of Orbital Debris Impacts on LDEF's Trailing Surfaces." in *LDEF, Second Post Retrieval Symposium*, San Diego, 1992.
- {6.36} Anderson, B.J. (1990). "Review of Meteoroid/Orbital Debris Revisions to SSP 30425", MSFC Internal document ES44-(193-90).
- {6.37} Anz-Meador, P.D., Rast, R.H. & Potter Jr, A.E. (1992). "Apparent Densities of Orbital Debris", for publication in Proc. IAF/COSPAR World Space Congress, Washington D.C. 1992.
- {6.38} Deshpande, S.P., Green, S.F. & Zarnecki, J.C. (1992). "Size Dependent Space Debris Density Distribution and Implications for Size to Mass Conversions", for publication in Proc. IAF/COSPAR World Space Congress, Washington D.C. 1992.
- {6.39} McKnight, D.S. & Lorenzen, G. (1989). "Collision Matrix for Low Earth Orbit Satellites", *J. Spacecraft*, Vol. 26, No. 2, pp90-94.
- {6.40} Jehn, R. (1991). "Dispersion of Debris Clouds from In-Orbit Fragmentation Events", *ESA Journal*, Vol. 15, No. 1, pp63-79.
- {6.41} Deshpande, S.P. and Green, S.F., (1992). "Can Objects in Geostationary Transfer Orbit (GTO) Affect the Debris Population at Low Earth Orbit (LEO)?" *Hypervelocity Impacts in Space*, (ed. J.A.M. McDonnell), Unit for Space Sciences, University of Kent at Canterbury, pp100-106.
- {6.42} King-Hele, D.G. (1987). "Satellite Orbits In An Atmosphere: Theory and Applications." Blackie and Son Ltd, Glasgow, 1987.
- {6.43} Potter, A.E., Heinze, K.G. & Tanner, D.L. (1989). "Albedo Estimates for Debris", in *Orbital Debris from Upper Stage Breakup*, AIAA, Washington D.C., pp147-163.
- {6.44} Johnson, N.L. and McKnight, D.S. (1987). "Artificial Space Debris." Orbit Book Co., Malabar, Florida, 1987.
- {6.45} Mehrholz, D. (1992). "Space Object Observation with Radar", for publication in Proc. IAF/COSPAR World Space Congress, Washington D.C. 1992.

- {6.46} Ratcliff, P.R. and McDonnell, J.A.M. (1992). "The Leo Microparticle Population: Computer Studies of Space Debris Drag Depletion and of Interplanetary Capture Processes." for publication in Proc. IAF/COSPAR World Space Congress, Washington D.C. 1992.
- {6.47} Bernhard, R. & Hörz, F. (1992). "Compositional Analysis of Projectile Residues on LDEF Instrument A0187-1", in *LDEF, Second Post Retrieval Symposium*, San Diego, 1992.

Chapter 7

LDEF Predictions and Inferences

7.1 Introduction

Combining both the models developed and discussed in Chapter 6, and the analysis of impact morphology, it is possible to predict the contribution to each LDEF face from space debris impacts and interplanetary particulate impacts.

Crater morphology, penetration depth, and thin foil perforations used in conjunction with the penetration equations described in Chapter 3 can reveal impactor parameters, such as size, velocity and density. Combining direction information from crater shapes, and modelling of the two particulate sources it is possible to infer impactor origin without the need of residue chemistry. This approach is however somewhat subjective as the penetration equations are very closely constrained to assigning either a particular velocity or density to an impacting particulate.

The modelling of the two populations can give information on the impacting direction and velocity thus eliminating one of the assumptions needed to solve the penetration equations.

The Sullivan model was used to obtain a single velocity (V_{pe}) of 23.5kms^{-1} for the isotropic interplanetary particles impacting the LDEF {7.1}. This was based on transforming the West flux to the equivalent flux on the Space face and comparing this to the Space data, giving a velocity measurement required to match these two exactly. This was based on the MAP Space Face $5\mu\text{m}$ aluminium data point and the MAP $5\mu\text{m}$ West flux data. However, since the offset has now been added this value will change slightly, and is indeed dependant on which penetration equation is used for the velocity scaling (see Chapter 6). A new V_{pe} for this isotopic cloud has been derived but also it was found that over the size range available for transformation, that a velocity distribution is needed to accurately predict over the entire size range from $3\mu\text{m}$ to $1125\mu\text{m}$ foil thickness. This transformation assumed that the flux on the Space and West faces were from the same source, interplanetary particles, with negligible impacts from space debris, due to the geometry of the LDEF and the assumption of circular orbits for space debris. This has been shown in Chapter 6 and by recent publication by Bernhard et al. {7.2} not to be the case. In view of this, an amount attributed to space debris has been deducted from the West flux distribution, and the Space flux distribution based on data given by Bernhard and modelling to predict space debris impacts on the Space face. Using this a new V_{pe} has been determined for the interplanetary particles. The velocity distribution derived is compared to velocities given by Grün {7.3}, Divine {7.4}, for interplanetary particles and discussed.

Using this result predictions for the interplanetary component of impacts on any face of the LDEF is possible and comparing this to the flux data from Chapter 4, gives the orbital component. Possibly space debris, or possible interplanetary particles captured in LEO. The orbital component is compared to the Kessler based space debris model {7.5}.

The USS and Interplanetary Model for LDEF is used to compare flux distributions presented in Chapter 4 and to determine possibility of evaluating the origin of impacts based on the ellipticity the crater (Newman et al., 1992) {7.6}.

7.2 Interplanetary Particulate Predictions

7.2.1 Determination of the Geocentric Particle Velocity (V_{pe})

The Sullivan model {7.1}, as described in Chapter 6, was used to determine new particulate velocity, V_{pe} , values for the interplanetary component of impacts on the LDEF. The West face flux distribution, as presented in Chapter 4, was used as the basis for the transformation and compared to the Space face flux distribution (Chapter 4).

Assuming that the West and Space face flux distributions were entirely due to interplanetary particulate impacts, $V_{pe} = 23.28 \pm 4.5 \text{ km s}^{-1}$ for the single velocity isotropic model at the $5 \mu\text{m}$ foil thickness measure. This V_{pe} value is slightly lower than the value quoted by Sullivan (1992) {7.1} of $V_{pe} = 23.5 \pm 4.5 \text{ km s}^{-1}$ due to the 8° offset, as discussed in Chapter 6. V_{pe} was determined by solving equation (6.48) (Chapter 6), using the program EX3DFLUX.FOR to determine the relevant V_W , V_{Sp} , K_W and K_{Sp} as required by the equation. The velocity exponent is determined by the penetration equation employed and this was selected as the McDonnell & Sullivan equation (1991) {7.1}, with the velocity exponent of 0.664. The solution was determined iteratively implying:

$$\left(\frac{V_W}{V_{Sp}}\right) = 0.2254 \left(\frac{K_W}{K_{Sp}}\right)^{-1.541} \quad (7.1)$$

where K_W , K_{Sp} , V_W and V_{Sp} are given by equations (6.52, 6.53, 6.59 and 6.58) respectively. The program EX3DFLUX.FOR was run with a geocentric particle velocity of 23.28 km s^{-1} and Table 7.1 illustrates the results.

The transformation then leads to the interplanetary flux distribution for the Space face. This is compared to the Space face flux distribution in figure 7.1.

NATURAL					
Altitude: 458 km					
Geocentric Particle Velocity: 23.28 km/s					
Angular Offset in Degrees: 8.000					
Row	K Factors	Perp Vel	Impact Vel	% Arrival Fluxes	
9	1.709	21.319	28.357	12.058	
8	1.548	20.281	27.638	10.941	
7	1.246	18.145	25.969	8.815	
6	0.915	15.462	23.461	6.479	
5	0.653	12.954	20.583	4.617	
4	0.504	11.304	18.315	3.560	
3	0.476	10.971	17.807	3.359	
2	0.568	12.041	19.368	4.009	
1	0.780	14.218	22.112	5.506	
12	1.088	16.908	24.886	7.681	
11	1.418	19.386	26.979	10.008	
10	1.658	20.993	28.141	11.695	
13 (Space)	1.000	15.522	24.217	10.451	
14 (Earth)	1.000	4.352	23.944	0.820	

Table 7.1 Output for EX3DFLUX.DAT with 8° offset run at 23.28km⁻¹.

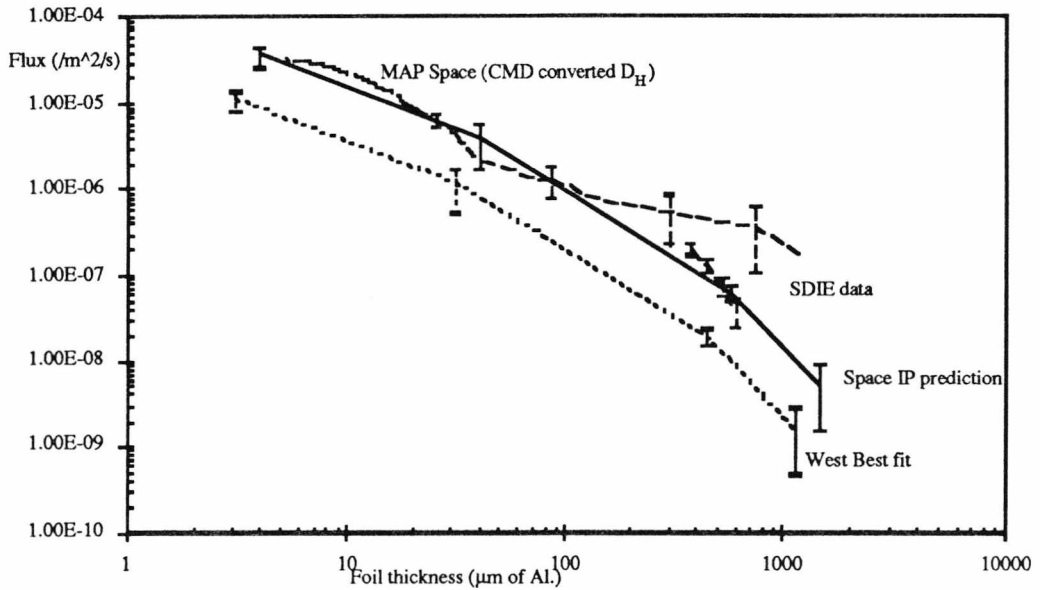


Figure 7.1 West interplanetary flux to Space interplanetary flux using $V_{pe}=23.28\text{km}^{-1}$

It is clear from figure 7.1 that this transformation is valid for the 5µm value but does not match the SDIE data at larger f_{max} values. This is the first indication that a size based velocity distribution for interplanetary particles is seen on the LDEF, assuming that an isotropic distribution of particles is valid.

The same iterative process was used to determine a V_{pe} of 18.01kms^{-1} at the $375\mu\text{m } f_{\text{max}}$, somewhat lower than the 23.28kms^{-1} determined at the $5\mu\text{m } f_{\text{max}}$ implying that:

$$\left(\frac{V_W}{V_{Sp}}\right) = 0.2265 \left(\frac{K_W}{K_{Sp}}\right)^{-0.963} \tag{7.2}$$

at $375\mu\text{m } f_{\text{max}}$.

It is worth noting here that these determinations of V_{pe} were based upon a best fit line through the MAP data and SDIE data and a simple straight line extrapolation between the two. Changing the velocity exponent in equation (6.47) (*i.e.* utilising a different penetration equation) implies a change in velocity such that if $\beta=0.738$ as opposed to 0.664 (as above) $V_{pe}=23.89\text{kms}^{-1}$ at the $5\mu\text{m } f_{\text{max}}$ and 18.54kms^{-1} at the $375\mu\text{m } f_{\text{max}}$.

In summary using the best fit lines through the limited data set an apparent velocity decrease of 5.3kms^{-1} is observed from $5\mu\text{m}$ to $375\mu\text{m } f_{\text{max}}$ and an apparent velocity increase of $\sim 0.6\text{kms}^{-1}$ if β increases by 0.074 (+11%). The transformation of West data to Space data to determine V_{pe} is illustrated in figure 7.2 with the graded V_{pe} using 23.28kms^{-1} and 18.01kms^{-1} .

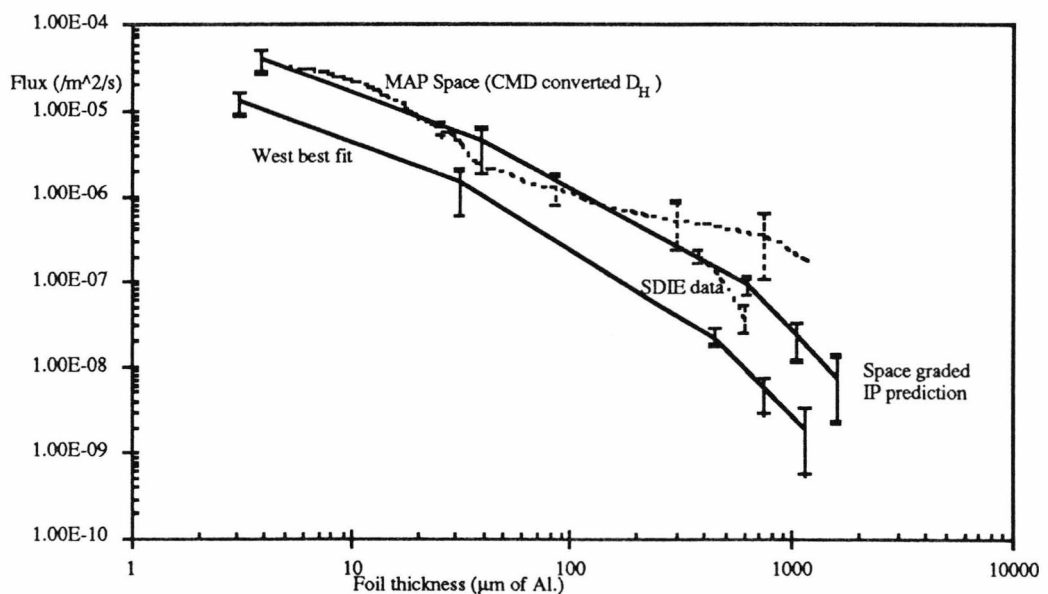


Figure 7.2 Graded transformation of West interplanetary flux to Space interplanetary flux using $V_{pe}=23.28\text{kms}^{-1}$ at $5\mu\text{m } f_{\text{max}}$ and 18.01kms^{-1} at $375\mu\text{m } f_{\text{max}}$.

With the addition of Intercostal (M+D SIG, 1992) and clamp (Newman, 1993) {7.7} data, to bridge the gap in data between MAP and SDIE, the f_{\max} flux curves became better defined and a smooth best fit line obtained for each of LDEF's faces as seen in Chapter 4 (McDonnell et al. 1993) {7.8}. With the smoothed data came the ability to list the flux data at given intervals and as such a transformation from West to Space possible at every point along the flux curve, as opposed to one or two. To better utilise this a C program VEL.C was developed to solve equation (6.48) using the equations outlined in Chapter 6 for the K Factors and velocities. The output of the program gives V_{pe} in terms of f_{\max} for a multiple set of points.

It has been mentioned previously (Bernhard et al) {7.2} that up to 15% of the impacts on the West face can be attributed to space debris particles. To account for this in the determination of the interplanetary component from this modelling the West flux has been reduced by some 15%. Now it follows that if 15% of West impacts are space debris then a percentage impacting the Space face will also be space debris. To determine exactly how much the USS Space Debris and Interplanetary model was run with a new space debris orbit set. This data set comprised of the original space debris orbits (Chapter 5) but orbits with low inclination, $i < 50^\circ$, and apogee height $> 10,000\text{km}$ (termed HEO) were increased by a factor of 20. This increase is the same increase published by Kessler (1992) {7.9} to account for the space debris impacts on the West face as reported by Bernhard et al. (1992) {7.2}. The model predicts that the Space face receives twice as much debris as the West face as illustrated in figure 7.3 (*i.e.* Space/West for space debris impacts **only** = 2). Now although the number of impacts attributed to space debris on the Space face appears to be twice that expected on the West face (from the modelling) this may only be a small fraction of the total number of impacts of the Space face. Figure 7.4 illustrates the change in the Space/West ratio for only space debris impacts based upon the USS Space Debris model, but changing the orbital distribution.

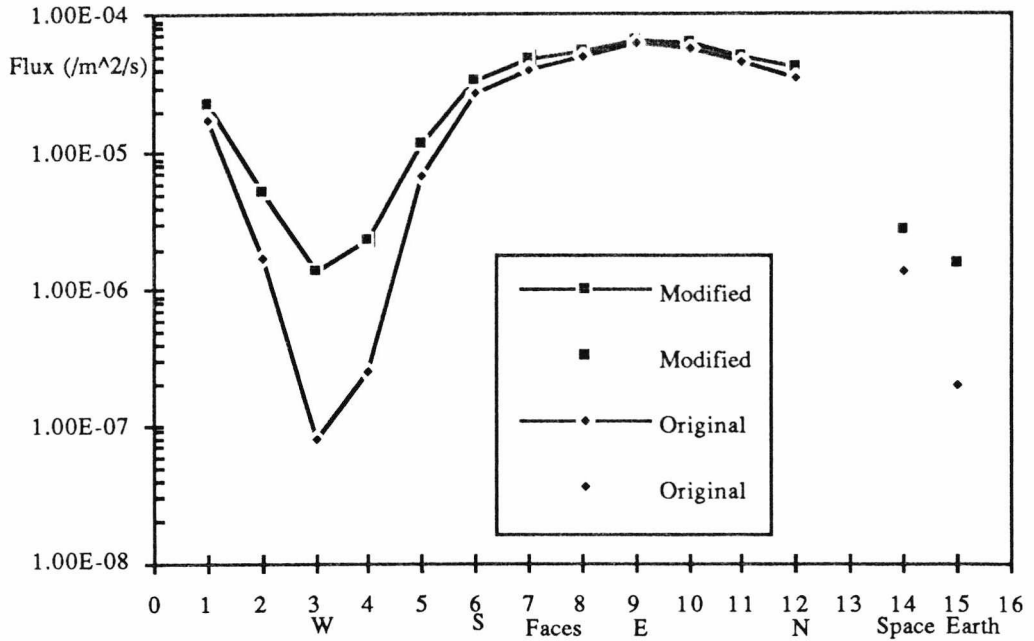


Figure 7.3 Comparison of orbital debris flux impating LDEF, normalised to the East face for a 5µm aluminium foil. The modified data are the HEO x20 orbit enhanced distribution and the original are the 6610 DISCOS orbits.

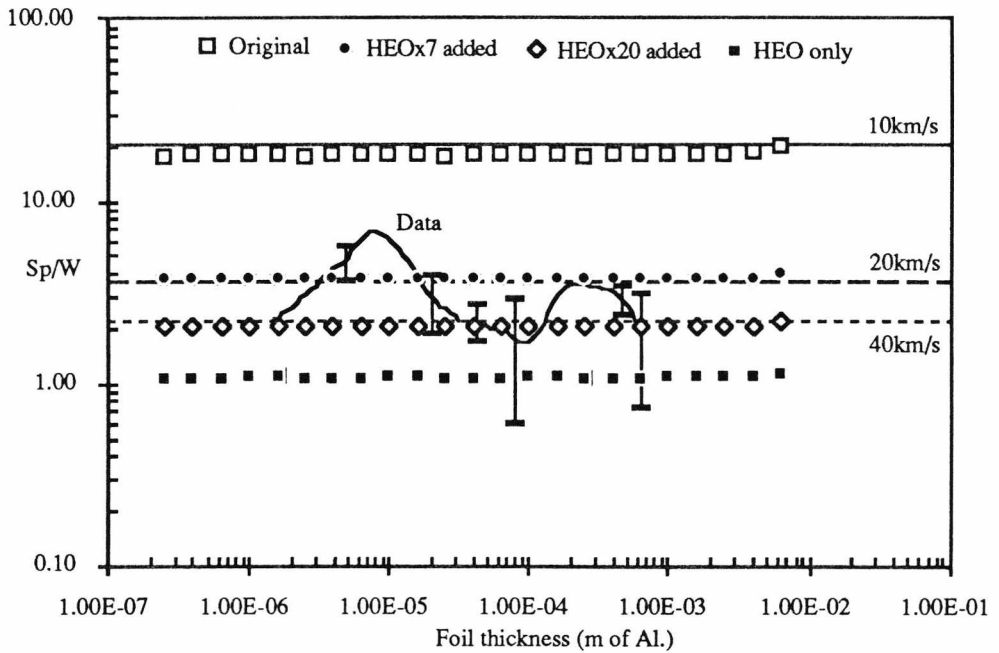


Figure 7.4 Comparison of Sp/W ratios for the measured data, varying content of HEO in the orbital model distribution and varying V_{pe} for the interplanetary model.

It is clear that if the original orbit distribution (as discussed in Chapters 5 and 6) is used then $Sp/W \sim 17.7$, introducing an increase in HEO by a factor of 7 (~5% space debris

impacts on the West face) implies $S_p/W \sim 3.7$, with HEO x20 (~15% debris on the West face) implies $S_p/W \sim 2.1$ and finally saturating the distribution with only HEO implies a $S_p/W \sim 1.1$. This result illustrates the preponderance of near circular orbits that can have grazing incidence on the Space face and no impact on the West (it is worth noting that the model is run with the 1.1° tilt). The S_p/W ratio from measured data is also shown, with associated error limits. The new Space face (with space debris subtracted) flux is therefore defined as:

$$\Phi_{Spip} = \Phi_{Sp} - 0.3\Phi_W \tag{7.3}$$

Where Φ_{Spip} is the newly determined interplanetary Space face flux, and Φ_{Sp} is the measured Space face flux as with Φ_W , the measured West face flux.

Using equation (7.3) the Space flux is reduced and now both the West and Space face fluxes are assumed to be only interplanetary in origin and are illustrated in figure 7.5.

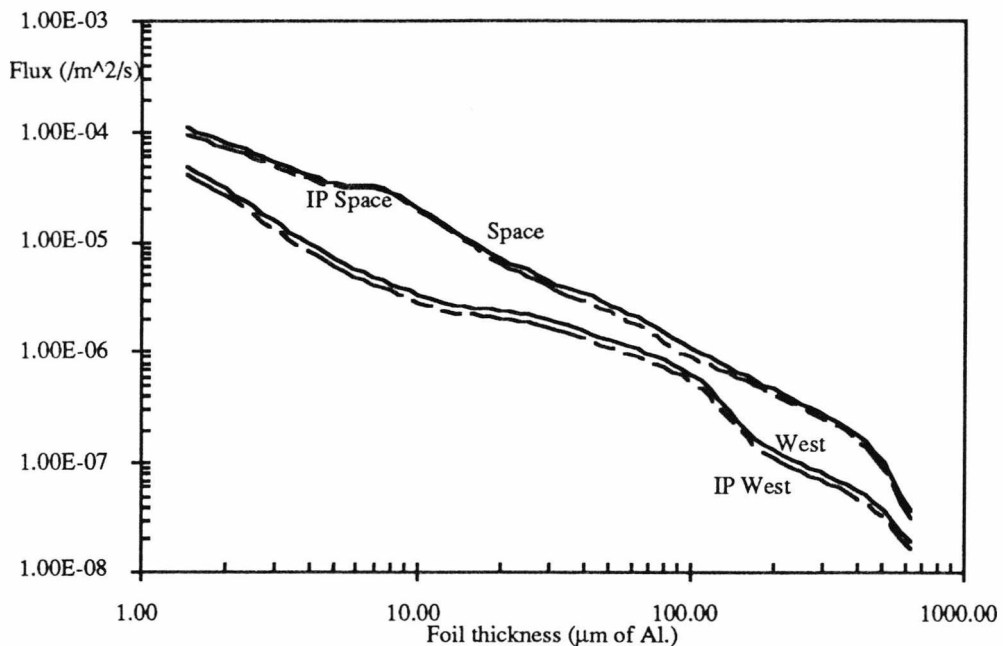


Figure 7.5 Comparison of Space and West data with the inferred IP flux determined from 15% debris impacting the West face.

The program VEL.C was run with the West and Space interplanetary flux distributions and V_{pe} for the whole f_{max} range were determined, again using the

McDonnell & Sullivan equation and $\beta=0.664$ as the penetration equation basis {7.1}. Figure 7.6 illustrates the good agreement of the transformed West flux distribution transformation and the Space flux.

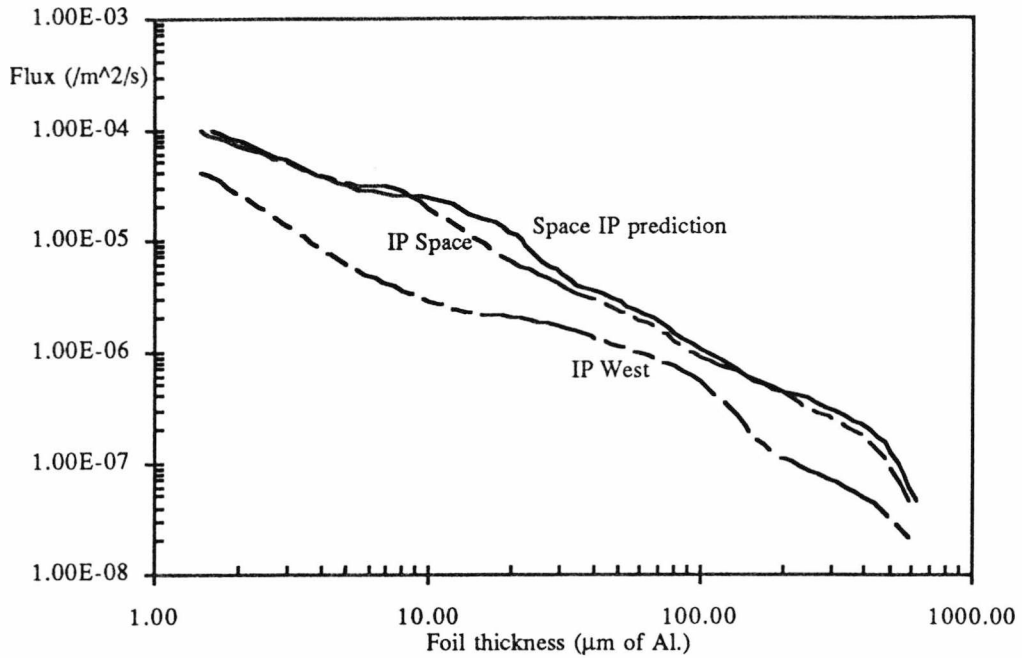


Figure 7.6 Comparison of predicted Space IP from West to Space transformation using V_{pe} determined from VEL.C, compared with inferred West and Space IP.

The V_{pe} distribution determined from VEL.C is used to determine the appropriate K Factors and velocities. Equations (6.45) and (6.46) as outlined in Chapter 6 are used to account for the apparent change in foil thickness (mass sensitivity) and flux (geometrical sensitivity) from transforming from the West face to the Space face.

Figure 7.7 illustrates the velocity distribution that is required for an isotropic model to satisfy the West to Space transformation, with the appropriate space debris component removed. The experimental data used in determining the flux distributions to determine this velocity distribution are also illustrated, by experiment or detector surface. The associated error bars are determined by taking the percentage error in the raw data sets and calculating the associated V_{pe} . The values of V_{pe} are determined from both the distance between the points being transformed (*i.e.* West flux and Space flux) and the gradient of the flux distribution at that associated f_{max} value.

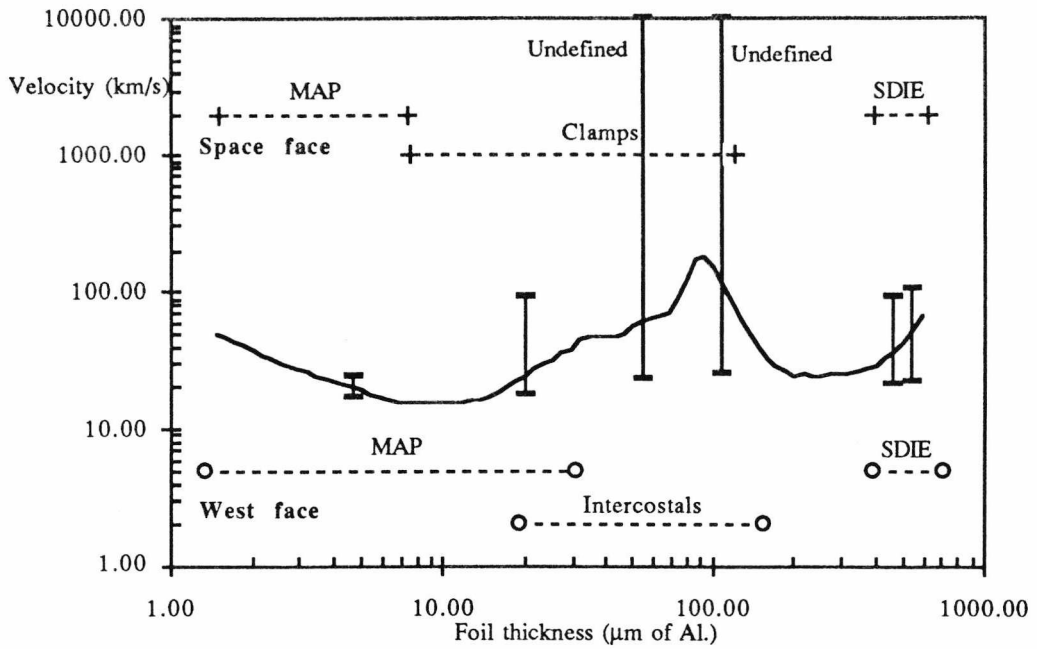


Figure 7.7 V_{pe} distribution derived from VEL.C in predicting the Space IP from the West inferred IP.

Comparing figures 7.6 and 7.7 it is clear that when the Space flux approaches the West flux the maximum value of V_{pe} is recorded. Therefore the lower error is determined from taking the lower error value on the West flux and the higher error value on the Space flux for the same f_{max} (i.e. the greatest separation of the error limits). Conversely is true for the higher error limit (i.e. the least separation of the error limits). With the overlap of error limits (see Chapter 4) in the $50\mu\text{m}$ to $200\mu\text{m}$ f_{max} range the higher error limit on V_{pe} is undefined (Space flux < West flux at these values). In this range the higher error limit becomes meaningless. If the original data sets for the West and Space faces, without an amount due to space debris removed, the values of V_{pe} increase by $\sim 2\text{kms}^{-1}$ over the majority of the f_{max} range. There is however a decrease in velocity between $50\mu\text{m}$ and $200\mu\text{m}$ f_{max} with a maximum decrease $\sim 37\text{kms}^{-1}$. In real terms the velocity distribution changes very little if the 15% debris assumption on the West face is ignored.

7.2.2 Interplanetary Flux Compared to Grün and Divine

Now that a range of V_{pe} has been established it is possible to use this to predict the interplanetary flux distributions on the North, South and East faces. The Space face has already been determined as a consequence of calculating V_{pe} and the West has been determined as a consequence of the results published by Bernhard et al. (1992) {7.2} (i.e. West data -15% attributed to space debris).

To transform the West face interplanetary flux to any other LDEF face equations (6.45) and (6.46) are employed to account for the mass sensitivity change and geometrical sensitivity change but with the appropriate subscripts. To transform the West interplanetary flux to the interplanetary flux on any face equation (6.45) becomes:

$$\Delta f|_m = \left(\frac{V_f}{V_W}\right)^B \quad (7.3)$$

and equation (6.46) becomes

$$\Delta \phi|_m = \frac{K_f \text{ESF}_f}{K_W \text{ESF}_W} \quad (7.4)$$

where subscript f denotes the face.

Figures 7.8 through to figure 7.10 illustrate the predicted interplanetary flux for the East, North and South faces, compared with the West interplanetary flux and the respective smoothed data set. It is clear from these figures that the predicted interplanetary flux does not account for the total data set and this is discussed in section 7.3.

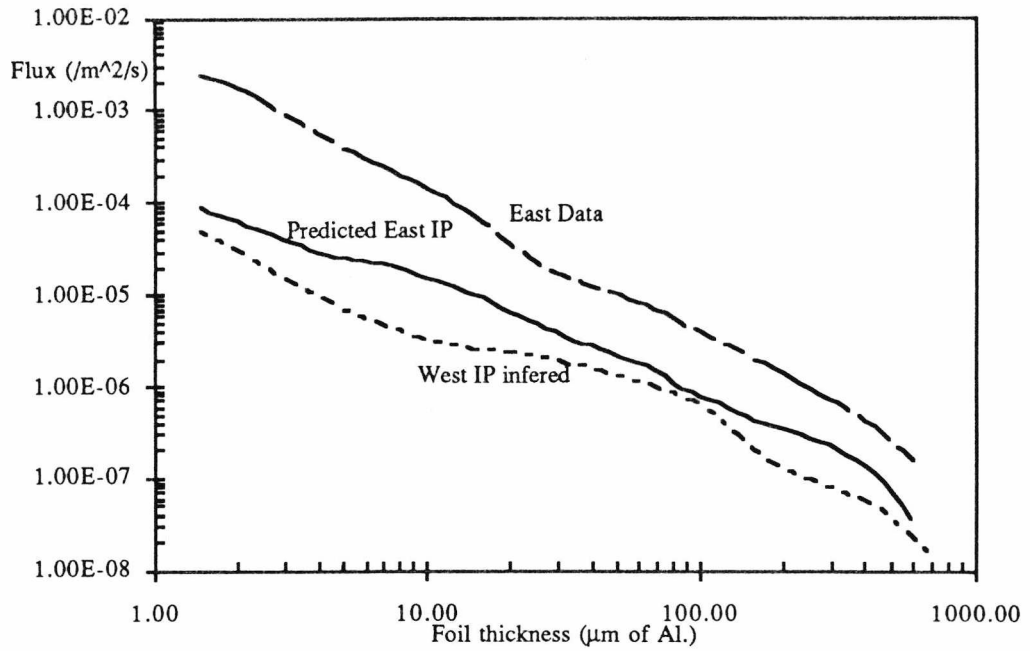


Figure 7.8 Comparison of East data with the predicted East IP determined from the inferred West IP.

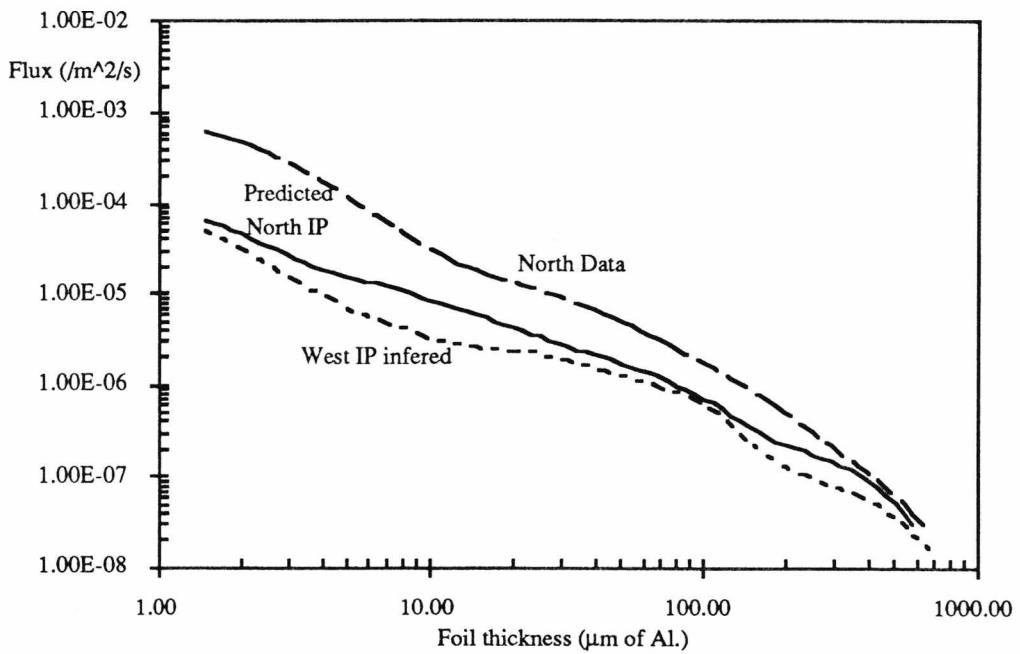


Figure 7.9 Comparison of North data with the predicted North IP determined from the inferred West IP.

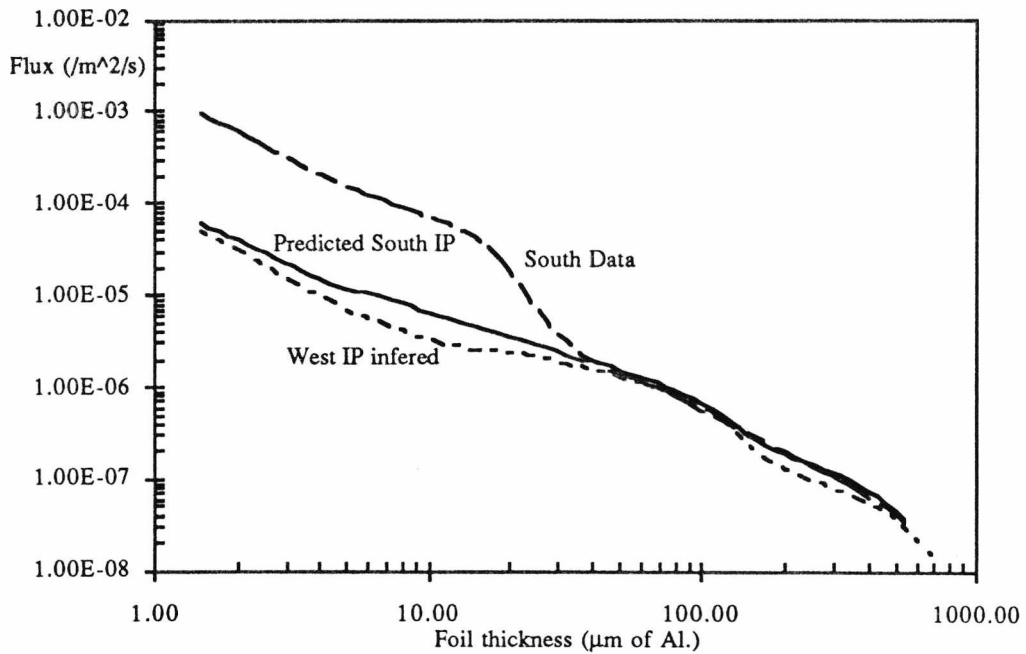


Figure 7.10 Comparison of South data with the predicted South IP determined from the inferred West IP.

The predicted interplanetary flux can be compared to the Grün flux at 1A.U. in terms of mass. However as figure 7.7 illustrates the velocity distribution is not linear with respect to f_{\max} . In converting f_{\max} to mass an associated penetration equation is required to determine the particle size and then an assumed particle density to calculate the mass. The particle diameter is strongly dependent upon velocity and therefore when converting the predicted interplanetary flux from f_{\max} to mass, the distribution is no longer cumulative. This occurs because of the increase in velocity $\sim 50\mu\text{m } f_{\max}$ followed by a decrease in velocity $\sim 100\mu\text{m}$. When converting f_{\max} to mass in this region the mass firstly increases then decreases as flux decreases. To compare this flux to the Grün flux {7.3} and Divine flux {7.4} a constant velocity of 24kms^{-1} is chosen as the average velocity, to be comparable to the Grün and Divine velocities. The predicted interplanetary flux at 1A.U. is determined by:

$$\phi (1\text{A.U.}) = \frac{\phi_f}{K_f \text{ESF}_f \chi} \tag{7.5}$$

where χ is the gravitational enhancement due to velocity as is given by equation (6.11). The flux, K Factor and ESF on a given face is denoted by the subscript f. Figure 7.11 illustrates the comparison of the predicted interplanetary flux with the Grün and Divine fluxes at 1A.U..

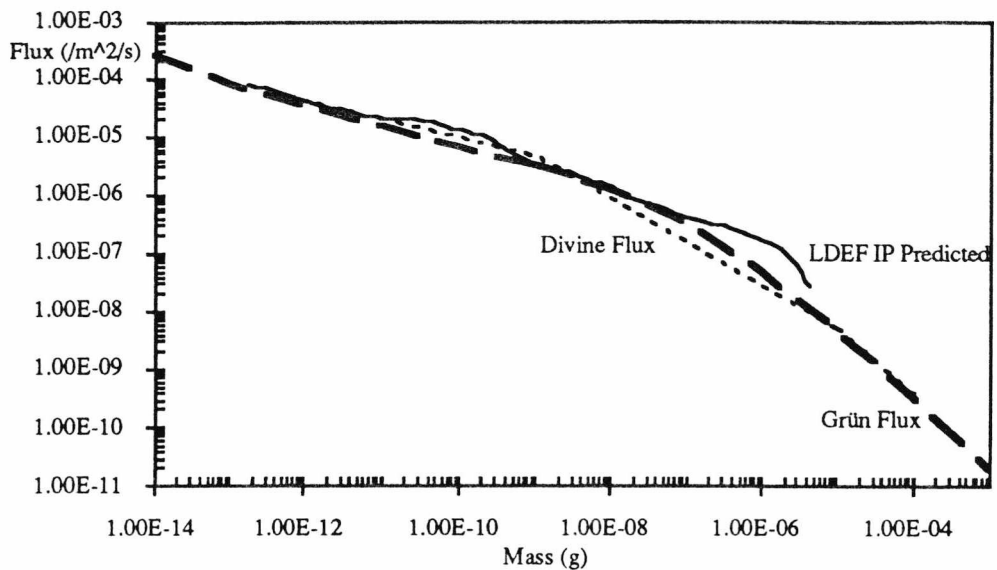


Figure 7.11 Comparison of LDEF predicted IP ($V_{pe}=24\text{kms}^{-1}$ giving $V=21.4\text{kms}^{-1}$ at 1A.U.) with that of Grün ($V=20\text{kms}^{-1}$) and Divine ($V=22.2\text{kms}^{-1}$) at 1A.U..

The Grün flux was determined for a velocity of 20kms^{-1} at 1A.U. and this corresponds to a V_{pe} of 22.7kms^{-1} at 458km (LDEF altitude). It can be seen that the flux distributions are comparable with the LDEF flux being slightly higher at the larger size range (10^{-7}g - 10^{-5}g). This may be due to the assumption of 15% debris impacts on the West face not being correct at these larger size ranges, but also the associated errors in the SDIE data which account for this region in the data set are large (see Chapter 4).

7.3 Orbital Predictions

7.3.1 Determination of Orbital Components

Figures 7.8 to 7.10 show that the predicted interplanetary flux does not account for the total data set for the East, North and South faces. The difference between the two can be attributed to an orbital flux component. This component may be anthropogenic space debris or alternatively captured interplanetary particles. Figure 7.12 shows the orbital component for the East, North and South faces resolved using the velocity distribution given in figure 7.7 by taking the difference between the data and the inferred interplanetary flux given in figures 7.8 through to 7.10.

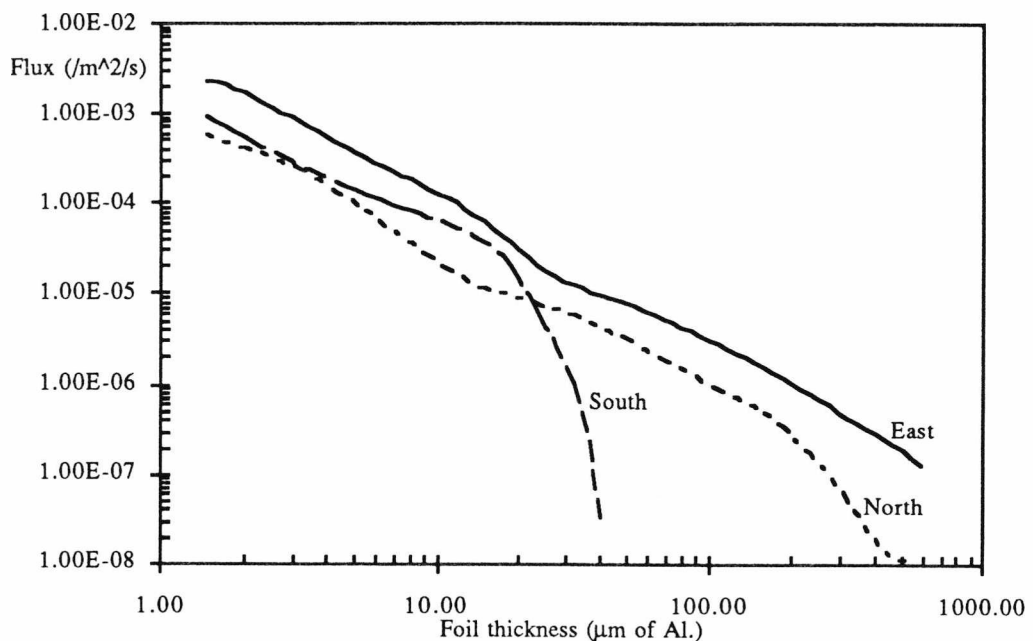


Figure 7.12 Orbital components for the East, North and South faces derived from subtracting the respective IP prediction from the data with V_{pe} distribution as given in figure 7.7.

The orbital component dominates over the predicted interplanetary component on the East and North faces, however this is not the case with the South face in which the orbital component has a clearly defined limit to $\sim 40\mu\text{m } f_{\text{max}}$. This is still the case when a mean $V_{pe}=24\text{kms}^{-1}$ is used as opposed to the figure 7.7 velocity distribution.

If however one were to use a graded velocity distribution based upon the MAP and SDIE points only but with the same 15% debris reduction in the West data then the orbital component changes drastically as illustrated in figure 7.13. The relative V_{pe} values now become 22kms^{-1} at $5\mu\text{m } f_{\text{max}}$ and 16.75kms^{-1} at $375\mu\text{m } f_{\text{max}}$. All the faces now show an orbital component dominating but only up to $\sim 60\mu\text{m } f_{\text{max}}$.

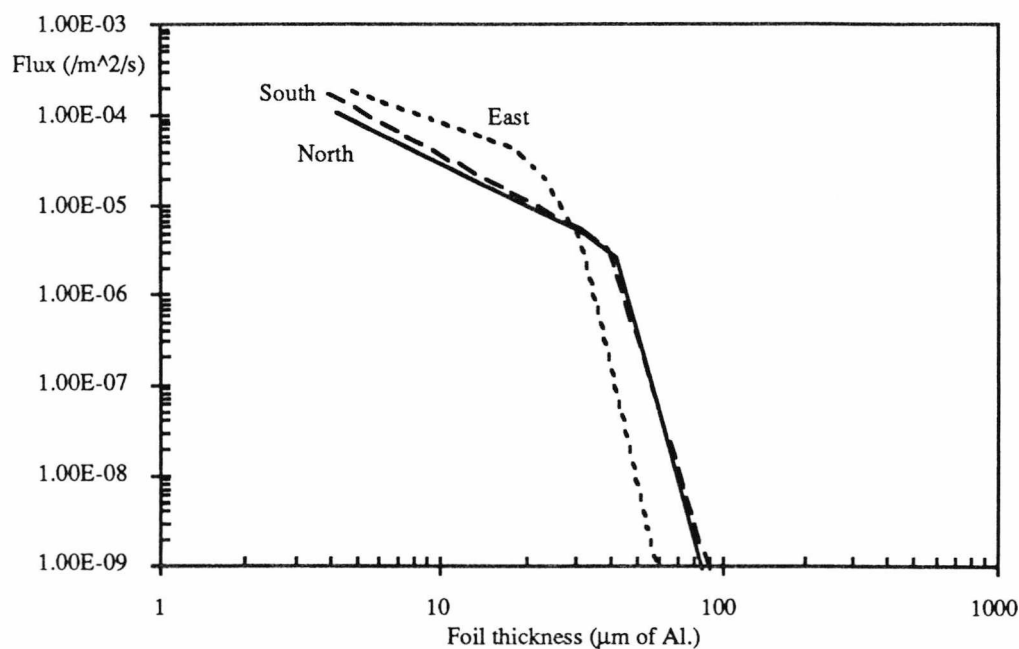


Figure 7.13 Orbital components for the East, North and South faces derived from subtracting the respective IP prediction from the data with $V_{pe}=22\text{kms}^{-1}$ at $5\mu\text{m}$ and 16.75kms^{-1} at $375\mu\text{m}$.

If one is to keep to the velocity distribution giving a mean of 24kms^{-1} , comparable to Grün etc, then figure 7.14 shows the ratio of debris on the East, North, South and Space faces with respect the measured data. The West face space debris level has been assumed at 15% over the size range to determine the relative contributions of interplanetary and orbital particles. The East face shows a large percentage attributed to an orbital component of some 76%, with the North next with 58%, South 33% and Space 8%. These percentages agree for a high proportion of debris on the ram faces, that is the East and North faces, with less on the South and Space.

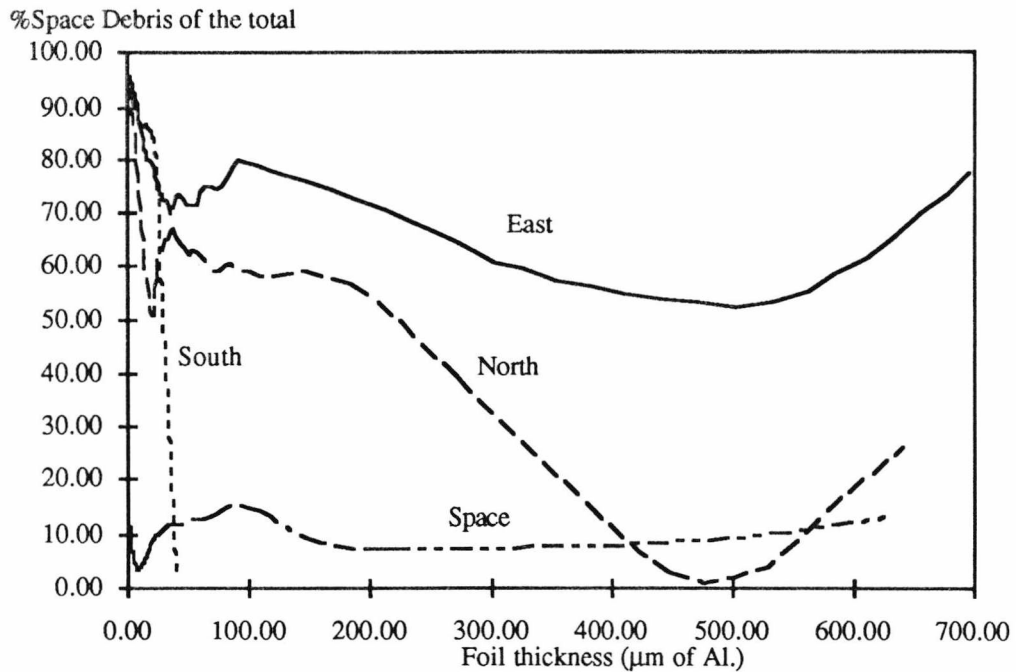


Figure 7.14 Ratio of orbital debris as determined from a comparison of predicted IP with measured data.

The Space face agrees well with the expected 5% of space debris impacts from See et al. (1992) {7.10}. The North and East face, however, seem to be rather high when taking into account that Bernhard et al. {7.2} have quoted 17% on Row 11, (30° toward the ram direction from North). Although care is needed here as this 17% constitutes only impact sites from debris particles that contained no aluminium, and indeed Hörz et al. {7.11} have quoted that >50% of all impact sites cannot release chemical data, either because no residue was found or that there are below the sensitivity threshold of their SEM. Kessler {7.9} takes a fraction 46% of total impacts on Row 11 as been attributed to space debris when determining that the present USSPACECOM orbital distribution is undersampling the true distribution of debris orbits.

One way of looking at the respective relationship between the interplanetary and space debris populations is to compare the LDEF face/West ratio for the debris and 3D isotropic interplanetary model. Figures 7.15 through to 7.17 (and including figure 7.4) illustrate the effect the changing of the space debris orbit distribution, by increasing the numbers in HEO and also the effect of an increase in velocity for the interplanetary model with the actual data ratios plotted for comparison.

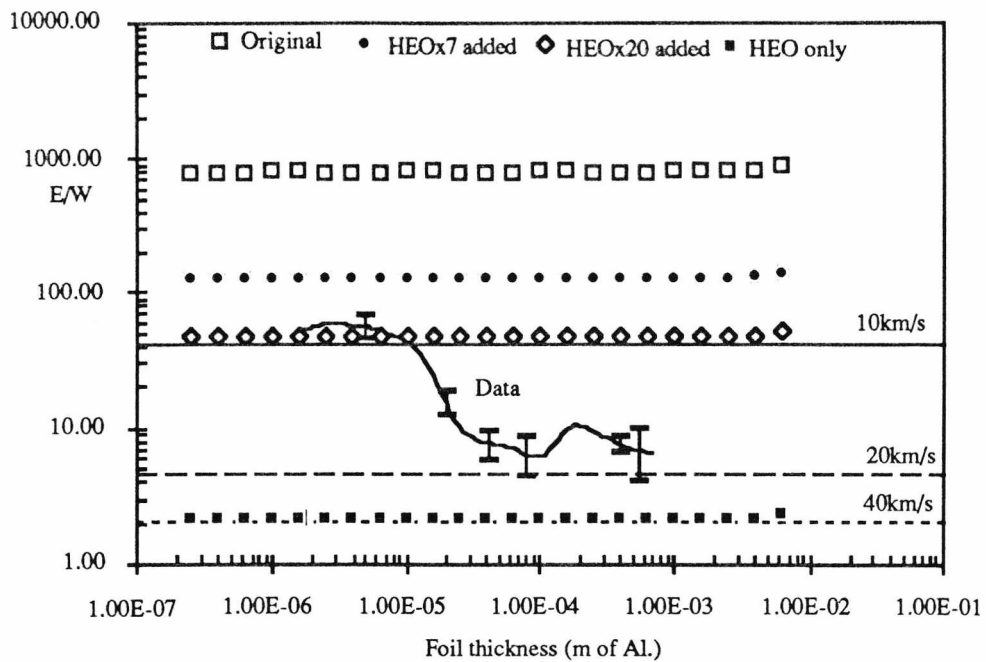


Figure 7.15 Comparison of E/W ratios for the measured data, varying content of HEO in the orbital model distribution and varying V_{pe} for the interplanetary model.

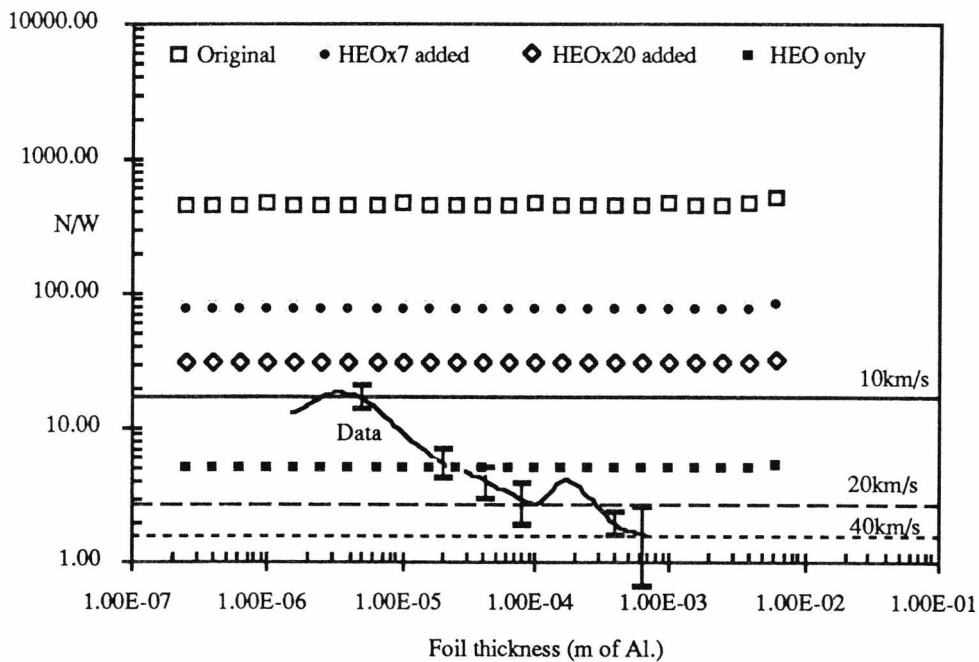


Figure 7.16 Comparison of N/W ratios for the measured data, varying content of HEO in the orbital model distribution and varying V_{pe} for the interplanetary model.

Figure 7.4 shows that the Space/West flux ratio could be gained from a space debris orbit distribution indicated by Kessler (HEO x 20) coupled with an interplanetary distribution

with a mean 25kms^{-1} . It is most noticeable from the figure 7.15 and 7.17 that the East/West and South/West ratio seems to point towards to definite space debris dominance below $\sim 30\mu\text{m } f_{\text{max}}$ accountable with the HEO x 20 orbital distribution and then a switch to an interplanetary particle dominance with a velocity distribution between 15kms^{-1} to 40kms^{-1} .

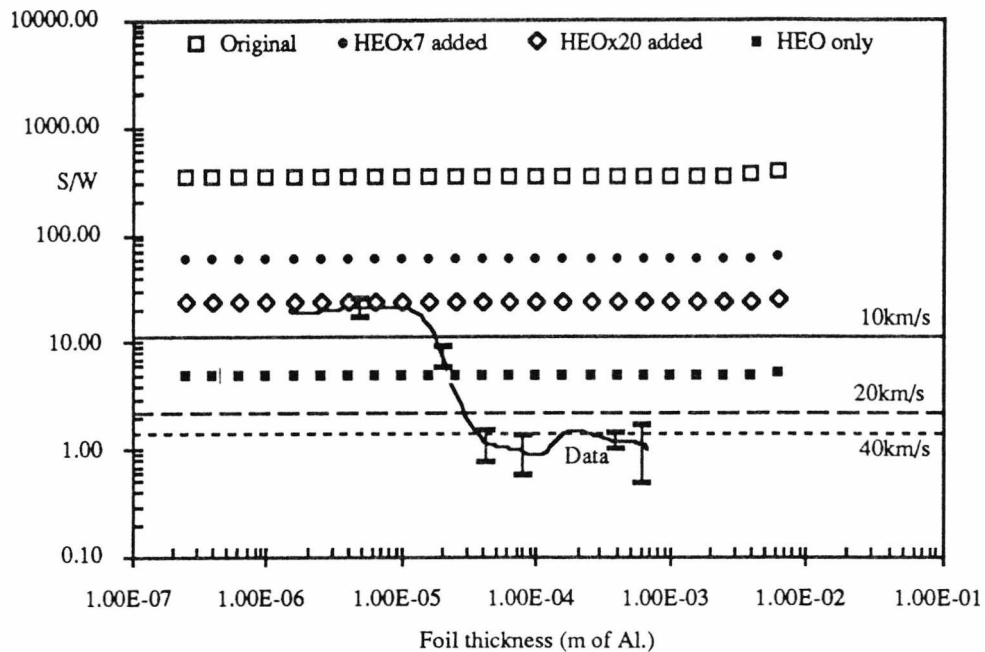


Figure 7.17 Comparison of S/W ratios for the measured data, varying content of HEO in the orbital model distribution and varying V_{pe} for the interplanetary model.

Now it follows that if the Sp/W ratio is taken as 2 from the USS model result using an enhanced HEO x 20 orbital distribution then using the E/W, N/W and S/W ratios, the space debris component for these faces may also be predicted and compared to figures 7.8 through to 7.10. Figures 7.18 through to 7.20 show the East, North and South anthropogenic orbital debris as compared with the measured data, predicted interplanetary component and the sum of the predicted fluxes for those faces (using a $V_{pe} = 24\text{kms}^{-1}$). It is clear that there is an inconsistency in assuming that once the predicted interplanetary component is determined then the difference with the measured data is accountable as anthropogenic space debris. Figure 7.18 shows that the anthropogenic orbital debris component could account for the measured flux above $50\mu\text{m } f_{\text{max}}$, below

which there is still an excess. This is a similar prediction for the North face, illustrated in figure 7.19, with the accountable excess appearing around the $30\mu\text{m } f_{\text{max}}$.

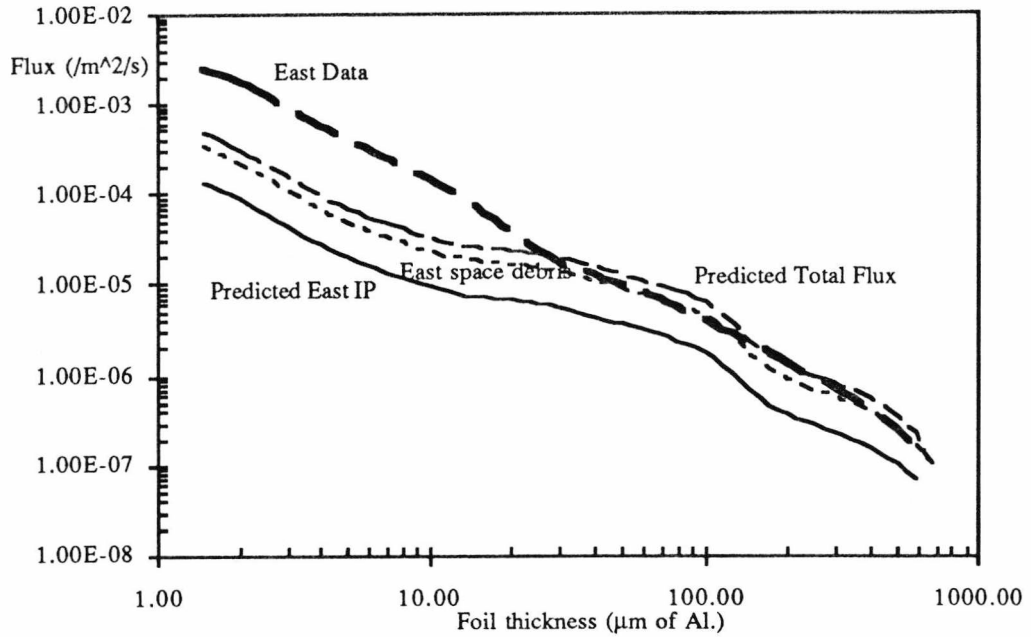


Figure 7.18 Comparison of East data with East IP predicted, East anthropogenic space debris calculated from E/W ratio from HEOx20 debris distribution and the sum of the two predictions. ($V_{pe}=24\text{kms}^{-1}$).

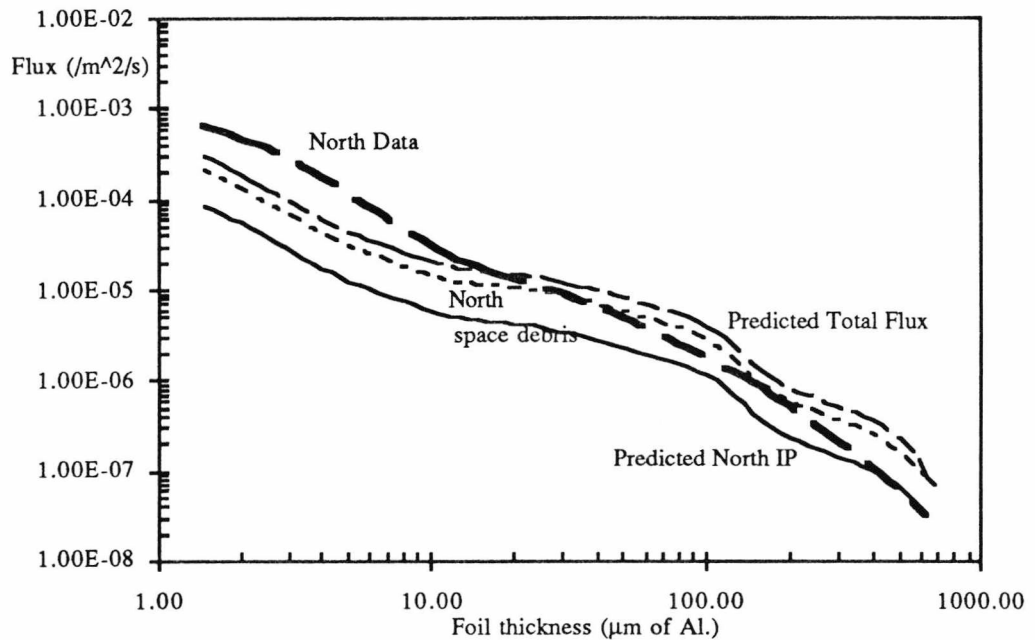


Figure 7.19 Comparison of North data with North IP predicted, North anthropogenic space debris calculated from N/W ratio from HEOx20 debris distribution and the sum of the two predictions. ($V_{pe}=24\text{kms}^{-1}$).

It is worthwhile noting here that the sum of the predicted fluxes exceeds that of the measured flux data.

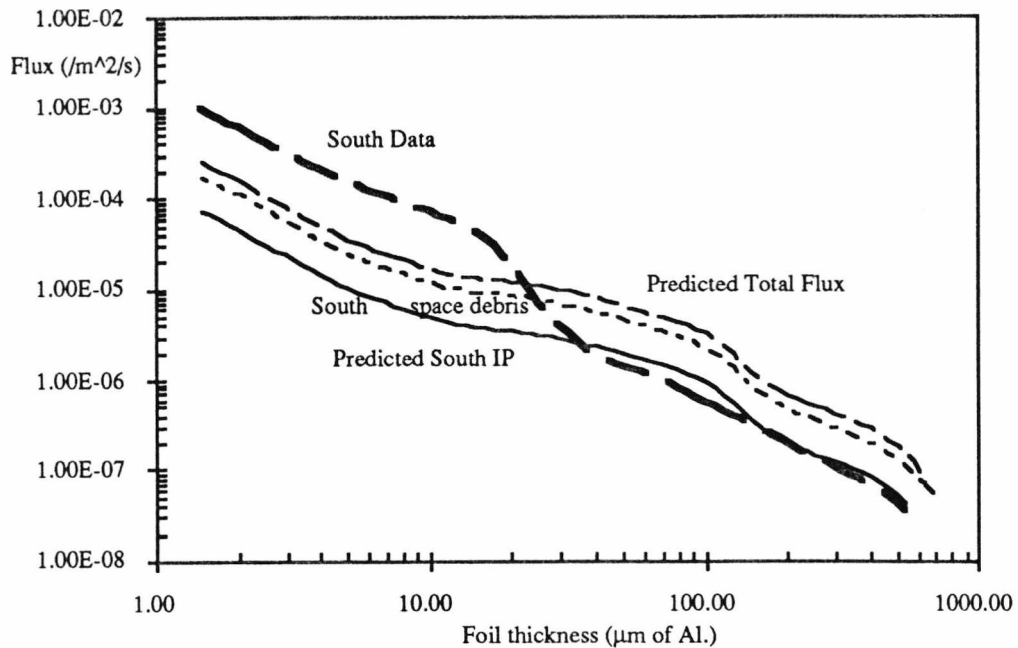


Figure 7.20 Comparison of South data with South IP predicted, South anthropogenic space debris calculated from S/W ratio from HEOx20 debris distribution and the sum of the two predictions. ($V_{pe}=24\text{kms}^{-1}$).

In figure 7.20 the opposite is true, where the predicted interplanetary component appears to satisfy the flux data for $40\mu\text{m } f_{\text{max}}$ and above and still an excess below this not accounted by the anthropogenic space debris prediction. In fact the space debris prediction is a gross over estimation on this face.

7.3.2 Probable Causes for Flux Differences

It is clear then that the models are not predicting the measured fluxes that are seen on the LDEF with the accuracy required to determine the origin of impactor. There seems to be a definite assymetry in both the interplanetary media and the anthropogenic orbital debris environment that is seen on the LDEF.

Current analysis at the USS by Neil McBride {7.12} is leading to an assymetry in the interplanetary media caused by the passage of meteor streams and comets intersecting

the Earth's orbit during LDEF's excursion in LEO. The analysis shows that the North face of LDEF would receive a higher flux than the South face, which could account for the disparity between predicted flux and measured flux. To account for this a lower predicted space debris component would be required, which would also lower the South face components and bring the over prediction more comparable to the measured data. This, however, still leaves the South and East face with an accountable excess at the lower size range.

Now if the assumption of an isotropic interplanetary particle distribution is in error there could also be errors in the assumptions in the orbital debris model, as described in Chapter 6. In terms of anthropogenic space debris the orbit distribution in geocentric space determines the flux on the LDEF. The assumptions of every particle size existing in every orbit, the randomising of nodes, line of apsides particle position in the orbit (true anomaly) leads to a very symmetric flux distribution on the LDEF. However, it is known that the rate of decay, and thus orbit distribution, of small particles is governed greatly by solar activity and as such there will be a definite size/orbit distribution. It has been shown that if the orbit distribution of space debris is taken utilising the true anomaly then an asymmetry is seen on the spacecraft (Flury et al . 1992) {7.13}. In this analysis the spacecraft modelled is the International Space Station Freedom which will utilise an orbit almost identical to that of the LDEF. The results show that the asymmetry is in favour of the right hand direction, or in terms of the LDEF, the South face and by a factor of 2. If this was the case for the smaller particles then the South face would receive a higher flux than the North face, thus accounting for the measured flux.

If one were to assume that a positive asymmetry toward the North face exists for the interplanetary distribution and positive asymmetry exists for the anthropogenic space debris distribution but towards the South face, then both would be seen on the East and West faces, depending upon the exact orbit asymmetry. The flux would still be higher on the East face because of the relative increase in impact velocity and the orbit geometry of space debris impacts. The South space debris asymmetry would have to be larger than

than the North interplanetary assymetry to account for the higher flux seen on the South face when compared to the North face. It is seen in Chapter 4 that the South face flux dominates the North face flux until $f_{max} \sim 30 \mu m$ whereas one would expect that the North Face would dominate over the whole size range due to the 8° offset and a geocentric isotropic flux distribution.

The USS space debris model uses the known orbit distribution and is therefore 3D in nature. The predicted results for the space debris component can be compared to the Kessler model, noting that the Kessler model is only 2D in that it assumes circular orbits for space debris (Chapter 6). The Kessler model has been adapted to calculate the K Factors required to transform an LDEF face flux to a comparable Kessler flux {7.1}. The Kessler model was run for the East, North and South faces with the K Factors and mean velocity being determined to be:

$$\begin{array}{ll}
 K_{East} = 2.64 & V_{East} = 8.25 \\
 K_{North} = 1.69 & V_{North} = 7.12 \\
 K_{South} = 1.11 & V_{South} = 6.32 \quad (7.6)
 \end{array}$$

with the input parameters for the model being height=458km, inclination=28.5°, Year 1987, Solar flux=90Jy, Growth rate=0.1.

Figure 7.21 shows the comparison of the Kessler model run with the above parameters and the orbital components converted to a Kessler distribution by dividing the flux by the appropriate Kessler K Factor. The orbital components are converted to mass using the McDonnell & Sullivan equation (Chapter 3) with a particle density of 2.71gcm^{-3} . They appear to match well the initial deployment debris environment, when taking into account the discussions on the possible interplanetary and space debris assymetries, although are somewhat higher above 10^{-8}g , this is probably due to the assumptions of circular orbits under estimating the actual space debris flux. The predicted anthropogenic space debris from the USS model is also illustrated and this appears to fit well between the possible deployment and retrieval flux for the small sizes but again over estimates the flux above 10^{-8}g .

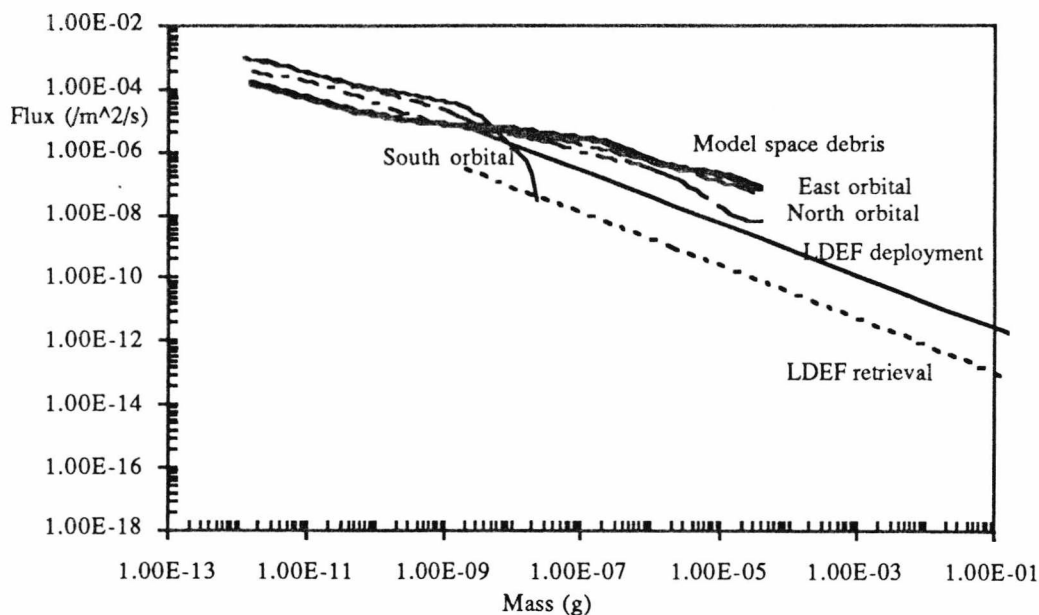


Figure 7.21 Comparison of the orbital components deduced from LDEF, the anthropogenic space debris deduced from HEOx20 orbit distribution and the Kessler model for LDEF deployment and retrieval.

It is somewhat difficult to compare the results as the difference between a 2D and 3D model are great and it is only due to the results of such comparisons and with LDEF data that the full merits of 3D anisotropic models are being realised.

7.4 Particle Density Distribution from Penetration Data

7.4.1 F_{max} Conversions for Space Face MAP D_H Data

In Chapter 3 various penetration equations were introduced to explain hypervelocity impacts in three scenarios, semi-infinite targets, supra marginal holes and marginal impacts. The Space face MAP experiment measured penetrations and as such a conversion to f_{max} is required, as the most convenient units to work in. This conversion can be obtained in a number of ways utilising the equations described in Chapter 3, with the appropriate assumptions.

The C program FMAX.C has been written to convert hole sizes to f_{\max} given the hole sizes and entering values for the prompted parameters, with a choice of penetration equation. Figure 7.22 illustrates the program's user interface and parameters required. The penetration equations used are the CMD equation (3.15), McDonnell and Sullivan (3.6) and the McDonnell equations 1992A,B,C (3.7 to 3.9) [7.14]. This program can be used to determine particle diameter and f_{\max} from D_H measurements using the full CMD equation, or alternatively the program FMAXD.C can be used to determine f_{\max} from particle diameters for any of the 5 equations listed above.

Silent?

Which equation for converting hole diameter to fmax?

1. Full CMD
2. McD&S 1992
3. McD 1992A
4. McD 1992B
5. McD 1992C

Count to flux multiplier?

Velocity (km/s)?

Foil thickness (microns)?

Projectile density (g/cc)?

Target density (g/cc)?

Strength of Al. (MPa)?

Target strength (MPa)?

Ballistic Limit?

Name of input file?

Name of output file?

Figure 7.22 User request for the program FMAX.C to convert D_H to f_{\max} utilising a choice of penetration equations and user's choice of ballistic limit.

The Space face D_H distribution for the aluminium surfaces (as illustrated in Chapter 4) is used as the initial data set. Using FMAX.C and the CMD equation one can convert D_H to f_{\max} values assuming a particle density and velocity. Figures 7.23 and 7.24 show the relationship of d/f with D_H/f as a function of density and velocity. It is

clear that for a constant velocity and a given D_H the particle size varies drastically with particle density.

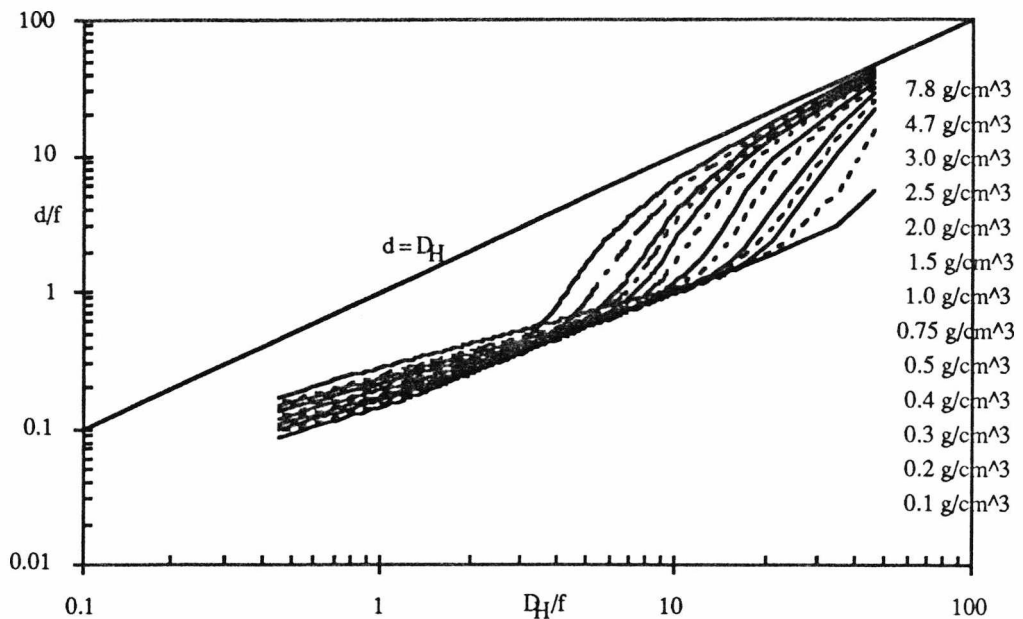


Figure 7.23 Relationship between d/f and D_H/f as a function of density using FMAX.C and the CMD equation with velocity= 16kms^{-1} .

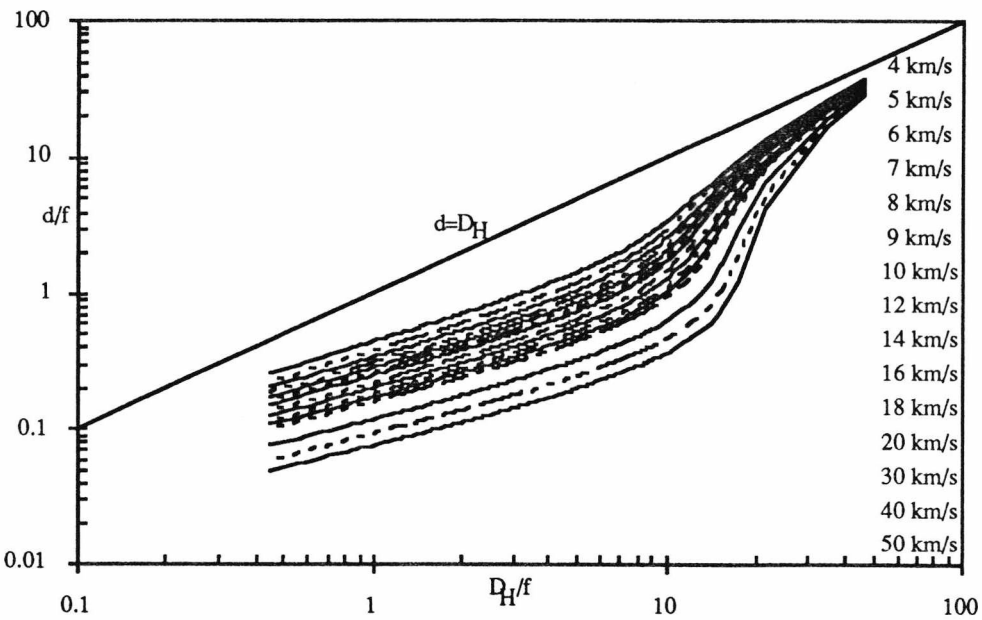


Figure 7.24 Relationship between d/f and D_H/f as a function of velocity using FMAX.C and the CMD equation with particle density= 1gcm^{-3} .

For a given particle size, velocity, with constant target density, the particle density decreases as the D_H value increases. This is due to the particle compressing on impact and spreading out forming a larger D_H . If the same particle were to hit the same target but with a higher particle density then the particle would simply punch out a hole and effectively not notice the target, thus as particle density increases D_H approaches d , keeping all other parameters constant.

This would suggest that in converting D_H to f_{max} values more emphasis is required on selecting the correct particle density than velocity. Figures 7.25 and 7.26 illustrate the conversion of Space face D_H to f_{max} keeping either velocity or density constant and varying the other parameter, also plotted is other Space face data from SDIE, Clamps and surface craters on MAP.

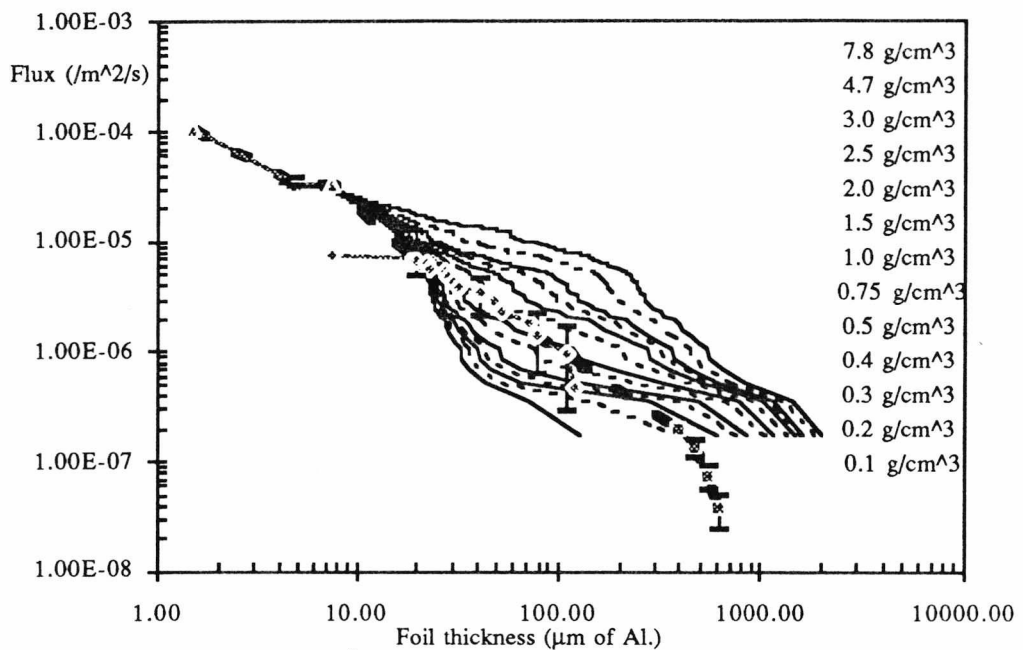


Figure 7.25 CMD conversion of MAP Space face D_H to f_{max} with constant velocity = 16kms^{-1} and varying particle density.

The impact velocity chosen in figure 7.25 is 16kms^{-1} , which corresponds to a $V_{pe}=24\text{kms}^{-1}$, as discussed in section 7.2.2. This shows very graphically the effect of changing the particle density in calculating f_{max} . The density chosen in figure 7.26 is 1gcm^{-3} , and this shows that at large f_{max} values the velocity plays a significant role,

however over the majority of the distribution the effect of changing velocity is minimum compared with changing particle density.

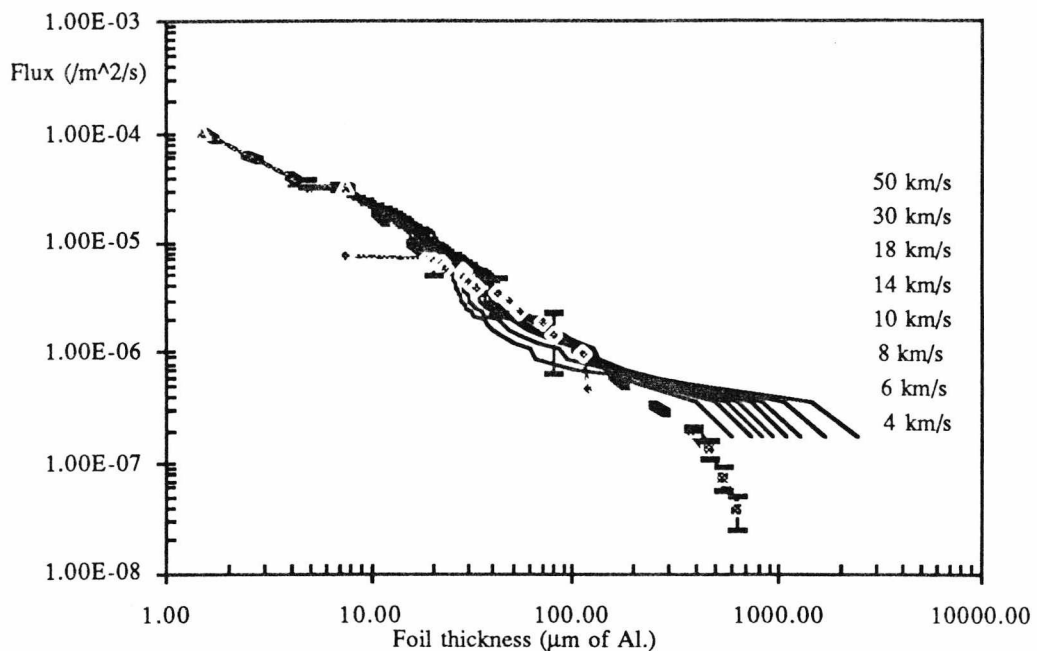


Figure 7.26 CMD conversion of MAP Space face D_H to f_{max} with constant particle density = 1 gcm^{-3} and varying impact velocity.

7.4.2 Deriving a Density Function

It is clear from figure 7.25 that a possible particle density distribution is required to convert D_H values to f_{max} that are in agreement with other experimental data. Assuming that an average impact velocity of 16 km s^{-1} is the most probable, from the modelling, then a further examination of figure 7.25 can reveal a particle density distribution.

It appears that for particles forming $f_{max} < \sim 20 \mu\text{m}$ that a number of particle densities are probable and mostly above 1.0 gcm^{-3} . As f_{max} increases a particle density of $\sim 1.0 \text{ gcm}^{-3}$ satisfies to $\sim 200 \mu\text{m}$ f_{max} and thereafter a somewhat lower particle density. This would be in line with the reasoning given earlier in this Chapter that anthropogenic space debris particles dominate at the lower sizes ($f_{max} < \sim 40 \mu\text{m}$), exhibiting a high particle density of the order of 4.7 gcm^{-3} , and the larger sizes being dominated by

interplanetary particles, with a particle density of $\sim 1.0\text{gcm}^{-3}$. The existence of lower density particles $< 1.0\text{gcm}^{-3}$ can be attributed to cometary ice particles and non-solid particles ($d \geq 50\mu\text{m}$) comparable to $f_{\text{max}} \geq 300\mu\text{m}$, intersecting the Earth. Such densities (e.g. $\rho = 0.5\text{gcm}^{-3}$) have been used in the NASA JSC models {7.15} and indeed particle densities varying from 0.16gcm^{-1} to 4.0gcm^{-3} have been cited from various photographic and radar meteor observations. {7.16}.

The program FMAX.C has been adapted to include a density distribution, and renamed DHDENS.C, using a density distribution derived from figure 7.25 based upon $D_H = 0.6f_{\text{max}}$ the ballistic limit, as discussed in Chapter 3. It is therefore possible to convert the f_{max} value into a D_H value at points where the f_{max} density profiles intersect the f_{max} experimental data distribution. This then gives the required density D_H relationship to convert the Space D_H values to f_{max} in agreement with the experimental f_{max} distribution. Table 7.2 illustrates the density profile in terms of f_{max} and D_H that is used in converting D_H to f_{max} illustrated in figure 7.27.

f_{max}	D_H	Density (gcm^{-3})
>400	>240	0.1
400 - 333.33	240 - 200	0.2
333.33 - 250	200 - 150	0.3
250 - 190	150 - 114	0.5
190 - 150	114 - 90	0.75
150 - 125	90 - 75	0.9
125 - 50	75 - 30	1
50 - 16.67	30 - 10	1.25
16.67 - 9.16	10 - 5.5	2
<9.16	<5.5	4.7

Table 7.2 Density profile used in figure 7.27.

It is clear from figure 7.27 that a density distribution similar to this is required to convert Space face D_H values to f_{max} values. The density profile given in table 7.2 is in agreement with the discussions on anthropogenic space debris and interplanetary particulate distributions as derived from the modelling.

The examination of flux data tends to the theory of two populations impacting the Space face and it therefore comes as no surprise that this density profile when converted from D_H to d values (using the CMD equation) is quite different to the meteoroid density distribution used by NASA JSC.

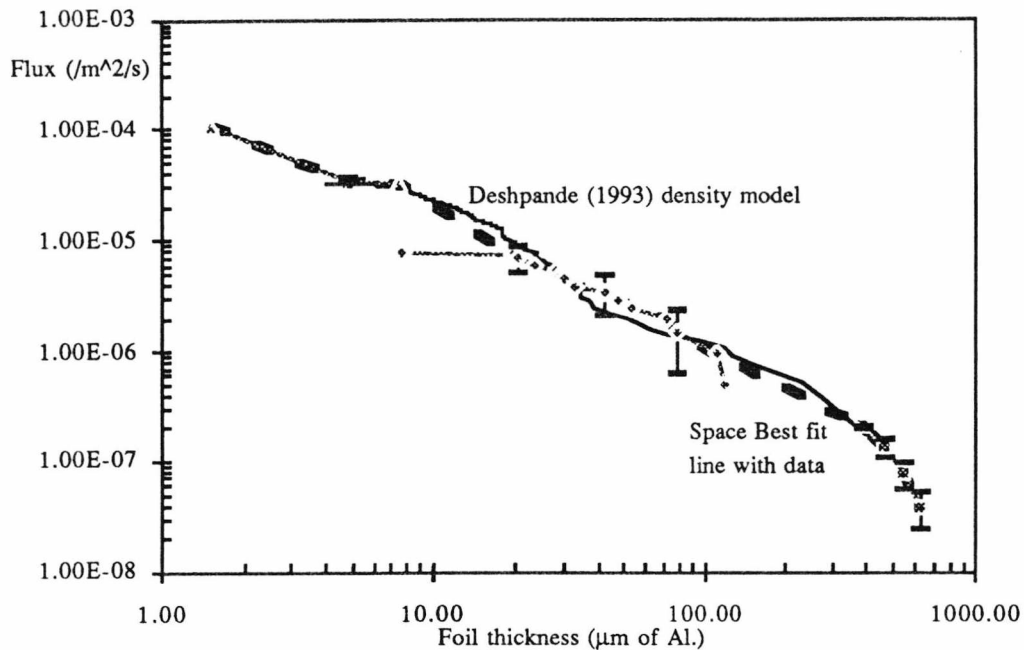


Figure 7.27 Deshpande density function, as given in table 7.2, is used to convert D_H to f_{max} for MAP Space face data, with $V=16\text{kms}^{-1}$ using the CMD equation and compared to the Space best fit line.

Figure 7.28 shows the comparison of the Deshpande density profile (LDEF Space face data) with both the Divine Halley model (1981) {7.17} and the NASA JSC meteoroid model {7.15}. The Deshpande model is in agreement with the meteoroid models for most of the size range however excursions do exist and are due to the space debris content at lower sizes and the need for somewhat lower densities at large sizes to account for Space face data in the SDIE experimental range.

The NASA model density, which is only meteoroid in origin, has been used to convert D_H to f_{max} for the Space face and is illustrated in figure 7.29, showing that for larger f_{max} values a lower density is required but also that indeed a meteoroid density profile could account for all Space face impacts $<100\mu\text{m } f_{max}$. This is not surprising when noting that only $\sim 7\%$ of impacts on the Space face can be attributed to

anthropogenic space debris ($\rho=4.7\text{gcm}^{-3}$), based upon the USS model, and hence the average particle density would be $\sim 1\text{gcm}^{-3}$ for all impacts detected on the Space face.

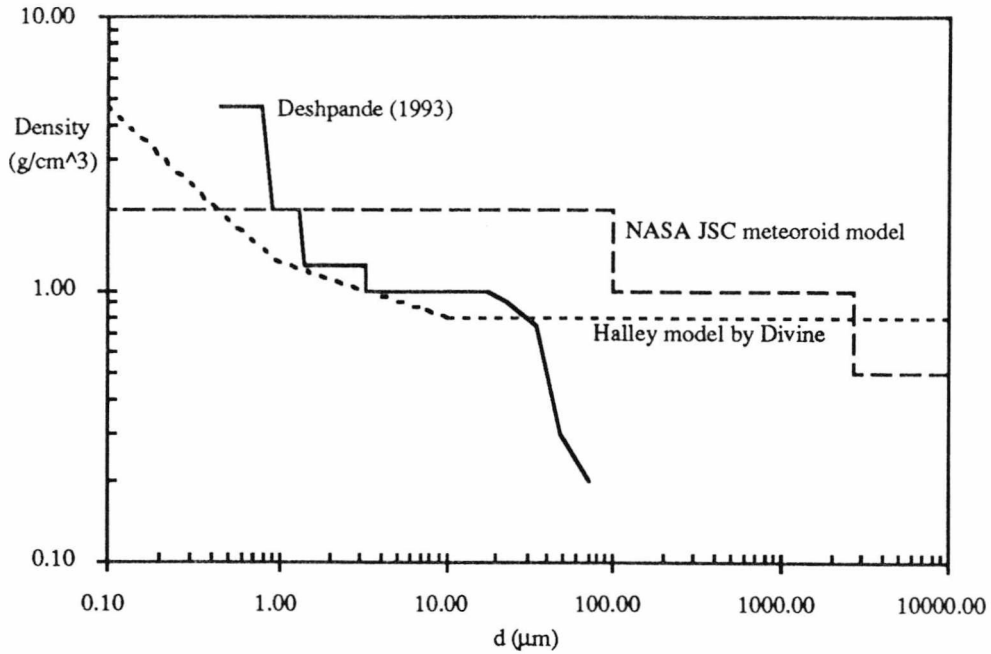


Figure 7.28 Comparison of the Deshpande density profile with that given by NASA JSC models and the Divine Halley model.

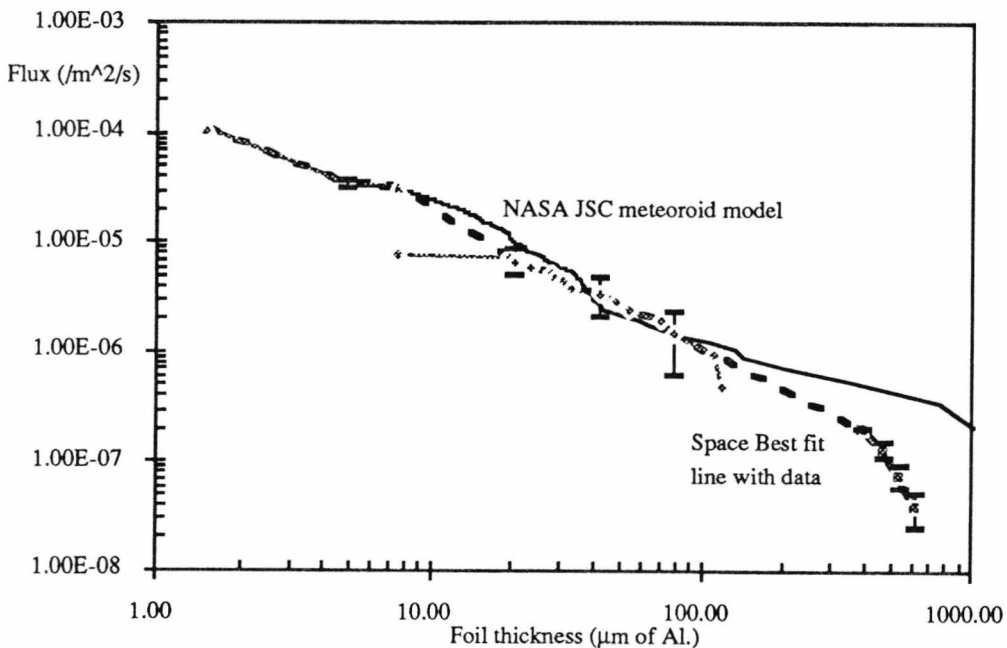


Figure 7.29 Conversion of MAP Space face D_H to f_{\max} using the NASA JSC meteoroid density profile and the CMD equation with $V=16\text{kms}^{-1}$.

7.5 *USS Modelled Impact Fluxes*

7.5.1 *Interplanetary and Space Debris Fluxes*

The USS Interplanetary and Space debris model was briefly introduced in Chapter 6 as a means to predict impact fluxes on the LDEF. For each population (interplanetary or debris) the numbers and velocities of particles as a function of geocentric direction are determined. The LDEF is flown through this distribution to give the relative impact probabilities, direction and velocities for the two populations, with the LDEF orbit being assigned an altitude of 458km, inclination of 28.5°, and an offset velocity vector of 8° from the nominal East face and a tilt of 1.1° toward the East face (Row 9) {7.18}.

The space debris inputs to the model have already been discussed in Chapter 6 and the limits are expressed in the assumptions of random line of apsides and nodes. There are orbits (Molniya) with no advance of apsides that would present an asymmetry to the modelling, but it is assumed that any fragmentation event will place objects into slightly different orbits to the parent orbit thus inducing a randomising of nodes and apsides. The input data files on orbit distribution and size distribution are those that are discussed in Chapters 5 and 6. The model is run for an altitude bin of ± 100 km about the LDEF altitude.

The interplanetary particle model utilises the Erickson (1968) velocity distribution {7.19} and the Grün (1980) size distribution {7.3}, also discussed in Chapter 6. The model has incorporated a penetration equation relationship developed by Hill (1989) {7.20} to determine the foil thickness penetrable and a simple empirical relationship for crater diameter. The parameters are well defined as V , particle velocity, ρ_P and ρ_T the particle and target densities and σ_P , σ_T the particle and target tensile strengths.

$$\frac{f}{d} = 0.60 \left(\frac{\rho_P}{\rho_T} \right)^{0.26} \left(\frac{\sigma_T}{\sigma_0} \right)^{-0.08} V^B \quad (7.7)$$

where

$$\beta = 0.69 \left(\frac{\rho_P}{\rho_T} \right)^{0.09} \tag{7.8}$$

and

$$D_H = f/0.75 \tag{7.9}$$

The main purpose of the model is to investigate the source of impacting material as a function of particle size, and determine the relative contributions of space debris and interplanetary particles. Figures 7.30 and 7.31 show the results of the model run for 5µm foil perforation and 0.5mm crater diameter compared to the data obtained from the LDEF for these size ranges.

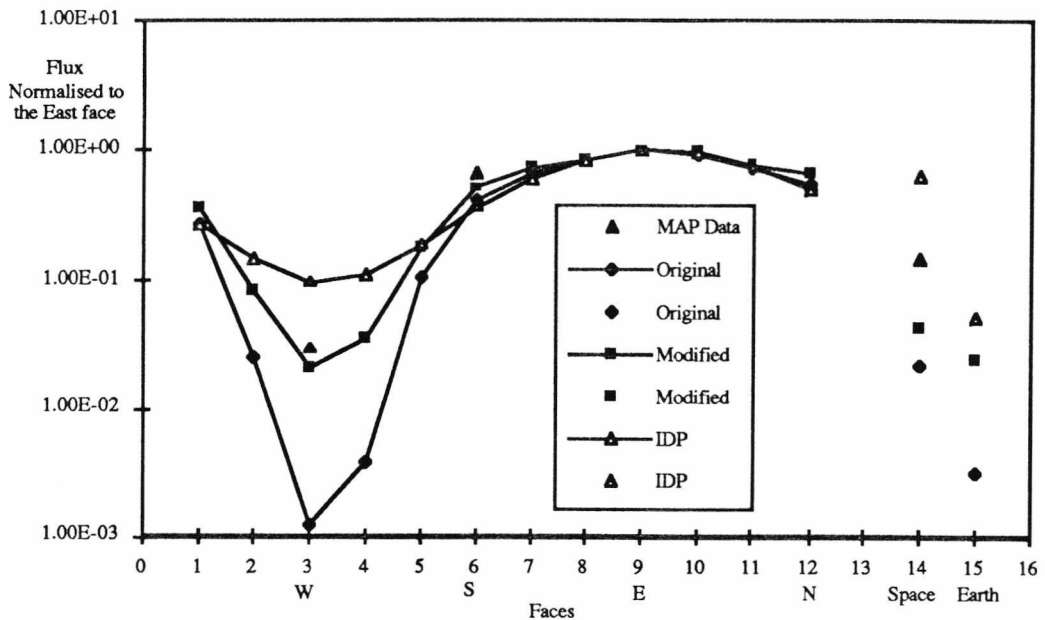


Figure 7.30 Comparison of IDP model with both the DISCOS orbital distribution and HEOx20 distribution space debris models for 5µm foil thickness perforation. The flux is normalised to the East face and compared with MAP 5µm foil data.

The model fluxes for the space debris and interplanetary sources on each face of the LDEF are shown normalised to the East face and compared to the 5µm perforation data from MAP and the 0.5mm crater diameter data documented in the M+D SIG database. Although the models predict total combined fluxes within a factor of three of the observed values, absolute predicted fluxes from each source are not a reliable estimate of the relative contributions.

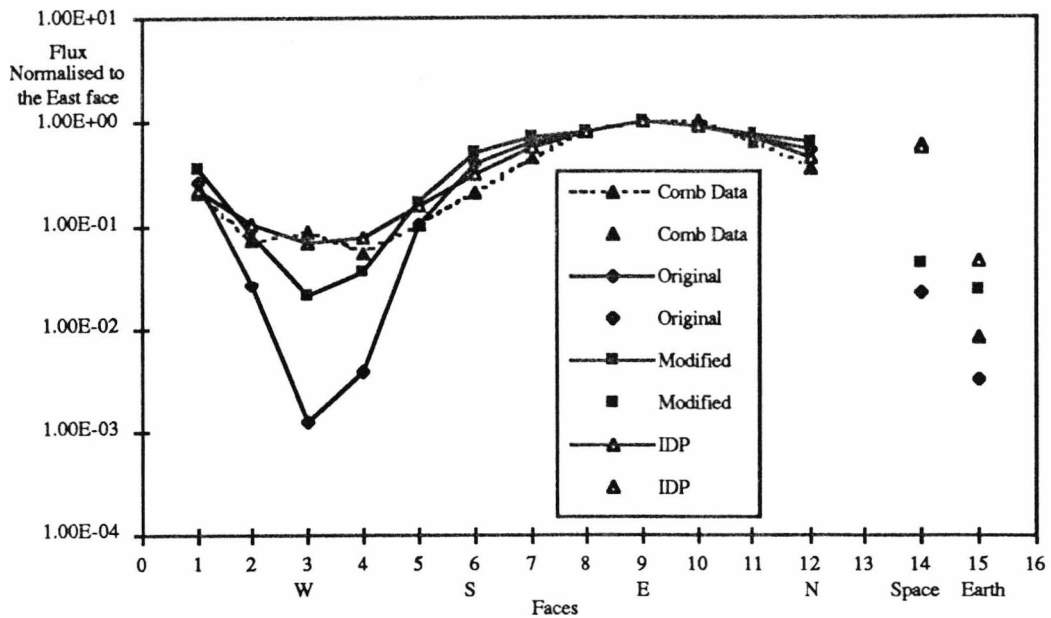


Figure 7.31 Comparison of IDP model with both the DISCOS orbital distribution and HEOx20 distribution space debris models for 0.5mm crater diameter. The flux is normalised to the East face and compared with M+D SIG 5mm crater diameter data.

This is mainly due to the uncertainties associated with the assumptions made in the space debris model. The only area of certainty that can be expressed would be in the verification of particle origin from residue chemistry from impacts. This would then shape the input model distributions and thus give a better accuracy on the model predictions. The ratios of East to West, and Space to Earth faces provide the best discrimination between the interplanetary particle and space debris, as has been discussed previously. The 5 μ m perforation data are consistent with a mixture of impacts from the two sources and illustrate the anomalous South to North ratio stated in Chapter 4. The 0.5mm craters appear to be predominately interplanetary in origin which differs somewhat to the results obtained by Bernhard et al (1992) {7.2}, showing a significant fraction of impacts attributed to space debris. This is probable the result of undersampling of the elliptical debris orbits and low inclination orbits discussed in Chapter 5 and 6.

To account for this undersampling the debris orbit distribution was altered to increase the low inclination, highly elliptical content as discussed in section 7.2.1. The results demonstrate an increase in debris impacts around the whole LDEF but with the

greatest change occurring on the trailing faces (West in particular) and only a small change on the leading faces. The change in orbit distribution also increase the number of impacts on the Earth and Space faces as can be seen in figures 7.30 and 7.31.

7.5.2 Comparison of Angular Distributions of Modelled Interplanetary and Space Debris Impacts

In determining impact rates on the LDEF the direction and velocity of particles is calculated. The angle at which particles can impact a given face on the LDEF is a function of the orbital characteristics of the particle and the LDEF. Hence it is possible to show the effects of the two particle sources in terms of angular distribution on a given face. This analysis can be used to determine the possible origin of impactor purely based upon crater morphology with a modelled direction (Newman et al., 1993 {7.6}, Mackay et al. (1993){7.21}).

The interplanetary particles are assumed to have an isotropic geocentric flux distribution, with the Erickson velocity distribution (see Chapter 6). At LDEF's altitude, Earth shielding removes particles from directions originating in a cone of semi-angle 73° from the Earth direction and an effective atmospheric altitude of 150km is used. The Grün mass distribution is used with a particle density of 1gcm^{-3} , and scaled for gravitational enhancement. Figures 7.32 through to 7.37 show the angular distribution of interplanetary particle impacts on the East, West, North, South, Earth and Space faces. The radial distance represents the impact incidence angle, the azimuthal directions are indicated with respect to other LDEF directions, and the height of each column represents the flux. It is clear that the interplanetary distribution is effected by the Earth shielding effect from figures 7.32 and 7.35 with the majority of impacts coming from a direction above the midline between the Space and Earth faces. The Space face (figure 7.37) shows the majority of impacts from the ram direction with very low flux counts for low angle impacts from the wake direction.

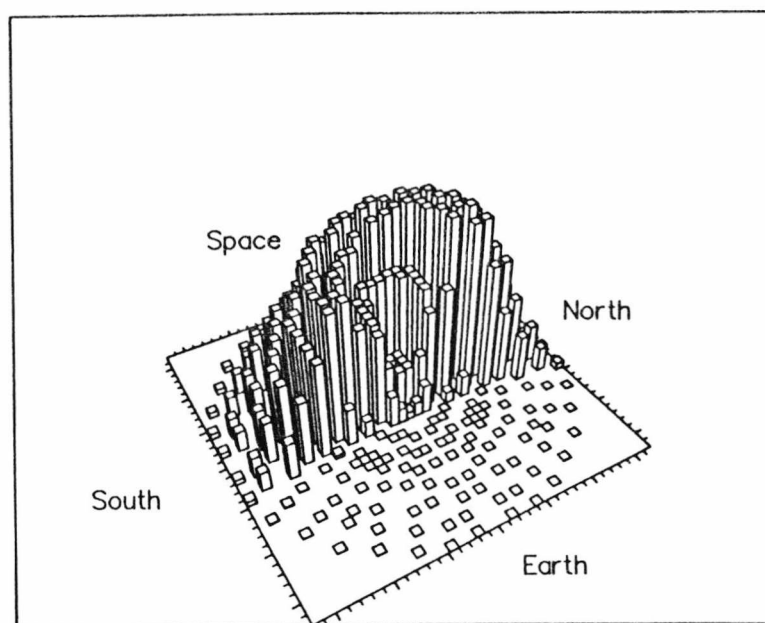


Figure 7.32 Angular distribution of interplanetary particles impacting the East face. Radial distance represents the impact incidence angle, with the azimuthal directions indicated. The height of each column indicates the flux. Flux scale $0 - 165 \times 10^{-8} \text{ m}^{-2}\text{s}^{-1}$.

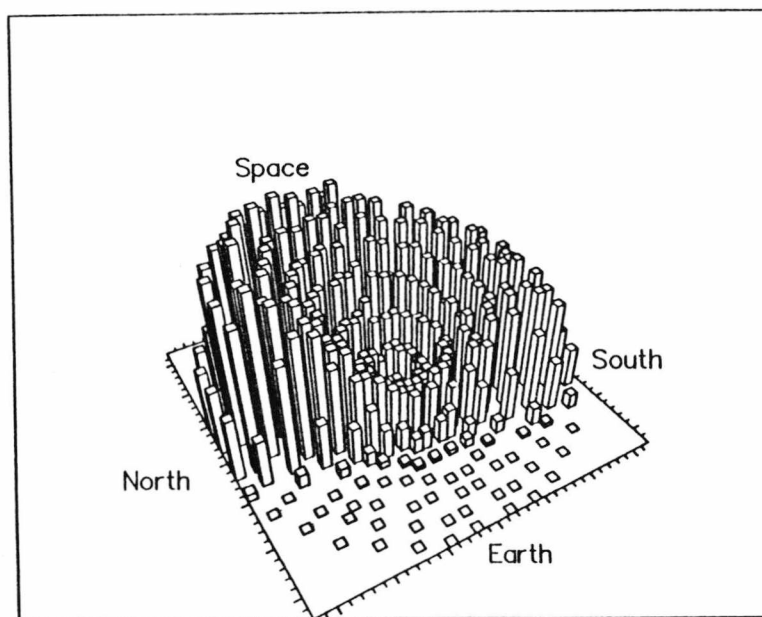


Figure 7.33 Angular distribution of interplanetary particles impacting the West face. As figure 7.32
Flux scale $0 - 11 \times 10^{-8} \text{ m}^{-2}\text{s}^{-1}$.

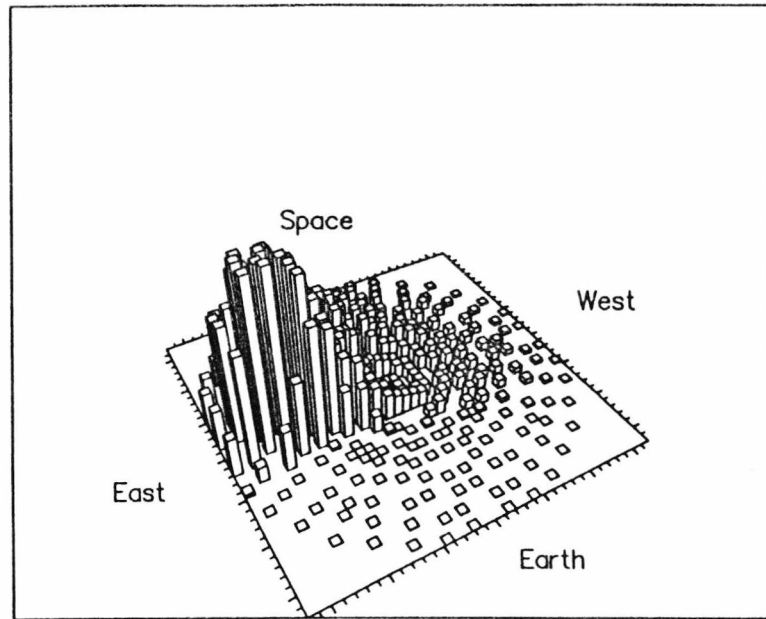


Figure 7.34 Angular distribution of interplanetary particles impacting the North face. As figure 7.32
Flux scale $0 - 165 \times 10^{-8} \text{ m}^{-2}\text{s}^{-1}$.

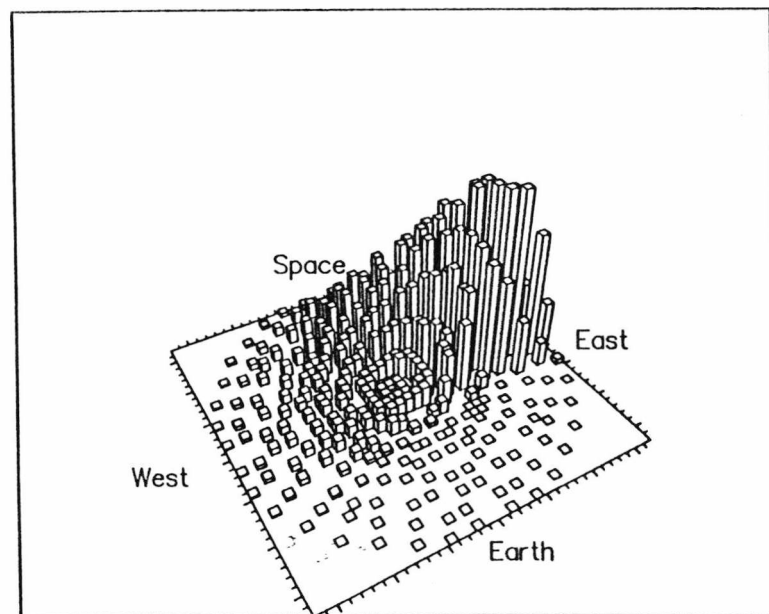


Figure 7.35 Angular distribution of interplanetary particles impacting the South face. As figure 7.32
Flux scale $0 - 110 \times 10^{-8} \text{ m}^{-2}\text{s}^{-1}$.

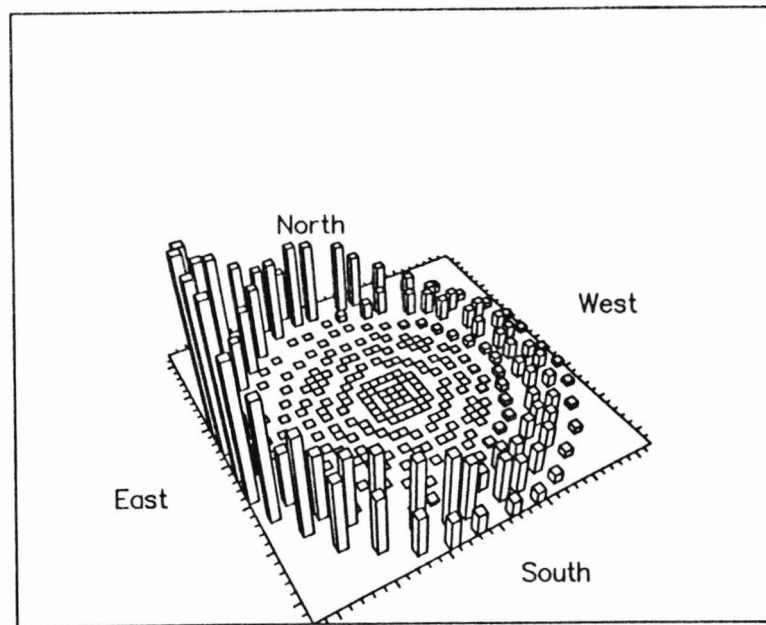


Figure 7.36 Angular distribution of interplanetary particles impacting the Earth face. As figure 7.32
Flux scale $0 - 38 \times 10^{-8} \text{ m}^{-2}\text{s}^{-1}$.

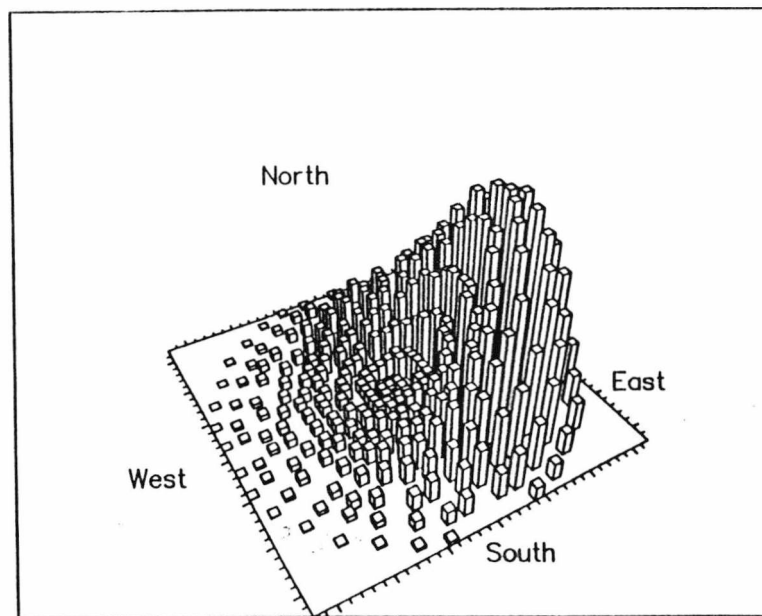


Figure 7.37 Angular distribution of interplanetary particles impacting the Space face. As figure 7.32
Flux scale $0 - 165 \times 10^{-8} \text{ m}^{-2}\text{s}^{-1}$.

The space debris model utilises the orbital distribution as described in Chapter 5, noting the shortfalls of this distribution in that HEO are undersampled, and the model described in Chapter 6. The Kessler size distribution modulated at larger sizes by DISCOS data, and a particle density of 2.8gcm^{-3} is used. Figures 7.38 through to 7.43 illustrate the distribution of debris impacts on the East, North, South, West, Earth and Space faces. The orientation and description of the axis is as in the interplanetary case (figures 7.32 to 7.37). As to be expected the debris distribution of impacts is quite different to the isotropic interplanetary distributions.

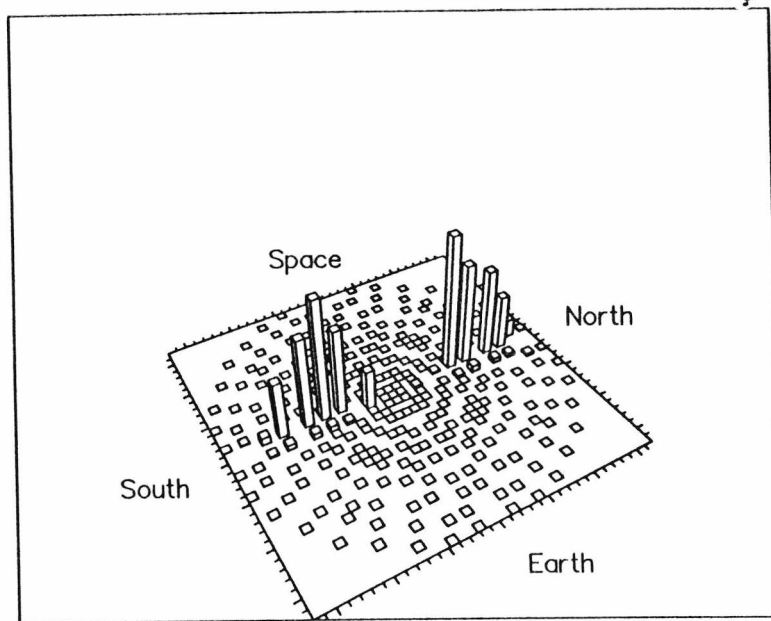


Figure 7.38 Angular distribution of Space debris, from DISCOS orbits, impacting the East face.
As figure 7.32
Flux scale $0 - 5500 \times 10^{-8} \text{ m}^{-2}\text{s}^{-1}$.

The East face (figure 7.38) shows the maximum flux with all the impacts emanating from a North/South direction slightly above the actual North/South line due to the 1.1° tilt. The shape is that which is to be expected from the “butterfly” distribution of space debris impacts on the ram face. The West face (figure 7.39) shows the lowest flux and impacts about the North/South line but with the majority coming from a southerly direction at low incidence due to the 8° offset.

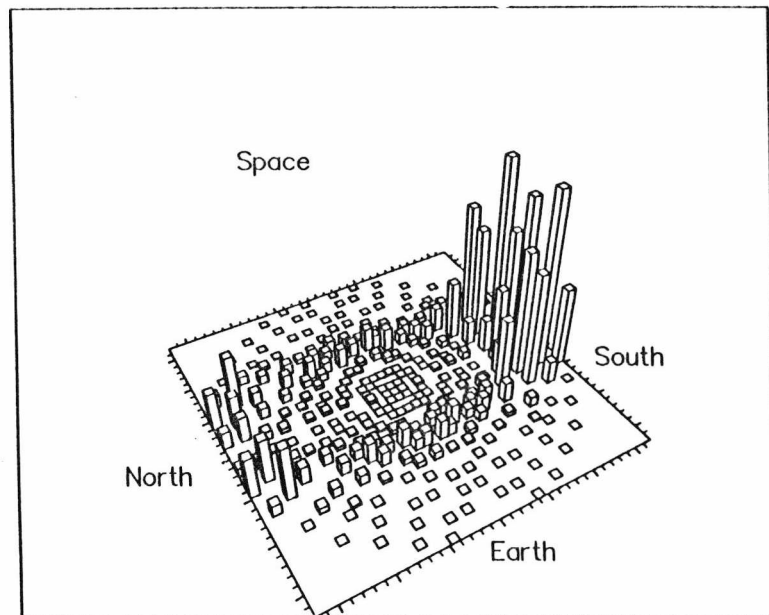


Figure 7.39 Angular distribution of Space debris, from DISCOS orbits, impacting the West face.
As figure 7.32
Flux scale $0 - 2.2 \times 10^{-8} \text{ m}^{-2}\text{s}^{-1}$.

The North and South faces (figures 7.40 and 7.41) show the impacts emanating from an easterly direction, above the East/West line (again due to the 1.1° tilt) but with the North flux somewhat higher than the South due to the 8° offset.

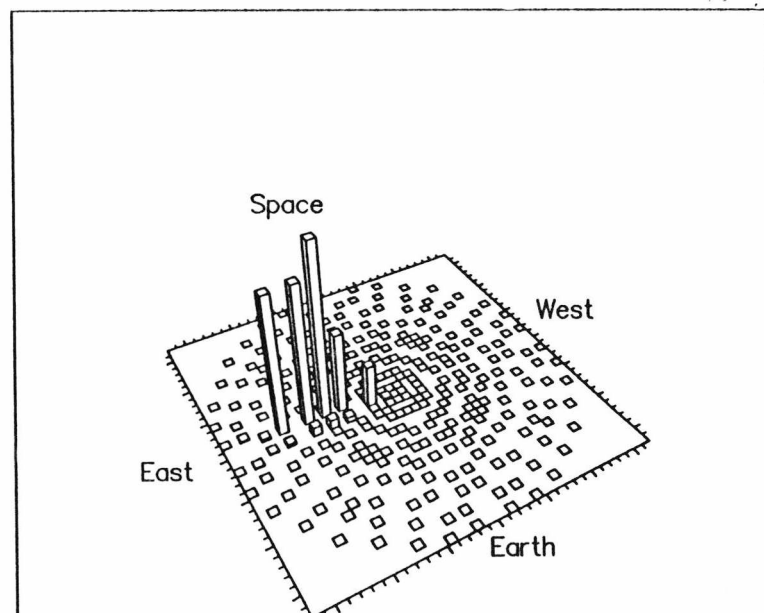


Figure 7.40 Angular distribution of Space debris, from DISCOS orbits, impacting the North face.
As figure 7.32
Flux scale $0 - 3850 \times 10^{-8} \text{ m}^{-2}\text{s}^{-1}$.

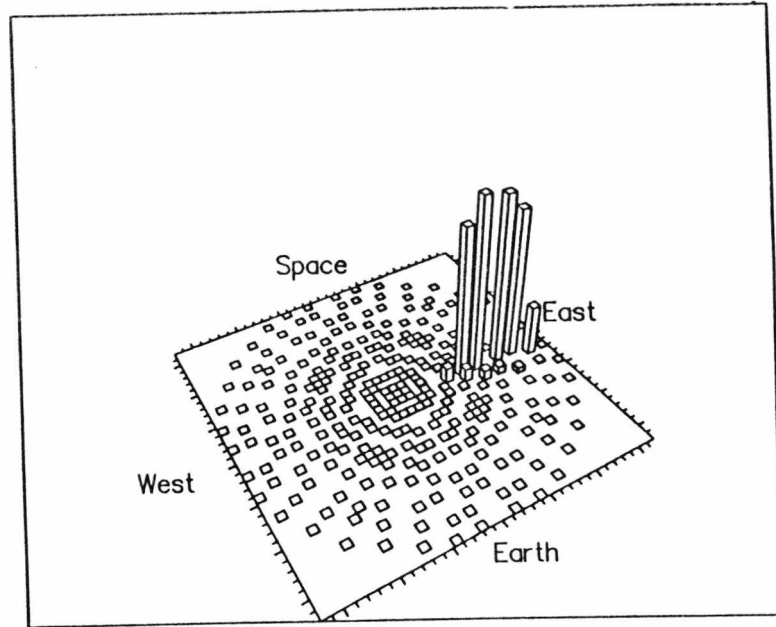


Figure 7.41 Angular distribution of Space debris, from DISCOS orbits, impacting the South face.
As figure 7.32
Flux scale $0 - 2750 \times 10^{-8} \text{ m}^{-2}\text{s}^{-1}$.

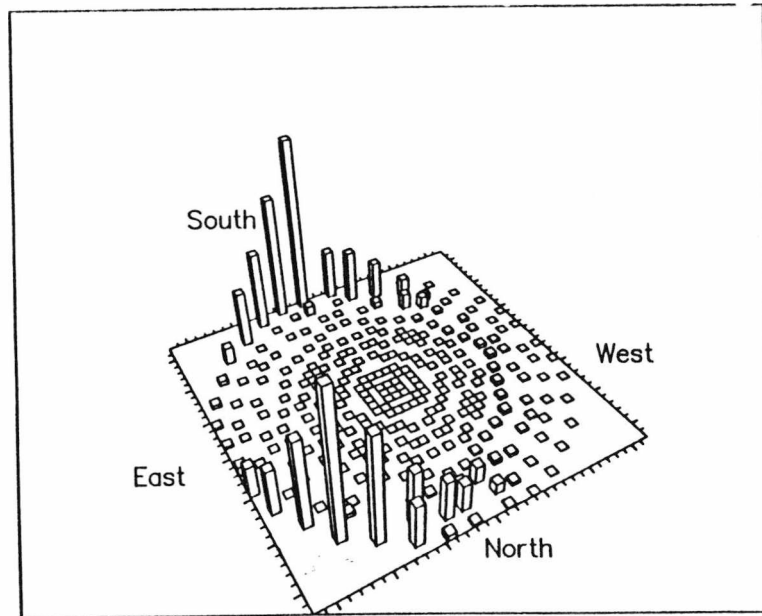


Figure 7.42 Angular distribution of Space debris, from DISCOS orbits, impacting the Earth face.
As figure 7.32
Flux scale $0 - 11 \times 10^{-8} \text{ m}^{-2}\text{s}^{-1}$.

The Earth and Space faces (figures 7.42 and 7.43) show the classical “butterfly” distribution offset by 8° toward the North face.

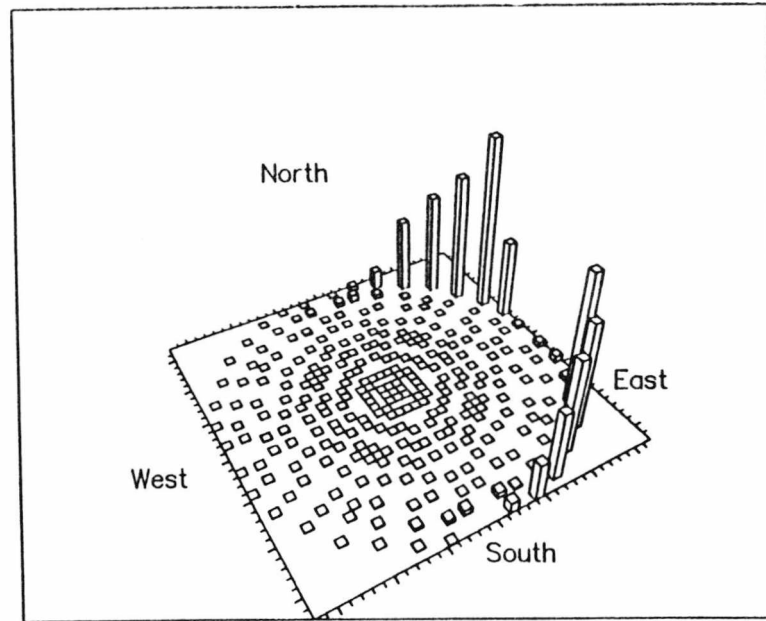


Figure 7.43 Angular distribution of Space debris, from DISCOS orbits, impacting the Space face.
As figure 7.32
Flux scale $0 - 110 \times 10^{-8} \text{ m}^{-2} \text{ s}^{-1}$.

Now if the orbital distribution is altered to account for the x20 increase in HEO debris then the debris distribution changes as illustrated in figures 7.44 through to 7.49.

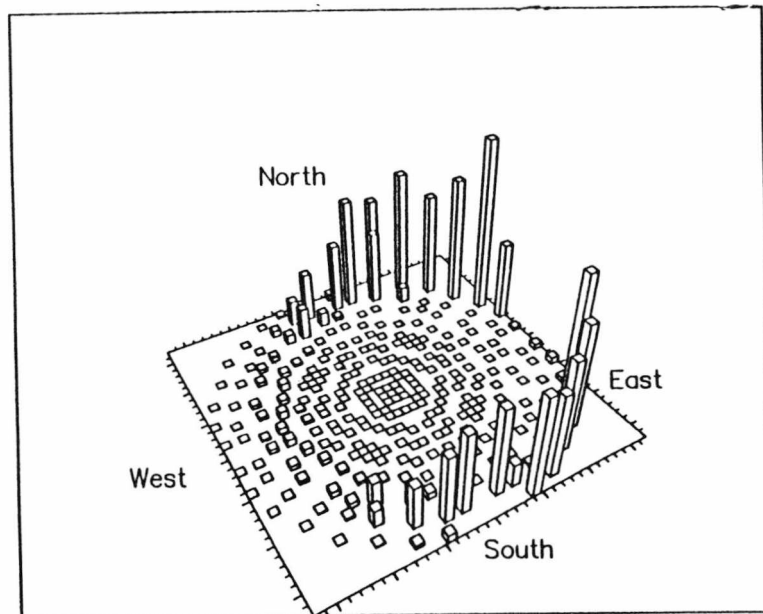


Figure 7.44 Angular distribution of Space debris, from DISCOS with HEOx20 orbits, impacting the Space face. As figure 7.32
Flux scale $0 - 110 \times 10^{-8} \text{ m}^{-2} \text{ s}^{-1}$.

The Space face direction distribution changes with more impacts coming from behind the LDEF as seen in figure 7.44.

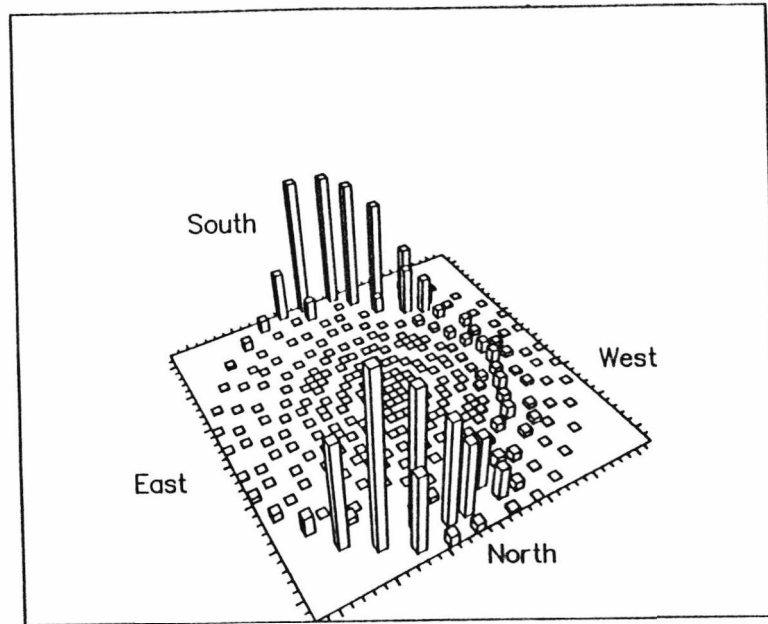


Figure 7.45 Angular distribution of Space debris, from DISCOS with HEOx20 orbits, impacting the Earth face. As figure 7.32
Flux scale 0 - $5500 \times 10^{-8} \text{ m}^{-2} \text{ s}^{-1}$.

The Earth face (figure 7.45) shows more impacts coming from steeper impact angles to the surface and more coming from the wake direction. The other faces remain the same in terms of spread and flux. The West face (figure 7.46) shows an increased flux and but with a similar direction distribution. The other faces (figures 7.47 through to 7.49), South, North and East remain practically the same as figures 7.41, 7.40 and 7.38.

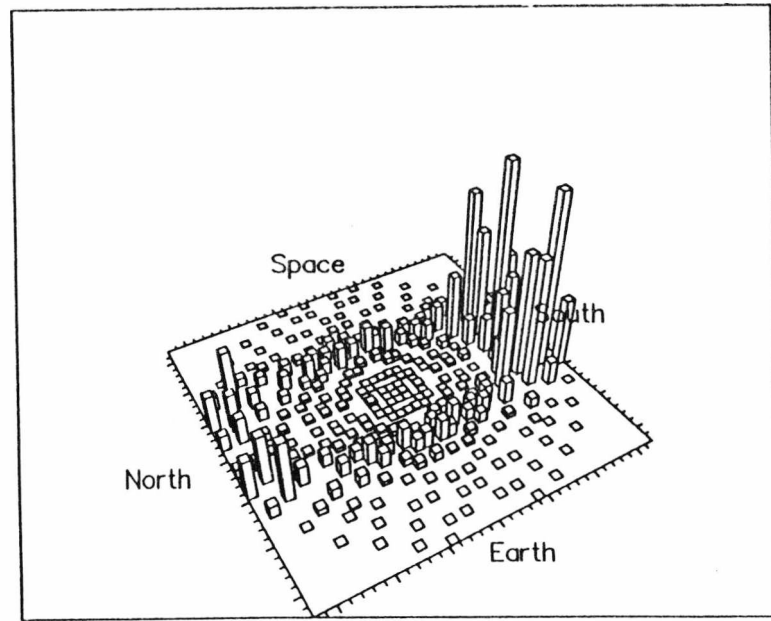


Figure 7.46 Angular distribution of Space debris, from DISCOS with HEOx20 orbits, impacting the West face. As figure 7.32
Flux scale $0 - 44 \times 10^{-8} \text{ m}^{-2}\text{s}^{-1}$.

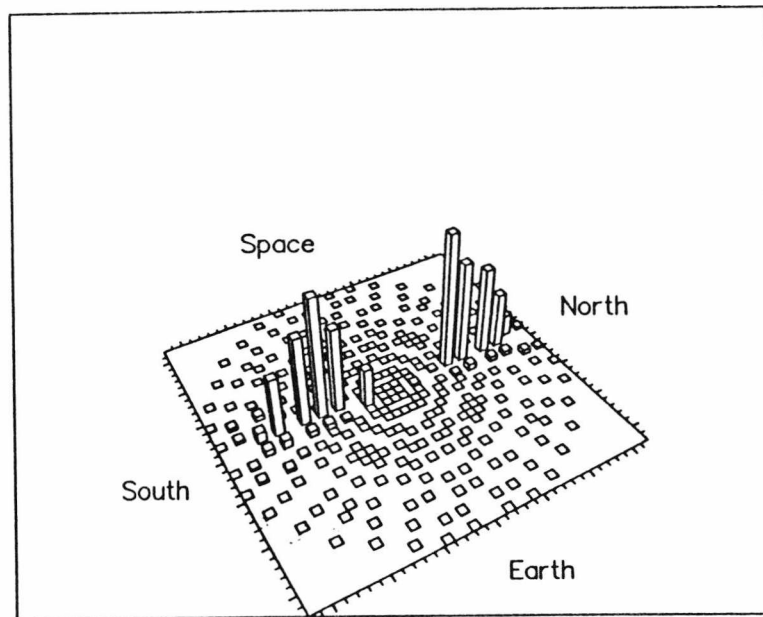


Figure 7.47 Angular distribution of Space debris, from DISCOS with HEOx20 orbits, impacting the East face. As figure 7.32
Flux scale $0 - 5500 \times 10^{-8} \text{ m}^{-2}\text{s}^{-1}$.

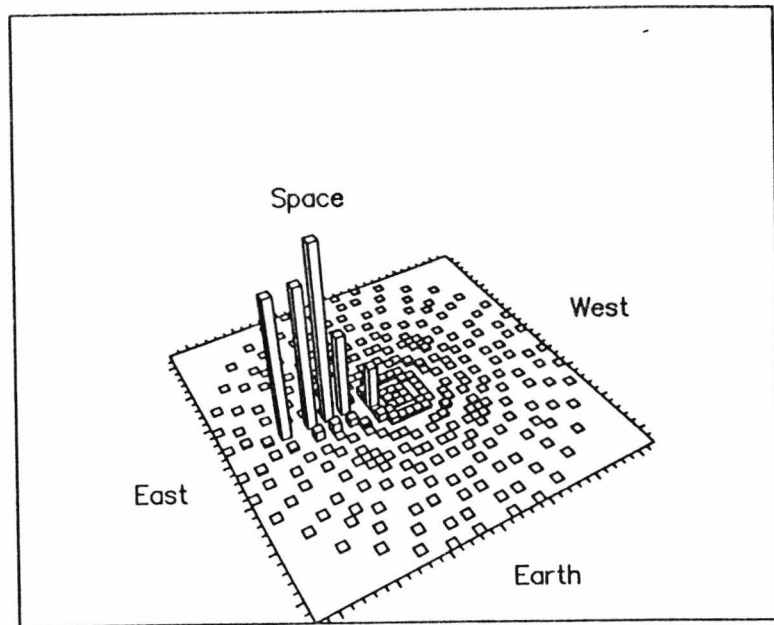


Figure 7.48 Angular distribution of Space debris, from DISCOS with HEOx20 orbits, impacting the North face. As figure 7.32
Flux scale $0 - 3850 \times 10^{-8} \text{ m}^{-2}\text{s}^{-1}$.

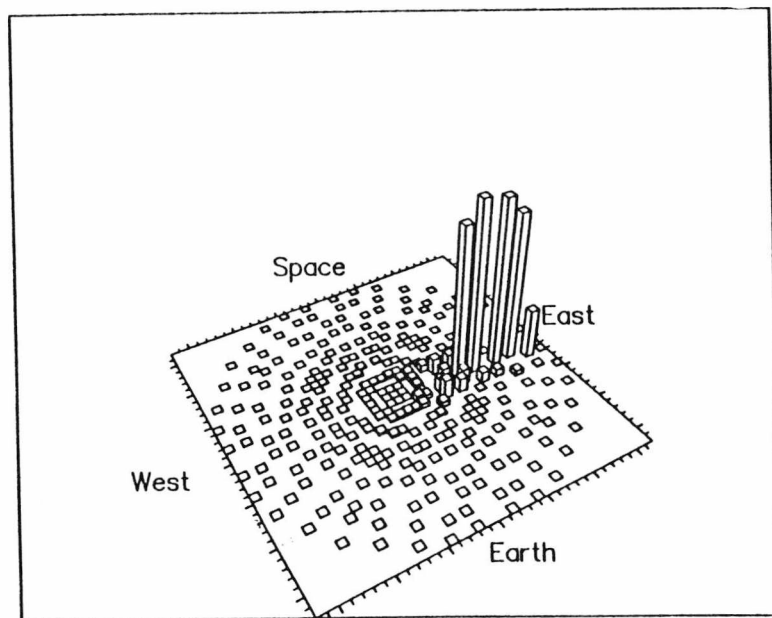


Figure 7.49 Angular distribution of Space debris, from DISCOS with HEOx20 orbits, impacting the South face. As figure 7.32
Flux scale $0 - 2750 \times 10^{-8} \text{ m}^{-2}\text{s}^{-1}$.

It is possible, then, to ascribe impact directions to specific particle populations from an analysis of impact direction and modelling. Such an analysis has been undertaken at USS {7.6 and 7.21} in which craters on clamps have been characterised into “circular”, “elliptical” and “undefined”. Images of impact sites are taken at $\pm 7.5^\circ$ to the normal in the Philips 525M SEM. A stereo viewer is used to verify that the impact is hypervelocity and allow depth, maximum and minimum crater diameters to be derived, using the surface as a reference point. For “elliptical” craters, an estimate of the direction of impact can also be made noting that such elliptical craters tend to have high raised lips on the entrance side and flattened lips on the exit side. The crater walls are steeper and sometimes undercut on the entrance side. The shape of the crater is not truly elliptical, but egg-shaped, being deeper and wider at the entrance side {7.22 and 7.23} as illustrated in figure 7.50.

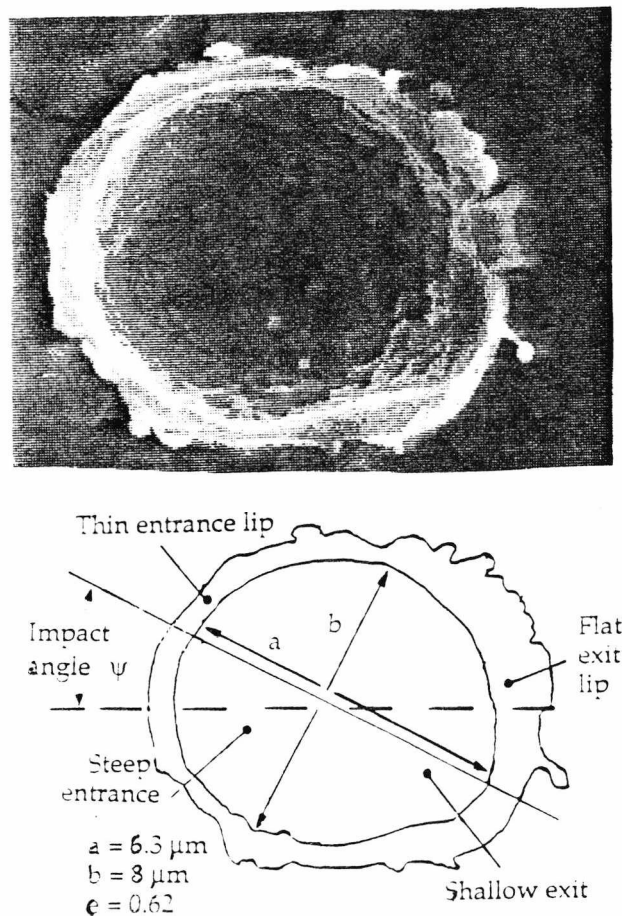


Figure 7.50 Illustration of an elliptical crater impact detected on the South clamp showing the entrance and exit sides marked on the schematic.

The term “ellipticity” in this context has been described as:

$$e = (1-b^2/a^2)^{1/2} \quad (7.10)$$

The categories are then defined as:

- “Circular” irregularities in the surface and uncertainties in the exact crater edge result in ellipticities smaller than 0.3 being indistinguishable from circular.
- “Elliptical” craters with morphology characteristic of oblique angle impacts. The direction of impact can be estimated with an accuracy of some 20°.
- “Undefined” craters with elliptical shapes but unusual morphology. It is not possible to determine which was the entrance or exit side or even if the crater was the result of an oblique impact. Such craters could be produced by low velocity irregularly shaped or heterogeneous particles.

Alongside these measurements an impact angle out of the plane has to be assumed for the impact direction based upon crater morphology and the ratio of flux/direction on the nearby faces. Impact experiments into metals {7.22} indicate that craters are circular for impacts up to a critical angle, above which they exhibit the characteristics described above.

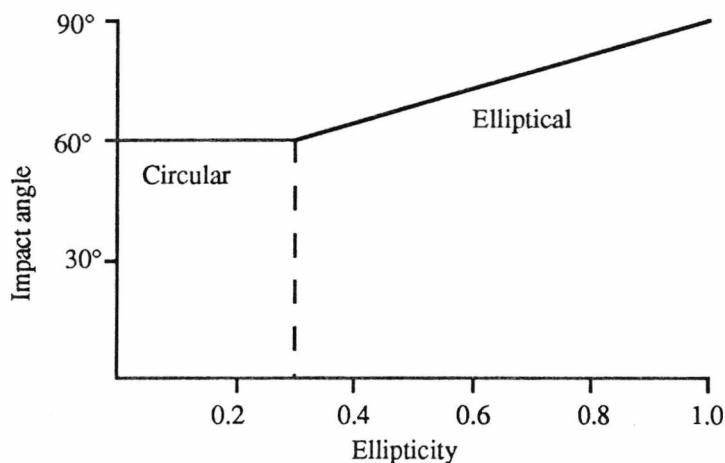


Figure 7.51 Graphical representation of the simple impact angle to ellipticity relationship derived for a first look comparison of South clamp data and modelled impact direction distributions.

For material with no cohesive strength, the critical angle is large ($>60^\circ$ from the normal) and dependant on velocity and physical properties of the target and projectile. These experimental results apply to a range of materials and velocity and impact angle regimes but the relationship between crater ellipticity and such properties is not well quantified. A simple relationship between impact angle and ellipticity, independent of impact velocity and particle properties, has been assumed and illustrated in figure 7.51. This is physically un-realistic and further better models will be used once the technique and charaterisation of impacts improves.

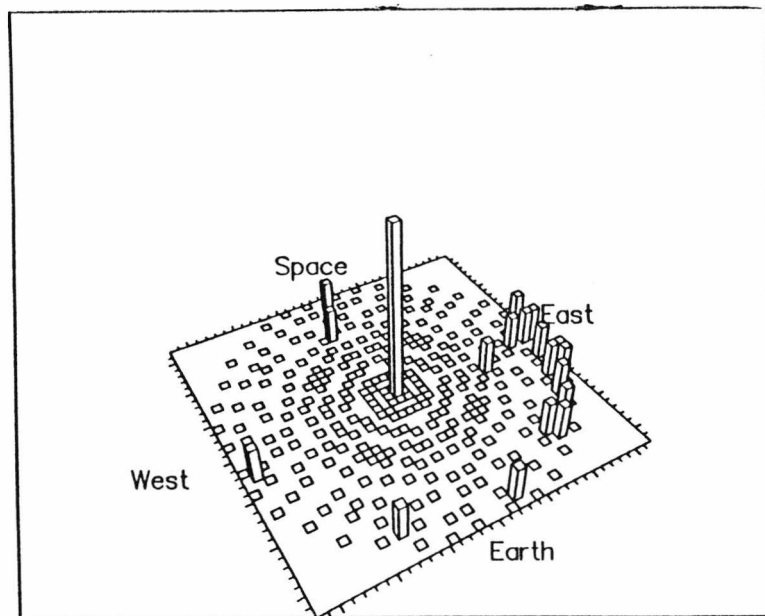


Figure 7.52 Elliptical crater data from a South face experimental tray clamp. The directions are as in figure 7.32. The central peak contains all craters with elliptical characteristics but ellipticity smaller than 0.3.
Flux scale $0 - 1045 \times 10^{-8} \text{ m}^{-2} \text{ s}^{-1}$.

Figure 7.52 illustrates the results of the analysis of a South face clamp (Mackay et al.) {7.21 and 7.7}. The measured data can be compared to the modelled interplanetary and space debris distributions of figures 7.34, 7.40 and 7.47 respectively. It is noted that

detailed comparison of modelled flux distributions and measured data are not possible due to uncertainties in the model parameters. However, the South data shows a concentration in the East direction as would be expected from debris impacts, but also a large number of impacts from the Earth, which do not tie in with the modelled results, for either debris or interplanetary. This leads to the possibility that such impacts are due to possible interplanetary particles just grazing the Earth and fragmenting or alternatively that the impacts are the result of operational debris from either STS-41C or STS-32, the deployment and retrieval missions. The only way to confirm this theory is to compare chemical residue found at these sites with that of species known to have been released by the STS in orbit manouvres and various water dumps that periodically occur.

Comparing both the modelled flux distributions for anthropogenic space debris and interplantary particle with measured ellipticity and impact direction it is possible to estimate the impactor origin. The only true identification, however, comes from the chemical analysis of impact residue, and this could, when found, determine the reliability of such modelling techniques, in predicting impactor origin..

References

- {7.1} Sullivan, K. (1992). "Characterisation and Dynamic Modelling of the Near-Earth Space Particulate Environment.", *Ph.D. Thesis*, University of Kent at Canterbury, U.K..
- {7.2} Bernhard, R. & Hörz, F. (1992). "Compositional Analysis of Projectile Residues on LDEF Instrument A0187-1", in LDEF - 69 Months in Space, *LDEF, Second Post Retrieval Symposium*, San Diego, 1992. **NASA CP 3194**.
- {7.3} Grün, E., Zook, H.A., Fechtig, H. & Giese, R.H. (1985). "Collisional Balance of the Meteoritic Complex", *Icarus* ,62, pp244-272.
- {7.4} Divine, N. (1992). "Five Populations of Interplanetary Meteoroids", JPL Interoffice Memorandum **IOM-5217-92-14/15**.
- {7.5} Anderson, B.J. (1990). "Review of Meteoroid/Orbital Debris Revisions to SSP 30425", MSFC Internal document ES44-(193-90).
- {7.6} Newman, P.J., Mackay, N.G., Deshpande, S.P., Green, S.F. & McDonnell, J.A.M. (1993). "Derivation of Particulate Directional Information from Analysis of Elliptical Impact Craters on LDEF", in in LDEF - 69 Months in Space, *LDEF, Second Post Retrieval Symposium*, San Diego, 1992. **NASA CP 3194**.
- {7.7} Newman, P.J. (*Ph.D. thesis to be submitted 1993*). University of Kent at Canterbury, U.K..
- {7.8} McDonnell, J.A.M., Deshpande, S.P., Niblett, D.H., Neish, M.J. & Newman, P.J. (1992). "The Near Earth Space Impact Environment - An LDEF Overview". for publication in Proc. IAF/COSPAR World Space Congress, Washington D.C. 1992.
- {7.9} Kessler, D.J. (1992). "Origin of Orbital Debris Impacts on LDEF's Trailing Surfaces." in LDEF - 69 Months in Space, *LDEF, Second Post Retrieval Symposium*, San Diego, 1992. **NASA CP 3134**.

- {7.10} See, T.H. et al. (1992). "Meteoroid and Debris Special Investigation Group Preliminary Results: Size-Frequency Distribution and Spatial Density of Large Impact Features on LDEF", in LDEF - 69 Months in Space, *LDEF, First Post Retrieval Symposium*, San Diego, 1992. NASA CP 3134.
- {7.11} Hörz, F. et al. (1992). "Preliminary Analysis of LDEF Instrument A0187-1 Chemistry of Micrometeoroids Experiment", in LDEF - 69 Months in Space, *LDEF, First Post Retrieval Symposium*, San Diego, 1992. NASA CP 3134.
- {7.12} McBride, N. *Personal communication*.
- {7.13} Flury, W, Janin, G, Jehn, R and Klinkrad, K. (1992). "Space Debris in Elliptical Orbits", *18th Symposium in Space Technology and Science*, Kagoshima, Japan.
- {7.14} McDonnell, J.A.M. & Sullivan, K. (1992). "Hypervelocity Impacts on Space Detectors: Decoding the Projectile Parameters.", *Hypervelocity Impacts in Space*, (ed. J.A.M. McDonnell), Unit for Space Sciences, University of Kent at Canterbury, pp 39-47
- {7.15} Anz-Meador, P. *Personal communication*.
- {7.16} Cour-Palais, B.G. (1969). "Meteoroid Environment Model - 1969 [Near Earth to Lunar Surface]", NASA SP-8013.
- {7.17} Divine, N. (1981). "Numerical Models for Halley Dust Environment", Proc. Joint NASA/ESA Working Group Meeting, ESA SP174, p25.
- {7.18} Green, S.F., Deshpande, S.P. & Mackay, N.G. (1992). "A 3-D Numerical Model for Space Debris and Interplanetary Dust Fluxes Incident on LDEF". for publication in Proc. IAF/COSPAR World Space Congress, Washington D.C. 1992.
- {7.19} Erickson, J.E. (1968). "Velocity Distribution of Photographic Meteors", *J. Geophys. Res.*, 73, pp3721-3726.
- {7.20} Hill, D.C. (1990). "The Micrometeoroid Hazard In Space: Techniques For Damage Simulation by Pulsed Lasers and Environmental Modelling", *Ph.D. Thesis*, University of Kent at Canterbury, U.K..

- {7.21} Mackay, N.G., Green, S.F., Deshpande, S.P. and Newman, P.J. (1993). "Interpretation of Impact Crater Morphology and Residues on LDEF Using 3-D Space Debris and Micrometeoroid Models", *Proc of the 1st European Conference on Space Debris*, 5-7 April 1993, Darmstadt, Germany.
- {7.22} Kineke, J.H. Jr, (1960). "An Experimental Study of Crater Formation in Metallic Targets", 4th Symposium of Hypervelocity Impact, Air Proving Ground Center, Eglin AFB, Florida, **APGC-TR-60-39 (I)**, section 4.
- {7.23} Bryan, G.M., (1960). "A Model of Oblique Impact", 4th Symposium of Hypervelocity Impact, Air Proving Ground Center, Eglin AFB, Florida, **APGC-TR-60-39 (III)**, section 33.

Chapter 8

Conclusions

The Long Duration Exposure Facility has proved to be the most complete record of LEO environmental processes currently available to man. This unique spacecraft will probably be flown only once as opposed to the reusable concept first envisaged, and as such the analysis of the results obtained will be invaluable in determining the rationale behind future LEO environment models.

The results obtained in this work show that simple assumptions incorporated in the models used can lead to hitherto concrete assumptions being overturned. The assumptions of anthropogenic space debris existing in only circular orbits is now a concept banished to the halls of history as more detailed models based upon actual tracked data become more sophisticated. The LDEF has been instrumental in prompting a re-evaluation of the effects of space debris on spacecraft in Earth orbit and in particular in the need to further clarify the orbit distribution and the dynamics involved with such particles.

An isotropic, single velocity particle distribution for the interplanetary media has been shown to be inaccurate in determining the measured fluxes seen on the LDEF, when

coupled with the predicted space debris impact distribution. The overall flux of interplanetary particles is in good agreement with the Grün flux at LDEF's altitude, when considered separately. It is probable that a mean velocity of $24 \pm 4.5 \text{ km s}^{-1}$ at LDEF's altitude for the interplanetary particle distribution is genuine when compared to the 22.7 km s^{-1} for the Grün distribution. It is clear from radar observations and photographic evidence that a velocity distribution exists and this would be seen on the LDEF it were not for the lack of dedicated particle velocity measuring system. The understanding of the hypervelocity cratering process leads to assumptions on either particle size or velocity and hence the characterisation of a size/velocity distribution is not possible. It is clear from the modelling of meteor streams and comets, passing close to the Earth, that asymmetries of almost any nature can occur on the LDEF faces, from these sources. This then leads to the need for these sources to be incorporated into the interplanetary particulate models alongside a general sporadic distribution dispensing with the 3D geocentric, single velocity, isotropic models.

The modelling of the anthropogenic space debris particle distribution requires further refinement in terms of the particle size/orbit interaction and a better understanding of the probable distribution of the smaller size particles which are currently undetectable. Once the operational limits on tracking objects in orbit decrease the space debris models can be refined and possible asymmetries that would explain the South flux data may become evident. This seems to be occurring as the international community becomes more aware of its responsibility to ensure the safing of spacecraft and prevention of operational and deliberate debris generation. DISCOS is one such demonstration of a this thrust toward understanding and defining the problem of space debris and combined with real data from the LDEF provides the basis for the containment and mitigation of space debris policy.

The choice of density of these space debris objects is hampered by the lack of genuine data on sizes of debris objects that pose a threat to spacecraft, only better tracking techniques can alleviate this problem. However, by looking at both the RCS data and actual calibration of objects in space, via calibration spheres it would be

possible to determine a more accurate density profile with continuous tracking of the object in question. Combining the flux data from a series of experiments and the D_H distribution from MAP data, it is possible to determine, with the appropriate choice of impact velocity and penetration equation, a particle density. For the Space face this corresponds to a particle density of $\sim 1.0 \text{gcm}^{-3}$ which is to be expected from a face whose interplanetary component accounts for $\sim 92\%$ of the total flux, noting the assumptions required in both the anthropogenic space debris models and the isotropic interplanetary model. There is however, some evidence that for the smaller sizes a higher particle density would also suffice. This is in agreement with a space debris component at associated $f_{\text{max}} < 40 \mu\text{m}$. To clarify the merits of this technique and to test the assumptions of small particle sized space debris this analysis should be carried out on the East, West, North and South faces of the LDEF where MAP D_H data is available.

The USS model for both interplanetary and anthropogenic space debris has proved to be most valuable in determining these populations. The relative levels are still not well defined and can only be defined from better chemical analysis on impactor residues. Once a statistically meaningful database on space debris and interplanetary particles is derived from such chemical analysis then the model assumptions and input data sets adjusted to predict this data. The models at present can predict the ratios of space debris or interplanetary particle fluxes for different faces and a novel technique has been developed to characterise elliptical craters into these populations. This technique is still in the development stage but coupled with calibration testing of the effect of impact angle on crater ellipticity, could be used to predict impactor origin, from the impact site.

The excess flux predicted on the leading faces (*i.e.* East, North and South) is probably due to asymmetry in the interplanetary and anthropogenic space debris distributions. The North face receives an increased flux not only due to the 8° offset of the velocity vector but also due to a natural asymmetry in the interplanetary dust environment from meteor streams and comets during the LDEF's excursion in LEO. The high flux rate on the South face could be attributed to the asymmetry in the anthropogenic space debris population and in particular to debris associated with the

Molniya type orbits whose argument of perigee remains in the southern hemisphere LEO region.

Ongoing analysis into the relative abundance of both these asymmetries is required to quantify these effects and in particular to express their merits in terms of the 69 month mission profile of the LDEF. The flux data for both the interplanetary and space debris components are currently being used to predict the impact damage to the EuReCa spacecraft that is scheduled for a detailed impact analysis programme in the summer of 1993. The flux data from both the LDEF and EuReCa combined will help define the criteria for the next generation of spacecraft and in particular the International Space Station Freedom.

This study has shown that both the anthropogenic space debris and interplanetary particle distribution need further defining and in particular the need for a detection system that incorporates, a velocity measurement system, chemical composition measuring system and an event time line system. This would then characterise the impact in terms of velocity, size/mass, and chemical composition and time of impact, thus correlation to known debris orbits, possible passage through meteor streams or close encounters with passing comets would be possible. Such systems are currently under development for interplanetary missions and could be easily adapted for use in LEO. There is also a great need to increase Earth based detection systems for all near Earth space regions to detect the smaller particles currently undetectable and indeed to calibrate further the existing systems.

Unfortunately after the EuReCa analysis and specifically the analysis of the Timeband Capture Cell Experiment (TiCCE) (the USS micrometeoroid and debris detection experiment) there are no further scheduled particle detectors to be flown in LEO or indeed in the near Earth space region. The opportunities exist to fly limited exposure detectors inside the cargo bay area on board the STS, and possibly on the rear side of solar arrays (which constitutes by far the greatest surface area on any spacecraft in orbit) on certain undetermined spacecraft, but there are definite needs for a continuous small particle monitoring system.

Hopefully the lessons learnt from the LDEF in terms of the particle environment will be used to further develop and understand the hypervelocity impact processes, the design of better detectors and to allure everybody to the dangers of space debris and the need to prevent further debris generation for the benefit of the whole space community.

Appendix I

This appendix tabulates the flux data that is used in Chapter 4 and in defining the flux distributions for the modelling. Table AI.1 illustrates smoothed flux data set for the East, West, North, South and Space faces. Table AI.2 illustrates the best fit parameters deduced from the cosine square fit to the peripheral data. Table AI.3 illustrates the offset corrected fluxes for the East, West, North and South faces. There is no correction needed for the Space face.

Table AI.1 Smoothed flux data sets for the East, West, North, South and Space faces.

Foil Thickness (μm)	Smoothed West Flux	Smoothed South Flux	Smoothed East Flux	Smoothed North Flux	Smoothed Space Flux
1.47	4.92E-05	9.81E-04	2.42E-03	6.42E-04	1.11E-04
1.58	4.46E-05	8.66E-04	2.29E-03	5.95E-04	1.03E-04
1.71	3.99E-05	7.63E-04	2.14E-03	5.51E-04	9.57E-05
1.85	3.53E-05	6.74E-04	1.96E-03	5.10E-04	8.87E-05
2.00	3.11E-05	5.96E-04	1.78E-03	4.72E-04	8.21E-05
2.15	2.74E-05	5.28E-04	1.59E-03	4.36E-04	7.61E-05
2.33	2.41E-05	4.67E-04	1.41E-03	4.01E-04	7.06E-05
2.51	2.11E-05	4.14E-04	1.24E-03	3.66E-04	6.54E-05
2.71	1.86E-05	3.67E-04	1.09E-03	3.32E-04	6.06E-05
2.93	1.63E-05	3.26E-04	9.57E-04	2.98E-04	5.62E-05
3.16	1.43E-05	2.90E-04	8.39E-04	2.64E-04	5.20E-05
3.41	1.26E-05	2.58E-04	7.36E-04	2.32E-04	4.82E-05
3.69	1.11E-05	2.30E-04	6.46E-04	2.03E-04	4.47E-05
3.98	9.81E-06	2.06E-04	5.68E-04	1.77E-04	4.14E-05
4.30	8.70E-06	1.85E-04	5.00E-04	1.54E-04	3.86E-05
4.64	7.77E-06	1.67E-04	4.42E-04	1.34E-04	3.62E-05
5.01	7.00E-06	1.51E-04	3.92E-04	1.16E-04	3.47E-05
5.41	6.35E-06	1.38E-04	3.49E-04	1.00E-04	3.39E-05
5.84	5.81E-06	1.26E-04	3.12E-04	8.67E-05	3.35E-05
6.31	5.34E-06	1.16E-04	2.79E-04	7.47E-05	3.32E-05
6.81	4.92E-06	1.07E-04	2.50E-04	6.44E-05	3.26E-05
7.36	4.54E-06	9.82E-05	2.25E-04	5.54E-05	3.13E-05
7.94	4.19E-06	9.05E-05	2.01E-04	4.77E-05	2.89E-05
8.58	3.87E-06	8.33E-05	1.81E-04	4.11E-05	2.60E-05
9.26	3.59E-06	7.67E-05	1.62E-04	3.55E-05	2.31E-05
10.00	3.33E-06	7.05E-05	1.44E-04	3.08E-05	2.05E-05
10.80	3.11E-06	6.47E-05	1.28E-04	2.69E-05	1.82E-05
11.66	2.93E-06	5.91E-05	1.13E-04	2.38E-05	1.61E-05
12.59	2.80E-06	5.37E-05	9.84E-05	2.13E-05	1.43E-05
13.59	2.69E-06	4.83E-05	8.48E-05	1.94E-05	1.26E-05
14.68	2.61E-06	4.26E-05	7.24E-05	1.78E-05	1.12E-05
15.85	2.55E-06	3.65E-05	6.14E-05	1.65E-05	9.91E-06
17.11	2.49E-06	3.00E-05	5.17E-05	1.54E-05	8.79E-06
18.48	2.44E-06	2.36E-05	4.34E-05	1.43E-05	7.83E-06
19.95	2.39E-06	1.78E-05	3.63E-05	1.34E-05	7.04E-06
21.54	2.33E-06	1.31E-05	3.06E-05	1.25E-05	6.44E-06
23.26	2.26E-06	9.56E-06	2.61E-05	1.17E-05	5.97E-06
25.12	2.17E-06	7.07E-06	2.26E-05	1.09E-05	5.57E-06
27.12	2.08E-06	5.35E-06	1.98E-05	1.01E-05	5.14E-06
29.29	1.97E-06	4.15E-06	1.77E-05	9.35E-06	4.64E-06
31.62	1.87E-06	3.30E-06	1.60E-05	8.62E-06	4.17E-06
34.15	1.76E-06	2.69E-06	1.46E-05	7.90E-06	3.84E-06
36.87	1.66E-06	2.25E-06	1.34E-05	7.22E-06	3.62E-06
39.81	1.57E-06	1.93E-06	1.23E-05	6.57E-06	3.43E-06
42.99	1.47E-06	1.70E-06	1.14E-05	5.97E-06	3.21E-06
46.42	1.38E-06	1.53E-06	1.06E-05	5.41E-06	2.95E-06

Foil Thickness (μm)	Smoothed	Smoothed	Smoothed	Smoothed	Smoothed
	West Flux	South Flux	East Flux	North Flux	Space Flux
50.12	1.30E-06	1.39E-06	9.83E-06	4.89E-06	2.68E-06
54.12	1.22E-06	1.29E-06	9.08E-06	4.41E-06	2.45E-06
58.43	1.14E-06	1.19E-06	8.33E-06	3.97E-06	2.26E-06
63.10	1.07E-06	1.10E-06	7.59E-06	3.55E-06	2.11E-06
68.13	9.99E-07	1.01E-06	6.87E-06	3.17E-06	1.93E-06
73.56	9.30E-07	9.14E-07	6.18E-06	2.82E-06	1.72E-06
79.43	8.61E-07	8.20E-07	5.54E-06	2.51E-06	1.50E-06
85.77	7.91E-07	7.28E-07	4.96E-06	2.23E-06	1.33E-06
92.61	7.17E-07	6.42E-07	4.43E-06	1.98E-06	1.20E-06
100.00	6.38E-07	5.67E-07	3.96E-06	1.76E-06	1.09E-06
107.98	5.53E-07	5.04E-07	3.54E-06	1.56E-06	9.92E-07
116.59	4.64E-07	4.49E-07	3.17E-06	1.38E-06	9.02E-07
125.89	3.79E-07	4.02E-07	2.83E-06	1.22E-06	8.20E-07
135.94	3.04E-07	3.60E-07	2.52E-06	1.08E-06	7.46E-07
146.78	2.44E-07	3.22E-07	2.25E-06	9.42E-07	6.77E-07
158.49	2.01E-07	2.87E-07	2.00E-06	8.19E-07	6.15E-07
171.13	1.70E-07	2.55E-07	1.77E-06	7.06E-07	5.59E-07
184.78	1.48E-07	2.26E-07	1.57E-06	6.04E-07	5.08E-07
199.53	1.32E-07	2.01E-07	1.39E-06	5.15E-07	4.62E-07
215.44	1.20E-07	1.78E-07	1.22E-06	4.37E-07	4.20E-07
232.63	1.09E-07	1.58E-07	1.08E-06	3.70E-07	3.81E-07
251.19	1.00E-07	1.40E-07	9.52E-07	3.14E-07	3.46E-07
271.23	9.18E-08	1.24E-07	8.41E-07	2.66E-07	3.15E-07
292.86	8.42E-08	1.10E-07	7.42E-07	2.25E-07	2.86E-07
316.23	7.73E-08	9.78E-08	6.54E-07	1.90E-07	2.60E-07
341.45	7.06E-08	8.71E-08	5.75E-07	1.60E-07	2.35E-07
368.69	6.42E-08	7.76E-08	5.04E-07	1.35E-07	2.11E-07
398.11	5.77E-08	6.88E-08	4.38E-07	1.13E-07	1.84E-07
429.87	5.09E-08	6.04E-08	3.74E-07	9.36E-08	1.56E-07
464.16	4.38E-08	5.20E-08	3.14E-07	7.73E-08	1.27E-07
501.19	3.68E-08	4.36E-08	2.58E-07	6.33E-08	9.86E-08
541.17	3.02E-08	3.55E-08	2.08E-07	5.12E-08	7.31E-08
584.34	2.44E-08	2.80E-08	1.65E-07	4.07E-08	5.22E-08
630.96	1.95E-08	2.15E-08	1.29E-07	3.17E-08	3.70E-08
681.29	1.55E-08	1.59E-08	1.02E-07	2.44E-08	

Table AI.2 Best fit cosine square parameters for the East, West, North and South faces.

Foil Thickness (μm)	A	B	C	\emptyset
1.47	1.02E-03	1.20E-03	2.21E-04	8.11
1.58	9.49E-04	1.13E-03	2.25E-04	6.88
1.71	8.73E-04	1.05E-03	2.20E-04	5.79
1.85	7.96E-04	9.68E-04	2.07E-04	4.87
2.00	7.20E-04	8.76E-04	1.88E-04	4.07
2.15	6.45E-04	7.83E-04	1.65E-04	3.36
2.33	5.75E-04	6.93E-04	1.42E-04	2.75
2.51	5.11E-04	6.11E-04	1.21E-04	2.24
2.71	4.52E-04	5.36E-04	1.03E-04	1.87
2.93	3.99E-04	4.70E-04	8.76E-05	1.72
3.16	3.52E-04	4.12E-04	7.49E-05	1.78
3.41	3.10E-04	3.62E-04	6.48E-05	2.02
3.69	2.73E-04	3.18E-04	5.61E-05	2.41
3.98	2.40E-04	2.79E-04	4.88E-05	2.93
4.30	2.12E-04	2.46E-04	4.26E-05	3.57
4.64	1.88E-04	2.18E-04	3.76E-05	4.32
5.01	1.67E-04	1.93E-04	3.35E-05	5.21
5.41	1.48E-04	1.72E-04	3.00E-05	6.24
5.84	1.33E-04	1.54E-04	2.70E-05	7.37
6.31	1.19E-04	1.39E-04	2.46E-05	8.57
6.81	1.07E-04	1.25E-04	2.24E-05	9.78
7.36	9.57E-05	1.12E-04	2.04E-05	11.00
7.94	8.59E-05	1.01E-04	1.85E-05	12.23
8.58	7.72E-05	9.09E-05	1.69E-05	13.42
9.26	6.94E-05	8.18E-05	1.52E-05	14.58
10.00	6.23E-05	7.33E-05	1.36E-05	15.72
10.80	5.57E-05	6.53E-05	1.19E-05	16.82
11.66	4.97E-05	5.77E-05	1.01E-05	17.83
12.59	4.41E-05	5.04E-05	8.21E-06	18.72
13.59	3.88E-05	4.35E-05	6.37E-06	19.37
14.68	3.39E-05	3.70E-05	4.71E-06	19.52
15.85	2.92E-05	3.11E-05	3.45E-06	18.75
17.11	2.49E-05	2.57E-05	2.63E-06	16.61
18.48	2.09E-05	2.10E-05	2.17E-06	12.81
19.95	1.75E-05	1.71E-05	1.93E-06	7.51
21.54	1.46E-05	1.41E-05	1.83E-06	1.28
23.26	1.24E-05	1.20E-05	1.81E-06	-5.01
25.12	1.07E-05	1.04E-05	1.82E-06	-10.53
27.12	9.34E-06	9.19E-06	1.87E-06	-14.93
29.29	8.30E-06	8.30E-06	1.93E-06	-18.23
31.62	7.46E-06	7.59E-06	1.90E-06	-20.29
34.15	6.74E-06	6.99E-06	1.75E-06	-21.22
36.87	6.13E-06	6.45E-06	1.61E-06	-21.60
39.81	5.60E-06	5.96E-06	1.49E-06	-21.54
42.99	5.14E-06	5.52E-06	1.38E-06	-21.15
46.42	4.73E-06	5.11E-06	1.28E-06	-20.57

Foil Thickness (μm)	A	B	C	\emptyset
50.12	4.35E-06	4.72E-06	1.18E-06	-19.88
54.12	4.00E-06	4.34E-06	1.09E-06	-19.17
58.43	3.66E-06	3.97E-06	9.91E-07	-18.52
63.10	3.33E-06	3.59E-06	8.98E-07	-17.95
68.13	3.01E-06	3.23E-06	8.08E-07	-17.49
73.56	2.71E-06	2.89E-06	7.23E-07	-17.13
79.43	2.43E-06	2.58E-06	6.46E-07	-16.88
85.77	2.18E-06	2.30E-06	5.76E-07	-16.70
92.61	1.94E-06	2.06E-06	5.14E-07	-16.57
100.00	1.73E-06	1.84E-06	4.60E-07	-16.43
107.98	1.54E-06	1.65E-06	4.13E-07	-16.29
116.59	1.37E-06	1.48E-06	3.71E-07	-16.11
125.89	1.21E-06	1.34E-06	3.34E-07	-15.89
135.94	1.07E-06	1.20E-06	3.01E-07	-15.58
146.78	9.39E-07	1.08E-06	2.70E-07	-15.17
158.49	8.26E-07	9.36E-07	2.18E-07	-14.28
171.13	7.25E-07	8.55E-07	2.14E-07	-13.94
184.78	6.36E-07	7.56E-07	1.89E-07	-13.13
199.53	5.58E-07	6.68E-07	1.67E-07	-12.27
215.44	4.89E-07	5.88E-07	1.47E-07	-11.39
232.63	4.29E-07	5.17E-07	1.29E-07	-10.52
251.19	3.76E-07	4.55E-07	1.14E-07	-9.66
271.23	3.31E-07	4.00E-07	1.00E-08	-8.85
292.86	2.90E-07	3.52E-07	8.80E-08	-8.07
316.23	2.55E-07	3.09E-07	7.74E-08	-7.29
341.45	2.23E-07	2.71E-07	6.78E-08	-6.52
368.69	1.95E-07	2.37E-07	5.92E-08	-5.77
398.11	1.69E-07	2.05E-07	5.12E-08	-5.08
429.87	1.45E-07	1.75E-07	4.37E-08	-4.50
464.16	1.22E-07	1.46E-07	3.65E-08	-4.09
501.19	1.00E-07	1.20E-07	2.99E-08	-3.89
541.17	8.12E-08	9.61E-08	2.40E-08	-3.87
584.34	6.45E-08	7.60E-08	1.90E-08	-3.93
630.96	5.05E-08	5.96E-08	1.49E-08	-4.02
681.29	3.94E-08	4.70E-08	1.18E-08	-4.14

Table AI.3 Offset corrected flux data sets for the East, West, North and South faces.
The Space face requires no offset correction.

Foil Thickness (μm)	Corrected West Flux	Corrected South Flux	Corrected East Flux	Corrected North Flux
1.47	5.97E-05	1.18E-03	2.36E-03	4.98E-04
1.58	5.16E-05	1.05E-03	2.23E-03	4.57E-04
1.71	4.47E-05	9.37E-04	2.09E-03	4.21E-04
1.85	3.88E-05	8.33E-04	1.92E-03	3.89E-04
2.00	3.40E-05	7.39E-04	1.75E-03	3.60E-04
2.15	2.99E-05	6.54E-04	1.56E-03	3.35E-04
2.33	2.64E-05	5.78E-04	1.39E-03	3.10E-04
2.51	2.33E-05	5.11E-04	1.22E-03	2.85E-04
2.71	2.06E-05	4.51E-04	1.08E-03	2.60E-04
2.93	1.82E-05	4.00E-04	9.44E-04	2.34E-04
3.16	1.61E-05	3.54E-04	8.28E-04	2.09E-04
3.41	1.43E-05	3.15E-04	7.26E-04	1.84E-04
3.69	1.27E-05	2.80E-04	6.37E-04	1.61E-04
3.98	1.14E-05	2.50E-04	5.59E-04	1.40E-04
4.30	1.02E-05	2.24E-04	4.92E-04	1.22E-04
4.64	9.27E-06	2.02E-04	4.34E-04	1.06E-04
5.01	8.47E-06	1.82E-04	3.84E-04	9.14E-05
5.41	7.81E-06	1.66E-04	3.41E-04	7.88E-05
5.84	7.24E-06	1.51E-04	3.04E-04	6.77E-05
6.31	6.73E-06	1.39E-04	2.72E-04	5.80E-05
6.81	6.26E-06	1.27E-04	2.43E-04	4.97E-05
7.36	5.83E-06	1.17E-04	2.17E-04	4.26E-05
7.94	5.44E-06	1.08E-04	1.94E-04	3.65E-05
8.58	5.06E-06	9.88E-05	1.74E-04	3.12E-05
9.26	4.73E-06	9.07E-05	1.55E-04	2.69E-05
10.00	4.44E-06	8.31E-05	1.38E-04	2.33E-05
10.80	4.22E-06	7.59E-05	1.22E-04	2.03E-05
11.66	4.05E-06	6.90E-05	1.08E-04	1.80E-05
12.59	3.95E-06	6.22E-05	9.38E-05	1.63E-05
13.59	3.87E-06	5.55E-05	8.09E-05	1.49E-05
14.68	3.78E-06	4.85E-05	6.92E-05	1.39E-05
15.85	3.60E-06	4.14E-05	5.89E-05	1.30E-05
17.11	3.32E-06	3.41E-05	4.99E-05	1.24E-05
18.48	2.99E-06	2.69E-05	4.21E-05	1.17E-05
19.95	2.67E-06	2.05E-05	3.56E-05	1.11E-05
21.54	2.42E-06	1.53E-05	3.03E-05	1.05E-05
23.26	2.25E-06	1.13E-05	2.61E-05	9.88E-06
25.12	2.12E-06	8.46E-06	2.29E-05	9.23E-06
27.12	2.02E-06	6.48E-06	2.03E-05	8.57E-06
29.29	1.94E-06	5.07E-06	1.83E-05	7.90E-06
31.62	1.86E-06	4.06E-06	1.66E-05	7.26E-06
34.15	1.75E-06	3.33E-06	1.52E-05	6.65E-06
36.87	1.65E-06	2.80E-06	1.39E-05	6.07E-06
39.81	1.55E-06	2.41E-06	1.29E-05	5.51E-06

Foil Thickness (μm)	Corrected West Flux	Corrected South Flux	Corrected East Flux	Corrected North Flux
42.99	1.46E-06	2.13E-06	1.19E-05	4.99E-06
46.42	1.37E-06	1.92E-06	1.10E-05	4.51E-06
50.12	1.29E-06	1.76E-06	1.02E-05	4.07E-06
54.12	1.21E-06	1.63E-06	9.40E-06	3.67E-06
58.43	1.13E-06	1.50E-06	8.62E-06	3.29E-06
63.10	1.06E-06	1.39E-06	7.84E-06	2.95E-06
68.13	9.94E-07	1.27E-06	7.09E-06	2.63E-06
73.56	9.26E-07	1.15E-06	6.37E-06	2.34E-06
79.43	8.57E-07	1.03E-06	5.71E-06	2.08E-06
85.77	7.87E-07	9.09E-07	5.11E-06	1.85E-06
92.61	7.14E-07	8.03E-07	4.56E-06	1.64E-06
100.00	6.35E-07	7.10E-07	4.08E-06	1.46E-06
107.98	5.51E-07	6.33E-07	3.65E-06	1.29E-06
116.59	4.62E-07	5.68E-07	3.26E-06	1.14E-06
125.89	3.77E-07	5.13E-07	2.91E-06	1.00E-06
135.94	3.03E-07	4.63E-07	2.59E-06	8.79E-07
146.78	2.43E-07	4.18E-07	2.31E-06	7.66E-07
158.49	1.97E-07	3.67E-07	2.04E-06	6.70E-07
171.13	1.69E-07	3.34E-07	1.81E-06	5.68E-07
184.78	1.47E-07	2.98E-07	1.60E-06	4.84E-07
199.53	1.32E-07	2.64E-07	1.41E-06	4.11E-07
215.44	1.19E-07	2.34E-07	1.25E-06	3.48E-07
232.63	1.09E-07	2.07E-07	1.10E-06	2.94E-07
251.19	9.99E-08	1.83E-07	9.65E-07	2.48E-07
271.23	9.89E-08	1.52E-07	8.47E-07	2.25E-07
292.86	8.42E-08	1.44E-07	7.49E-07	1.76E-07
316.23	7.72E-08	1.28E-07	6.59E-07	1.49E-07
341.45	7.06E-08	1.13E-07	5.79E-07	1.25E-07
368.69	6.42E-08	1.01E-07	5.06E-07	1.05E-07
398.11	5.77E-08	8.91E-08	4.39E-07	8.75E-08
429.87	5.09E-08	7.79E-08	3.75E-07	7.27E-08
464.16	4.38E-08	6.68E-08	3.14E-07	6.01E-08
501.19	3.68E-08	5.58E-08	2.58E-07	4.94E-08
541.17	3.02E-08	4.53E-08	2.08E-07	4.00E-08
584.34	2.44E-08	3.58E-08	1.65E-07	3.19E-08
630.96	1.95E-08	2.74E-08	1.29E-07	2.48E-08
681.29	1.55E-08	2.05E-08	1.02E-07	1.90E-08

Appendix II

This appendix illustrates the data sources used in the DISCOS database held at ESA/ESOC in Darmstadt, Germany.

Table AII.1 illustrates the USSPACECOM ELSETS, Table AII.2 illustrates the RAE Table of Earth Satellites, Table AII.3 the NASA Satellite Situation Report and Table AII.4 the Teledyne Brown Engineering History of On-Orbit Fragmentations.

Table AII.1 USSPACECOM ELSETS.

1	00005U	58DLT	2	88282.69541562	.00000021	00000-0	26644-4	0	3593
2	00005	J4.2413	131.9084	1873687	271.3025	67.4937	10.79163211	56323	
1	00016U	58DLT	1	88282.36386385	.00000503	00000-0	72128-3	0	1240
2	00016	J4.2524	13.6353	2048989	154.1619	217.7312	10.43927575115267		
1	00016U	58DLT	1	88281.59861833	.00000499	00000-0	71421-3	0	1239
2	00016	J4.2523	15.8248	2046052	150.9665	222.2043	10.43926738116163		
1	00020U	59ETA	1	88282.32802499	.00001351	00000-0	59246-3	0	6662
2	00020	J3.3517	135.5518	1789045	244.5099	96.0107	11.29719673186601		
1	00022U	59IOT	1	88281.25746227	.00001688	00000-0	32443-3	0	2523
2	00022	50.3032	189.4949	0284377	248.2774	108.7453	14.45707810516023		
1	00023U	59IOT	2	88282.15043900	.00046961	00000-0	24845-2	0	3478
2	00023	50.2828	179.2699	0100904	355.8870	4.1314	15.11024587537880		
1	00023U	59IOT	2	88281.15842608	.00046974	00000-0	24082-2	0	3463
2	00023	50.2827	184.0401	0101268	352.1099	7.8268	15.10926610537432		
1	00028U	60DET	1	88283.05674260	.00009611	00000-0	10777-2	0	4677
2	00028	48.3837	147.6018	0017319	7.8284	352.2897	14.67155295526097		
1	00046U	60ETA	2	88281.33757962	.00000877	00000-0	26256-3	0	2907
2	00046	66.6934	30.2676	0262667	34.8821	326.9188	14.29644989469401		
1	00046U	60ETA	2	88281.33757962	.00000877	00000-0	26256-3	0	2918
2	00046	66.6934	30.2676	0262667	34.8821	326.9188	14.29644989469401		
1	00046U	60ETA	2	88280.70796768	.00000877	00000-0	26214-3	0	2893
2	00046	66.6934	31.9155	0262578	35.3398	326.4612	14.29643738469317		
1	00047U	60ETA	3	88281.10126228	.00000432	00000-0	28889-3	0	88
2	00047	66.6672	295.3397	0289200	78.6277	284.3841	14.29898986470948		
1	00060U	60 XI	1	88282.72748615	.00007916	00000-0	78662-3	0	1293
2	00060	49.9188	13.6987	0652675	39.6586	326.3603	13.59461638339274		
1	00074U	60 PI	3	88283.66763066	.00050892	00000-0	15636-2	0	2011
2	00074	48.5643	19.3020	0016222	217.2800	142.7036	15.32999678512900		
1	00074U	60 PI	3	88282.36395273	.00049786	00000-0	15363-2	0	1992
2	00074	48.5643	26.0161	0016944	210.4475	149.5977	15.32857683512701		
1	00074U	60 PI	3	88281.32100618	.00048047	00000-0	14890-2	0	1973
2	00074	48.5603	31.3891	0016940	204.9774	165.0976	15.32737396612543		
1	00075U	60 PI	4	88283.64204432	.00021245	00000-0	11628-2	0	7671
2	00075	48.5200	27.2167	0029112	249.1221	90.6521	15.13745541923290		
1	00075U	60 PI	4	88282.71794483	.00020882	00000-0	11440-2	0	7667
2	00075	48.5188	31.8414	0029674	263.8182	93.9401	15.13699264923151		
1	00075U	60 PI	4	88281.33175377	.00020301	00000-0	11138-2	0	7647
2	00075	48.5160	38.7761	0030900	256.3393	103.4552	15.13630713922949		
1	00085U	61DCL	3	88283.03635360	.00007034	00000-0	37215-2	0	926
2	00085	38.9014	184.8637	0935702	315.0637	37.7939	12.87535231346200		

Table AII.2 RAE Table of Earth Satellites.

Year of launch 1985 continued

Page 835

	Name	Launch date, lifetime and descent date	Shape and weight (kg)	Size (m)	Date of orbital determination	Orbital inclination (deg)	Nodal period (min)	Semi major axis (km)	Perigee height (km)	Apogee height (km)	Orbital eccentricity	Argument of perigee (deg)
D	Cosmos 1664 engine	1985-54E 1985 Jun 26.53 24 days 1985 Jul 20	Cone 600? full	1.5 long? 2 dia?	1985 Jul 6.1	72.84	89.25	6613	209	262	0.004	110
D	Fragments	1985-54C,D,F,G										
T	Intelsat 5A F-11 [Atlas Centaur]	1985-55A 1985 Jun 30.03 > million years	Box + dishes + 2 vanes 2013 full 1098 empty	15.9 span 6.4 wide	1985 Jul 1.6 1985 Jul 21.2	0.11 0.29	1400.40 1436.18	41465 42168	34400 35735	35774 35845	0.017 0.001	2 287
	Intelsat 5A F-11 rocket	1985-55B 1985 Jun 30.03 100 years	Cylinder 1815	8.6 long 3.0 dia	1985 Jul 1.1	23.13	602.54	23644	285	34247	0.718	179
	Ariane 1-10 third stage Fragment	1985-56B 1985 Jul 2.47 50 years	Cylinder 1634	8.6 long 2.6 dia	1985 Jul 4.0	7.03	623.46	24191	206	35420	0.728	180
D R	Cosmos 1665	1985-56C 1985-57A 1985 Jul 3.51 13.8 days 1985 Jul 17.3	Sphere-cylinder 6300?	6.5 long? 2.4 dia	1985 Jul 4.5	72.87	89.69	6636	225	290	0.005	74
D	Cosmos 1665 rocket	1985-57B 1985 Jul 3.51 7 days 1985 Jul 10	Cylinder 2500	7.5 long 2.6 dia	1985 Jul 3.7	72.85	89.31	6617	196	281	0.006	91
D	Cosmos 1665 engine	1985-57G 1985 Jul 3.51 61 days 1985 Sep 2	Cone 600? full	1.5 long? 2 dia?	1985 Jul 19.1	72.86	89.76	6639	227	295	0.005	49
D	Fragments	1985-57C-F,H										

Space Vehicle: Giotto, 1985-56A. European Space Agency probe injected into Earth-escape trajectory 1985 Jul 3.81 and flew by Comet Halley at 605 km, 1986 Mar 14.00.

Table AII.3 NASA Satellite Situation Report.

INTER- NATIONAL DESIGNATION	NATIONAL NAME	OBJECTS IN ORBIT										NOTES
		CATALOG NUMBER	SOURCE	LAUNCH	PERIOD MINUTES	INCLI- NATION	APOGEE KM.	PERIGEE KM.	TRANSMITTING FREQ.(MHZ)			
1985 LAUNCHES (CONT.)												
1985 103A	MOLNIYA 1-66	16220	USSR	28 OCT	717.7	63.2	39871	779				
1985 103D		16223	USSR	28 OCT	701.1	63.2	38576	951				
1985 105A	COSMOS 1701	16235	USSR	9 NOV	718.9	66.4	38897	1510				
1985 105D		16243	USSR	9 NOV	706.2	66.8	38287	1493				
1985 107A	RADUGA 17	16250	USSR	15 NOV	1436.2	1.6	35811	35765				
1985 107F		16339	USSR	15 NOV	1477.0	1.7	36677	36490				
1985 108A	COSMOS 1703	16262	USSR	22 NOV	97.6	82.5	660	627				
1985 108B		16263	USSR	22 NOV	97.6	82.5	660	628				
1985 109B	MORELOS B	16274	MEXICO	27 NOV	1436.1	0.6	35795	35779				356
1985 109C	AUSSAT 2	16275	AUSTRL	27 NOV	1436.2	0.1	35809	35768				366
1985 109D	SATCOM KUZ	16276	US	28 NOV	1436.2	0.0	35794	35782				366
1985 109F		16293	US	27 NOV	648.6	25.5	36443	442				
1985 109G		16294	US	27 NOV	645.2	25.8	36282	426				
1985 109H		16295	US	28 NOV	624.8	26.1	35224	437				
1985 110A	COSMOS 1704	16291	USSR	28 NOV	104.0	82.9	1007	960				
1985 110B		16292	USSR	28 NOV	104.6	82.9	996	957				
1985 113A	COSMOS 1707	16326	USSR	12 DEC	97.6	82.5	658	628				
1985 113B		16327	USSR	12 DEC	97.6	82.5	658	628				
1985 114A		16328	US	13 DEC	92.8	37.1	527	292				
1985 116A	COSMOS 1709	16368	USSR	19 DEC	104.8	82.9	1011	957				
1985 116B		16369	USSR	19 DEC	104.6	82.9	1003	951				
1985 117A	MOLNIYA 3-27	16393	USSR	24 DEC	717.7	63.1	38312	2038				
1985 117F		16402	USSR	24 DEC	732.6	63.2	38974	2110				
1985 118A	COSMOS 1710	16396	USSR	24 DEC	65.5	65.5	19145	19112				
1985 118B	COSMOS 1711	16397	USSR	24 DEC	675.7	65.5	19151	19107				
1985 118C	COSMOS 1712	16398	USSR	24 DEC	676.3	65.4	19155	19132				
1985 118F		16404	USSR	24 DEC	675.5	65.5	19132	19117				
1985 118K		16445	USSR	24 DEC	340.4	65.2	18684	600				
1985 118L		16446	USSR	24 DEC	340.4	65.1	18906	633				
1985 119A	METEOR 2-13	16408	USSR	26 DEC	104.0	82.5	959	933				
1985 1196		16409	USSR	26 DEC	104.0	82.5	958	933				
1985 121D		16437	USSR	28 DEC	96.8	78.1	781	432				
1985 121E		16438	USSR	28 DEC	96.4	71.0	763	412				
1985 121F		16439	USSR	28 DEC	90.3	71.0	759	408				
1985 121G		16440	USSR	28 DEC	96.0	71.0	735	395				
1986 LAUNCHES												
1986 002A	COSMOS 1716	16449	USSR	9 JAN	115.5	74.0	1490	1462				
1986 002B	COSMOS 1717	16450	USSR	9 JAN	115.6	74.0	1511	1473				
1986 002C	COSMOS 1718	16451	USSR	9 JAN	115.6	74.0	1494	1473				
1986 002D	COSMOS 1719	16452	USSR	9 JAN	115.3	74.0	1483	1452				
1986 002E	COSMOS 1720	16453	USSR	9 JAN	115.1	74.0	1483	1438				
1986 002F	COSMOS 1721	16454	USSR	9 JAN	115.0	74.0	1481	1424				
1986 002G	COSMOS 1722	16455	USSR	9 JAN	114.8	74.0	1482	1410				
1986 002H	COSMOS 1723	16456	USSR	9 JAN	114.6	74.0	1480	1397				
1986 002J		16457	USSR	9 JAN	117.9	74.0	1695	1479				
1986 003B	SATCOM KUI	16462	US	12 JAN	1436.1	0.0	35801	35772				
1986 003C		16483	US	12 JAN	628.6	26.9	35511	348				
1986 005A	COSMOS 1726	16493	USSR	17 JAN	104.8	83.0	1002	966				

Table AII.4 Teledyne Brown Engineering History of On-Orbit Fragmentation.

TABLE 1. SATELLITE BREAKUP STATUS AS OF 4 OCTOBER 1987 (LISTED BY DATE OF EVENT)

INTERNATIONAL DESIGNATOR	COMMON NAME	CATALOG NUMBER	LAUNCH DATE	DATE OF EVENT	SATELLITE DEBRIS			PARENT SATELLITE			REMARKS
					CATALOGED	EVENT	IN ORBIT	INCL. (°)	APOGEE (KM)	PERIGEE (KM)	
1961-Omicron	TRANSIT 4A	119	29 Jun 61	29 Jun 61	281	279	215	66.8	998	880	Able Start Rocket
1962-B Iota	SPUTHNIK-29	443	24 Oct 62	29 Oct 62	26	24	0	65.1	261	202	Payload
1963-47	ATLAS CERTAUR 2	694	27 Nov 63	27 Nov 63	17	17	14	29.9	1735	502	More Debris Cataloged With 65-82 Rocket
1964-70	COSMOS 50	919	28 Oct 64	5 Nov 63	97	96	0	51.2	233	188	Payload
1965-12	COSMOS 57	1093	22 Feb 65	22 Feb 65	168	167	0	64.8	708	159	Yoshkod Test Flight
1965-20	COSMOS 61-63	1270	15 Mar 65	15 Mar 65	130	147	26	54.0	1827	260	Rocket
1965-82	TITAN 3C-4	1640	15 Oct 65	15 Oct 65	488	467	91	32.6	791	708	Titan 3C-4 Transtage Fragmented
1965-88	COSMOS 95	1706	4 Nov 65	Mid Nov 65	24	22	0	48.4	521	211	Payload?
1966-12	BLUEBELL 2 (OPS 3031)	2015	15 Feb 66	15 Feb 66	40	38	0	96.5	268	147	Inflated Sphere
1966-46	ATDA	2188	1 Jun 66	Jun 66	54	51	0	28.8	300	281	Atlas Rocket
1966-59	AS-203	2289	5 Jul 66	5 Jul 66	35	34	0	31.9	214	185	Saturn Rocket
1966-88	USSR/UNK.1	2437	17 Sep 66	17 Sep 66	53	53	0	49.6	792	138	Alleged FOBS Test
1966-101	USSR/UNK.2	2536	2 Nov 66	2 Nov 66	41	41	0	49.7	651	184	Alleged FOBS Test
1968-91	COSMOS 249	3504	20 Oct 68	20 Oct 68	99	98	59	62.3	2159	496	Alleged ASAT
1968-90	COSMOS 248	3503	19 Oct 68	8 Nov 68	5	5	0	62.2	543	473	Alleged ASAT Target
1968-97	COSMOS 252	3530	1 Nov 68	8 Nov 68	126	126	56	62.3	2139	534	Alleged ASAT